

Model Complexes for Active Sites of Diiron Metalloproteins; Dioxygen  
Reactivity and Water Effects

by  
Sungho Yoon  
M.Sc., Chemistry  
Korea University, 1998

SUBMITTED TO THE DEPARTMENT OF CHEMISTRY IN PARTIAL FULFILLMENT  
OF THE REQUIREMENTS FOR THE DEGREE OF

DOCTOR OF PHILOSOPHY IN INORGANIC CHEMISTRY  
AT THE  
MASSACHUSETTS INSTITUTE OF TECHNOLOGY

August 2004

© Massachusetts Institute of Technology, 2004  
All rights reserved

Signature of Author: \_\_\_\_\_

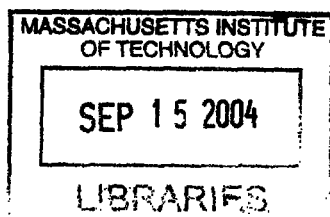
Department of Chemistry  
August XX, 2004

Certified By: \_\_\_\_\_

Stephen J. Lippard  
Arthur Amos Noyes Professor of Chemistry  
Thesis Supervisor

Accepted by: \_\_\_\_\_

Robert W. Field  
Chairman, Departmental Committee on Graduate Studies



ARCHIVES 17

This doctoral thesis has been examined by a committee of the Department of Chemistry as follows:



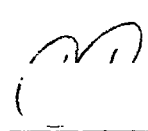
---

Daniel G. Nocera  
W. M. Keck Professor of Energy and Professor of Chemistry  
Committee Chairman



---

Stephen J. Lippard  
Arthur Amos Noyes Professor of Chemistry  
Thesis Supervisor



---

Christopher C. Cummins  
Professor of Chemistry

---

**Model Complexes for Active Sites of Diiron Metalloproteins; Dioxygen  
Reactivity and Water Effects**

By  
Sungho Yoon

Submitted to the Department of Chemistry on August 31, 2004, in partial  
fulfillment of the requirements for the degree of Doctor of Philosophy.

**Abstract**

**Chapter 1. Modeling Studies for Diiron Sites with Carboxylate Rich  
Coordination Environments in Dioxygen-Dependent Non-Heme Enzymes:  
Compounds Synthesized, Understanding Achieved, and Directions to Take**

Our efforts to better understand of dioxygen-dependent diiron proteins with carboxylate-rich coordination environments through synthesis of small model complexes are summarized. We describe both not only the significant results that have contributed toward this goal, but also the rationale behind how one generation of model systems gave way to the next.

**Chapter 2. Mechanistic Studies of the Oxidative *N*-Dealkylation of a Benzyl  
Group Substrates Tethered to Carboxylate-Bridged Diiron(II) Complexes,  
[Fe<sub>2</sub>(μ-O<sub>2</sub>CAr<sup>Tol</sup>)<sub>2</sub>(O<sub>2</sub>CAr<sup>Tol</sup>)<sub>2</sub>(*N,N*-Bn<sub>2</sub>en)<sub>2</sub>]**

Hammett and intramolecular kinetic isotope effect (KIE<sub>intra</sub>) analyses for oxidative *N*-dealkylation of [Fe<sub>2</sub>(μ-O<sub>2</sub>CAr<sup>Tol</sup>)<sub>2</sub>(O<sub>2</sub>CAr<sup>Tol</sup>)<sub>2</sub>(*N,N*-Bn<sub>2</sub>en)<sub>2</sub>] rule out previously proposed concerted and hydrogen atom transfer mechanisms. We conclude that the reaction operates through single-electron transfer from the non-bonding electron pair of the amine substrate to the dioxygen-generated intermediate, followed by proton transfer and rearrangement.

### Chapter 3. Synthesis, Characterization, and Dioxygen Reactivity of Tetracarboxylate-Bridged Diiron(II) Complexes with Coordinated Substrates

The synthesis and characterization of  $[\text{Fe}_2(\mu\text{-O}_2\text{CAr}^{\text{Tol}})_4\text{L}_2]$  complexes, where L is benzylamine (BA) or 4-methoxybenzylamine ( $\text{BA}^{p\text{-OMe}}$ ), and their oxygenation are described. Various methods, including resonance Raman (rR) and electron paramagnetic resonance (EPR) spectroscopy, have been applied to understand the mechanism and the intermediates involved. In addition, upon dissolution of the tetracarboxylate-bridged diiron(II) complex in methanol, an asymmetric tetrairon(II) cubane complex was identified and structurally characterized.

### Chapter 4. Synthesis and Characterization of $\{\text{Fe}_2(\mu\text{-OH})_2(\mu\text{-O}_2\text{CR})\}^{3+}$ and $\{\text{Fe}_2(\mu\text{-O})(\mu\text{-O}_2\text{CR})\}^{3+}$ Complexes with Carboxylate-Rich Metal Coordination Environment as Models for Diiron Centers in Oxygen-Dependent Non-Heme Enzymes

Utilizing hydrogen bonding interactions and sterically bulky carboxylates, synthetic routes were developed to prepare the mononuclear iron(II) complexes with the vacant coordination sites for  $\text{O}_2$  binding. Reactions of such complexes with  $\text{O}_2$  resulted in rare asymmetric complexes having an  $\{\text{Fe}_2(\mu\text{-O})(\mu\text{-O}_2\text{CR})\}^{3+}$  or  $\{\text{Fe}_2(\mu\text{-OH})_2(\mu\text{-O}_2\text{CR})\}^{3+}$  unit. These diiron(III) complexes with carboxylate-rich metal coordination environments reproduce the diiron(III) cores housed in four-helix bundles found in nature. Compound **3**, which replicates the  $\{\text{Fe}_2(\mu\text{-OH})_2(\mu\text{-O}_2\text{CR})\}$  core of sMMOH<sub>ox</sub>, shares several physical properties with the enzyme, electronic transitions, Mössbauer spectra, and magnetic exchange interactions. On the other hand, the structure of **4**, ( $\mu$ -oxo)( $\mu$ -carboxylato)diiron(III) complex, mimics the diiron(III) sites of RNR-R2. The electronic and Mössbauer spectral transitions of **4** are typical of diiron(III) complexes with an Fe–O–Fe moiety. Magnetic exchange coupling interaction between the two iron atoms is within the expected range for oxo-bridged diiron(III) sites. These results demonstrate how the diiron(III) structures in different metalloproteins, namely, the  $\mu$ -oxo

cores of RNR-R2 and the  $\mu$ -dihydroxo unit in MMOH, can be replicated by subtle changes in ligand composition.

### **Chapter 5. Synthesis and Characterization of Dinuclear Iron Complexes Having Proton Donors in the Ligand Framework**

We prepared carboxylate-rich diiron(II) complexes having proton donors in the close proximity to the bimetallic center. Two isomers, a windmill and a paddlewheel structure, were isolated from the same reaction mixture, attesting their similar energies and the likely interconversion between the two isomers by carboxylate shifts. Use of a sterically bulkier 3,5-dimethylpyrazole *N*-donor ligand compared to pyrazole ligand led exclusively to the isolation of a dicarboxylate-bridged diiron(II) complex.

### **Chapter 6. Di- and Tetra-Bridged Diiron(II) Complexes with Four Terphenyl-Derived Carboxylates and Two Water Molecules**

The water-containing diiron(II) complexes  $[\text{Fe}_2(\mu\text{-O}_2\text{CR})_2(\text{O}_2\text{CR})_2(\text{THF})_2(\text{OH}_2)_2]$  (1),  $[\text{Fe}_2(\mu\text{-OH}_2)_2(\mu\text{-O}_2\text{CR})_2(\text{O}_2\text{CR})_2(\text{THF})_2]$  (2) and  $[\text{Fe}_2(\mu\text{-OH}_2)_2(\mu\text{-O}_2\text{CR})_2(\text{O}_2\text{CR})_2(4\text{-}^t\text{BuC}_5\text{H}_4\text{N})_2]$  (3) were synthesized and structurally characterized. Two octahedral iron(II) centers in 2 and 3 are bridged by *m*-terphenyl-derived carboxylates and two water molecules, generating diamond cores. The bridging water molecules in 3 are in an on/off equilibrium with the dehydrated complex  $[\text{Fe}_2(\mu\text{-O}_2\text{CR})_4(4\text{-}^t\text{BuC}_5\text{H}_4\text{N})_2]$ .

### **Chapter 7. Water-Dependent Reactions of Diiron(II) Carboxylate Complexes**

Carboxylate-rich iron(II) complexes with varying numbers of water ligands have been characterized, including the first asymmetric complex with a  $\{\text{Fe}_2(\mu\text{-OH}_2)_2(\mu\text{-O}_2\text{CAr}^{4\text{F-Ph}})\}^{3+}$  unit. The isolations of those complexes attest to the idea that the carboxylate-bridged diiron(II) complexes act as sponges in response to water influx. The Mössbauer and variable temperature, variable field magnetic susceptibility experiments indicate that the compound  $[\text{Fe}_2(\mu\text{-OH}_2)_2(\mu\text{-O}_2\text{CAr}^{4\text{F-Ph}})]^{3+}$

$\text{Ph})(\text{O}_2\text{CAr}^{4\text{F-Ph}})_3(\text{THF})_2(\text{OH}_2)]$  has a high-spin diiron(II) core with little significant exchange coupling interaction.

## **Chapter 8. Water Affects the Dioxygen Reactivity of Carboxylate-Rich Diiron(II) Complexes as Models for Diiron Centers in Dioxygen-Dependent Non-Heme Enzymes**

High-spin diiron(II) complexes with distinct visible electronic transitions have been prepared to quantitatively measure the water-dependent equilibria. By utilizing a metal-to-ligand charge-transfer band, the effects of water molecules on the oxygenation of diiron(II) complex  $[\text{Fe}_2(\mu\text{-O}_2\text{CAr}^{\text{Tot}})_4(4\text{-NCC}_5\text{H}_4\text{N})_2]$  has been addressed. Water binds to the diiron(II) site, generating an open coordination site by shifting carboxylate from bridging to terminal. The available open coordination site for dioxygen binding may accelerate the oxygenation rate compared to oxygenation under anhydrous conditions.

Thesis Supervisor: Stephen J. Lippard

Title: Department Head and Arthur Amos Noyes Professor of Chemistry

*To my parents, my sisters and brothers, and my lovely wife Dongsook*

## Acknowledgements

### “ The Infinite Corridor ”

The last four years at MIT seemed to me a tunnel without any sign of ending. I wanted to sit down and give up, but was inspired and rescued by people who I want to acknowledge.

First, I thank my advisor, an excellent scientist, Steve Lippard for his encouragement and confidence in me. I am grateful for the advice that he provides for his students and the training I received in his lab to be prepared for anything in the world. I also thank other Inorganic Chemistry faculty members, especially Professor Dan Nocera, for his helpful suggestions. I also give my gratitude to my former advisor, Professor Ho-Gyum Jang at Korea University for inspiring and guiding me.

One of the best things about working in the Lippard lab is the wonderful group of coworkers that I have had. When I joined the lab in the fall of 2000, I moved from one bench to another to find a space to work, but ended up bothering Dan Kopp and Joey Bautistia. I really appreciate them for sharing their bench and teaching me stopped-flow kinetics and EPR technique, respectively. I am greatly indebted to Dr. Jane Kuzelka for helping me settle down in the lab and teaching Mössbauer and SQUID collection. I am grateful for her patience and willingness to answer all my questions. I appreciate the friendship and guidance offered by Edit Tshuva, who was my bench-mate for one year in the new lab in 4<sup>th</sup> floor. Rayane Moreira, Jeremy Kodanko, Laurance Beauvais, Christiana Xin Zhang, Liz Nolan, and Matthew Clark are all valuable members of the group and my dear friends, and my experiences here were great because of them.



I appreciate my classmates and lab-mates, Katie Barnes, Yongwon Jung, and Emily Carson who shared laughs and concerns with throughout the years. Katie proves that a cheerful personality is always a gift to coworkers and Emily has real strength with cookies and laughs that saved us from many dreadful situations. Yongwon also showed me why we need good friends to go through hard times. Other members enriched me with ideas and care. Mi Hee was like a younger sister and relieved my homesickness, and YooJin, I wish you the very best luck. Jessica Blazyk, thanks to you, I had no worries concerning computers. Dong Wang, Matthew Sazinsky and Caroyln Woodrooffe, we did it! It has been a less lonely journey to finish up because of you guys. You all will be great addition to your new teams.

Last, certainly the most important I must express my gratitude to my family. I feel like my grandfather and grandmother are still here with me. Because of their love and nurture, I am who I am. My parents are my strength and beacon. I thank my sisters and brothers for supporting and believing in me. I also thank all of my nieces and nephews who remind me how lucky I am to be in this wonderful family. My lovely wife, Dongsook, is a friend and partner to whom I can lean without any conditions. You know what! I really love you and appreciate your sacrifice over my humble Ph.D. It is for you.

**Table of Contents**

Abstract.....	3
Dedication.....	7
Acknowledgements .....	8
Table of Contents .....	10
List of Tables.....	15
List of Charts .....	17
List of Schemes.....	18
List of Figures.....	20
<b>Chapter 1. Modeling Studies for Diiron Sites with Carboxylate Rich Coordination Environments in Dioxygen-Dependent Non-Heme Enzymes: Compounds Synthesized, Understanding Achieved, and Directions to Take.....</b>	<b>29</b>
Introduction.....	30
Diiron Model Complexes with Oxygen Rich Metal Coordination Environments.....	32
General Comments.....	32
Dicarboxylate Bridging Diiron Complexes with Nitrogen Rich Coordination Environments .....	33
Small Diiron Complexes with Carboxylate Rich Coordination Environment.....	35
Carboxylate Rich Diiron Complexes with Pre-organized Bis(carboxylate) Platforms .....	36
Diiron Complexes with Four Sterically Hindered <i>m</i> -Terphenyl-based Carboxylate Ligands.....	38
Advanced Model Complexes from Diiron(II) Compounds with Oxygen Rich Metal Coordination Environment.....	40
General Comment .....	40
Understanding the water effect.....	41
Modeling the Syn Disposition of Nitrogen Donors.....	43
Conclusion and Perspective.....	43
References.....	45
<b>Chapter 2. Mechanistic Studies of the Oxidative N-Dealkylation of a Benzyl Group Substrates Tethered to Carboxylate-Bridged Diiron(II) Complexes, <math>[\text{Fe}_2(\mu\text{-O}_2\text{CAr}^{\text{Tot}})_2(\text{O}_2\text{CAr}^{\text{Tot}})_2(\text{N,N-Bn}_2\text{en})_2]</math>.....</b>	<b>59</b>
Introduction.....	60

Experimental Section .....	61
General Considerations .....	61
Physical Measurements .....	62
Synthesis of Benzyl(4-R-benzyl)aminoacetonitrile Compounds.....	62
Synthesis of Benzyl(4-R-benzyl)ethylenediamine Compounds ( <i>N,N</i> -(4-R-Bn)Bnen) .....	64
Synthesis of $[\text{Fe}_2(\mu\text{-O}_2\text{CAr}^{\text{Tol}})_2(\text{O}_2\text{CAr}^{\text{Tol}})_2(\text{N,N}\text{-}(4\text{-R-Bn})\text{Bnen})_2]$ Complexes .....	67
X-ray Crystallographic Studies .....	69
General Procedures for Oxidative <i>N</i> -Dealkylation Studies Using GC and GC/MS Analysis.....	70
Kinetic Isotope Effect Measurements .....	71
Results.....	71
Ligand Syntheses.....	71
Synthesis and Structural Characterization of Diiron(II) Complexes .....	72
Hammett Study of the Diiron(II) Complexes with Dioxygen .....	73
Kinetic Isotope Effects.....	73
Discussion.....	75
References.....	79
<b>Chapter 3. Synthesis, Characterization, and Dioxygen Reactivity of Tetracarboxylate- Bridged Diiron(II) Complexes with Coordinated Substrates .....</b>	<b>102</b>
Introduction.....	103
Experimental Section.....	104
General Considerations .....	104
X-ray Crystallographic Studies .....	107
<sup>57</sup> Fe Mössbauer Spectroscopy .....	108
Magnetic Susceptibility.....	108
Electrochemistry.....	109
Resonance Raman Spectroscopy.....	109
EPR .....	110
Stopped-flow Kinetics.....	110
GC/MS Studies .....	110
Kinetic Isotope Effect .....	111
Results and Discussion.....	111

Synthesis and Structural Characterization of Compounds .....	112
Mössbauer Spectroscopy .....	113
Magnetochemistry.....	113
Electrochemistry.....	115
Reactivity with Dioxygen and Characterization of Intermediates.....	115
Oxygenation Product Analysis and Kinetic Isotope Effect (KIE).....	116
Summary.....	117
References.....	118
<b>Chapter 4. Synthesis and Characterization of <math>\{\text{Fe}_2(\mu\text{-OH})_2(\mu\text{-O}_2\text{CR})\}^{3+}</math> and <math>\{\text{Fe}_2(\mu\text{-O})(\mu\text{-O}_2\text{CR})\}^{3+}</math> Complexes with Carboxylate-Rich Metal Coordination Environment as Models for Diiron Centers in Oxygen-Dependent Non-Heme Enzymes .....</b>	<b>139</b>
Introduction.....	140
Experimental Section.....	142
General Procedures.....	142
Synthetic Procedures.....	142
Physical Measurements .....	144
X-ray Crystallographic Studies .....	145
Results and Discussion.....	146
Synthesis .....	146
Description of Structures.....	147
Electronic Absorption Properties.....	150
Summary.....	152
References.....	154
<b>Chapter 5. Synthesis and Characterization of Dinuclear Iron Complexes Having Proton Donors in the Ligand Framework.....</b>	<b>173</b>
Introduction.....	174
Experimental Section.....	175
General Considerations .....	175
Synthetic Procedures.....	175
X-ray Crystallography .....	176
Mössbauer Spectroscopy .....	177
EPR.....	177
Results.....	178

Synthesis and Structural Characterization of Compounds .....	178
Mössbauer Spectroscopic Properties of Compounds.....	181
Summary.....	181
References.....	183
<b>Chapter 6. Di- and Tetra-Bridged Diiron(II) Complexes with Four Terphenyl-Derived Carboxylates and Two Water Molecules .....</b>	<b>196</b>
Introduction.....	197
Experimental .....	198
General Considerations .....	198
Synthetic Procedures.....	198
X-ray Crystallography .....	200
Electrochemistry.....	200
Results and Discussion.....	201
Synthesis and Characterization of the Diiron(II) Complexes.....	201
Vibrational and Electrochemical Properties.....	204
Summary.....	206
References.....	207
<b>Chapter 7. Water-Dependent Reactions of Diiron(II) Carboxylate Complexes .....</b>	<b>221</b>
Introduction.....	222
Experimental .....	223
General Considerations .....	223
Synthetic Procedures.....	224
X-ray Crystallography .....	224
<sup>57</sup> Fe Mössbauer Spectroscopy .....	225
Magnetic Susceptibility.....	225
Results and Discussion.....	225
Synthesis and Structural Characterization of the Iron(II) Complexes.....	226
Mössbauer Spectroscopic Properties of Complex 2 .....	228
Multifield Saturated Magnetic Susceptibility of Complex 2 .....	228
Conclusions and Summary .....	230
References.....	232

**Chapter 8. Water Affects the Dioxygen Reactivity of Carboxylate-Rich Diiron(II) Complexes as Models for Diiron Centers in Dioxygen-Dependent Non-Heme**

<b>Enzymes</b> .....	245
<b>Introduction</b> .....	246
<b>Experimental Section</b> .....	247
General Considerations .....	247
Synthetic Procedures.....	247
X-ray Crystallographic Studies .....	250
<sup>57</sup> Fe Mössbauer Spectroscopy .....	251
Electrochemistry.....	251
Resonance Raman Spectroscopy.....	251
Stopped-flow Kinetics.....	252
<b>Results and Discussion</b> .....	252
Syntheses and Structural Characterization of Diiron(II) Complexes.....	253
Mössbauer Properties .....	255
Magnetic Properties .....	257
Electronic and Resonance Raman Spectroscopy .....	257
The Equilibrium Related to Coordinating Solvents .....	258
The Water Dependent Equilibrium .....	259
Electrochemistry.....	260
Water Effect on the Oxygenation Rate of Compound 1.....	261
Isolation and Structural Characterization of Iron(III) Complexes .....	263
Mechanistic Considerations .....	264
<b>Summary</b> .....	264
<b>References</b> .....	266

## List of Tables

### Chapter 2

Table 2.1.	Summary of X-ray crystallographic data.....	82
Table 2.2.	Selected interatomic distances (Å) and angles (deg) for 2 - 8 .....	84
Table 2.3.	Yield and product distribution of reaction of 2 – 6 with dioxygen .....	86

### Chapter 3

Table 3.1.	Summary of X-ray crystallographic information for 1 - 3 .....	120
Table 3.2.	Selected interatomic bond lengths (Å) and angles (deg) for 1 and 2.....	121
Table 3.3.	Selected interatomic bond lengths (Å) and angles (deg) for 3 .....	122
Table 3.4.	Summary of Mössbauer parameters for 1 - 3 recorded at 4.2 K.....	123

### Chapter 4

Table 4.1.	Summary of X-ray crystallographic data for compounds 1 - 4.....	156
Table 4.2.	Selected interatomic distances (Å) and angles (deg) for 1 and 2 .....	157
Table 4.3.	Selected interatomic distances (Å) and angles (deg) for 3 and 4 .....	158
Table 4.4.	Summary of pertinent spectroscopic data for 3, 4, sMMOH <sub>ov</sub> and RNR-R2 .....	159

### Chapter 5

Table 5.1.	Summary of X-ray crystallographic data for 1 -4.....	184
Table 5.2.	Selected interatomic distances (Å) and angles (deg) for 1 and 2 .....	185
Table 5.3.	Selected interatomic distances (Å) and angles (deg) for 3.....	186
Table 5.4.	Selected interatomic distances (Å) and angles (deg) for 4.....	187

### Chapter 6

Table 6.1.	Summary of X-ray crystallographic information for compound 1 - 3.....	210
Table 6.2.	Selected interatomic bond lengths (Å) and angles (deg) for compound 1 - 3 .....	211

### Chapter 7

Table 7.1.	Summary of X-ray crystallographic information for 1 - 3 .....	234
------------	---	-----

Table 7.2.	Selected interatomic distances (Å) and angles (deg) for 1.....	235
Table 7.3.	Selected interatomic distances (Å) and angles (deg) for 2.....	236

## Chapter 8

Table 8.1.	Summary of X-ray Crystallographic Data .....	268
Table 8.2.	Selected interatomic bond lengths (Å) and angles (deg) for 1 and 2.....	270
Table 8.3.	Selected interatomic bond lengths (Å) and angles (deg) for 3 and 4.....	271
Table 8.4.	Selected interatomic bond lengths (Å) and angles (deg) for 6 .....	272
Table 8.5.	Selected interatomic bond lengths (Å) and angles (deg) for 7 .....	273
Table 8.6.	4.2 K zero-field Mössbauer parameters for 2, 3, 5, reported carboxylate rich iron(II) complexes, and enzymes of interest .....	274
Table 8.7.	Rate constants ( $k_{1_{obs}}$ ) for oxygenation of 1 in $\text{CH}_2\text{Cl}_2$ .....	275
Table 8.8.	Rate Constants ( $k_{2_{obs}}$ and $k_{3_{obs}}$ ) for oxygenation of 2 in water containing $\text{CH}_2\text{Cl}_2$ .....	276



## List of Charts

### Chapter 4

- Chart 4.1. Representations of the active sites of  $\text{MMOH}_{\text{ox}}$  and  $\text{RNR-R2}_{\text{act}}$  ..... 160  
 Table 4.2. Representations of the diiron core of oxyHr and 4 ..... 161

### Chapter 5

- Table 5.1. Representations of the active sites of  $\text{MMOH}$ ,  $\text{RNR-R2}$ , and  $\Delta 9\text{D}$  ..... 188

### Chapter 6

- Chart 6.1. Representations of the structures of  $\text{MMOH}_{\text{red}}$  and proposed  $\text{MMOH}_{\text{superoxo}}$   
 ..... 212  
 Chart 6.2. Representations of the quadrilateral diiron cores..... 213

## List of Schemes

### Chapter 1

Schemes 1.1. Observed carboxylate shifts and proposed mechanism for oxygenation of 4 .....	49
Schemes 1.2. Proposed equilibrium between di- and tetracarboxylate bridged diiron(II) complexes .....	50
Schemes 1.3. Proposed reaction pathway for oxygenation of 11 .....	51
Schemes 1.4. Proposed reaction pathway for oxygenation of 13 .....	52
Schemes 1.5. Observed water-dependent equilibrium .....	53

### Chapter 2

Scheme 2.1. Three proposed reaction mechanisms for oxygenation of 1 .....	87
Scheme 2.2. Synthesis and reactivity of compounds 2 - 6 .....	88
Scheme 2.3. Schematic representations of two different KIEs for 7 and 8 .....	89
Scheme 2.3. The proposed mechanism for oxidative N-dealkylation of 1.....	90

### Chapter 4

Scheme 4.1. Representations of bimolecular combination of two mononuclear complexes, generating dinuclear species.....	162
Scheme 4.2. Synthesis of mono and dinuclear iron complexes.....	163

### Chapter 5

Scheme 5.1. Synthesis of dinuclear iron complexes 1 - 4.....	189
--	-----

### Chapter 6

Scheme 6.1. Proposed redox cycles for complex 3 .....	214
---	-----

### Chapter 7

Scheme 7.1. Synthesis of iron(II) complexes 1 - 3.....	237
Scheme 7.2. Possible reduction of a diiron(III) complex with the $\{\text{Fe}_2(\mu\text{-OH})_2(\mu\text{-O}_2\text{CR})\}^{3+}$ core to a diiron(III) complex with $\{\text{Fe}_2(\mu\text{-OH})_2(\mu\text{-O}_2\text{CR})\}^{3+}$ core .....	238

**Chapter 8**

Scheme 8.1. Synthesis of complexes <b>1</b> and <b>2</b> and their reactivity .....	277
Scheme 8.2. Observed solvent-dependent equilibrium of <b>1</b> .. .....	278
Scheme 8.3. Observed water-dependent equilibrium of <b>1</b> .....	279
Scheme 8.4. Proposed redox cycles for complex <b>3</b> .....	280
Scheme 8.5. Schematic diagram for oxygenation of <b>1</b> with or without water .....	281

## List of Figures

### Chapter 1

- Figure 1.1. Representations of the active sites of the non-heme diiron proteins with carboxylate rich coordination environment. A) The reduced sMMMO B) Oxidized sMMOH C) reduced RNR-R2 D) oxidized RNR-R2 E) reduced  $\Delta 9D$  ..... 54
- Figure 1.2. Examples of dicarboxylate bridged diiron(III) complexes with nitrogen rich coordination environments ..... 55
- Figure 1.3. The XDK family of ligands and resulting bis(-carboxylato)diiron(II) complex..... 56
- Figure 1.4. Examples of sterically hindered carboxylate ligands derived from *m*-terphenyl carboxylate and examples of diiron(II) complexes containing these carboxylates ..... 57
- Figure 1.5. Representation of the cation  $[\text{Fe}_2(\text{Et}_2\text{BCQEB}^{\text{Et}})(\mu\text{-O}_2\text{CAr}^{\text{Tol}})_3]^+$  (19) featuring syn disposition of nitrogen donors..... 58

### Chapter 2

- Figure 2.1. ORTEP drawing of  $[\text{Fe}_2(\mu\text{-O}_2\text{CAr}^{\text{Tol}})_2(\text{O}_2\text{CAr}^{\text{Tol}})_2(\text{N},\text{N}\text{-}(4\text{-Cl-Bn})\text{Bnen})_2]$  (2) showing 50 % probability thermal ellipsoids. The solvent molecules and hydrogen atoms are omitted for clarity ..... 91
- Figure 2.2. ORTEP drawing of  $[\text{Fe}_2(\mu\text{-O}_2\text{CAr}^{\text{Tol}})_2(\text{O}_2\text{CAr}^{\text{Tol}})_2(\text{N},\text{N}\text{-}(4\text{-F-Bn})\text{Bnen})_2]$  (3) showing 50 % probability thermal ellipsoids. The solvent molecules and hydrogen atoms are omitted for clarity ..... 92
- Figure 2.3. ORTEP drawing of  $[\text{Fe}_2(\mu\text{-O}_2\text{CAr}^{\text{Tol}})_2(\text{O}_2\text{CAr}^{\text{Tol}})_2(\text{N},\text{N}\text{-}(4\text{-Me-Bn})\text{Bnen})_2]$  (4) showing 50 % probability thermal ellipsoids. The solvent molecules and hydrogen atoms are omitted for clarity ..... 93
- Figure 2.4. ORTEP drawing of  $[\text{Fe}_2(\mu\text{-O}_2\text{CAr}^{\text{Tol}})_2(\text{O}_2\text{CAr}^{\text{Tol}})_2(\text{N},\text{N}\text{-}(4\text{-}^t\text{Bu-Bn})\text{Bnen})_2]$  (5) showing 50 % probability thermal ellipsoids. The solvent molecules and hydrogen atoms are omitted for clarity ..... 94
- Figure 2.5. ORTEP drawing of  $[\text{Fe}_2(\mu\text{-O}_2\text{CAr}^{\text{Tol}})_2(\text{O}_2\text{CAr}^{\text{Tol}})_2(\text{N},\text{N}\text{-}(4\text{-OMe-Bn})\text{Bnen})_2]$  (6) showing 50 % probability thermal ellipsoids. The solvent molecules and hydrogen atoms are omitted for clarity..... 95

- Figure 2.6. ORTEP drawings of  $[\text{Fe}_2(\mu\text{-O}_2\text{CAr}^{\text{Tol}})_2(\text{O}_2\text{CAr}^{\text{Tol}})_2((\text{C}_6\text{H}_5\text{CDH})_2\text{en})_2]$  (7) (Top) showing 50 % probability thermal ellipsoids. The solvent molecules and hydrogen atoms are omitted for clarity. (Bottom) All atoms of  $\text{Ar}^{\text{Tol}}\text{CO}_2^-$  ligands in 7, except for the carboxylate groups and the  $\alpha$ -carbon atoms, were omitted for clarity..... 96
- Figure 2.7. ORTEP drawing of  $[\text{Fe}_2(\mu\text{-O}_2\text{CAr}^{\text{Tol}})_2(\text{O}_2\text{CAr}^{\text{Tol}})((\text{D}_2\text{-Bn})\text{Bnen})_2]$  (8) (Top) showing 50 % probability thermal ellipsoids. The solvent molecules and hydrogen atoms are omitted for clarity. (Bottom) all atoms of  $\text{Ar}^{\text{Tol}}\text{CO}_2^-$  ligands in 8, except for the carboxylate groups and the  $\alpha$ -carbon atoms, were omitted for clarity ..... 97
- Figure 2.8. The oxygenation product distributions of  $[\text{Fe}_2(\mu\text{-O}_2\text{CAr}^{\text{Tol}})_2(\text{O}_2\text{CAr}^{\text{Tol}})_2\text{-}(\text{N,N}\text{-}(4\text{-F-Bn})\text{Bnen})_2]$  (3) and  $[\text{Fe}_2(\mu\text{-O}_2\text{CAr}^{\text{Tol}})_2(\text{O}_2\text{CAr}^{\text{Tol}})(\text{N,N}\text{-}(4\text{-}^t\text{Bu-Bn})\text{Bnen})_2]$  (5) at 23 °C, determined  $^1\text{H}$  NMR spectroscopy, are shown in A) and B), respectively ..... 98
- Figure 2.9. Hammett plot for the oxygenation of  $[\text{Fe}_2(\mu\text{-O}_2\text{CAr}^{\text{Tol}})_2(\text{O}_2\text{CAr}^{\text{Tol}})_2((4\text{-R})\text{-BnBnen})_2]$  (R = Cl, F, H, Me, *t*-Bu, and OCH<sub>3</sub>) in CH<sub>2</sub>Cl<sub>2</sub> at 23 °C.  $Y_{\text{H}}$  and  $Y_{\text{R}}$  stand for the product yields of PhCHO and 4-R-PhCHO, respectively. The line represents a least squares fit to the data with the slope  $\rho = 0.48$  ( $R = 0.98$ ) ..... 99
- Figure 2.10. The oxygenation product distribution of 7 at 23 °C. A) GC-MS: 20.011 min, PhCHO ( $M^+ = 106$ ); 20.08 min, PhCDO ( $M^+ = 107$ ) B)  $^1\text{H}$  NMR spectrum: 10.01, (s, 1H from PhCHO), 7.88, (d, 2H from the combination of PhCHO and PhCDO) ..... 100
- Figure 2.11. The oxygenation product distribution of 8 at 23 °C. A) and B)  $^1\text{H}$  NMR spectrum: 10.01, (s, 1H from PhCHO), 7.88, (d, 2H from the combination of PhCHO and PhCDO)..... 101
- Chapter 3**
- Figure 3.1. Top: ORTEP diagram of  $[\text{Fe}_2(\mu\text{-O}_2\text{CAr}^{\text{Tol}})_4(\text{BA})_2]$  (1) showing 50 % probability thermal ellipsoids for all non-hydrogen atoms. Bottom: The aromatic rings of  $\text{Ar}^{\text{Tol}}\text{CO}_2^-$  ligands are omitted for clarity ..... 126

- Figure 3.2. Top: ORTEP diagram of  $[\text{Fe}_2(\mu\text{-O}_2\text{CAr}^{\text{Tol}})_4(\text{BA}^{p\text{-OMe}})_2]$  (2) showing 50 % probability thermal ellipsoids for all non-hydrogen atoms. Bottom left: The aromatic rings of  $\text{Ar}^{\text{Tol}}\text{CO}_2^-$  ligands are omitted for clarity. Bottom right: Crystal packing diagram of 2..... 127
- Figure 3.3. Top: ORTEP diagram of  $[\text{Fe}_4(\mu\text{-OMe})_4(\text{O}_2\text{CAr}^{\text{Tol}})_4(\text{HOMe})_6]$  (3) showing 50 % probability thermal ellipsoids for all non-hydrogen atoms. Bottom left: The aromatic rings of  $\text{Ar}^{\text{Tol}}\text{CO}_2^-$  ligands are omitted for clarity and hydrogen-bonding interactions are depicted with dot lines. Bottom right: The cubane core diagram with carboxylates and bridging methoxides .. 128
- Figure 3.4. Zero-field Mössbauer spectrum (experimental data (|), calculated fit (—)) recorded at 4.2 K of the solid sample of  $[\text{Fe}_2(\mu\text{-O}_2\text{CAr}^{\text{Tol}})_4(\text{BA})_2]$  (1) and  $[\text{Fe}_2(\mu\text{-O}_2\text{CAr}^{\text{Tol}})_4(\text{BA}^{p\text{-OMe}})_2]$  (2), top and bottom, respectively..... 129
- Figure 3.5. Zero-field Mössbauer spectrum (experimental data (|), calculated fit (—)) recorded at 4.2 K of the solid sample of  $[\text{Fe}_4(\mu\text{-OMe})_4(\text{O}_2\text{CAr}^{\text{Tol}})_4(\text{HOMe})_6]$  (3)..... 130
- Figure 3.6. Plots of the effective magnetic moment ( $\mu_{\text{eff}}$ ) per molecule versus temperature (filled circles) and molar susceptibility ( $\chi_{\text{M}}$ ) versus temperature (unfilled circles) for  $[\text{Fe}_2(\mu\text{-O}_2\text{CAr}^{\text{Tol}})_4(\text{BA})_2]$  (1)..... 131
- Figure 3.7. Plots of the effective magnetic moment ( $\mu_{\text{eff}}$ ) per molecule versus temperature (Top) and molar susceptibility ( $\chi_{\text{M}}$ ) versus temperature (Bottom) for  $[\text{Fe}_2(\mu\text{-O}_2\text{CAr}^{\text{Tol}})_4(\text{BA}^{p\text{-OMe}})_2]$  (2). The line represents the fit .. 132
- Figure 3.8. Plots of molar susceptibility ( $\chi_{\text{M}}$ ) versus inverse temperature for  $[\text{Fe}_2(\mu\text{-O}_2\text{CAr}^{\text{Tol}})_4(\text{BA}^{p\text{-OMe}})_2]$  (2), measured at 0.5 T ..... 133
- Figure 3.9. Cyclic voltammograms of  $[\text{Fe}_2(\mu\text{-O}_2\text{CAr}^{\text{Tol}})_4(\text{BA}^{p\text{-OMe}})_2]$  (2) in  $\text{CH}_2\text{Cl}_2$  with 0.5 M  $(\text{Bu}_4\text{N})\text{PF}_6$  as supporting electrolyte and a scan rate of 25 mV/s... 134
- Figure 3.10. (a) Spectral changes that occur during the reaction of 2 ( $1.46 \times 10^{-4}$  M) with dioxygen in  $\text{CH}_2\text{Cl}_2$  at  $-78$  °C. (Inset) Kinetic trace for the development and decay of the intermediate recorded at 645 nm. (b) UV-vis spectrum of  $[\text{Fe}_2(\mu\text{-O}_2\text{CAr}^{\text{Tol}})_4(\text{BA}^{p\text{-OMe}})_2](\text{PF}_6)$  in  $\text{CH}_2\text{Cl}_2$  ..... 135
- Figure 3.11. Resonance Raman spectra of the frozen solution of intermediates derived from the oxygenation of  $[\text{Fe}_2(\mu\text{-O}_2\text{CAr}^{\text{Tol}})_4(\text{BA}^{p\text{-OMe}})_2]$  (2) with  $^{16}\text{O}_2$  (top

- spectrum) and  $^{18}\text{O}_2$  (bottom spectrum) at  $-78\text{ }^\circ\text{C}$ . The asterisk indicates a solvent band ..... 136
- Figure 3.12. X-band EPR spectra of a frozen  $\text{CH}_2\text{Cl}_2$  solution sample of (a) intermediate species generated by the oxygenation of **2** at  $-78\text{ }^\circ\text{C}$ , (b)  $[\text{Fe}_2(\mu\text{-O}_2\text{CAr}^{\text{Tol}})_4\text{-}(\text{BA}^{p\text{-OMe}})_2](\text{PF}_6)$ , measured at 5 K ..... 137
- Chapter 4**
- Figure 4.1. Top: ORTEP diagrams of  $[\text{Fe}(\text{O}_2\text{CAr}^{\text{Tol}})_2(\text{Hdmpz})_2]$  (**1**) showing 50 % probability thermal ellipsoids for all non-hydrogen atoms. The hydrogen atoms in the N–H group of Hdmpz ligands are added to show the hydrogen bond interaction. Bottom: Space-filling representation of **1**, drawn as in top ..... 164
- Figure 4.2. ORTEP diagrams of  $[\text{Fe}(\text{O}_2\text{CAr}^{\text{4F-Ph}})_2(\text{Hdmpz})_2]$  (**2**) showing 50 % probability thermal ellipsoids for all non-hydrogen atoms. The hydrogen atoms in the N–H group of Hdmpz ligands are added to show the hydrogen bond interaction..... 165
- Figure 4.3. Top: ORTEP diagrams of  $[\text{Fe}_2(\mu\text{-OH})_2(\mu\text{-O}_2\text{CAr}^{\text{Tol}})(\text{O}_2\text{CAr}^{\text{Tol}})_3(\text{OH}_2)\text{-}(\text{Hdmpz})_2]$  (**3**) showing 50 % probability thermal ellipsoids for all non-hydrogen atoms. The hydrogen atoms in the N–H group of Hdmpz, the bridging O–H group, and water ligands are added. The aromatic rings of  $\text{Ar}^{\text{Tol}}\text{CO}_2^-$  ligands are omitted for clarity. Bottom: Crystal packing diagram of **3**..... 166
- Figure 4.4. Top: ORTEP diagrams of  $[\text{Fe}_2(\mu\text{-O})(\mu\text{-O}_2\text{CAr}^{\text{4F-Ph}})(\text{O}_2\text{CAr}^{\text{4F-Ph}})_3(\text{Hdmpz})_3]$  (**4**) showing 50 % probability thermal ellipsoids for all non-hydrogen atoms. The hydrogen atoms in the N–H group of Hdmpz ligands are added. Bottom: The phenyl rings of  $\text{Ar}^{\text{4F-Ph}}\text{CO}_2^-$  ligands are omitted for clarity. Bottom left: Crystal packing diagram of **4**..... 167
- Figure 4.5. UV-vis spectra of  $[\text{Fe}_2(\mu\text{-OH})_2(\mu\text{-O}_2\text{CAr}^{\text{Tol}})(\text{O}_2\text{CAr}^{\text{Tol}})_3(\text{OH}_2)(\text{Hdmpz})_2]$  (**3**) (dashed line) and  $[\text{Fe}_2(\mu\text{-O})(\mu\text{-O}_2\text{CAr}^{\text{4F-Ph}})(\text{O}_2\text{CAr}^{\text{4F-Ph}})_3(\text{Hdmpz})_3]$  (**4**) (solid line) in  $\text{CH}_2\text{Cl}_2$  ..... 168
- Figure 4.6. Mössbauer spectrum (experimental data (|), calculated fit (–)) recorded at 4.2 K for a solid sample of  $[\text{Fe}(\text{O}_2\text{CAr}^{\text{4F-Ph}})_2(\text{Hdmpz})_2]$  (**2**) ..... 169

- Figure 4.7. Mössbauer spectra (experimental data (|), calculated fit (–)) recorded at 4.2 K for a solid sample of **3** (A) and **4** (B) ..... 170
- Figure 4.8. Plots of  $\chi_M$  (o) and  $\mu_{\text{eff}}$  (•) vs  $T$  for solid **3**. The solid lines represents the best least-squares fit of eq 1 (see text) to the experimental susceptibility data..... 171
- Figure 4.9. Plots of  $\chi_M$  (o) and  $\mu_{\text{eff}}$  (•) vs  $T$  for solid **4**. The solid lines represents the best least-squares fit of eq 1 (see text) to the experimental susceptibility data..... 172
- Chapter 5**
- Figure 5.1. ORTEP drawing of  $[\text{Fe}_2(\mu\text{-O}_2\text{CAr}^{\text{Tot}})_4(\text{pz})_2]$  (**1**) showing 50 % probability thermal ellipsoids. (Top, Left) The hydrogen atoms are omitted for clarity. (Top, Right) Side on view showing pocket generated by four carboxylates. (Bottom) Drawing with the aromatic rings of  $\text{Ar}^{\text{Tot}}\text{CO}_2^-$  ligands omitted for clarity ..... 190
- Figure 5.2. ORTEP drawing of  $[\text{Fe}_2(\mu\text{-O}_2\text{CAr}^{\text{Tot}})_2(\text{O}_2\text{CAr}^{\text{Tot}})(\text{pz})_2]$  (**2**) showing 50 % probability thermal ellipsoids. (Top) The solvent molecules and hydrogen atoms are omitted for clarity. (Bottom) The aromatic rings of  $\text{Ar}^{\text{Tot}}\text{CO}_2^-$  ligands were omitted for clarity ..... 191
- Figure 5.3. ORTEP drawing of  $[\text{Fe}_2(\mu\text{-O}_2\text{CAr}^{\text{Tot}})_2(\text{O}_2\text{CAr}^{\text{Tot}})_2(\text{Hdmpz})_2]$  (**3**) showing 50 % probability thermal ellipsoids. (Top) The solvent molecules and hydrogen atoms are omitted for clarity. (Bottom) The aromatic rings of  $\text{Ar}^{\text{Tot}}\text{CO}_2^-$  ligands were omitted for clarity ..... 192
- Figure 5.4. X-band EPR spectra collected at 5 K. A) The toluene solution of **3** B) Samples were prepared by exposing a toluene solution of **3** to  $\text{O}_2$  at  $-78^\circ\text{C}$  and freeze-quenching after 10 sec in liquid  $\text{N}_2$ . C) The fully oxidized toluene solution of **3** at the room temperature..... 193
- Figure 5.5. ORTEP drawing of  $[\text{Fe}_2(\mu\text{-O})(\text{O}_2\text{CAr}^{\text{Tot}})_4(\text{Hdmpz})_2]$  (**4**) showing 50 % probability thermal ellipsoids. (Top) The solvent molecules and hydrogen atoms are omitted for clarity. (Bottom) The aromatic rings of  $\text{Ar}^{\text{Tot}}\text{CO}_2^-$  ligands were omitted for clarity ..... 194



- Figure 5.6. Mössbauer spectra (experimental data (|), calculated fit (—)) recorded at 4.2 K for a solid sample of  $[\text{Fe}_2(\mu\text{-O}_2\text{CAr}^{\text{Tol}})_2(\text{O}_2\text{CAr}^{\text{Tol}})_2(\text{Hdmpz})_2]$  (3) (Left) and  $[\text{Fe}_2(\mu\text{-O})(\text{O}_2\text{CAr}^{\text{Tol}})_4(\text{Hdmpz})_2]$  (4) (Right) ..... 195

## Chapter 6

- Figure 6.1. Top: ORTEP diagrams of  $[\text{Fe}_2(\text{OH}_2)_2(\mu\text{-O}_2\text{CAr}^{4\text{F-Ph}})_2(\text{O}_2\text{CAr}^{4\text{F-Ph}})_2(\text{THF})_2]$  (1) showing 50 % probability thermal ellipsoids for all non-hydrogen atoms. Bottom: Drawing with the phenyl rings of  $\text{Ar}^{4\text{F-Ph}}\text{CO}_2^-$  ligands omitted for clarity ..... 215
- Figure 6.2. ORTEP diagram of  $[\text{Fe}_2(\mu\text{-OH}_2)_2(\mu\text{-O}_2\text{CAr}^{\text{Tol}})_2(\text{O}_2\text{CAr}^{\text{Tol}})_2(\text{THF})_2]$  (2) showing 50 % probability thermal ellipsoids for all non-hydrogen atoms. The phenyl rings of  $\text{Ar}^{\text{Tol}}\text{CO}_2^-$  ligands are omitted for clarity ..... 216
- Figure 6.3. ORTEP diagrams of  $[\text{Fe}_2(\mu\text{-OH}_2)_2(\mu\text{-O}_2\text{CAr}^{\text{Tol}})_2(\text{O}_2\text{CAr}^{\text{Tol}})_2(4\text{-}^t\text{BuC}_5\text{H}_4\text{N})_2]$  (3) showing 50 % probability thermal ellipsoids for all non-hydrogen atoms. Drawing with the phenyl rings of  $\text{Ar}^{\text{Tol}}\text{CO}_2^-$  ligands omitted for clarity . 217
- Figure 6.4. IR spectra of (A, B)  $[\text{Fe}_2(\mu\text{-OH}_2)_2(\mu\text{-O}_2\text{CAr}^{\text{Tol}})_2(\text{O}_2\text{CAr}^{\text{Tol}})_2(4\text{-}^t\text{BuC}_5\text{H}_4\text{N})_2]$  (3), before and after heating, and (C)  $[\text{Fe}_2(\mu\text{-O}_2\text{CAr}^{\text{Tol}})_4(4\text{-}^t\text{BuC}_5\text{H}_4\text{N})_2]$  ..... 218
- Figure 6.5. Cyclic voltammograms of (A and B)  $[\text{Fe}_2(\mu\text{-OH}_2)_2(\mu\text{-O}_2\text{CAr}^{\text{Tol}})_2(\text{O}_2\text{CAr}^{\text{Tol}})_2(4\text{-}^t\text{BuC}_5\text{H}_4\text{N})_2]$  (3) in  $\text{CH}_2\text{Cl}_2$  with 0.5 M  $(\text{Bu}_4\text{N})\text{PF}_6$  as supporting electrolyte and a scan rate of 50 mV/s ..... 219
- Figure 6.6. Cyclic voltammograms of  $[\text{Fe}_2(\mu\text{-O}_2\text{CAr}^{\text{Tol}})_4(4\text{-}^t\text{BuC}_5\text{H}_4\text{N})_2]$  with variable amounts of  $\text{H}_2\text{O}$  in  $\text{CH}_2\text{Cl}_2$  with 0.5 M  $(\text{Bu}_4\text{N})\text{PF}_6$  as supporting electrolyte and a scan rate of 50 mV/s ..... 220

## Chapter 7

- Figure 7.1. Top: ORTEP diagrams of  $[\text{Fe}(\text{H}_2\text{O})_6(\text{O}_2\text{CAr}^{4\text{F-Ph}})_2(\text{THF})_2]$  (1), showing 50 % probability thermal ellipsoids for all non-hydrogen atoms in one unit cell. Bottom: Ball and stick diagrams of 8 unit cells ..... 239
- Figure 7.2. Ball and stick diagram of  $[\text{Fe}(\text{H}_2\text{O})_6(\text{O}_2\text{CAr}^{4\text{F-Ph}})_2(\text{THF})_2]$  (1) The aromatic rings of  $\text{Ar}^{4\text{F-Ph}}\text{CO}_2^-$  ligands and hydrogen atoms in THF molecules are omitted for clarity. Left and right are the side on views to each other .... 240

- Figure 7.3. (Top) ORTEP diagrams of  $[\text{Fe}_2(\mu\text{-OH}_2)_2(\mu\text{-O}_2\text{CAr}^{4\text{F-Ph}})(\text{O}_2\text{CAr}^{4\text{F-Ph}})_3(\text{THF})_2\text{-}(\text{OH}_2)]$  (2) showing 50 % probability thermal ellipsoids for all non-hydrogen atoms in one unit cell. (Bottom) The aromatic rings of  $\text{Ar}^{4\text{F-Ph}}\text{CO}_2^-$  ligands and hydrogen atoms in THF molecules are omitted for clarity ..... 241
- Figure 7.4. Top: ORTEP diagram of  $[\text{Fe}_2(\text{OH}_2)_2(\mu\text{-O}_2\text{CAr}^{4\text{F-Ph}})_2(\text{O}_2\text{CAr}^{4\text{F-Ph}})_2(\text{THF})_2]\text{-}[\text{Fe}_2(\mu\text{-O}_2\text{CAr}^{4\text{F-Ph}})_2(\text{O}_2\text{CAr}^{4\text{F-Ph}})_2(\text{THF})_2]$  (3) showing 50 % probability thermal ellipsoids for all non-hydrogen atoms. Bottom left: The aromatic rings of  $\text{Ar}^{\text{Tot}}\text{CO}_2^-$  ligands are omitted for clarity and hydrogen-bonding interactions are depicted with dot lines..... 242
- Figure 7.5. Zero-field Mössbauer spectrum (experimental data (|), calculated fit (—)) recorded at 4.2 K of the solid sample of  $[\text{Fe}_2(\mu\text{-OH}_2)_2(\mu\text{-O}_2\text{CAr}^{4\text{F-Ph}})(\text{O}_2\text{CAr}^{4\text{F-Ph}})_3(\text{THF})_2(\text{OH}_2)]$  (2) ..... 243
- Figure 7.6. Plots of the effective magnetic moment ( $\mu_{\text{eff}}$ ) per molecule versus temperature (Top) and molar susceptibility ( $\chi_{\text{M}}$ ) versus temperature (Bottom) for  $[\text{Fe}_2(\mu\text{-OH}_2)_2(\mu\text{-O}_2\text{CAr}^{4\text{F-Ph}})(\text{O}_2\text{CAr}^{4\text{F-Ph}})_3(\text{THF})_2(\text{OH}_2)]$  (2). The line represent the fit..... 244
- Chapter 8**
- Figure 8.1. Top: ORTEP diagram of  $[\text{Fe}_2(\mu\text{-O}_2\text{CAr}^{\text{Tot}})_4(4\text{-NCC}_5\text{H}_4\text{N})_2]$  (1) showing 50 % probability thermal ellipsoids for all non-hydrogen atoms. Bottom: The aromatic rings of  $\text{Ar}^{\text{Tot}}\text{CO}_2^-$  ligands are omitted for clarity ..... 284
- Figure 8.2. ORTEP diagram of  $[\text{Fe}_2(\mu\text{-O}_2\text{CAr}^{4\text{F-Ph}})_4(4\text{-NCC}_5\text{H}_4\text{N})_2]$  (2) showing 50 % probability thermal ellipsoids for all non-hydrogen atoms..... 285
- Figure 8.3. Top: ORTEP diagram of 3 showing 50 % probability thermal ellipsoids for all non-hydrogen atoms. Bottom: The phenyl rings of  $\text{Ar}^{\text{Tot}}\text{CO}_2^-$  ligands are omitted for clarity ..... 286
- Figure 8.4. Top: ORTEP diagram of 4 showing 50 % probability thermal ellipsoids for all non-hydrogen atoms. Bottom: The phenyl rings of  $\text{Ar}^{\text{Tot}}\text{CO}_2^-$  ligands are omitted for clarity ..... 287
- Figure 8.5. Ball and stick diagram of  $[\text{Fe}_2(\mu\text{-O}_2\text{CAr}^{\text{Tot}})_3(4\text{-NCC}_5\text{H}_4\text{N})_2][\text{BAr}'_4]$  (5) for all non-hydrogen atoms ..... 288

- Figure 8.6. Mössbauer spectra (experimental data (|), calculated fit (—)) recorded at 4.2 K for a solid sample of  $[\text{Fe}_2(\mu\text{-O}_2\text{CAr}^{\text{Tol}})_4(4\text{-NCC}_5\text{H}_4\text{N})_2]$  (1) and  $[\text{Fe}_2(\mu\text{-O}_2\text{CAr}^{4\text{F-Ph}})_4(4\text{-NCC}_5\text{H}_4\text{N})_2]$  (2). Left to right ..... 289
- Figure 8.7. Mössbauer spectra (experimental data (|), calculated fit (—)) recorded at 4.2 K for a solid sample of 3 and 5. Left to right ..... 290
- Figure 8.8. Plots of  $\chi_M$  (o) and  $\mu_{\text{eff}}$  (•) vs T for solid  $[\text{Fe}_2(\mu\text{-O}_2\text{CAr}^{\text{Tol}})_4(4\text{-NCC}_5\text{H}_4\text{N})_2]$  (1) ..... 291
- Figure 8.9. UV-vis spectra of  $[\text{Fe}_2(\mu\text{-O}_2\text{CAr}^{\text{Tol}})_4(4\text{-NCC}_5\text{H}_4\text{N})_2]$  (1) and  $[\text{Fe}_2(\mu\text{-O}_2\text{CAr}^{4\text{F-Ph}})_4(4\text{-NCC}_5\text{H}_4\text{N})_2]$  (2) in  $\text{CH}_2\text{Cl}_2$ ..... 292
- Figure 8.10. A) Resonance Raman spectrum of a  $\text{CH}_2\text{Cl}_2$  solution of  $[\text{Fe}_2(\mu\text{-O}_2\text{CAr}^{\text{Tol}})_4(4\text{-NCC}_5\text{H}_4\text{N})_2]$  (1) at 23 °C. The asterisk indicates a solvent band. B) Resonance Raman spectrum of 4-NCC<sub>5</sub>H<sub>4</sub>N at 23 °C (Literature data) ... 293
- Figure 8.11. (Top) UV-vis spectra of  $[\text{Fe}_2(\mu\text{-O}_2\text{CAr}^{\text{Tol}})_4(4\text{-NCC}_5\text{H}_4\text{N})_2]$  (1) in THF, measured at variable temperatures. (Bottom) The absorbance change at 490 nm was fit to eq (2)..... 294
- Figure 8.12. (Top) UV-vis spectra of  $[\text{Fe}_2(\mu\text{-O}_2\text{CAr}^{\text{Tol}})_4(4\text{-NCC}_5\text{H}_4\text{N})_2]$  (3) in  $\text{CH}_2\text{Cl}_2$ , measured at variable temperatures. (Bottom) The absorbance change at 510 nm was fit to eq (3)..... 295
- Figure 8.13. Cyclic voltammograms of  $[\text{Fe}_2(\mu\text{-O}_2\text{CAr}^{\text{Tol}})_4(4\text{-NCC}_5\text{H}_4\text{N})_2]$  (1) in  $\text{CH}_2\text{Cl}_2$  with 0.5 M  $(\text{Bu}_4\text{N})\text{PF}_6$  as supporting electrolyte and a scan rate of 25 mV/s ..... 296
- Figure 8.14. Cyclic voltammograms of 3 in  $\text{CH}_2\text{Cl}_2$  with 0.5 M  $(\text{Bu}_4\text{N})\text{PF}_6$  as supporting electrolyte and a scan rate of 25 mV/s..... 297
- Figure 8.15. Spectral changes that occur during oxygenation of 1 ( $1.74 \times 10^{-4}$  M) with dioxygen and water in  $\text{CH}_2\text{Cl}_2$  at -0 °C over 20 sec..... 298
- Figure 8.16. (Top) Spectral changes that occur during the hydration of 1 ( $1.60 \times 10^{-4}$  M) with dioxygen and water in  $\text{CH}_2\text{Cl}_2$  at -60 °C over 1 sec. (Bottom) Spectral changes that occur during oxygenation of 1 ( $1.60 \times 10^{-4}$  M) with dioxygen and water in  $\text{CH}_2\text{Cl}_2$  at -20 °C over 10 sec..... 299
- Figure 8.17. Top: ORTEP diagram of  $[\text{Fe}_2(\mu\text{-OH})_2(\mu\text{-O}_2\text{CAr}^{\text{Tol}})_2(\text{O}_2\text{CAr}^{\text{Tol}})_2(4\text{-NCC}_5\text{H}_4\text{N})_2(\text{OH}_2)_2] \cdot 2(\text{HO}_2\text{CAr}^{\text{Tol}})_2$  (6) showing 50 % probability thermal

ellipsoids for all non-hydrogen atoms. Bottom: The phenyl rings of  $\text{Ar}^{\text{Tol}}\text{CO}_2^-$  ligands are omitted for clarity .....300

Figure 8.18. Top left: ORTEP diagram of 7 showing 50 % probability thermal ellipsoids for all non-hydrogen atoms. Top Right: The aromatic rings of  $\text{Ar}^{\text{Tol}}\text{CO}_2^-$  ligands are omitted for clarity. Bottom: The aromatic rings of  $\text{Ar}^{\text{Tol}}\text{CO}_2^-$  and 4-NCC<sub>5</sub>H<sub>4</sub>N ligands are omitted for clarity.....301

## **Chapter 1**

# **Modeling Studies for Diiron Sites with Carboxylate Rich Coordination Environments in Dioxygen-Dependent Non-Heme Enzymes: Compounds Synthesized, Understanding Achieved, and Directions to Take**

## I. Introduction

Bioinorganic complexes containing diiron units with carboxylate rich coordination environments constitute a commonly occurring element in a large number of dioxygen-dependent metalloproteins. Examples include the R2 subunit of ribonucleotide reductase (RNR-R2),<sup>1,2</sup> soluble methane monooxygenase (sMMO),<sup>3,4</sup> fatty acid desaturase ( $\Delta^9$ D),<sup>5,6</sup> and toluene monooxygenase (ToMO).<sup>7,8</sup> Schematic diagrams of the protein cores are depicted in Figure 1.1. The functions of these diiron sites vary from the generation and storage of a catalytically essential tyrosyl radical (Tyr-O $\cdot$ ) in RNR-R2,<sup>9-11</sup> catalysis of the selective oxidation of methane to methanol in sMMO,<sup>3,4,12</sup> and insertion of a *cis* double bond into the alkyl chain of an acyl carrier protein-linked fatty acid in  $\Delta^9$ D,<sup>5,13</sup> to hydroxylation of toluene to *o*- and *p*-cresol in ToMO.<sup>8,14</sup> The polypeptide folds of these enzymes all contain a four-helix bundle motif that houses the diiron center. These diiron sites share similar coordination environments, composed of both bridging and free carboxylate ligands as well as two histidine ligands in a *syn* disposition with respect to the Fe-Fe vector. Only subtle differences in the enzyme active sites, such as the binding modes of the carboxylates and the occurrence of water molecules, have been identified. It is clear from the diverse range of reactivities exhibited by these redox-active proteins that subtle differences in the diiron coordination environments and surrounding polypeptide matrix tune their chemical properties to achieve a particular function. Understanding how these diiron-carboxylate proteins operate and how they relate to one another represents a challenging and active area of research in bioinorganic chemistry.

One approach to addressing these issues and decoding the structure-function relationships that operate for these proteins is to study the bio-molecules themselves. Although such investigations are often conducted *in vitro*, they provide the most direct

way to gain insights into the evolutionarily defined functions. Using the tools of molecular biology, specific changes in amino acid composition can be introduced in order to probe the importance of certain residues, thereby providing additional information about the properties of the native systems. A detailed and quantitative description of the chemistry is often difficult to obtain, however, owing to potential limitations in the accessibility of the protein and in the range of experimental conditions that can be achieved.

An alternative approach involves the use of theoretical methods to explain, test, or predict a given phenomenon at a computational level. With the continually expanding power of computers, analyses of increasingly sophisticated constructs are becoming possible. Nonetheless, results based on theory can always be challenged with respect to their relevance to reality. The predictive power of a theoretical technique can sometimes be evaluated by comparing calculated outputs with corresponding experimental values. In certain cases, however, theory may offer the only practical means to a physical model for a short-lived reactive intermediate or transition state.

A third and complementary approach involves synthetic chemistry, where artificial systems, much smaller than the protein and its isolated active site motif, are designed to reproduce the chemistry exhibited by the macromolecules. Synthetic models offer the opportunity to explore a wide range of reaction conditions, from which a detailed understanding of the chemistry can often be obtained. Properties intrinsic to the model compounds, such as steric and electronic factors, can be controlled through appropriate synthetic modifications. In addition, external parameters such as solvent and temperature can be manipulated over a wide range in an effort to characterize reactive intermediates that may serve as synthetic analogs of species observed in protein systems. The utility of this approach is reliant, however, on the existence of an

appropriate model system. The initial challenge associated with these types of studies therefore rests on creating a molecular system that bears a close resemblance to the biological one. Modeling an enzymatic transformation by creating an environment that stabilizes the ligand composition at the metal ion while offering labile sites for catalysis, however, has been one of the greatest challenges for the synthetic inorganic chemist. In a biological molecule, ligands are typically supplied by amino acid side chains and are therefore held in relatively fixed positions, prohibiting disassembly or rearrangement to thermodynamically more stable entities.

In this Chapter, we summarize our efforts to understand the chemistry of dioxygen-dependent diiron proteins with carboxylate rich coordination environments through the synthesis of small model complexes. We describe not only the significant results that have contributed toward this goal, but also the rationale behind how one generation of model systems gave way to the next.

## **II. Diiron Model Complexes with Oxygen-Rich Metal Coordination Environments.**

**A. General Comments.** The incorporation of carboxylates as a major ligand framework for the iron centers constitutes a recurring theme that distinguishes our model systems from many others in the literature. The desire to reproduce faithfully the carboxylate-rich diiron sites in the proteins of interest introduces additional synthetic complications, owing both to the kinetic lability of iron and multiplicity of binding modes of the carboxylate ligand. Major complications include the generation of mononuclear complexes and polynuclear clusters, commonly encountered products in iron-carboxylate chemistry.<sup>15-18</sup> Nonetheless, a diverse collection of carboxylate diiron complexes can be prepared through the careful control of reaction conditions such as



the utilization of specific precursor complexes, steric bulk of the ligands, and the solvent system.

When the demand for more elaborate synthetic models increased, ligand design played a central role in the bioinorganic modeling field. The synthesis of carboxylate-rich diiron complexes relies heavily on the ability of the ligand framework to stabilize dimetallic sites and block mono- and polynuclear structures. Modern methods in ligand design include computer modeling, whereby structures are analyzed to reveal important features that might aid in obtaining the desired compound. An efficient route to multigram quantities of the desired ligand is an important practical matter that must also be considered during the design process. We describe below specific examples of synthetic models that have been developed out of these considerations. Before directly discussing carboxylate-rich diiron model complexes, however, two nitrogen-rich systems will be described that represent our initial motivation in this area and suggested that the desired chemistry should be possible to achieve.

**B. Dicarboxylate-Bridged Diiron Complexes with Nitrogen-Rich Coordination Environments.** In 1983, we published the first well-characterized example of a synthetic carboxylate-bridged diiron(III) complex  $[\text{Fe}_2(\mu\text{-O})(\mu\text{-O}_2\text{CCH}_3)_2(\text{HB}(\text{Pz})_3)_2]$  (**1**) (Figure 1.2).<sup>19,20</sup> A second, independently reported example,  $[\text{Fe}_2(\mu\text{-O})(\mu\text{-O}_2\text{CCH}_3)_2(\text{TACN})_2]^{2+}$  (**2**), also appeared in the literature in the same year.<sup>21</sup> The chemical compositions of **1** and **2** differ only in the identity of the tridentate  $\text{N}_3$  donor ligand,  $\text{HB}(\text{Pz})_3^-$  or  $\text{TACN}$ ,<sup>22</sup> prevents polyiron cluster formation by capping the  $(\mu\text{-oxo})\text{bis}(\mu\text{-acetato})\text{diiron(III)}$  core that is featured in both structures. The resulting dinuclear structures reproduced for the first time the basic features of the active site of azide-bound hemerythrin (azidometHr),

which utilizes diiron sites with  $N_3O_3$  and  $N_2O_3$  coordination environments to carry dioxygen in marine invertebrates.<sup>23</sup> Although the crystal structure of azidometHr had been elucidated by X-ray crystallography several years earlier, the synthesis of these complexes are historically significant because they demonstrated that synthetic models of diiron-carboxylate proteins could be prepared in the laboratory, laying the foundation for future studies in this area. Compound **1** has been investigated thoroughly, and it continues to serve as a well-defined benchmark for comparison in diiron-carboxylate chemistry.

Three landmark papers in diiron-carboxylate modeling chemistry appeared in 1996, reporting X-ray crystal structures of peroxo diiron(III) complexes.<sup>24-26</sup> The structure of one of these compounds,  $[Fe_2(\mu-O_2)(\mu-O_2CBn)_2(HB(3,5-^iPr_2pz)_3)_2]$  (**3**),<sup>24</sup> contained two  $\{(HB(3,5-^iPr_2pz)_3)Fe\}^{2+}$  units connected by a  $\mu$ -1,2-peroxo ligand and two  $\mu$ -1,3-phenylacetates (Figure 1.2). An Fe...Fe separation of 4.004(4) Å was determined with a gauche Fe–O–O–Fe dihedral angle of 52.9°. The Mössbauer parameters of a frozen solution of **3**,  $\delta = 0.66$  mm/s and  $\Delta E_Q = 1.40$  mm/s, are remarkably close to those of the peroxo intermediate ( $\delta = 0.66$  mm/s and  $\Delta E_Q = 1.51$  mm/s)<sup>27</sup> in the oxygenation cycle of MMOH. Although the coordination environments in this nitrogen-rich peroxo diiron(III) species differ significantly from those of the more oxygen-rich metalloprotein core, it served to demonstrate that one could achieve with small molecules the structural characterization of spectroscopically defined intermediate(s) in the biological system. The reactivity of the peroxo model complex **3** is quite, however, different from that of the carboxylate-rich diiron sites in metalloproteins, which prompted our effort to prepare more carboxylate-rich model systems.

### C. Small Diiron Complexes with Carboxylate Rich Coordination Environment.

The synthesis of a carboxylate-bridged diiron(II) complex with an oxygen rich coordination environment was achieved by combining equimolar amounts of  $\text{Fe}(\text{O}_2\text{CH})_2 \cdot \text{H}_2\text{O}$  with  $\text{BIPhMe}$ ,<sup>22</sup> a bidentate ligand that was designed to serve a replacement for bis(histidine) ligation (Scheme 1.1). The neutral colorless product  $[\text{Fe}_2(\mu\text{-O}_2\text{CH})_3(\text{O}_2\text{CH})(\text{BIPhMe})_2]$ <sup>28,29</sup> (**4**) was isolated in high yield and shown by X-ray crystallography to include an Fe...Fe separation of 3.57 Å and an unprecedented tris( $\mu$ -carboxylato)diiron core, in which one formate ligand adopts a monodentate bridging ( $\mu$ -1,1) coordination mode. When ferrous acetate was used instead of formate in the self-assembly reaction, the trinuclear complex  $[\text{Fe}_3(\mu\text{-O}_2\text{CCH}_3)_6(\text{BIPhMe})_2]$  (**5**), containing a linear arrangement of iron atoms, was obtained. The characterization of these complexes contributed to the discovery of the carboxylate shift, in which a carboxylate ligand alters its binding mode in response to a chemical event.

Although only speculated at the time, the significance of a  $\mu$ -1,1 carboxylate bridged diiron(II) center in diiron-carboxylate proteins later became important when it was subsequently observed as the active-site core structure of  $\text{MMOH}_{\text{red}}$  (Figure 1.1).

The terminal coordination sites at the Fe2 in complex **4** are occupied by two N-donors of the  $\text{BIPhMe}$  chelating ligands and one monodentate formate trans to the  $\mu$ -1,1-formate, giving rise to a dinuclear complex containing one six- and one five-coordinate iron center. The reason for employing  $\text{BIPhMe}$  in this diiron(II) model system was to generate a coordinatively unsaturated model complex to allow for dioxygen binding and activation. Complex **4** is oxidized readily in the presence of dioxygen to generate the  $\text{C}_2$  symmetric ( $\mu$ -oxo)bis( $\mu$ -carboxylato)diiron(III) complex  $[\text{Fe}_2(\mu\text{-O})(\mu\text{-O}_2\text{CH})_2(\text{O}_2\text{CH})_2(\text{BIPhMe})_2]$  (**6**). The dioxygen-dependent conversion of **4** to **6**

is accompanied by metal-centered redox changes, incorporation of an oxygen atom into the product, and significant rearrangements in the positions of the formate and BIPhMe ligands. Stopped-flow kinetic studies indicated that this transformation is first-order in dioxygen and second-order in metal complex, and a chemically reasonable mechanism consistent with these results was proposed (Scheme 1.1). The first step involves reversible addition of dioxygen to complex **4** to form a peroxo adduct, a reaction that occurs concurrently with a carboxylate shift of the  $\mu$ -1,1-formate into a mondentate coordination mode, followed by irreversible and rate-limiting reaction with another molecule of **4** to generate a mixed valent ( $\mu$ -peroxo) $\text{Fe}^{\text{II}}_2\text{Fe}^{\text{III}}_2$  species (**I4**). Subsequent cleavage of the O–O bond affords two equivalents of **6**. The intermediacy of **I4** represented a key feature in this autoxidation process because it requires dimerization of a dinuclear species to form a tetranuclear one. The preparation and structural characterization of complexes having such a ( $\mu$ -peroxo) $\text{Fe}^{\text{III}}_4$  tetrairon-peroxide core geometry supported the plausibility of the postulated structure **I4**.<sup>30,31</sup> Although this transformation has no direct bearing on the oxygenation cycle of the diiron enzymes, the finding led to the design and utilization of ligands with enough bulk to block such deleterious bimolecular decomposition. In the metalloproteins of interest, the active site is buried in a cavity that is surrounded by a heterophobic shield rendering such chemistry impossible.

**D. Carboxylate Rich Diiron Complexes with Pre-organized Bis(carboxylate) Ligand Platforms.** The search for a ligand that would act as a dinucleating dicarboxylate and block the bimolecular decomposition pathway led to the use of *m*-xylylenediamine bis (Kemp's triacid imide) ( $\text{H}_2\text{XDK}$ ).<sup>32</sup> The XDK ligands with methyl, propyl, and benzyl substituents were prepared in order to isolate the diiron core from the surface of

generated molecules (Figure 1.3).<sup>33,34</sup> Incorporation of two additional carboxylate and two N-donor ligands afforded compounds having the correct stoichiometric composition as found at the active sites of carboxylate-rich diiron proteins (Figure 1.1). The complex  $[\text{Fe}_2(\mu\text{-BXDK})(\mu\text{-O}_2\text{CCPhCy})(\text{O}_2\text{CCPhCy})(\text{MeIm})_2]$ <sup>22,33,34</sup> (7) exemplifies this strategy. Complex 7 (Figure 1.3) contains one ferrous site in an octahedral geometry and a second, coordinatively unsaturated  $\text{NO}_4$  site. Two N-donor ligands coordinated in the anti disposition via Fe–Fe vector and regardless of the ancillary N-donor ligands used in the assembly of the dimetallic cores, the Fe...Fe separation is  $\sim 3.4$  Å in this series of compounds. These results attest to the rigidity conferred by the XDK platform to the diiron centers. Upon oxygenation of derivatives of 7 having various carboxylates at  $-78$  °C, ( $\mu$ -peroxo)diiron(III) intermediates are generated. The rate of formation of the peroxo species is inversely proportional to the steric demands imposed by the ancillary carboxylate ligands, suggesting that a carboxylate shift occurs in the rate-determining step to accommodate the dioxygen binding to the diiron site. The stability of the  $\text{O}_2$ -adducts is heavily dependent upon the bulk provided by the supporting XDK units,<sup>33,35</sup> confirming that the peroxo intermediate is protected from bimolecular decomposition, as was designed.

Although the peroxo species are accurate compositional models for the ( $\mu$ -peroxo)diiron(III) intermediates that form in the related non-heme diiron enzymes, their reactivity towards hydrocarbon substrates once again differs substantially from that of the natural systems. In particular, oxidation of hydrocarbon solvent by  $[\text{Fe}_2(\mu\text{-O}_2)(\mu\text{-PXDK})(\mu\text{-O}_2\text{CPhCy})(\text{O}_2\text{CPhCy})(\text{Bu-Im})_2]$  (8) appeared to proceed by radical autoxidation chemistry.<sup>35</sup> This result is a marked contrast to the selective hydroxylation chemistry affected by dioxygen-dependent non-heme diiron enzymes, despite the

obvious structural similarities between these XDK models and the diiron cofactors in Nature. One reason for this difference may be the inherent inflexibility of XDK ligand family. These rigidly held dicarboxylate ligands may not allow conversion of the peroxo intermediate to high-valent  $\{\text{Fe}_2(\text{O})_2\}^{4+}$  species,<sup>36,37</sup> proposed to be the an ultimate oxidant that achieves the functions of non-heme diiron enzymes. The Fe...Fe separations of the diiron species involved in the oxygenation cycle of MMOH, for example, are postulated to vary from 3.5 Å in  $\text{MMOH}_{\text{red}}$  to ~ 2.5 Å in the high-valent oxidant  $\{\text{Fe}_2(\text{O})_2\}^{4+}$  species.<sup>36</sup>

These results accentuate the importance of designing ligand systems that permit the diiron unit sufficient flexibility to convert the peroxo intermediate to the putative di( $\mu$ -oxo)diiron(IV) species. From studies of the XDK family of diiron complexes, therefore, one more criterion in designing the ligand framework, flexibility at the diiron center, was added to that of steric bulk to prevent bimolecular decomposition.

**E. Diiron Complexes with Four Sterically Hindered *m*-Terphenyl-based Carboxylate Ligands.** The steric bulk provided by the *m*-terphenyl-based carboxylate ligands  $\text{CO}_2\text{Ar}^X$ , where X is tolyl or 4-fluorophenyl, facilitates the synthesis of carboxylate-bridged diiron(II) compounds that combine four carboxylate and two N-donor groups to model the active sites of the metalloproteins (Figure 1.4).<sup>38-48</sup> Some related complexes have been prepared and characterized by other. Diiron(II) complexes with these sterically bulky carboxylate contains flexible diiron unit and bridging ligand binding modes, as evidenced by a diverse range of inter-metal distance. Crystal structures of complexes having a dicarboxylate bridged structure reveal relatively long Fe...Fe distances of 3.8 – 4.4 Å, with the terminal carboxylate bound in either a monodentate or bidentate mode. On the other hand, complexes bridged by four

carboxylates have a shorter Fe...Fe distance of  $\sim 2.8$  Å. Variable temperature NMR studies established the interconversion between tetra- and dicarboxylate bridged structures, which can occur through carboxylate shifts. In addition, several structures of tricarboxylate bridged diiron(II) complexes were determined, suggesting possible the intermediates in the equilibrium involved in the conversion of tetra- and dicarboxylate bridged diiron(II) complexes (Scheme 1.2).<sup>41,46</sup>

Diiron(II) complexes such as  $[\text{Fe}_2(\text{O}_2\text{CAr}^{\text{Tol}})_4(\text{L})_2]$  (9 - 11), where L is  $\text{C}_5\text{H}_4\text{N}$ , 4- $^t\text{BuC}_5\text{H}_4\text{N}$ ,<sup>22</sup> and  $\text{BA}^{p\text{-OMe}}$ ,<sup>22,48</sup> respectively, react with dioxygen at  $-78$  °C to afford interesting metastable green intermediates. Addition of dioxygen to the complex  $[\text{Fe}_2(\mu\text{-O}_2\text{CAr}^{\text{Tol}})_4(4\text{-}^t\text{BuC}_5\text{H}_4\text{N})_2]$ <sup>38</sup> (11) can effect the oxidation of phenolic substrates to the corresponding phenoxy radicals. Out of the resulting yellow solution can be isolated as the final product a unique bis( $\mu$ -hydroxo)bis( $\mu$ -carboxylato)diiron(III) complex  $[\text{Fe}_2(\mu\text{-OH})_2(\mu\text{-O}_2\text{CAr}^{\text{Tol}})_4(\text{O}_2\text{CAr}^{\text{Tol}})_2(4\text{-}^t\text{BuC}_5\text{H}_4\text{N})_2]$  (12). The proposed reaction mechanism for these processes is summarized in Scheme 1.3. Reaction between the diiron(II) complexes and dioxygen generates peroxo Fe(III,III) species, which may convert to electrophilic high-valent Fe(IV,IV) species. Electron transfer (ET) from the starting diiron(II) complex to the putative high-valent dioxygen-adduct(s) could occur to afford equimolar amounts of the Fe(III,IV) and the Fe(II,III) species. The latter is able to oxidize phenolic substrates to the corresponding phenoxy radicals. This proposed process parallels the mechanism established for RNR-R2, in which a high-valent Fe(III,IV) intermediate X species oxidizes an adjacent tyrosine residue. Although the catalytic cycle of RNR-R2 system has been partially reproduced by oxygenation of compound 11, to model the function of high-valent diiron species in MMOH, hydroxylation of aliphatic C-H bonds, the generated intermediate(s) need to be protected from intermolecular ET processes.

One way to accomplish this goal has been to tether an oxidizable C–H bonds in proximity to the generated oxidant. The compound  $[\text{Fe}_2(\mu\text{-O}_2\text{CAr}^{\text{Tol}})_2(\text{O}_2\text{CAr}^{\text{Tol}})_2(\text{N,N-Bn}_2\text{en})_2]$ <sup>40,43</sup> (13) reacts with  $\text{O}_2$  to afford the diiron(III) complex  $[\text{Fe}_2(\mu\text{-OH})_2(\mu\text{-O}_2\text{CAr}^{\text{Tol}})(\text{O}_2\text{CAr}^{\text{Tol}})_3(\text{N,N-Bn}_2\text{en})(\text{N-Bnen})]$  (14), in which oxidative *N*-dealkylation of the tethered benzyl group on the diamine ligand has occurred (Scheme 1.4). The diiron(III) complex generated contains the long-sought  $\{\text{Fe}_2(\mu\text{-OH})_2(\mu\text{-O}_2\text{CR})\}^{3+}$  core structure of sMMOH in its resting state,<sup>49</sup> drawing a parallel to the chemistry of the enzyme, in which an  $\text{O}_2$ -derived oxygen atom is incorporated into the C–H bond of methane. Detailed mechanistic studies, including a Hammett analysis and kinetic isotope effects, suggest that sequential one-electron oxidation of the dangling nitrogen atom, followed by  $\alpha$ -proton abstraction and sequential oxygen rebound, occurs. Replacement of the C–H bond in the benzylic position with heteroatoms to provide phosphino and sulfide substrate facilitated oxidation of the heteroatom moiety. Oxygenation of the diiron(II) complex  $[\text{Fe}_2(\mu\text{-O}_2\text{CAr}^{4\text{F-Ph}})_3(\text{O}_2\text{CAr}^{4\text{F-Ph}})(2\text{-Ph}_2\text{Ppy})]$  (15) afforded the diiron(III) complex  $[\text{Fe}_2(\mu\text{-OH})_2(\mu\text{-O}_2\text{CAr}^{4\text{F-Ph}})(\text{O}_2\text{CAr}^{4\text{F-Ph}})_3(2\text{-Ph}_2\text{P(O)py})(\text{OH}_2)]$  (16), in which the oxidized ligand, 2- $\text{Ph}_2\text{POpy}$ ,<sup>22</sup> is bound to the  $\{\text{Fe}_2(\mu\text{-OH})_2(\mu\text{-O}_2\text{CR})\}^{3+}$  core structure. Therefore, perhaps due to the immediate accessibility of a substrate, intermediates have not been detected in these systems.

### III. Advanced Model Complexes Containing Diiron(II) Centers with an Oxygen-Rich Metal Coordination Environment

**A. General Comment.** The model complexes with four terphenyl-based carboxylate ligands are able to hydroxylate benzylic C–H bonds and to oxidize phosphine and sulfide moieties with simultaneous generation of diiron(III) species having the  $\{\text{Fe}_2(\mu\text{-$



$\text{OH})_2(\mu\text{-O}_2\text{CR})^{3+}$  core structure. Although the observation of intermediates and the activation of strong C–H bonds from carboxylate-rich diiron model complexes has been a major focus of our research, we have recently begin to address certain geometric and compositional difference from the diiron(II) cores at the active site of the targeted metalloproteins. In the last part of this Chapter, our efforts to understand the effect of water molecule(s) in the first and second coordination spheres as well as the syn disposition of N-donor ligands at the diiron center are summarized(Figure 1.1).

**B. Understanding the Effect of Coordinated Water.** In recently published DFT calculations,<sup>50</sup> the utilization of a coordinated  $\text{H}_2\text{O}$  molecule as a hydrogen-bond donor was considered to be a key component in the formation of reactive intermediate(s) upon oxygenation of the diiron(II) site. It was strongly suggested that a ligated water molecule is required for the enzyme to function. Accordingly, we have undertaken the synthesis of model complexes to reproduce this feature. The reaction between water and carboxylate rich diiron(II) complexes was investigated, allowing ferrous species with varying numbers of water ligands to be isolated.<sup>51</sup> A striking observation is that the tetracarboxylate bridged diiron(II) complexes readily bind water and alter their structures.<sup>52</sup> The diiron(II) sites in enzymes similarly adopt different forms depending on the availability of water in the active site. For example, two water molecules are bound by diiron center in  $\text{MMOH}_{\text{red}}$ , but none were found in the X-ray structure of reduced RNR-R2. This observation indicates that the accessible amount water in different non-heme diiron(II) sites varies and may be a controlling factor in determining their chemistry.

In the work discussed thus far, equilibria were postulated on the basis of single crystal X-ray studies. High-spin iron(II) complexes are typically colorless, limiting the utility of more convenient UV-vis spectroscopy to determine underlying

thermodynamic and kinetic parameters in water-dependent equilibria and to study the effect of water on the oxygenation chemistry of these complexes. We found, however, that by placing an electronic withdrawing group such as a nitrile on the N-donor ligand we could shift the metal-to-ligand charge-transfer band into the visible region of the spectrum. In particular, the 4-cyanopyridine complex  $[\text{Fe}_2(\mu\text{-O}_2\text{CAr}^{\text{Tot}})_4(4\text{-NCC}_5\text{H}_4\text{N})_2]$  (**17**) has a strong electronic transition at 510 nm, with  $\epsilon = 2,200 \text{ cm}^{-1}\text{M}^{-1}$ . Treatment of **17** with excess water in  $\text{CH}_2\text{Cl}_2$  solution generated the aqua complex  $[\text{Fe}_2(\text{O}_2\text{CAr}^{\text{Tot}})_4(4\text{-NCC}_5\text{H}_4\text{N})_2(\text{OH}_2)_2]$  (**18**) (Scheme 1.5). A distinguishing feature of a solution of **18** is its thermochroism, in which the water-dependent equilibrium is temperature dependent with thermodynamic parameters of  $\Delta H = -95$  (11) kJ/mol and  $\Delta S = -250$  (50) J/mol K for the reaction in Scheme 1.5.

Study of the reactions of water and dioxygen with complex **17** revealed in sequential binding first of water to the carboxylate-rich diiron(II) complex, followed by oxygenation. Notably, the hydration rate is ca 1000 times faster than oxygenation of **17**. Oxygenation of the water-containing complex is ca 10-fold faster than of the anhydrous analogous complex **17**. Water binding may induce a carboxylate shift, opening a coordination site required for dioxygen binding and accelerating oxidation. Although no intermediate have yet been observed upon oxygenation of the water-containing complex, the effect of water on the conformation at the diiron(II) sites and the reactivity of water with diiron(II) species were demonstrated for the first time by these studies.<sup>53</sup>

**C. Modeling the Syn Disposition of Nitrogen Donors.** As shown in Figure 1.1, the primary coordination spheres of carboxylate-bridged diiron centers in the metalloproteins contain four glutamate or asparatate side chains and two histidine residues. Whereas the coordination modes of the carboxylate groups vary among the

enzymes, the two nitrogen donors are consistently bound in a syn fashion, on the same side of the Fe–Fe vector. In MMOH, the substrate pocket is positioned opposite these two nitrogen donors. Considering that just one oxygen atom from dioxygen is transferred to methane, delivered within the substrate binding pocket, the syn *N*-donor geometric feature may be important in facilitating substrate oxidation. The relative orientation of nitrogen donors may significantly influence the reactivity of the generated high-valent Fe<sub>2</sub>(O)<sub>2</sub> intermediate.

In contrast to the syn disposition of *N*-donor ligands commonly encountered in the natural systems, self-assembly methods have thus far failed to produce such a feature. The [Fe<sub>2</sub>(O<sub>2</sub>CR)<sub>4</sub>(N)<sub>2</sub>] cores formed in the synthesis of XDK or *m*-terphenyl-based carboxylate complexes invariably feature anti coordination of the *N*-donors. The synthesis of targeted diiron(II) complexes with a syn *N*-donor ligand disposition was accomplished by introducing the *N*-donors as quinoline moieties provided by 1,2-diethynylbenzene-based Et<sub>2</sub>BCQEB<sup>Et</sup> (Figure 1.5).<sup>22,54</sup> Reaction of this ligands with an iron(II) precursor afforded [Fe<sub>2</sub>(Et<sub>2</sub>BCQEB<sup>Et</sup>)(μ-O<sub>2</sub>CAr<sup>Tol</sup>)<sub>3</sub>]<sup>+</sup>(19), in which the *N*-donors are in syn positions. Although this complex provides a proof of principle for the approach, a significant amount of work remained to be carried out to achieve a stoichiometric and geometric match to the reduced diiron(II) sites in the metalloenzymes.

#### IV. Conclusion and Perspective

Several generations of ligand design and diiron complex synthesis have evolved to meet the requirements for accurately reproducing the chemistry of carboxylate-rich diiron sites in Nature. The following features have emerged as being important for achieving this challenging goal. The ligand framework should be sufficiently bulky to

prevent deleterious bimolecular decomposition of generated intermediates. The model complex should have open coordination sites for dioxygen-binding and room for substrate to access to the oxygenated diiron site. The ligand framework should render the diiron site with enough flexibility to accommodate variable Fe–Fe separations as observed in metalloenzymes catalytic cycles. Most of these requirements are fulfilled by bulky *m*-terphenyl-based carboxylates, now such that we are able to investigate additional factors, such as the influence of water and the effect of the syn disposition of *N*-donors.

Despite these accomplishments, more work must be carried out to achieve remaining important goals of the synthetic modeling chemistry. The first is to obtain a system having the syn disposition of *N*-atoms that matches the stoichiometry of the diiron core of the proteins. Another is to generate and characterize intermediate following oxygenation. The ultimate answers are to build a substrate-binding unit in the second coordination sphere and to achieve the catalytic oxygenation of molecules that bind them.

**References**

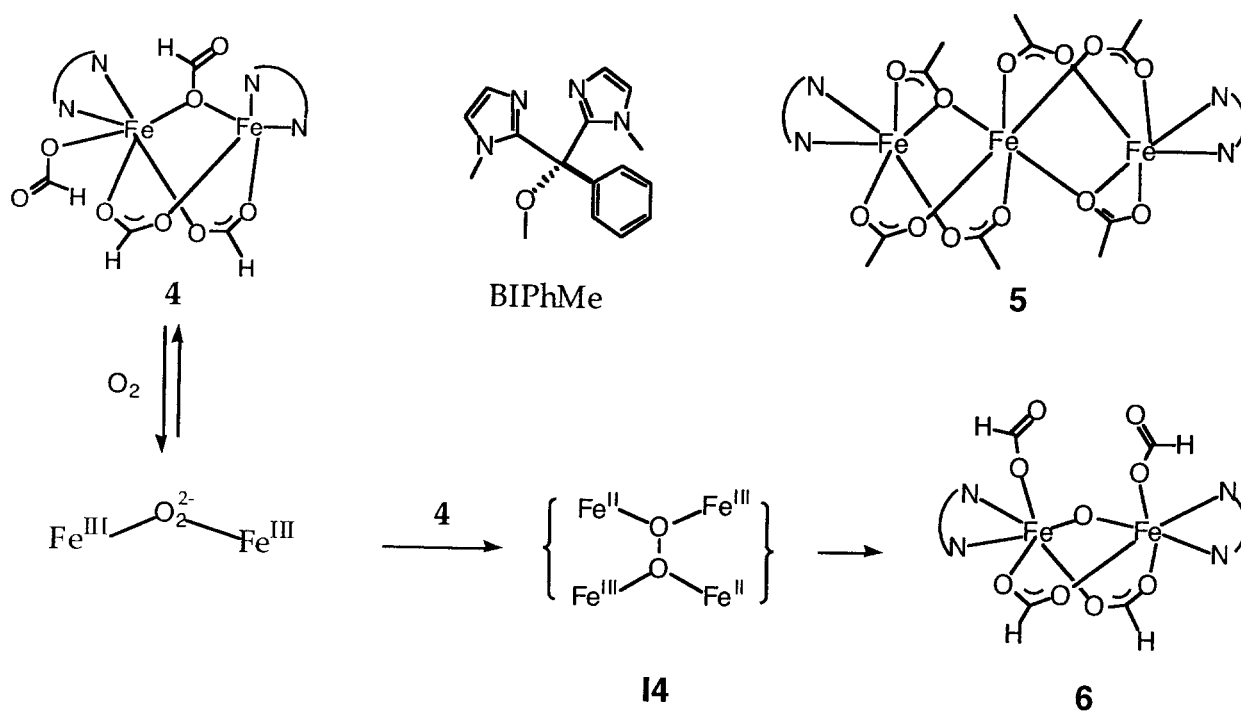
- (1) Stubbe, J.; van der Donk, W. A. *Chem. Rev.* **1998**, *98*, 705-762.
- (2) Logan, D. T.; Su, X.-D.; Åberg, A.; Regnström, K.; Hajdu, J.; Eklund, H.; Nordlund, P. *Structure* **1996**, *4*, 1053-1064.
- (3) Wallar, B. J.; Lipscomb, J. D. *Chem. Rev.* **1996**, *96*, 2625-2657.
- (4) Merckx, M.; Kopp, D. A.; Sazinsky, M. H.; Blazyk, J. L.; Müller, J.; Lippard, S. J. *Angew. Chem. Int. Ed.* **2001**, *40*, 2782-2807.
- (5) Lindqvist, Y.; Huang, W.; Schneider, G.; Shanklin, J. *EMBO Journal* **1996**, *15*, 4081-4092.
- (6) Shanklin, J.; Whittle, E.; Fox, B. G. *Biochemistry* **1994**, *33*, 12787-12794.
- (7) Sazinsky, M. H.; Bard, J.; Di Donato, A.; Lippard, S. J. *J. Biol. Chem.* **2004**, *279*, 30600-30610.
- (8) Pikus, J. D.; Studts, J. M.; Achim, C.; Kauffmann, K. E.; Münck, E.; Steffan, R. J.; McClay, K.; Fox, B. G. *Biochemistry* **1996**, *35*, 9106-9119.
- (9) Ravi, N.; Bollinger, J. M., Jr.; Huynh, B. H.; Edmondson, D. E.; Stubbe, J. *J. Am. Chem. Soc.* **1994**, *116*, 8007-8104.
- (10) Bollinger, J. M., Jr.; Tong, W. H.; Ravi, N.; Hyunh, B. H.; Edmondson, D. E.; Stubbe, J. *J. Am. Chem. Soc.* **1994**, *116*, 8015-8023.
- (11) Bollinger, J. M., Jr.; Tong, W. H.; Ravi, N.; Huynh, B. H.; Edmondson, D. E.; Stubbe, J. *J. Am. Chem. Soc.* **1994**, *116*, 8024-8032.
- (12) Dalton, H.; Wilkins, P. *Biochem. Soc. Trans* **1997**, *25*, 69-74
- (13) Broadwater, J. A.; Ai, J.; Loehr, T. M.; Sanders-Loehr, J.; Fox, B. G. *Biochemistry* **1998**, *37*, 14664-14671.

- (14) Pikus, J. D.; Studts, J. M.; McClay, K.; Steffan, R. J.; Fox, B. G. *Biochemistry* **1997**, *36*, 9283-9289.
- (15) Lippard, S. J. *Angew. Chem. Int. Ed.* **1988**, *27*, 344-361.
- (16) Rardin, R. L.; Bino, A.; Poganiuch, P.; Tolman, W. B.; Liu, S.; Lippard, S. J. *Angew. Chem. Int. Ed.* **1990**, *29*, 812-814.
- (17) Rardin, R. L.; Tolman, W. B.; Lippard, S. J. *New J. Chem.* **1991**, *15*, 417-430.
- (18) Taft, K. L.; Lippard, S. J. *J. Am. Chem. Soc.* **1990**, *112*, 9629-9630.
- (19) Armstrong, W. H.; Lippard, S. J. *J. Am. Chem. Soc.* **1983**, *105*, 4837-4838.
- (20) Armstrong, W. H.; Spool, A.; Papaefthymiou, G. C.; Frankel, R. B.; Lippard, S. J. *J. Am. Chem. Soc.* **1984**, *106*, 3653-3667.
- (21) Wieghart, K.; Pohl, K.; Gebert, W. *Angew. Chem. Int. Ed.* **1983**, *22*, 727-730.
- (22) Abbreviations used: PhCyCO<sub>2</sub><sup>-</sup> = 1-phenylcyclohexanecarboxylate; Et<sub>2</sub>BCQEBEt = 1,2-bis(3-ethyl-8-carboxylatequinoline)benzene ethyl ether; TACN = 1,4,7-triazacyclononane; HB(pz)<sub>3</sub> = hydrotris-1-(pyrazolyl)borate; HB(3,5-<sup>i</sup>Pr<sub>2</sub>pz)<sub>3</sub> = hydrotris(3,5-disisopropylpyrazol-1-yl)-borate; BIPhMe = bis(1-methylimidazol-2-yl)phenyl-methoxymethane; BXDK = benzyl derivative of XDK (Figure 1.3); MeIm = methylimidazole.
- (23) Stenkamp, R. E. *Chem. Rev.* **1994**, *94*, 715-726.
- (24) Kim, K.; Lippard, S. J. *J. Am. Chem. Soc.* **1996**, *118*, 4914-4915.
- (25) Ookudo, T.; Sugimoto, H.; Nagayama, T.; Masuda, H.; Sato, T.; Tanaka, K.; Maeda, Y.; Okawa H.; Hayashi, Y.; Uehara, A.; Suzuki, M. *J. Am. Chem. Soc.* **1996**, *118*, 701-702
- (26) Dong, Y.; Yan, S.; Young, V. G., Jr.; Que, L., Jr. *Angew. Chem. Int. Ed.* **1996**, *35*, 618
- (27) Liu, K. E.; Wang, D.; Huynh, B. H.; Edmondson, D. E.; Salifoglou, A.; Lippard, S. J. *J. Am. Chem. Soc.* **1994**, *116*, 7465-7466.

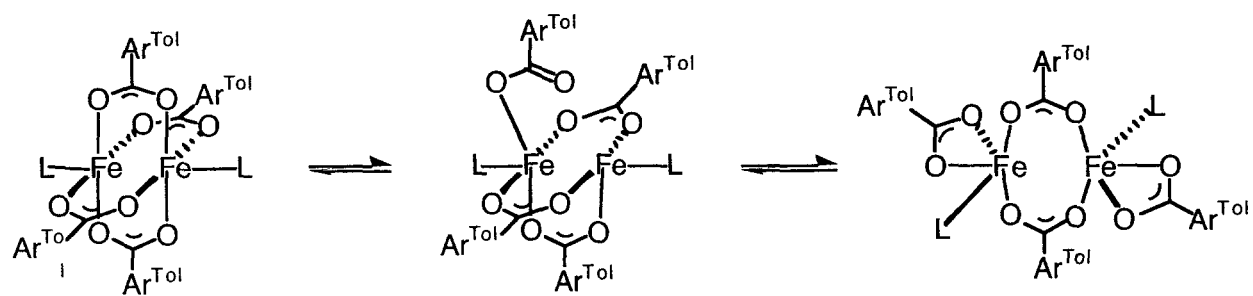
- (28) Tolman, W. B.; Liu, S.; Bentsen, J. G.; Lippard, S. J. *J. Am. Chem. Soc.* **1991**, *113*, 152-164.
- (29) Tolman, W. B.; Bino, A.; Lippard, S. J. *J. Am. Chem. Soc.* **1989**, *111*, 8522-8523.
- (30) Shweky, I.; Pence, L. E.; Papaefthymiou, G. C.; Sessoli, R.; Yun, J. W.; Bino, A.; Lippard, S. J. *J. Am. Chem. Soc.* **1997**, *119*, 1037-1042.
- (31) Micklitz, W.; Bott, S. G.; Bentsen, J. G.; Lippard, S. J. *J. Am. Chem. Soc.* **1989**, *111*, 372-374.
- (32) Wilkins, P. C.; Wilkins, R. G. *Chem. Rev.* **1987**, *79*, 195.
- (33) LeCloux, D. D.; Barrios, A. M.; Mizoguchi, T. J.; Lippard, S. J. *J. Am. Chem. Soc.* **1998**, *120*, 9001-9014.
- (34) Herold, S.; Lippard, S. J. *J. Am. Chem. Soc.* **1997**, *119*, 145-156.
- (35) LeCloux, D. D.; Barrios, A. M.; Lippard, S. J. *Bioorganic & Medicinal Chem.* **1999**, *7*, 763-772.
- (36) Shu, L.; Nesheim, J. C.; Kauffmann, K.; Münck, E.; Lipscomb, J. D.; Que, L., Jr. *Science* **1997**, *275*, 515.
- (37) Liu, K. E.; Valentine, A. M.; Wang, D.; Huynh, B. H.; Edmondson, D. E.; Salifoglou, A.; Lippard, S. J. *J. Am. Chem. Soc.* **1995**, *117*, 10174-10185.
- (38) Lee, D.; Pierce, B.; Krebs, C.; Hendrich, M. P.; Huynh, B. H.; Lippard, S. J. *J. Am. Chem. Soc.* **2002**, *124*, 3993-4007.
- (39) Lee, D.; DuBois, J. L.; Pierce, B.; Hedman, B.; Hodgson, K. O.; Hendrich, M. P.; Lippard, S. J. *Inorg. Chem.* **2002**, *41*, 3172-3182.
- (40) Lee, D.; Lippard, S. J. *Inorg. Chem.* **2002**, *41*, 827-837.
- (41) Lee, D.; Lippard, S. J. *Inorg. Chem.* **2002**, *41*, 2704-2719.
- (42) Lee, D.; Sorace, L.; Caneschi, A.; Lippard, S. J. *Inorg. Chem.* **2001**, *40*, 6774-6781.
- (43) Lee, D.; Lippard, S. J. *J. Am. Chem. Soc.* **2001**, *123*, 4611-4612.

- (44) Lee, D.; Du Bois, J.; Petasis, D.; Hendrich, M. P.; Krebs, C.; Huynh, B. H.; Lippard, S. J. *J. Am. Chem. Soc.* **1999**, *121*, 9893-9894.
- (45) Lee, D.; Lippard, S. J. *J. Am. Chem. Soc.* **1998**, *120*, 12153-12154.
- (46) Carson, E. H.; Lippard, S. J. *J. Am. Chem. Soc.* **2004**, *126*, 3412-3413.
- (47) Yoon, S.; Lippard, S. J. *J. Am. Chem. Soc.* **2004**, *126*, 2666-2667.
- (48) Yoon, S.; Lippard, S. J. *Inorg. Chem.* **2003**, *42*, 8606-8608.
- (49) Whittington, D. A.; Lippard, S. J. *J. Am. Chem. Soc.* **2001**, *123*, 827-838.
- (50) Gherman, B. F.; Baik, M.-H.; Lippard, S. J.; Friesner, R. A. *J. Am. Chem. Soc.* **2004**, *126*, 2978-2990.
- (51) Yoon, S.; Kelly, A. E.; Lippard, S. J. *Polyhedron* **2004**, In press.
- (52) Yoon, S. In *Department of Chemistry*; M.I.T.: Cambridge, 2004, 221-244.
- (53) Yoon, S., In *Department of Chemistry*; M.I.T.: Cambridge, 2004, 245-302.
- (54) Kuzelka, J.; Farrell, J. R.; Lippard, S. J. *Inorg. Chem.* **2003**, *42*, 8652-8662.
-

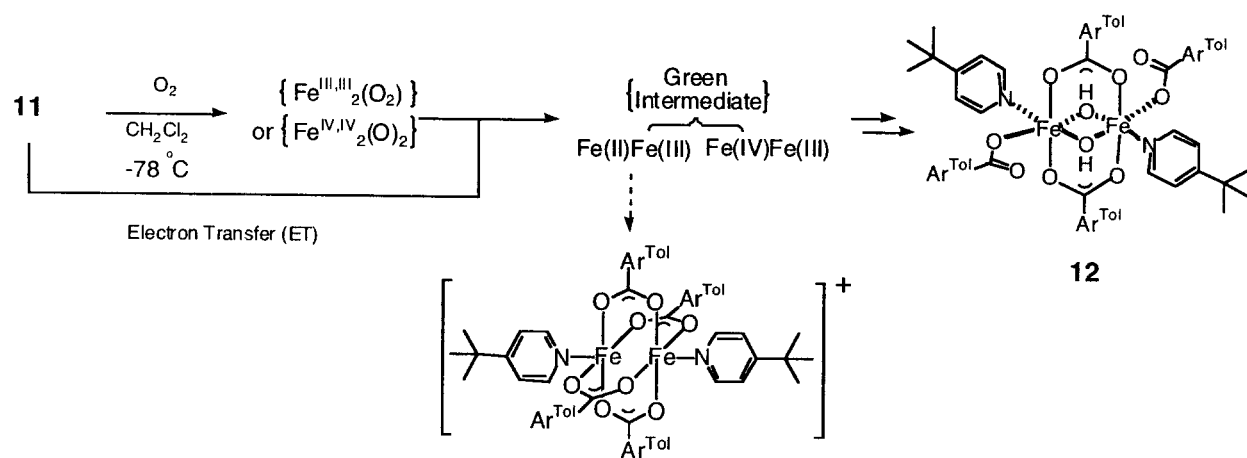




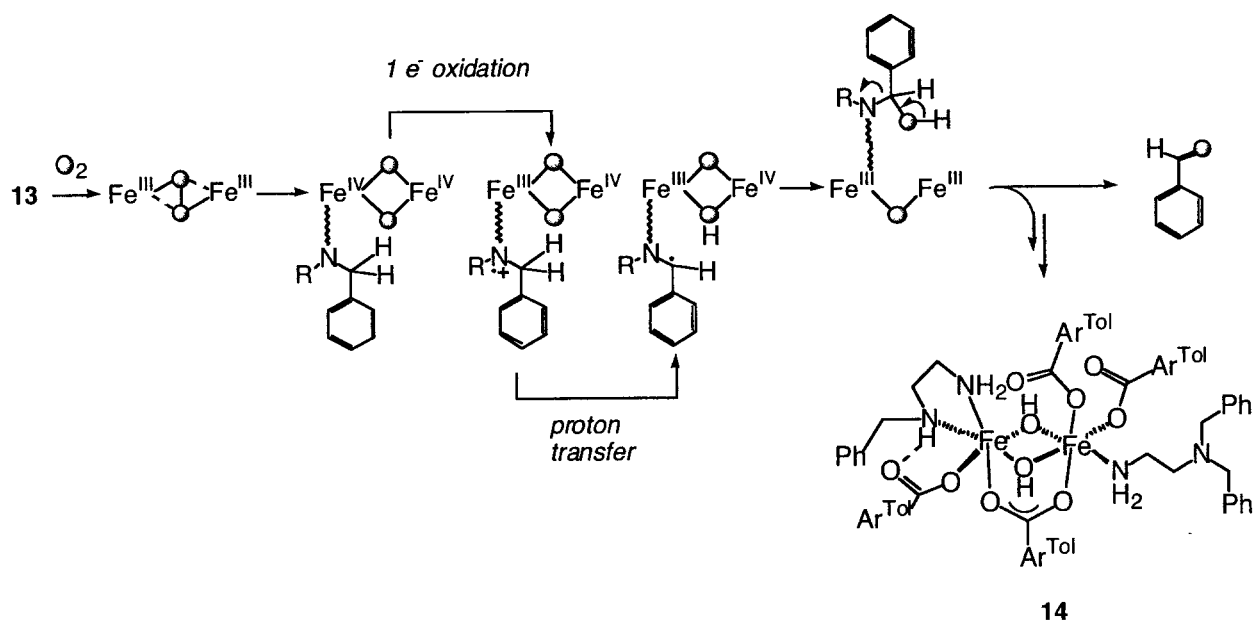
Scheme 1.1



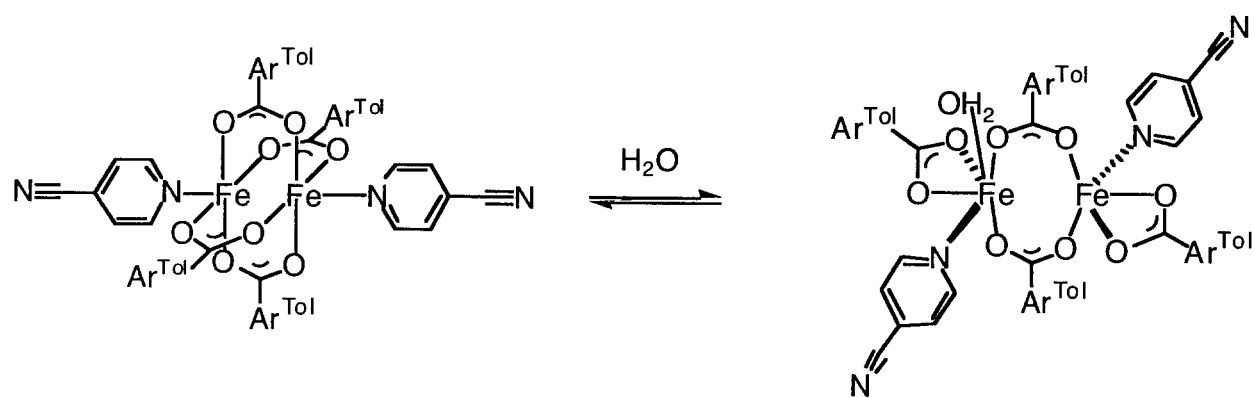
Scheme 1.2



Scheme 1.3



Scheme 1.4



Scheme 1.5

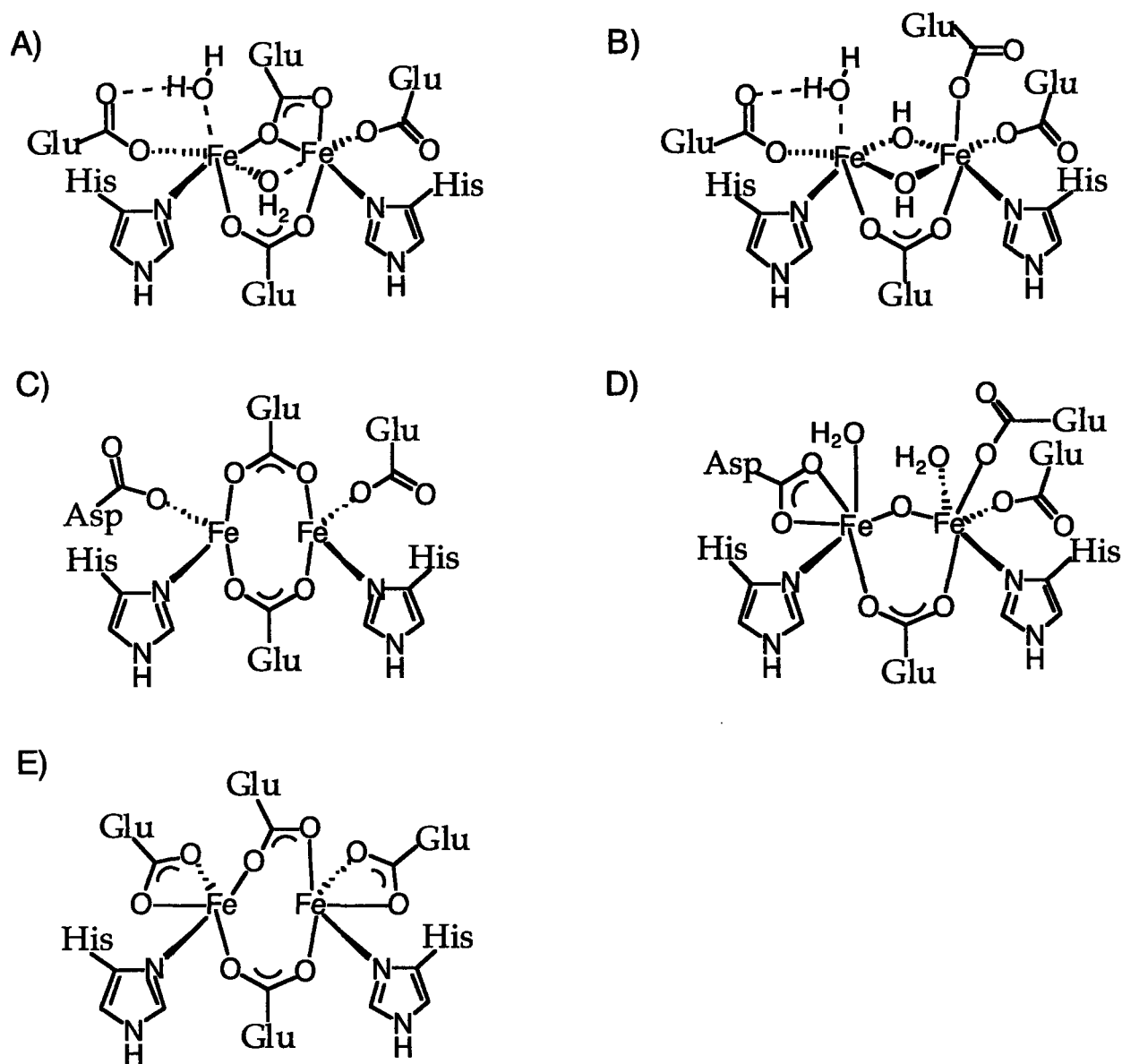


**Figure 1.1.** Schematic representations of the active sites of the non-heme diiron proteins having carboxylate-rich coordination environments. A) Reduced sMMOH B) Oxidized sMMOH C) Reduced RNR-R2 D) Oxidized RNR-R2 E) Reduced Δ9D.

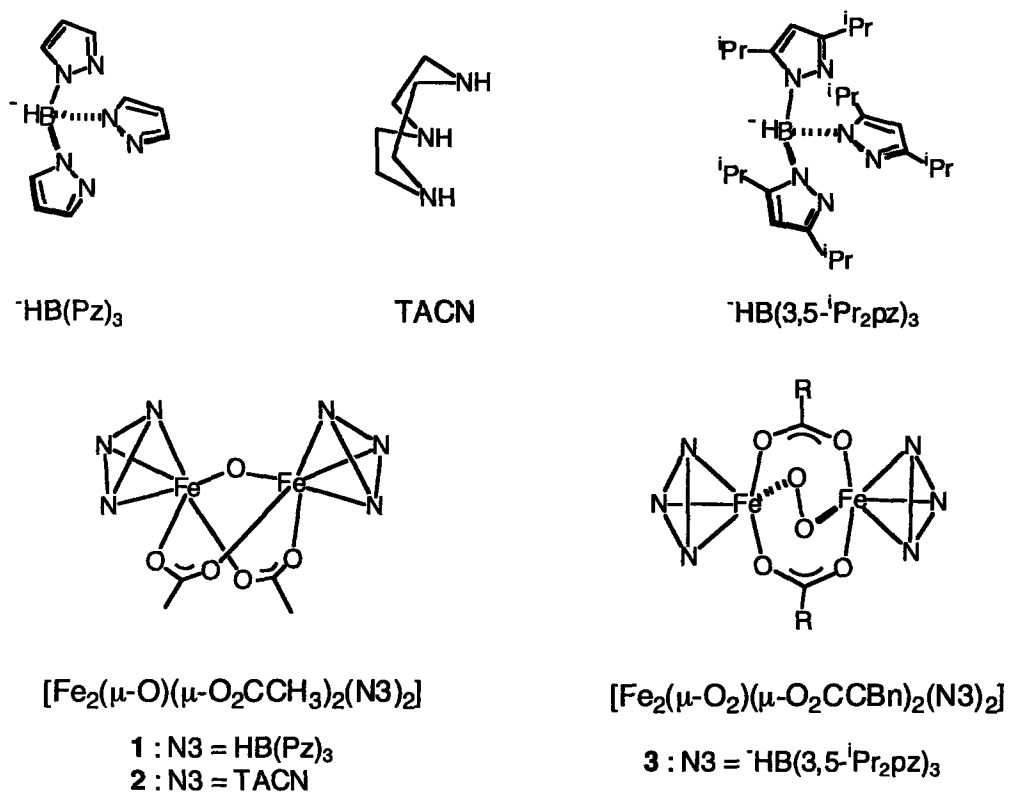
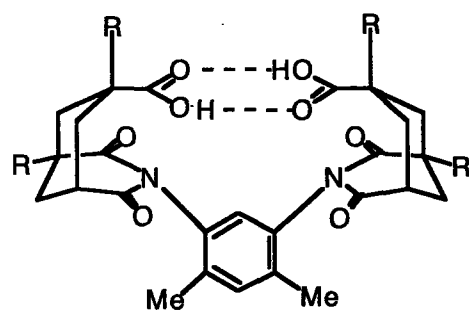
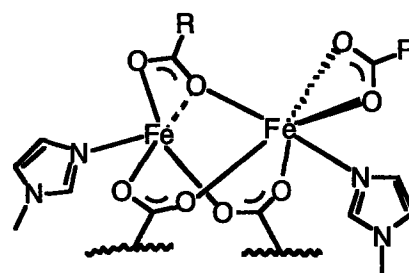


**Figure 1.2.** Examples of dicarboxylate-bridged diiron(III) complexes with nitrogen-rich coordination environments.



R = Me    H<sub>2</sub>XDK  
 R = <sup>n</sup>Pr    H<sub>2</sub>PXDK  
 R = Bn    H<sub>2</sub>BXDK



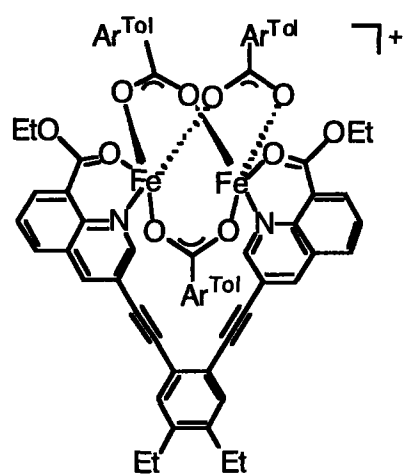
R = O<sub>2</sub>CCPhCy

7

**Figure 1.3.** The XDK family of ligands and resulting bis( $\mu$ -carboxylato)diiron(II) complex.







19

**Figure 1.5.** Representation of the cation  $[\text{Fe}_2(\text{Et}_2\text{BCQEB}^{\text{Et}})(\mu\text{-O}_2\text{CAr}^{\text{Tol}})_3]^+$  (19) featuring a syn disposition of nitrogen donors.

## Chapter 2

### **Mechanistic Studies of the Oxidative *N*-Dealkylation of a Benzyl Group Substrates Tethered to Carboxylate-Bridged Diiron(II) Complexes,**



## Introduction

The activation of triplet ground state dioxygen and the hydroxylation of unactivated C–H bonds under ambient conditions by iron- and copper-containing metalloenzymes have attracted considerable interest due to their potentially numerous catalytic and synthetic applications.<sup>1-4</sup> Monooxygenase enzymes, which catalyze hydroxylation of aliphatic hydrocarbons, are of particular interest because of their unique ability to functionalize C–H bonds.<sup>5,6</sup> The hydroxylase component of methane monooxygenase (MMOH) is one such enzyme that activates dioxygen to afford reactive intermediate(s).<sup>7</sup> The resulting oxidant can insert one oxygen atom into a C–H bond that is inherently difficult to activate. Understanding such a remarkable process in molecular detail is an important objective that may lead to new insights into how the metalloproteins work and how to design catalysts for dioxygen activation and C–H bond hydroxylation.

The active site of MMOH utilizes diiron sites, coordinated by four carboxylates and two histidine ligands derived from amino acid side chains, as a working module to achieve its physiological role.<sup>8</sup> Although a number of small model complexes can reproduce the composition of the diiron(II) site in MMOH,<sup>9-14</sup> few of these can function in a manner similar to the enzyme.<sup>9,15,16</sup> In particular, the carboxylate-rich composition of the protein diiron core has been reproduced with the use of sterically hindered terphenyl-derived carboxylate ligands.<sup>9-12,14-18</sup> Moreover, the diiron(II) complex  $[\text{Fe}_2(\mu\text{-O}_2\text{CAr}^{\text{Tot}})_2(\text{O}_2\text{CAr}^{\text{Tot}})_2(\text{N,N-Bn}_2\text{en})_2]$  (**1**), where  $\text{Ar}^{\text{Tot}}\text{CO}_2^-$  is 2,6-di(*p*-tolyl)benzoate and *N,N*-Bn<sub>2</sub>en is *N,N*-dibenzylethylenediamine, decomposes upon exposure to dioxygen, resulting in the formation of benzaldehyde (PhCHO) and  $[\text{Fe}_2(\mu\text{-OH})_2(\mu\text{-O}_2\text{CAr}^{\text{Tot}})(\text{O}_2\text{CAr}^{\text{Tot}})_3(\text{N,N-Bn}_2\text{en})(\text{N-Bnen})]$ , the latter being structurally homologous to the active site of oxidized MMOH (Scheme 2.1).<sup>9,15</sup> The oxidative *N*-dealkylation of a substrate tethered to a carboxylate-bridged diiron(II) complex by reaction with dioxy-

gen has been a highlight in the pursuit of structural and functional MMOH model complexes.

The stoichiometric correspondence of **1** with the diiron active site of MMOH and early experimental results indicated that the *N*-dealkylation reaction might involve an oxidant similar to that of the enzyme, perhaps a di( $\mu$ -oxo)diiron(IV) species.<sup>9,15</sup> Three possible pathways were suggested for insertion of the oxygen atom from such a high-valent intermediate into the benzylic C–H bond of the *N,N*-Bn<sub>2</sub>en ligand. Concerted insertion of the oxygen atom into the C–H bond (Top, Scheme 2.1) and conventional recoil with hydrogen atom transfer (HAT) followed by rebound (Middle, Scheme 2.1) for oxygenation of **1** follow commonly proposed mechanisms for the MMOH catalytic cycle.<sup>19</sup> Sequential single electron transfer (SET), deprotonation, and internal electron transfer (Bottom, Scheme 2.1) can equally well account for the observed chemistry. This possibility was suggested by the proximity of the lone pair of electrons on the uncoordinated nitrogen atom of the Bn<sub>2</sub>en ligand to the proposed electrophilic high-valent intermediate and also by the precedence for such chemistry in heme iron oxidations.<sup>20</sup>

The work described here was performed to clarify the mechanistic details of the hydroxylation reaction through a Hammett analysis and the measurement of intramolecular deuterium kinetic isotope effects (KIEs), both based on product distributions. These objectives were achieved by the synthesis and characterization of a series of diiron(II) complexes with *N,N*-Bn<sub>2</sub>en ligands containing *para* substituents on the phenyl ring or deuterium atoms at the benzylic position.

## Experimental Section

**General Considerations.** All reagents were obtained from commercial suppliers and used as received unless otherwise noted. Dichloromethane, diethylether and pentanes were saturated with argon and purified by passing through activated Al<sub>2</sub>O<sub>3</sub> col-

umns under argon.<sup>21</sup> Dioxygen (99.994%, BOC Gases) was dried by passing the gas stream through a column of Drierite. The compounds  $\alpha$ -*d*<sub>2</sub>-benzylamine,<sup>22</sup>  $[\text{Fe}_2(\mu\text{-O}_2\text{CAr}^{\text{Tol}})_2(\text{O}_2\text{CAr}^{\text{Tol}})_2(\text{THF})_2]$ ,<sup>10</sup> and  $[\text{Fe}_2(\mu\text{-O}_2\text{CAr}^{\text{Tol}})_2(\text{O}_2\text{CAr}^{\text{Tol}})_2(\text{N,N-Bn}_2\text{en})_2]$ <sup>9,15</sup> were prepared as described in the literature. All syntheses and air-sensitive manipulations were carried out under nitrogen in an MBraun glovebox.

**Physical Measurements.** <sup>1</sup>H and <sup>13</sup>C-NMR spectra were recorded on a Bruker 400 spectrometer in the Massachusetts Institute of Technology Department of Chemistry Instrument Facility (DCIF); chemical shifts were referenced to residual solvent peaks. FT-IR spectra were recorded either with a Thermo Nicolet Avatar 360 spectrometer or Perkin Elmer FTIR model 2000.

**Synthesis of Benzyl(4-R-benzyl)aminoacetonitrile Compounds.** The general reaction pathway is shown in Scheme 2.2. A solution of 4-R-benzaldehyde (0.100 mol), where R = Cl, F, CH<sub>3</sub>, *t*-Bu, and OCH<sub>3</sub>, in 27 mL of benzene was cooled to 0 °C. To this solution was added 10.8 g (0.101 mol) of benzylamine in 17 mL of benzene. The solution was warmed to ambient temperature. The flask was connected to a Dean-Stark water separator, followed by refluxing overnight, resulting in separation of ca 1.5 mL of water. The volatile portion was removed under reduced pressure, resulting in a light yellow oil, which was dissolved in 150 mL of methanol. The solution was cooled to 0 °C and 5.4 g (0.14 mol) of NaBH<sub>4</sub> was added slowly. The reaction mixture was allowed to warm to ambient temperature and stored overnight. The volume was reduced to half under reduced pressure and water (200 mL) was added. The product was extracted with 3 × 50 mL of dichloromethane, dried using anhydrous MgSO<sub>4</sub> and filtered through Celite. The volatile portion of the filtrate was removed under reduced pressure, resulting in a light yellow oil. To a rapidly stirred DMF (50 mL) solution of *N,N*-benzyl(4-R-benzyl)amine (96.7 mmol), were added first triethylamine (13.5 mL) and 6.8 mL of chloroacetonitrile in a dropwise manner. The solution turned cloudy and was stirred

overnight. DMF was removed under reduced pressure, and 40 mL of water were added. Anhydrous  $\text{Na}_2\text{CO}_3$  was added to increase the pH of solution to ca 14. The product was extracted with  $3 \times 50$  mL of dichloromethane, dried with  $\text{MgSO}_4$ , and filtered through Celite. The targeted compound was isolated by using silica column chromatography with ethylacetate as the eluent.

*Benzyl(4-chlorobenzyl)aminoacetonitrile*. Yield (77 %).  $^1\text{H}$  NMR ( $\text{CDCl}_3$ , 400 MHz):  $\delta$  7.41-7.32 (9 H, m), 3.74 (2 H, s), 3.72 (2 H, s), 3.37 (2 H, s).  $^{13}\text{C}$  NMR ( $\text{CDCl}_3$ , 100 MHz):  $\delta$  137.08, 135.84, 133.78, 130.43, 129.13, 129.05, 128.91, 128.11, 114.69, 58.43, 57.72, 40.99. FT-IR (NaCl disk,  $\text{cm}^{-1}$ ) 3063 (w), 3030 (w), 2933 (w), 2831 (m), 2228 (w,  $\nu_{\text{C}\equiv\text{N}}$ ), 1598 (w), 1492 (s), 1453 (m), 1419 (w), 1369 (w), 1324 (w), 1119 (w), 1090 (m), 1015 (m), 858 (w), 800 (m), 743 (m), 699 (m). GC/MS (EI)  $\text{M}^+$ : Calcd for  $\text{C}_{16}\text{H}_{15}\text{ClN}_2$ , 270; Found, 270.

*Benzyl(4-fluoro-benzyl)aminoacetonitrile*. Yield (72 %).  $^1\text{H}$  NMR ( $\text{CDCl}_3$ , 400 MHz):  $\delta$  7.41-7.31 (7 H, m), 7.07 (2H, t, 8.7 Hz), 3.74 (2 H, s), 3.72 (2 H, s), 3.37 (2 H, s).  $^{13}\text{C}$  NMR ( $\text{CDCl}_3$ , 100 MHz):  $\delta$  162.57 (d,  $^1J_{\text{CF}} = 246.1$  Hz), 137.16, 133.02 (d,  $^4J_{\text{CF}} = 3.1$  Hz), 130.7 (d,  $^3J_{\text{CF}} = 7.9$  Hz), 129.01, 128.90, 128.08, 115.74 (d,  $^2J_{\text{CF}} = 21.4$  Hz), 114.74, 58.40, 57.66, 40.90. FT-IR (NaCl disk,  $\text{cm}^{-1}$ ) 3031 (w), 2935 (w), 2826 (m), 2228 (w,  $\nu_{\text{C}\equiv\text{N}}$ ), 1602 (w), 1509 (s), 1454 (w), 1419 (w), 1369 (w), 1350 (w), 1324 (w), 1294 (w), 1223 (s), 1156 (w), 1119 (w), 1093 (w), 976 (w), 855 (m), 820 (m), 743 (m), 699 (m), 504(w). GC/MS (EI)  $\text{M}^+$ : Calcd for  $\text{C}_{16}\text{H}_{15}\text{FN}_2$ , 254; Found, 254.

*Benzyl(4-methyl-benzyl)aminoacetonitrile*. Yield (69 %).  $^1\text{H}$  NMR ( $\text{CDCl}_3$ , 400 MHz):  $\delta$  7.43-7.29 (7 H, m), 7.18 (2 H, d, 7.9 Hz), 3.75 (2 H, s), 3.73 (2 H, s), 3.38 (2 H, s), 2.37 (3 H, S).  $^{13}\text{C}$  NMR ( $\text{CDCl}_3$ , 100 MHz):  $\delta$  137.67, 137.41, 134.24, 129.50, 129.13, 129.10, 128.82, 127.94, 114.91, 58.39, 58.21, 40.86, 21.34. FT-IR (NaCl disk,  $\text{cm}^{-1}$ ) 3028 (m), 2923 (m), 2826 (m), 2230 (w,  $\nu_{\text{C}\equiv\text{N}}$ ), 1603 (w), 1515 (s), 1496 (m), 1454 (s), 1419 (m), 1369 (m), 1349 (w), 1324 (w), 1303 (w), 1249 (w), 1204 (w), 1179 (w), 1117 (m), 1105 (m), 1075 (w), 1022 (w),

975 (m), 858 (m), 803 (m), 758 (m), 742 (s), 699 (s), 488 (m). GC/MS (EI)  $M^+$ : Calcd for  $C_{17}H_{18}N_2$ , 250; Found, 250.

*Benzyl(4-tert-butyl-benzyl)aminoacetonitrile*. Yield (87 %).  $^1H$  NMR ( $CDCl_3$ , 400 MHz):  $\delta$  7.43-7.30 (9 H, m), 3.76 (2 H, s), 3.74 (2 H, s), 3.39 (2 H, s), 1.33 (9 H, s).  $^{13}C$  NMR ( $CDCl_3$ , 100 MHz):  $\delta$  150.96, 137.45, 134.26, 129.13, 128.84, 128.83, 127.94, 125.73, 114.95, 58.45, 58.11, 40.96, 34.74, 31.55. FT-IR (NaCl disk,  $cm^{-1}$ ) 3087 (w), 3062 (w), 3029 (w), 2963 (s), 2904 (m), 2868 (m), 2826 (m), 2228 (w,  $\nu_{C-N}$ ), 1513 (w), 1496 (w), 1454 (m), 1417 (w), 1363 (m), 1393 (w), 1323 (w), 1269 (w), 1111 (m), 1076 (w), 1028 (w), 859 (m), 740 (m), 737 (m), 699 (m). GC/MS (EI)  $M^+$ : Calcd for  $C_{20}H_{24}N_2$ , 292; Found, 292.

*Benzyl(4-methoxy-benzyl)aminoacetonitrile*. Yield (76 %).  $^1H$  NMR ( $CDCl_3$ , 400 MHz):  $\delta$  7.43-7.32 (7 H, m), 6.92 (2 H, d, 8.4 Hz), 3.83 (3 H, s), 3.75 (2 H, s), 3.71 (2 H, s), 3.37 (2 H, s).  $^{13}C$  NMR ( $CDCl_3$ , 100 MHz):  $\delta$  159.35, 137.39, 130.31, 129.25, 129.08, 128.78, 127.90, 114.87, 114.13, 58.28, 57.80, 55.42, 40.72. FT-IR (NaCl disk,  $cm^{-1}$ ) 3062 (w), 3030 (w), 3004 (w), 2934 (w), 2835 (m), 2230 (w,  $\nu_{C-N}$ ), 1611 (m), 1512 (s), 1454 (m), 1419 (w), 1302 (m), 1250 (s), 1173 (m), 1105 (w), 1076 (w), 1034 (m), 854 (w), 813 (w), 743 (m), 700 (m). GC/MS (EI)  $M^+$ : Calcd for  $C_{17}H_{18}N_2O$ , 266; Found, 266.

**Synthesis of Benzyl(4-R-benzyl)ethylenediamine Compounds (*N,N*-(4-R-Bn)Bnen).** To a rapidly stirred diethylether (25 mL) suspension of lithium aluminum hydride (LAH) (1.5 g, 36 mmol) was added a diethylether solution (25 mL) of benzyl(4-R-benzyl)aminoacetonitrile (19 mmol) at  $-78\text{ }^\circ\text{C}$ . The reaction mixture was stirred for 10 min, warmed to ambient temperature, and stirred overnight under argon. The sequential addition of 1.5 g of water, 1.5 g of 15 % NaOH(aq), and  $3 \times 1.5$  g of water was performed cautiously. The product was extracted with  $CH_2Cl_2$ , dried over  $MgSO_4$ , filtered through Celite, and evaporated under reduced pressure to afford light yellow oil.



*N,N*-Benzyl(4-chlorobenzyl)ethylenediamine (*N,N*-(4-Cl-Bn)Bnen). Yield (88 %). <sup>1</sup>H NMR (CDCl<sub>3</sub>, 400 MHz): δ 7.35-7.25 (9 H, mm), 3.57 (2 H, s), 3.54 (2 H, s), 2.75 (2 H, t, J = 6.0 Hz), 2.50 (2 H, t, J = 6.0 Hz). <sup>13</sup>C NMR (CDCl<sub>3</sub>, 100 MHz): δ 139.42, 138.27, 132.76, 130.30, 128.57, 128.50, 127.24, 58.74, 58.10, 56.81, 39.72. FT-IR (NaCl disk, cm<sup>-1</sup>) 3084 (w), 3061 (w), 3027 (w), 2939 (m), 2801 (s), 1597 (w), 1490 (s), 1452 (m), 1407 (w), 1366 (m), 1244 (w), 1126 (w), 1088 (m), 1028 (w), 1015 (m), 978 (w), 908 (w), 841 (m), 804 (m), 739 (m), 699 (m), 671 (w). ESIMS MH<sup>+</sup>: Calcd for C<sub>16</sub>H<sub>20</sub>ClN<sub>2</sub>, 275.4; Found, 275.4.

*N,N*-Benzyl(4-fluoro-benzyl)ethylenediamine (*N,N*-(4-F-Bn)Bnen). Yield (87 %). <sup>1</sup>H NMR (CDCl<sub>3</sub>, 400 MHz): δ 7.34-7.25 (7 H, mm), 7.01 (2H, t, 8.7 Hz), 3.57 (2 H, s), 3.54 (2 H, s), 2.75 (2 H, t, J = 6.0 Hz), 2.51 (2 H, t, J = 6.0 Hz). <sup>13</sup>C NMR (CDCl<sub>3</sub>, 100 MHz): δ 162.06 (d, <sup>1</sup>J<sub>CF</sub> = 244.7 Hz), 139.56, 135.36 (d, <sup>4</sup>J<sub>CF</sub> = 3.0 Hz), 130.43 (d, <sup>3</sup>J<sub>CF</sub> = 7.9 Hz), 128.98, 128.46, 127.19, 115.21 (d, <sup>2</sup>J<sub>CF</sub> = 21.3 Hz), 58.69, 58.01, 56.77, 39.74. FT-IR (NaCl disk, cm<sup>-1</sup>) 3028 (w), 2939 (w), 2802 (m), 1602 (w), 1508 (s), 1452 (w), 1366 (w), 1292 (w), 1220 (s), 1154 (w), 1126 (w), 1091 (w), 1070 (w), 1028 (w), 1015 (w), 978 (w), 824 (m), 791 (w), 767 (w), 739 (m), 699 (m), 502 (w). ESIMS MH<sup>+</sup>: Calcd for C<sub>16</sub>H<sub>20</sub>FN<sub>2</sub>, 259.3; Found, 259.4.

*N,N*-Benzyl(4-methyl-benzyl)ethylenediamine (*N,N*-(4-Me-Bn)Bnen). Yield (78 %). <sup>1</sup>H NMR (CDCl<sub>3</sub>, 400 MHz): δ 7.40-7.27 (7 H, mm), 7.16 (2 H, d, 7.5 Hz), 3.61 (2 H, s), 3.58 (2 H, s), 2.77 (2 H, t, J = 6.0 Hz), 2.53 (2 H, t, J = 5.9 Hz), 2.37 (3 H, s). <sup>13</sup>C NMR (CDCl<sub>3</sub>, 100 MHz): δ 139.82, 136.62, 136.56, 129.10, 129.00, 128.98, 128.39, 127.05, 58.70, 58.45, 56.84, 39.82, 21.28. FT-IR (NaCl disk, cm<sup>-1</sup>) 3372 (w), 3084 (w), 3025 (m), 2924 (s), 2798 (s), 1602 (w), 1513 (m), 1494 (m), 1452 (m), 1365 (m), 1104 (w), 1070 (w), 1027 (m), 845 (m), 737 (s), 698 (s), 486 (w). ESIMS MH<sup>+</sup>: Calcd for C<sub>17</sub>H<sub>23</sub>N<sub>2</sub>, 255.4; Found, 255.4.

*N,N*-Benzyl(4-tert-butyl-benzyl)ethylenediamine (*N,N*-(4-<sup>t</sup>Bu-Bn)Bnen). Yield (85 %). <sup>1</sup>H NMR (CDCl<sub>3</sub>, 400 MHz): δ 7.38-7.24 (9 H, mm), 3.59 (2 H, s), 3.57 (2 H, s), 2.76 (2 H, t, J = 6.0 Hz), 2.52 (2 H, t, J = 6.0 Hz), 1.32 (9 H, S). <sup>13</sup>C NMR (CDCl<sub>3</sub>, 100 MHz): δ 149.97, 139.88, 136.60, 129.03, 128.66, 128.43, 127.09, 125.34, 58.95, 58.38, 56.85, 39.82, 34.65, 31.61.

FT-IR (NaCl disk,  $\text{cm}^{-1}$ ) 3375 (w), 3085 (w), 3060 (w), 3026 (w), 2961 (s), 2903 (m), 2868 (m), 2798 (m), 1602 (w), 1512 (w), 1494 (w), 1453 (m), 1362 (m), 1269 (w), 1109 (w), 1070 (w), 1027 (w), 834 (m), 741 (m), 698 (m), 546 (w). ESIMS  $\text{MH}^+$ : Calcd for  $\text{C}_{20}\text{H}_{29}\text{N}_2$ , 297.5; Found, 297.5.

*N,N*-Benzyl(4-methoxy-benzyl)ethylenediamine (*N,N*-(4-OMe-Bn)Bnen). Light brown yellow crystals. Yield (83 %).  $^1\text{H}$  NMR ( $\text{CDCl}_3$ , 400 MHz):  $\delta$  7.34-7.22 (7 H, m), 6.86 (2 H, d, 8.6 Hz), 3.79 (3 H, s), 3.57 (2 H, s), 3.53 (2 H, s), 2.76 (2 H, t,  $J = 6.0$  Hz), 2.59 (2 H, t,  $J = 5.9$  Hz).  $^{13}\text{C}$  NMR ( $\text{CDCl}_3$ , 100 MHz):  $\delta$  158.88, 139.36, 131.12, 130.29, 129.11, 128.55, 127.26, 113.92, 58.54, 58.01, 55.44, 54.92, 39.09. FT-IR (NaCl disk,  $\text{cm}^{-1}$ ) 3027 (w), 2998 (w), 2933 (w), 2833 (m), 1611 (w), 1584 (w), 1511 (s), 1494 (w), 1452 (w), 1366 (w), 1301 (w), 1248 (s), 1178 (w), 1104 (w), 1035 (w), 819 (w), 740 (w), 699 (w). ESIMS  $\text{MH}^+$ : Calcd for  $\text{C}_{17}\text{H}_{23}\text{N}_2\text{O}$ , 271.4; Found, 271.4.

**$\alpha,\alpha'$ - $d_2$ -*N,N*-Dibenzylethylene-1,2-diamine (( $\text{C}_6\text{H}_5\text{CDH}$ ) $_2$ en).** To a stirred anhydrous suspension of lithium aluminum deuteride (2.6 g, 62 mmol) in diethylamine (25 mL) was added a solution of benzaldehyde oxime (3.0 g, 25 mmol), using a pressure-compensated dropping funnel at  $-78$  °C. The mixture was warmed to room temperature and stirred for 6 h before being carefully hydrolyzed by sequential addition of 2.6 g of water, 2.6 g of 15 % NaOH (aq), and  $3 \times 2.6$  g of water. Inorganic salts were removed by filtration and washed with 200 mL of ethylacetate. The filtrate was dried over  $\text{MgSO}_4$  and concentrated. The amine product was separated from starting oxime by extraction with  $\text{CHCl}_3$ , resulting in a turbid solution. The solution was filtered through Celite and concentrated. To a solution of  $d_1$ -benzylamine (1.6 g, 15 mmol) in 5 mL of benzene in a 50 mL round-bottom flask, cooled to 0 °C, was added a solution of PhCHO (2.0 g, 19 mmol) in 5 mL of benzene. The solution was warmed to room temperature, resulting in a turbid suspension. After 1 h stirring, the flask was connected to a Dean-Stark water separator and refluxed overnight at 92 °C. The solution was concentrated under vac-

uum, and without further purification, the resulting Schiff base was taken up in 60 mL of methanol and cooled to 0 °C. A 0.8 g (19 mmol) of solid NaBD<sub>4</sub> was carefully added, and the reaction mixture allowed to warm to room temperature and then stirred for an additional 12 h. The solvent was concentrated under vacuum, 100 mL of water was added, and the solution was extracted with 4 × 50 mL portions of ethylacetate. The solution was dried (MgSO<sub>4</sub>) and concentrated. With the resulting *d*<sub>2</sub>-*N,N*-dibenzylamine, the colorless oil (C<sub>6</sub>H<sub>5</sub>CDH)<sub>2</sub>en compound was prepared as described for the synthesis of benzyl(4-*R*-benzyl)ethylenediamine. Yield (54 %). <sup>1</sup>H NMR (CDCl<sub>3</sub>, 400 MHz): δ 7.38-7.24 (9 H, m), 3.59 (1 H, s), 3.57 (1 H, s), 2.76 (2 H, t, J = 6.0 Hz), 2.52 (2 H, t, J = 6.0 Hz). <sup>13</sup>C NMR (CDCl<sub>3</sub>, 100 MHz): δ 138.49, 129.14, 128.57, 127.37, 58.13 (t, <sup>1</sup>J<sub>CD</sub> = 18.98 Hz), 52.48, 38.04. FT-IR (NaCl disk, cm<sup>-1</sup>) 3059 (w), 3025 (w), 2938 (w), 2080 (w), 1662 (m), 1603 (m), 1494 (s), 1449 (s), 1397 (w), 1342 (w), 1313 (w), 1213 (w), 1155 (w), 1075 (w), 1028 (w), 924 (w), 738 (s), 698 (s), 614 (w). ESIMS MH<sup>+</sup>: Calcd for C<sub>16</sub>H<sub>19</sub>D<sub>2</sub>N<sub>2</sub>, 243.4; Found, 243.4.

***α,α-d*<sub>2</sub>-*N,N*-Dibenzylethylene-1,2-diamine ((C<sub>6</sub>H<sub>5</sub>CD<sub>2</sub>)Bnen).** The compound *α,α-d*<sub>2</sub>-benzylamine was prepared by reduction of cyanobenzene using lithium aluminum deuteride as described in the literature.<sup>10</sup> With the resulting *α,α-d*<sub>2</sub>-benzylamine, the colorless oil (D<sub>2</sub>-Bn)Bnen was prepared as described for the synthesis of benzyl-(4-*R*-benzyl)ethylenediamine. Yield (71 %). <sup>1</sup>H NMR (CDCl<sub>3</sub>, 400 MHz): δ 7.38-7.24 (9 H, m), 3.60 (2 H, s), 2.76 (2 H, t, J = 6.0 Hz), 2.52 (2 H, t, J = 6.0 Hz). ESIMS MH<sup>+</sup>: Calcd for C<sub>16</sub>H<sub>19</sub>D<sub>2</sub>N<sub>2</sub>, 243.4; Found, 243.4.

**Synthesis of [Fe<sub>2</sub>(μ-O<sub>2</sub>CAr<sup>Tol</sup>)<sub>2</sub>(O<sub>2</sub>CAr<sup>Tol</sup>)<sub>2</sub>(*N,N*-(4-*R*-Bn)Bnen)<sub>2</sub>] Complexes.** To a rapidly stirred CH<sub>2</sub>Cl<sub>2</sub> (3 mL) solution of [Fe<sub>2</sub>(μ-O<sub>2</sub>CAr<sup>Tol</sup>)<sub>2</sub>(O<sub>2</sub>CAr<sup>Tol</sup>)<sub>2</sub>(THF)<sub>2</sub>] (37 mg, 0.026 mmol) were added 2 equiv of *N,N*-(4-*R*-Bn)Bnen or deuterated Bn<sub>2</sub>en. After 2 h, the solution was filtered through Celite and reduced to 3 mL under reduced pressure.

Colorless block crystals were isolated upon the vapor diffusion of pentane into the solution and characterized by X-ray crystallography and elemental analysis.

$[Fe_2(\mu-O_2CAr^{Tol})_2(O_2CAr^{Tol})_2(N,N-(4-Cl-Bn)Bnen)_2]$  (2). Yield 68 %. FT-IR (KBr,  $cm^{-1}$ ) 3321 (m), 3250 (w), 3056 (w), 3027 (m), 2920 (m), 2875 (w), 2835 (m), 1609 (s), 1549 (s), 1515 (s), 1489 (m), 1456 (s), 1408 (m), 1384 (s), 1346 (w), 1186 (w), 1098 (w), 1075 (m), 1018 (m), 856 (m), 837 (m), 818 (m), 801 (s), 784 (m), 764 (m), 735 (m), 704 (m), 610 (m), 584 (m), 546 (w), 522 (m), 456 (w). Anal. Calcd for  $2 \cdot 0.5(CH_2Cl_2)$  or  $C_{116.5}Cl_3H_{107}Fe_2N_4O_8$ : C, 73.29; H, 5.65; N, 2.93. Found: C, 73.21; H, 5.42; N, 2.67.

$[Fe_2(\mu-O_2CAr^{Tol})_2(O_2CAr^{Tol})_2(N,N-(4-F-Bn)Bnen)_2]$  (3). Yield 46 %. FT-IR (KBr,  $cm^{-1}$ ) 3316 (m), 3268 (w), 3057 (w), 3024 (w), 2919 (s), 2861 (w), 1605 (s), 1547 (s), 1508 (s), 1454 (s), 1410 (m), 1383 (s), 1307 (w), 1263 (w), 1221 (s), 1187 (w), 1152 (w), 1110 (w), 1070 (w), 1041 (w), 1020 (w), 974 (w), 855 (w), 819 (s), 801 (s), 784 (s), 765 (s), 736 (s), 700 (s), 584 (m), 546 (m), 521 (m). Anal. Calcd for 3,  $C_{116}F_2H_{106}Fe_2N_4O_8$ : C, 75.98; H, 5.83; N, 3.06. Found: C, 75.45; H, 5.83; N, 3.50.

$[Fe_2(\mu-O_2CAr^{Tol})_2(O_2CAr^{Tol})_2(N,N-(4-Me-Bn)Bnen)_2]$  (4). Yield 67 %. FT-IR (KBr,  $cm^{-1}$ ) 3319 (m), 3254 (w), 3057 (w), 3023 (w), 2917 (w), 2790 (w), 1604 (s), 1565 (s), 1514 (s), 1454 (s), 1410 (m), 1373 (s), 1307 (w), 1269 (w), 1242 (s), 1187 (w), 1142 (w), 1118 (w), 1082 (w), 1044 (w), 1017 (w), 974 (w), 852 (w), 819 (s), 801 (s), 787 (s), 765 (m), 739 (s), 698 (s), 584 (m), 543 (m), 521 (s). Anal. Calcd for  $4 \cdot 0.5(CH_2Cl_2)$ ,  $C_{118.5}Cl_1H_{113}Fe_2N_4O_8$ : C, 76.18; H, 6.10; N, 3.00. Found: C, 76.01; H, 6.37; N, 3.17.

$[Fe_2(\mu-O_2CAr^{Tol})_2(O_2CAr^{Tol})_2(N,N-(4-t-Bu-Bn)Bnen)_2]$  (5). Yield 57 %. FT-IR (KBr,  $cm^{-1}$ ) 3321 (m), 3270 (w), 3057 (m), 3025 (m), 2961 (s), 2919 (m), 2866 (m), 2799 (m), 1608 (s), 1545 (s), 1515 (s), 1495 (m), 1455 (s), 1410 (s), 1384 (s), 1306 (m), 1269 (m), 1212 (w), 1187 (w), 1145 (w), 1109 (m), 1070 (m), 1041 (w), 1020 (m), 984 (m), 943 (w), 855 (m), 818 (m), 800 (s), 785 (m), 766 (m), 737 (m), 712 (m), 699 (m), 608 (w), 584 (m), 544 (m), 521 (m), 455

(w). Anal. Calcd for  $5 \cdot 0.5(\text{CH}_2\text{Cl}_2)$ ,  $\text{C}_{124.5}\text{ClH}_{125}\text{Fe}_2\text{N}_4\text{O}_8$ : C, 76.59; H, 6.45; N, 2.87. Found: C, 76.70; H, 6.71; N, 3.00.

$[\text{Fe}_2(\mu\text{-O}_2\text{CAr}^{\text{Tot}})_2(\text{O}_2\text{CAr}^{\text{Tot}})_2(\text{N,N-(4-OMe-Bn)Bnen})_2]$  (6). Yield 54 %. FT-IR (KBr,  $\text{cm}^{-1}$ ) 3318 (w), 3256 (w), 3057 (w), 3024 (m), 2918 (m), 2833 (w), 2795 (w), 1610 (s), 1584 (m), 1593 (m), 1513 (s), 1454 (s), 1407 (w), 1378 (m), 1329 (s), 1305 (m), 1246 (s), 1179 (w), 1143 (w), 1110 (m), 1070 (w), 1038 (m), 1021 (w), 977 (w), 820 (s), 802 (s), 786 (m), 766 (m), 739 (m), 716 (w), 699 (m), 609 (m), 546 (m), 524 (m), 467 (w). Anal. Calcd for  $6 \cdot \text{CH}_2\text{Cl}_2$ ,  $\text{C}_{119}\text{Cl}_2\text{H}_{114}\text{Fe}_2\text{N}_4\text{O}_{10}$ : C, 73.57; H, 5.91; N, 2.88. Found: C, 73.61; H, 6.12; N, 3.26.

$[\text{Fe}_2(\mu\text{-O}_2\text{CAr}^{\text{Tot}})_2(\text{O}_2\text{CAr}^{\text{Tot}})_2((\text{C}_6\text{H}_5\text{CDH})_2\text{en})_2]$  (7). Yield 26 %. FT-IR (KBr,  $\text{cm}^{-1}$ ) 3348 (m), 3293 (m), 3058 (w), 3025 (w), 2925 (m), 2881 (w), 1606 (s), 1576 (s), 1515 (s), 1495 (m), 1455 (s), 1413 (s), 1387 (s), 1306 (w), 1264 (m), 1186 (w), 1138 (w), 1110 (m), 1073 (m), 1020 (m), 820 (s), 801 (s), 786 (w), 766 (w), 736 (m), 701(s).

$[\text{Fe}_2(\mu\text{-O}_2\text{CAr}^{\text{Tot}})_2(\text{O}_2\text{CAr}^{\text{Tot}})((\text{C}_6\text{H}_5\text{CD}_2)\text{Bnen})_2]$  (8). Yield 63 %. FT-IR (KBr,  $\text{cm}^{-1}$ ) 3315 (m), 3268 (m), 3058 (m), 3023 (m), 2919 (m), 2859 (w), 1612 (s), 1544 (s), 1515 (s), 1493 (m), 1454 (s), 1410 (m), 1381 (s), 1109 (w), 1038 (w), 1021 (w), 986(w), 913 (w), 857 (w), 820 (m), 800 (s), 783 (m), 765 (w), 736 (m), 714 (m), 699 (m), 584 (w), 546 (w), 520 (w), 452 (w).

**X-ray Crystallographic Studies.** Single crystals were mounted at room temperature on the tips of quartz fibers, coated with Paratone-N oil, and cooled under a stream of cold nitrogen. Intensity data were collected on a Bruker (formerly Siemens) APEX CCD diffractometer running the SMART software package, with Mo  $\text{K}\alpha$  radiation ( $\lambda = 0.71073 \text{ \AA}$ ). Data collection and reduction protocols are described in detail elsewhere.<sup>23</sup> The structures were solved by Patterson methods and refined on  $F^2$  by using the SHELXTL software package.<sup>24</sup> Empirical absorption corrections were applied with SADABS,<sup>25</sup> part of the SHELXTL program package, and the structures were checked for higher symmetry by the program PLATON.<sup>26</sup> All non-hydrogen atoms

were refined anisotropically. In general, hydrogen atoms were assigned idealized positions and given thermal parameters equivalent to either 1.5 (methyl hydrogen atoms) or 1.2 (all other hydrogen atoms) times the thermal parameter of the carbon atom to which they were attached. In the structures of 2 - 6, two CH<sub>2</sub>Cl<sub>2</sub> solvent molecules were assigned in the lattice. In the structure of 7, one carbon atom connected to the primary amine in (C<sub>6</sub>H<sub>5</sub>CDH)<sub>2</sub>en ligand is disordered over two places with 0.7 and 0.3 occupancy factors; hydrogen atoms for the disordered atom were omitted. One CH<sub>2</sub>Cl<sub>2</sub> solvent molecule was assigned in the lattice in the structure of 8. Data collection and experimental details for the complexes are summarized in Table 2.1 and relevant interatomic bond lengths and angles are listed in Table 2.2.

**General Procedures for Oxidative N-Dealkylation Studies Using GC and GC/MS Analysis.** Analyses were carried out on an HP-5970 gas chromatograph connected to a HP-5971 mass analyzer. An Alltech Econo-cap EC-WAX capillary column of dimensions (30 m × 0.25 mm × 0.25 μm) and HP-5 cross-linked 5% PhMe-silicone column (25 m × 0.32 mm × 0.5 μm) were used for GC/MS and GC studies, respectively. The following method was used to effect all separations: initial temperature = 50 °C; initial time = 6 min; temperature ramp = 50 – 200 °C at 20 deg/min. The products were identified by comparing their retention times and mass spectral patterns to those of authentic standards. FID response was calibrated by running with authentic samples containing an internal standard of 1,2-dichlorobenzene. All samples were prepared in an anaerobic glove box. Analytical conditions were maintained to match those reported in the initial studies of compound 1. The 12.0 mM CH<sub>2</sub>Cl<sub>2</sub> solutions of compounds [Fe<sub>2</sub>(μ-O<sub>2</sub>CAr<sup>Tol</sup>)<sub>2</sub>(O<sub>2</sub>CAr<sup>Tol</sup>)<sub>2</sub>(N,N-(4-R-Bn)Bnen)<sub>2</sub>] were prepared under nitrogen. The solutions turn brownish-yellow immediately upon the exposure to dioxygen at 23 °C. After 1 h of additional stirring, 1,2-dichlorobenzene was added as an internal standard, and the reaction mixture was filtered through a 1-cm silica column to separate the or-

ganic products from inorganic materials. The resulting transparent solution was analyzed by GC. Standard deviations were obtained from the results of at least three independently prepared samples.

**Kinetic Isotope Effect Measurements.** The product distribution was initially monitored by using GC-MS analysis. Because the peaks for PhCHO and deuterated benzaldehyde (PhCDO) were not well separated,  $^1\text{H-NMR}$  intensities were ultimately employed to determine the product distribution. A 12.0 mM  $\text{CH}_2\text{Cl}_2$  solution of **7** or **8** was gently purged with dioxygen gas for 1 h, maintaining the temperature at 23 °C, and filtered through a 1-cm dry silica column. The  $^1\text{H}$  NMR spectrum was used to determine the product distribution. Standard deviations were obtained from the results of three independently prepared samples.

## Results

**Ligand Syntheses.** A drawback in planning the mechanistic study of the oxygenation pathway of **1** is the absence of unique optical spectroscopic features that can be used to follow the course of reaction. No band corresponding to the electronic transition of an intermediate develops when dioxygen is introduced a solution of **1**, even at – 78 °C. Deeper insight into the nature of the C–H bond-breaking step, for which three pathways has been proposed (Scheme 2.1.), were therefore sought by Hammett and KIE studies based on the distribution of oxygenation products of the complexes  $[\text{Fe}_2(\mu\text{-O}_2\text{CAr}^{\text{Tol}})_2(\text{O}_2\text{CAr}^{\text{Tol}})_2\text{L}_2]$ , where L is *N,N*-(4-R-Bn)Bnen or  $(\text{C}_6\text{H}_5\text{CDH})_2\text{en}$ .

A series of asymmetric ligands *N,N*-(4-R-Bn)Bnen with *para*-R-groups Cl, F, Me, *t*Bu, or  $\text{OCH}_3$  was prepared by the four-step route depicted in Scheme 2.2, starting from commercially available benzylamine and the respective benzaldehyde. Reaction of benzylamine with the *para*-substituted benzaldehyde (4-R-PhCHO) yielded (4-R-benzyl)benzylimines, which were converted to the compounds (4-R-

benzyl)benzylamines by treatment with  $\text{NaBH}_4$ . Reaction of the (4-R-benzyl)benzylamines with chloroacetonitrile afforded the (4-R-benzyl)benzylaminoacetonitriles. Reduction of these acetonitriles with  $\text{LiAlH}_4$  generated the targeted asymmetric (4-R-benzyl)benzylethylenediamines with overall good yields. The ligand  $(\text{C}_6\text{H}_5\text{CDH})_2\text{en}$  was synthesized from  $\alpha$ -*d*-benzylamine, prepared by the reduction of benzaldehyde oxime with lithium aluminum deuteride. Reaction of  $\alpha$ -*d*-benzylamine with benzaldehyde ( $\text{PhCHO}$ ) yielded ( $\alpha$ -*d*-benzyl)-benzyl-imine, which was converted to  $\alpha,\alpha'$ -*d*<sub>2</sub>-dibenzylamine by treatment with  $\text{NaBD}_4$ . With the resulting  $\alpha,\alpha$ -*d*<sub>2</sub>-dibenzylamine, the compound  $(\text{C}_6\text{H}_5\text{CDH})_2\text{en}$  was prepared as described for the synthesis of  $N,N$ -(4-R-Bn)Bnen. The asymmetric dideuterated  $\text{Bn}_2\text{en}$  ligand,  $(\text{C}_6\text{H}_5\text{CD}_2)\text{Bnen}$ , was prepared from  $\alpha$ -*d*<sub>2</sub>-benzylamine,<sup>22</sup> following a similar reaction route previously described for the synthesis of  $N,N$ -(4-R-Bn)Bnen ligands.

**Synthesis and Structural Characterization of Diiron(II) Complexes.** The reaction of the precursor complex,  $[\text{Fe}_2(\mu\text{-O}_2\text{CAr}^{\text{Tol}})_2(\text{O}_2\text{CAr}^{\text{Tol}})_2(\text{THF})_2]$ , with 2 equiv of the diamine ligands  $N,N$ -(4-R-Bn)Bnen ( $\text{R} = \text{MeO}, \text{}^t\text{Bu}, \text{Me}, \text{F}, \text{Cl}$ ),  $(\text{C}_6\text{H}_5\text{CDH})_2\text{en}$ , and  $(\text{C}_6\text{H}_5\text{CD}_2)\text{Bnen}$  afforded the neutral diiron(II) complexes 2 – 8. Their structures, shown in Figures 2.1 – 2.7, were determined by X-ray diffraction. All compounds contain a crystallographic inversion center. The pseudo-trigonal bipyramidal iron(II) centers in 5, 7, and 8 have an  $\text{NO}_4$  coordination environment with chelating terminal carboxylate ligands. In 2, 3, 4 and 6, however, the terminal carboxylates are monodentate, resulting in four coordinate  $\text{NO}_3$  coordination environments. The relatively long  $\text{Fe1}\cdots\text{O}$ (terminal carboxylate) distance of ca 2.5 Å may be compared to the shorter distances of ~2.25 Å in 5, 7, and 8 (Table 2.2). In the all compounds, the coordinatively unsaturated iron(II) centers are bridged by two carboxylates and the  $\text{Fe}\cdots\text{Fe}$  distances vary from 3.8680(8) Å to 4.360(5) Å. The  $\text{Fe}\cdots\text{Fe}$  distances in 7 and 8, which have similar chemical compositions, are 4.360(5) and 3.934(2) Å, respectively. These diverse  $\text{Fe}\cdots\text{Fe}$  and  $\text{Fe-O}$  distances in-



volving terminal carboxylates indicate the flexible character of the carboxylate-rich diiron(II) units. The 4-R groups in the *N,N*-(4-R-Bn)Bnen ligands of **2**, **3**, **4**, and **6** are disordered over two positions, each assigned a 0.5 occupancy factor; however, the *tert*-butyl group in **5**, which is a bigger relative to the other 4-R groups, are localized on just one of the phenyl rings of the Bn<sub>2</sub>en moiety.

#### Hammett Study of the Reactions of Diiron(II) Complexes **2** - **6** with Dioxygen.

The series of diiron(II) complexes prepared with ligands <sup>4</sup>R-BnBnen (R = Cl, F, Me, *t*-Bu, or OCH<sub>3</sub>) were allowed to react with O<sub>2</sub> at ambient temperature. Both 4-R-PhCHO and PhCHO were identified in the oxygenation product mixture by GC-MS spectroscopy (Scheme 2.2). The product distributions were analyzed by GC and the overall yields were ~ 60 % based on the Fe<sub>2</sub> unit (Table 2.3). In addition to GC analysis, the products ratios in the oxygenation reactions of **2** and **5** were confirmed by using <sup>1</sup>H-NMR spectroscopy, comparing the integrated intensities of the aldehyde C–H protons of 4-R-PhCHO and PhCHO (Table 2.3, Figure 2.8). The resulting product ratios were the same within error as those determined by GC analysis. A plot of the product ratios against Hammett  $\sigma$  values<sup>27</sup> (Figure 2.9) revealed a linear relationship, supporting the existence of similar transition states (TS) for the set of reactants. The positive slope,  $\rho = + 0.48$  ( $R = 0.98$ ), indicates that the TS is stabilized by electron withdrawing substituents. This result strongly suggests that C–H bond breaking occurs through generation of anionic character at the benzylic position in the transition state.

**Kinetic Isotope Effects.** The determination and interpretation of intramolecular KIEs is one approach to unravel C–H bond breaking mechanisms in spectroscopically silent reactions.<sup>28-30</sup> The method interrogates the effect on the product distribution of replacing an atom, from at least two equivalent atoms, by one of its isotopes. These types of intramolecular KIEs are not affected by steps that occur before and after C–H bond

breaking. The observation of a  $KIE_{intra}$  reflects the changes in the C–H(D) bonds from reactants to the TS in the C–H bond breaking step.<sup>28,30</sup>

A  $KIE_{intra}$  value of 1.3 (1) at 23 °C was obtained from the PhCDO/PhCHO ratio for oxygenation of  $[Fe_2(\mu-O_2CAr^{Tol})_2(O_2CAr^{Tol})_2((C_6H_5CDH)_2en)_2]$  (7). This value was determined by using product distribution analysis between PhCDO and PhCHO based on GC-MS and  $^1H$  NMR spectroscopy (Figure 2.10). Breaking of the C–H bond in 7 yields the amino alcohol, which eliminates PhCDO (see Scheme 2.3). The near unity value of the KIE raise the question of whether it is a secondary instead of a primary effect. To address this issue, the compound  $[Fe_2(\mu-O_2CAr^{Tol})_2(O_2CAr^{Tol})_2((C_6H_5CD_2)Bnen)_2]$  (8) having asymmetrically deuterated  $Bn_2en$  ligands was prepared. If the KIE value for 7 was to originate from a secondary isotope effect, the KIE values for 8 should be the reciprocal of 1.3, whereas, the primary KIE values for oxygenation of 7 and 8 are expected to be identical (Scheme 2.3). C–H bond breaking at the benzylic position of the  $(C_6H_5CDH)_2en$  ligand and C–D bond breaking within the  $(C_6H_5CD_2)Bnen$  ligand both afford a C–D bond at the benzylic position.

The  $KIE_{intra}$  value of 8, measured by the same methods as used for 7, is 2.2 (2) at 23 °C, obtained from the ratio of PhCHO/PhCDO (Figure 2.11). In the case of 8, the C–H bond breaking generates PhCHO (Scheme 2.3). The  $KIE_{intra}$  value, 2.2, is still small but larger than that obtained by oxygenation of 7. We interpret these results in the following manner. The observed KIE for 7 is a primary effect; although small, it is not the reciprocal of the KIE of 8. Evidently, the differences in two KIE values indicate that secondary effects contribute to the C–H bond breaking step in addition to the primary KIEs. The combination of primary and secondary effects for the oxygenation of 7 and 8 is described by eqs 1 and 2, respectively.

$$KIE_{obs} \text{ for } 7 = KIE_{primary} \times (1/KIE_{secondary}) \quad (1)$$

$$\text{KIE}_{\text{obs}} \text{ for } \mathbf{8} = \text{KIE}_{\text{primary}}^{75} \times \text{KIE}_{\text{secondary}} \quad (2)$$

In the case of **7**, the secondary KIE may detract from the primary KIE as shown in Scheme 2.3, whereas both primary and secondary effects are expected to contribute the oxygenation of **8**. The result is a larger KIE value for **8** than for **7**. Based on these measured KIEs, primary and secondary KIE values were calculated to be 1.7 and 1.3, respectively. A secondary KIE that occurs for the oxygenation of complexes is often interpreted in terms of differing inductive and steric effects for the isotopic forms (a CD<sub>3</sub> group is ca 10 % smaller than a CH<sub>3</sub> group).<sup>31</sup> The steric effect cannot apply to the oxygenation of **7** and **8**, however, since a secondary KIE <1 should have been obtained for the intramolecular competition (the CD<sub>2</sub> group in **8** is less hindered than the CH<sub>2</sub> group). Therefore, the observed secondary KIE may originate from the fact that deuterium is slightly more electron-donating than the proton.<sup>32</sup> The generated anionic character at the benzylic position in TS state (see Hammett study) may be more destabilized by the electron-donating deuterium in the benzylic position, resulting in a secondary KIE reinforcing the primary effect in **8**, but canceling that in the case of **7**.

## Discussion

Oxidative *N*-dealkylation of the complex [Fe<sub>2</sub>(μ-O<sub>2</sub>CAr<sup>Tol</sup>)<sub>2</sub>(O<sub>2</sub>CAr<sup>Tol</sup>)<sub>2</sub>(*N,N*-Bn<sub>2</sub>en)<sub>2</sub>] (**1**) upon introduction of dioxygen<sup>9,15</sup> parallels the activation of O<sub>2</sub> and C–H bond hydroxylation by non-heme diiron enzyme active sites and is analogous to the dealkylation reactions catalyzed by cytochrome P450 enzymes.<sup>33</sup> Reaction of compound **1** with dioxygen may afford a transient adduct [1-O<sub>2</sub>], which never builds up because the tethered substrates readily react with any species so generated. Formal possibilities for the dioxygen adduct include Fe<sub>2</sub><sup>II,III</sup>(O<sub>2</sub><sup>-</sup>), Fe<sub>2</sub><sup>III</sup>(O<sub>2</sub><sup>2-</sup>), and Fe<sub>2</sub><sup>IV</sup>(O<sup>2-</sup>)<sub>2</sub>. We previously reported the formation and characterization of a high-valent Fe(III)Fe(IV) species in the

reaction between dioxygen and diiron(II) complexes built with the  $\text{Ar}^{\text{Tot}}\text{CO}_2^-$  ligand system, through bimolecular electron transfer between a putative  $\text{Fe}_2^{\text{IV}}(\text{O}^2)_2$  species and the  $\text{Fe}_2^{\text{II,II}}$  starting material.<sup>10,11</sup> These results suggest the involvement of a high-valent iron(IV)-oxo species as a potential oxidant in the *N*-dealkylation reaction of **1**, analogous to well-studied *N*-dealkylations by cP450,<sup>33</sup>  $\text{Cu}_2(\text{O})_2$ ,<sup>34-36</sup> and  $\text{Ni}_2(\text{O})_2$ <sup>37</sup> metal centers. Assuming the participation of such a high-valent iron oxo species, three reaction pathways were proposed for the oxidative *N*-dealkylation reaction of dioxygen with the diiron(II) complex  $[\text{Fe}_2(\mu\text{-O}_2\text{CAr}^{\text{Tot}})_2(\text{O}_2\text{CAr}^{\text{Tot}})_2(\text{N,N-Bn}_2\text{en})_2]$  (Scheme 2.1).<sup>9</sup> An electrophilic high-valent diiron oxo unit may perform 2-electron oxidative *N*-dealkylation by hydrogen atom abstraction followed by oxygen rebound or by concerted insertion of the oxygen atom into a C–H bond. Alternatively, sequential one-electron oxidation of the dangling nitrogen atom by the proposed electrophilic high-valent iron(IV) oxo species, followed by  $\alpha$ -proton abstraction and sequential oxygen rebound, may also be the mechanism.

The present Hammett plot and  $\text{KIE}_{\text{intra}}$  results indicate that anionic character develops in the transition state during the C–H bond breaking step, thus ruling out Paths A and B in Scheme 2.4. Both hydrogen atom abstraction (Path A) and concerted oxygen atom insertion (Path B) generate positive character at the benzylic position. Large KIE values (>20) have been reported for *N*-dealkylations, effected through HAT mechanisms by  $\text{Cu}^{35}$  and  $\text{Ni}^{37}$  complexes, in contrast to the small KIE values for oxygenation of **7** and **8**. Single electron transfer from the nitrogen atom followed by  $\alpha$ -proton abstraction (Path C in Scheme 2.4) may proceed through a TS that has anionic character at the benzylic position. As shown in Path C, the KIEs would occur in the deprotonation step that occurs following electron transfer. The size of primary deuterium KIEs for proton transfer processes are generally considered to be a measure of the symmetry of the transition state. The maximal primary KIE (~ 7) occurs for the most symmetrical activated complex, usually one in which the proton is bound with equal strength to both the do-

nor and acceptor. This situation occurs when the donor and acceptor have equal  $pK_a$  values. The small primary KIE for **7** and **8** may originate from the asymmetric character in the benzylic carbon donor and oxygen atom acceptor in a generated high-valent Fe–O intermediate. Tunneling, an effect that is claimed to occur in catalytic systems including both enzymes<sup>19</sup> and their small molecule mimics,<sup>35,37</sup> is not involved in the C–H bond breaking steps of **7** and **8**.

The reaction mechanism for *N*-dealkylation by high valent Fe-oxo porphyrinates has been continuously debated; both ET and HAT pathways have been claimed. In the case of cP450, it is possible that *N*-dealkylation by the enzyme may operate by the ET pathway for easily oxidized substrates, but by HAT for others. For synthetic model systems, studies<sup>35,36</sup> suggest that  $Cu_2(O)_2$  complexes are capable of performing HAT reactions for benzylic amine substrates, which is in contrast to the present mechanistic studies on diiron complexes with tethered benzylamines. It should be noted, however, that the nitrogen atom in the copper complexes through which the substrate is tethered to the metal site does not have the free, non-bonding electron pair that occurs in a *N,N*- $Bn_2en$  ethylenediamine ligand. Consequently, it may be much more difficult for these systems to proceed by an ET pathway. Recently, a mechanistic study of dicopper complexes with substrates having nitrogen atom with free electron pair was reported.<sup>34</sup> A shift in mechanism for oxidative *N*-dealkylation from ET to HAT was proposed, depending on the ease of substrate one-electron oxidation.<sup>34</sup>

In summary, from our present Hammett and  $KIE_{intra}$  analyses for oxidative *N*-dealkylation of  $[Fe_2(\mu-O_2CAr^{Tol})_2(O_2CAr^{Tol})_2(N,N-Bn_2en)_2]$ , we can rule out previously proposed concerted and hydrogen atom transfer mechanisms. We conclude that the reaction operates through single electron transfer from free non-bonding electron pair in the dangling amine substrate to the generated intermediate, followed by proton transfer and rearrangement. Efforts are currently in progress to understand the oxidative *N*-

dealkylation mechanism of substrates that lack a non-bonding electron pair, but still can be oxygenated by carboxylate-rich diiron(II) complexes.<sup>18</sup>

**References**

- (1) Sono, M.; Roach, M. P.; Coulter, E. D.; Dawson, J. H. *Chem. Rev.* **1996**, *96*, 2841-2887.
- (2) Solomon, E. I.; Brunold, T. C.; Davis, M. I.; Kemsley, J. N.; Lee, S.-K.; Lehnert, N.; Neese, F.; Skulan, A. J.; Yang, Y.-S.; Zhou, J. *Chem. Rev.* **2000**, *100*, 235-349.
- (3) Holm, R. H.; Kennepohl, P.; Solomon, E. I. *Chem. Rev.* **1996**, *96*, 2239-2314.
- (4) Solomon, E. I.; Sundaram, U. M.; Machonkin, T. E. *Chem. Rev.* **1996**, *96*, 2563 - 2605.
- (5) Lindqvist, Y.; Huang, W.; Schneider, G.; Shanklin, J. *EMBO J.* **1996**, *15*, 4081-4092.
- (6) Tshuva, E. Y.; Lippard, S. J. *Chem. Rev.* **2004**, *104*, 987-1012.
- (7) Merckx, M.; Kopp, D. A.; Sazinsky, M. H.; Blazyk, J. L.; Müller, J.; Lippard, S. J. *Angew. Chem., Int. Ed.* **2001**, *40*, 2782-2807.
- (8) Whittington, D. A.; Lippard, S. J. *J. Am. Chem. Soc.* **2001**, *123*, 827-838.
- (9) Lee, D.; Lippard, S. J. *Inorg. Chem.* **2002**, *41*, 827-837.
- (10) Lee, D.; Lippard, S. J. *Inorg. Chem.* **2002**, *41*, 2704-2719.
- (11) Lee, D.; Pierce, B.; Krebs, C.; Hendrich, M. P.; Huynh, B. H.; Lippard, S. J. *J. Am. Chem. Soc.* **2002**, *124*, 3993-4007.
- (12) Hagadorn, J. R.; Que, L., Jr.; Tolman, W. B. *J. Am. Chem. Soc.* **1998**, *120*, 13531-13532.
- (13) Hsu, H.-F.; Dong, Y.; Shu, L.; Young, V. G., Jr.; Que, L., Jr. *J. Am. Chem. Soc.* **1999**, *121*, 5230-5237.
- (14) Lee, D.; DuBois, J. L.; Pierce, B.; Hedman, B.; Hodgson, K. O.; Hendrich, M. P.; Lippard, S. J. *Inorg. Chem.* **2002**, *41*, 3172-3182.
- (15) Lee, D.; Lippard, S. J. *J. Am. Chem. Soc.* **2001**, *123*, 4611-4612.
- (16) Carson, E. C.; Lippard, S. J. *J. Am. Chem. Soc.* **2004**, *126*, 3412-3413

- (17) Chavez, F. A.; Ho, R. Y. N.; Pink, M.; Young, V. G., Jr.; Kryatov, S. V.; Rybak-Akimova, E. V.; Andres, H.; Münck, E.; Que, L., Jr.; Tolman, W. B. *Angew. Chem., Int. Ed.* **2002**, *41*, 149-152.
- (18) Yoon, S.; Lippard, S. J. *Inorg. Chem.* **2003**, *42*, 8606-8608.
- (19) Du Bois, J.; Mizoguchi, T. J.; Lippard, S. J. *Coord. Chem. Rev.* **2000**, *200-202*, 443-485.
- (20) Sato, H.; Guengerich, F. P. *J. Am. Chem. Soc.* **2000**, *122*, 8099-8100.
- (21) Pangborn, A. B.; Giardello, M. A.; Grubbs, R. H.; Rosen, R. K.; Timmers, F. J. *Organometallics* **1996**, *15*, 1518-1520.
- (22) Wintner, E. A.; Tsao, B.; Rebek, J., Jr. *J. Org. Chem.* **1995**, *60*, 7997-8001.
- (23) Kuzelka, J.; Mukhopadhyay, S.; Spingler, B.; Lippard, S. J. *Inorg. Chem.* **2004**, *43*, 1751-1761.
- (24) Sheldrick, G. M.; University of Göttingen: Göttingen, Germany, 1997.
- (25) Sheldrick, G. M.; University of Göttingen: Göttingen, Germany, 1996.
- (26) Spek, A. L.; Utrecht University: Utrecht, The Netherlands, 1998.
- (27) Hansch, C.; Leo, A.; Taft, R. W. *Chem. Rev.* **1991**, *91*, 165-195.
- (28) Adam, W.; Krebs, O.; Orfanopoulos, M.; Stratakis, M.; Vougioukalakis, G. C. *J. Org. Chem.* **2003**, *68*, 2420-2425.
- (29) Naróg, D.; Lechowicz, U.; Pietryga, T.; Sobkowiak, A. *J. Mol. Catal. A Chem.* **2004**, *212*, 25-33.
- (30) Frantom, P. A.; Pongdee, R.; Sulikowski, G. A.; Fitzpatrick, P. F. *J. Am. Chem. Soc.* **2002**, *124*, 4202-4203.
- (31) Mislow, K.; Graeve, R.; Gordon, A. J.; Wahl, G. H., Jr. *J. Am. Chem. Soc.* **1963**, *85*, 1199-1200.
- (32) Laidler, K. J. *Chemical Kinetics*; 3th ed.; HarperCollinsPublishers, Inc., 1987.



- (33) Karki, S. B.; Dinnocenzo, J. P.; Jones, J. P.; Korzekwa, K. R. *J. Am. Chem. Soc.* **1995**, *117*, 3657-3664.
- (34) Shearer, J.; Zhang, C. X.; Hatcher, L. Q.; Karlin, K. D. *J. Am. Chem. Soc.* **2003**, *125*, 12670-12671.
- (35) Mahapatra, S.; Halfen, J. A.; Tolman, W. B. *J. Am. Chem. Soc.* **1996**, *118*, 11575-11586.
- (36) Itoh, S.; Nakao, H.; Berreau, L. M.; Kondo, T.; Komatsu, M.; Fukuzumi, S. *J. Am. Chem. Soc.* **1998**, *120*, 2890-2899.
- (37) Itoh, S.; Bando, H.; Nagatomo, S.; Kitagawa, T.; Fukuzumi, S. *J. Am. Chem. Soc.* **1999**, *121*, 8945-8946.

Table 2.1. Summary of X-ray Crystallographic Data for Compounds 2 – 8.

Compound	2·2CH <sub>2</sub> Cl <sub>2</sub>	3·2CH <sub>2</sub> Cl <sub>2</sub>	4·2CH <sub>2</sub> Cl <sub>2</sub>	5·2CH <sub>2</sub> Cl <sub>2</sub>
empirical formula	Fe <sub>2</sub> C <sub>118</sub> H <sub>110</sub> N <sub>4</sub> O <sub>8</sub> Cl <sub>6</sub>	Fe <sub>2</sub> C <sub>118</sub> H <sub>110</sub> N <sub>4</sub> O <sub>8</sub> Cl <sub>4</sub> F <sub>2</sub>	Fe <sub>2</sub> C <sub>120</sub> H <sub>116</sub> N <sub>4</sub> O <sub>8</sub> Cl <sub>4</sub>	Fe <sub>2</sub> C <sub>126</sub> H <sub>128</sub> N <sub>4</sub> O <sub>8</sub> Cl <sub>4</sub>
weight	2036.50	2003.60	1995.67	2079.82
space group	P $\bar{1}$	P $\bar{1}$	P $\bar{1}$	P2 <sub>1</sub> /c
a, Å	13.341(3)	13.2882(18)	13.373(2)	12.044(2)
b, Å	14.160(3)	14.107(2)	14.135(3)	21.855(4)
c, Å	16.147(3)	16.170(2)	16.105(3)	21.563(4)
$\alpha$ , deg	68.32(3)	102.139(2)	68.356(2)	103.068(2)
$\beta$ , deg	66.26(3)	114.168(2)	66.356(2)	
$\gamma$ , deg	79.14(3)	100.610(2)	79.231(3)	
V, Å <sup>3</sup>	2591.7(9)	2576.5(6)	2589.6(7)	5528.7(16)
Z	1	1	1	2
$\rho_{\text{calc}}$ , g/cm <sup>3</sup>	1.305	1.291	1.280	1.249
crystal size, mm	0.15×0.15×0.10	0.20×0.10×0.10	0.15×0.15×0.10	0.15×0.12×0.10
T, °C	-70	-90	-100	-100
m (Mo Ka), mm <sup>-1</sup>	0.494	0.449	0.443	0.418
total no. of data	14296	16297	20062	41700
no. of unique data points	9536	9458	9540	10284
no. of parameters	638	636	638	675
R1 (%) <sup>a</sup>	5.34	4.33	5.55	5.49
wR2 (%) <sup>b</sup>	11.30	11.63	13.86	14.17
max, min peaks, e/Å <sup>3</sup>	0.587, -0.529	0.795, -0.731	0.776, -0.714	0.920, -0.791

<sup>a</sup> R1 =  $\Sigma ||F_o| - |F_c|| / \Sigma |F_o|$ . <sup>b</sup> wR2 =  $\{\Sigma [w(F_o^2 - F_c^2)^2] / \Sigma [w(F_o^2)]\}^{1/2}$

Table 2.1. Summary of X-ray Crystallographic Data for Compounds 2 - 8

Compound	2·2CH <sub>2</sub> Cl <sub>2</sub>	3·2CH <sub>2</sub> Cl <sub>2</sub>	4·2CH <sub>2</sub> Cl <sub>2</sub>	5·2CH <sub>2</sub> Cl <sub>2</sub>
empirical formula	Fe <sub>2</sub> C <sub>118</sub> H <sub>110</sub> N <sub>4</sub> O <sub>8</sub> Cl <sub>6</sub>	Fe <sub>2</sub> C <sub>118</sub> H <sub>110</sub> N <sub>4</sub> O <sub>8</sub> Cl <sub>4</sub> F <sub>2</sub>	Fe <sub>2</sub> C <sub>120</sub> H <sub>116</sub> N <sub>4</sub> O <sub>8</sub> Cl <sub>4</sub>	Fe <sub>2</sub> C <sub>126</sub> H <sub>128</sub> N <sub>4</sub> O <sub>8</sub> Cl <sub>4</sub>
weight	2036.50	2003.60	1995.67	2079.82
space group	P $\bar{1}$	P $\bar{1}$	P $\bar{1}$	P2 <sub>1</sub> /c
a, Å	13.341(3)	13.2882(18)	13.373(2)	12.044(2)
b, Å	14.160(3)	14.107(2)	14.135(3)	21.855(4)
c, Å	16.147(3)	16.170(2)	16.105(3)	21.563(4)
$\alpha$ , deg	68.32(3)	102.139(2)	68.356(2)	
$\beta$ , deg	66.26(3)	114.168(2)	66.356(2)	103.068(2)
$\gamma$ , deg	79.14(3)	100.610(2)	79.231(3)	
V, Å <sup>3</sup>	2591.7(9)	2576.5(6)	2589.6(7)	5528.7(16)
Z	1	1	1	2
$\rho_{\text{calc}}$ , g/cm <sup>3</sup>	1.305	1.291	1.280	1.249
crystal size, mm	0.15×0.15×0.10	0.20×0.10×0.10	0.15×0.15×0.10	0.15×0.12×0.10
T, °C	-70	-90	-100	-100
m (Mo Ka), mm <sup>-1</sup>	0.494	0.449	0.443	0.418
total no. of data	14296	16297	20062	41700
no. of unique data points	9536	9458	9540	10284
no. of parameters	638	636	638	675
R1 (%) <sup>a</sup>	5.34	4.33	5.55	5.49
wR2 (%) <sup>b</sup>	11.30	11.63	13.86	14.17
max, min peaks, e/Å <sup>3</sup>	0.587, -0.529	0.795, -0.731	0.776, -0.714	0.920, -0.791

<sup>a</sup> R1 =  $\Sigma ||F_o| - |F_c|| / \Sigma |F_o|$ , <sup>b</sup> wR2 =  $\{\Sigma [w(F_o^2 - F_c^2)^2] / \Sigma [w(F_o^2)]\}^{1/2}$

Table 2.2. Selected Interatomic Distances (Å) and Angles (deg) for 2 - 8.<sup>a</sup>

Compound	2·2CH <sub>2</sub> Cl <sub>2</sub>	3·2CH <sub>2</sub> Cl <sub>2</sub>	4·2CH <sub>2</sub> Cl <sub>2</sub>	5·2CH <sub>2</sub> Cl <sub>2</sub>
Fe1...Fe1A	3.9189(17)	3.9260(7)	3.9388(8)	3.8680(8)
Fe1-O1	1.897(3)	1.896(2)	1.895(2)	1.921(2)
Fe1-O2	2.013(3)	2.0149(19)	2.002(2)	2.025(2)
Fe1-O3	2.005(3)	2.0083(17)	1.9992(19)	2.0747(18)
Fe1-O4	2.503(3)	2.5142(18)	2.5289(19)	2.2571(17)
Fe1-N1	2.143(3)	2.1391(19)	2.129(2)	2.142(2)
O1-Fe1-O2	124.79(19)	124.15(15)	124.31(15)	127.56(17)
O1-Fe1-O3	126.29(16)	126.95(12)	125.86(13)	128.25(14)
O1-Fe1-O4	97.76(11)	97.73(8)	97.56(9)	96.75(9)
O1-Fe1-N1	97.69(14)	98.23(10)	97.58(10)	93.04(10)
O2-Fe1-O3	105.66(11)	105.47(10)	109.70(7)	101.51(11)
O2-Fe1-O4	95.16(11)	95.28(7)	95.38(8)	93.83(8)
O2-Fe1-N1	102.11(11)	102.37(8)	102.18(9)	92.95(9)
O3-Fe1-O4	57.29(9)	57.03(6)	56.70(7)	60.77(6)
O3-Fe1-N1	87.69(11)	87.40(7)	88.58(8)	100.57(7)
O4-Fe1-N1	144.17(10)	143.57(7)	144.48(7)	161.10(7)

<sup>a</sup>Numbers in parentheses are estimated standard deviations of the last significant figures.

Table 2.2. Continued

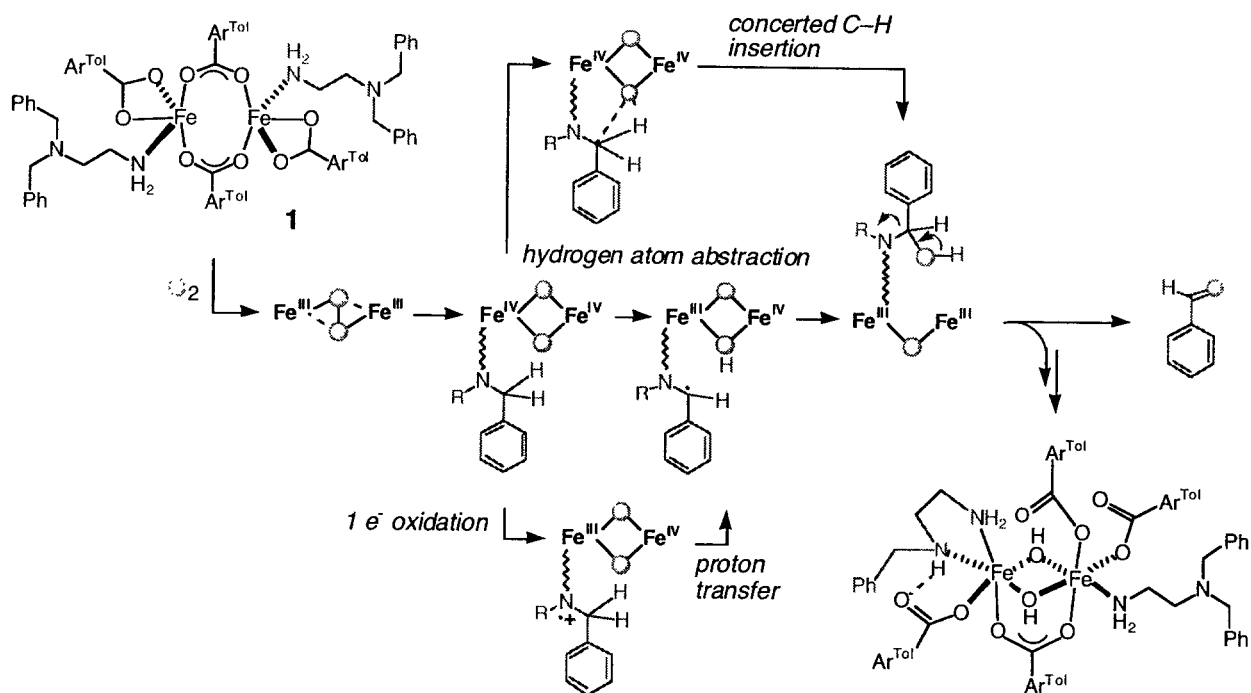
Compound	6·2CH <sub>2</sub> Cl <sub>2</sub>	7	8·CH <sub>2</sub> Cl <sub>2</sub>
Fe1...Fe1A	3.8781(13)	4.360(5)	3.934(2)
Fe1-O1	1.899(3)	1.966(4)	1.952(4)
Fe1-O2	2.021(3)	2.011(4)	1.949(5)
Fe1-O3	2.024(3)	2.111(4)	2.064(4)
Fe1-O4	2.473(3)	2.213(4)	2.267(4)
Fe1-N1	2.131(4)	2.136(6)	2.141(5)
O1-Fe1-O2	128.4(2)	114.86(18)	128.0(2)
O1-Fe1-O3	122.8(2)	123.50(16)	110.94(19)
O1-Fe1-O4	96.18(15)	105.27(16)	94.12(16)
O1-Fe1-N1	95.98(16)	92.7(2)	98.76(18)
O2-Fe1-O3	106.07(17)	119.75(16)	118.1(2)
O2-Fe1-O4	97.72(13)	92.09(16)	95.36(17)
O2-Fe1-N1	101.97(14)	92.3(2)	90.10(19)
O3-Fe1-O4	57.38(11)	60.65(15)	60.35(14)
O3-Fe1-N1	87.64(13)	98.4(2)	98.91(16)
O4-Fe1-N1	143.89(12)	157.6(2)	158.61(15)

<sup>a</sup>Numbers in parentheses are estimated standard deviations of the last significant figures.

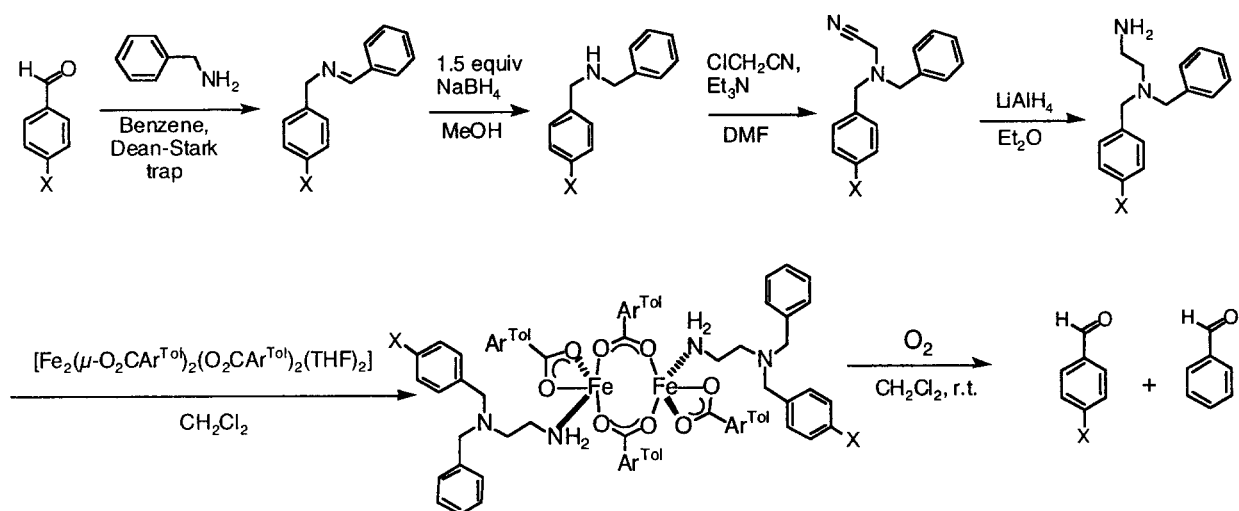
Table 3.2. Yield and Product Distribution of Reaction of 2 – 6 with Dioxygen

Complex	4-R	$\sigma_p^a$	$Y_H$ (%) <sup>b</sup> PhCHO	$Y_R$ (%) <sup>b</sup> 4-R-PhCHO	$Y_R/Y_H$ <sup>c</sup>	$Y_R/Y_H$ <sup>d</sup>	$\log(Y_R/Y_H)$
2	Cl	0.23	24(2)	31(4)	1.26 (7)		0.10 (3)
3	F	0.06	28(2)	32(1)	1.16 (8)	1.22	0.06 (3)
4	CH <sub>3</sub>	-0.17	34(1)	29(2)	0.85 (6)		-0.07 (3)
5	<i>t</i> -Bu	-0.20	33(1)	24(3)	0.78 (5)	0.79	-0.11 (3)
6	OCH <sub>3</sub>	-0.27	34(4)	25(2)	0.74 (10)		-0.13 (6)

<sup>a</sup>Hansch, C. ; Leo, A.; Taft, R. W. *Chem. Rev.* 1991, 91, 165-195. <sup>b</sup> $Y_H$  and  $Y_R$  represent the product yields of PhCHO and 4-R-PhCHO, respectively. <sup>c</sup>Ratios were determined from GC analytical data. <sup>d</sup>Ratios were determined by using <sup>1</sup>H NMR spectroscopy.

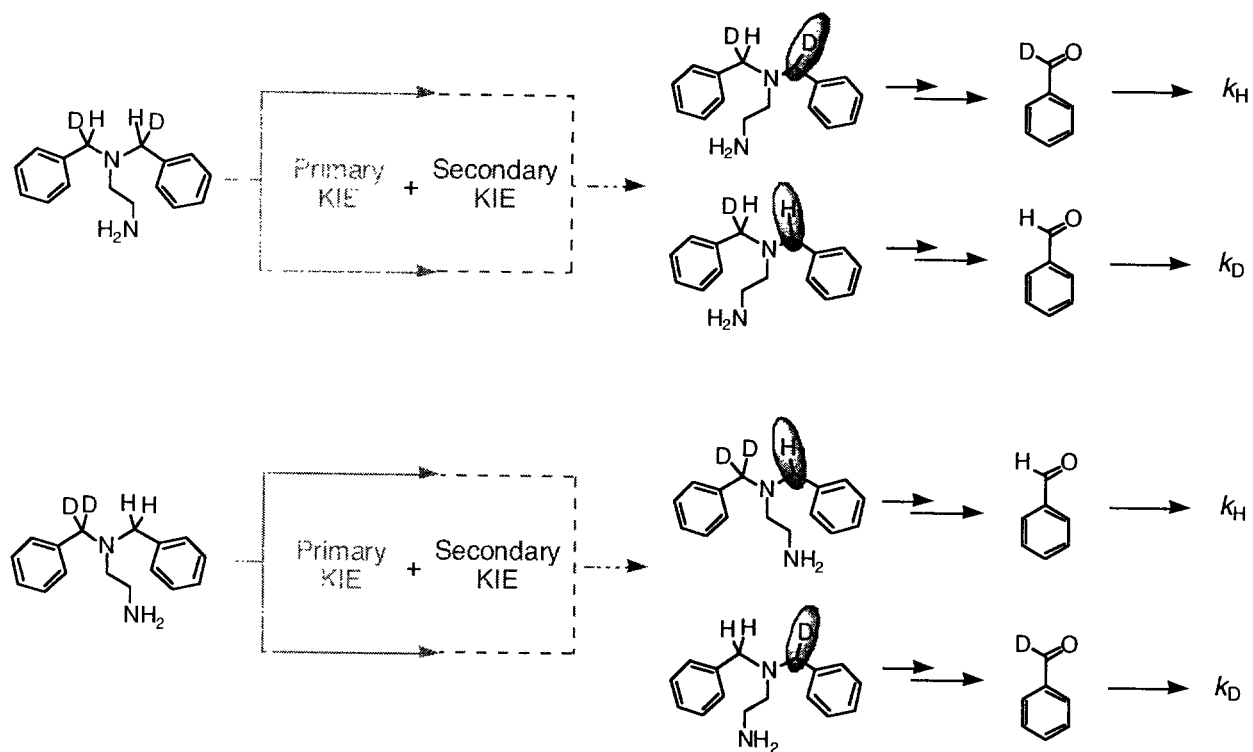


Scheme 2.1

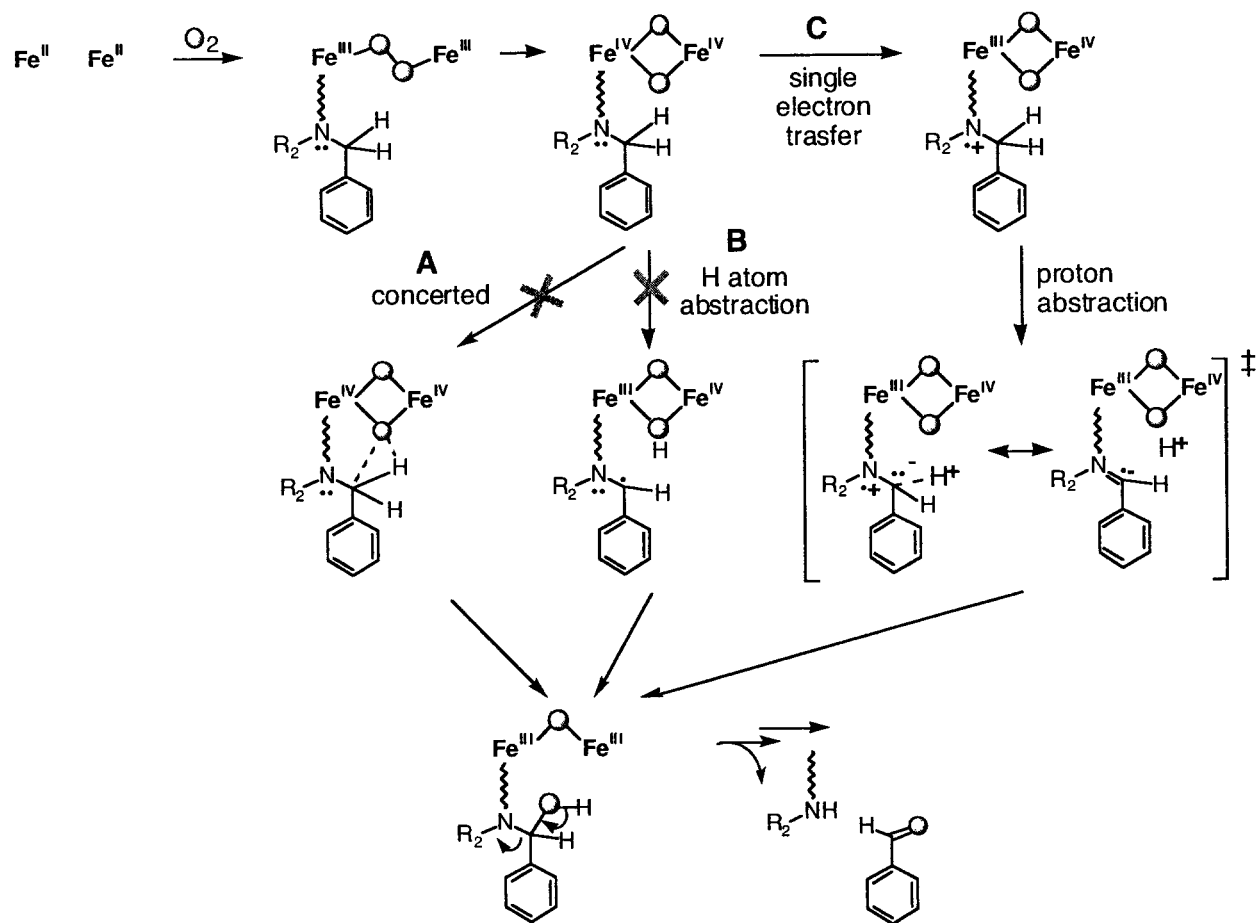


Scheme 2.2





Scheme 2.3



Scheme 2.4

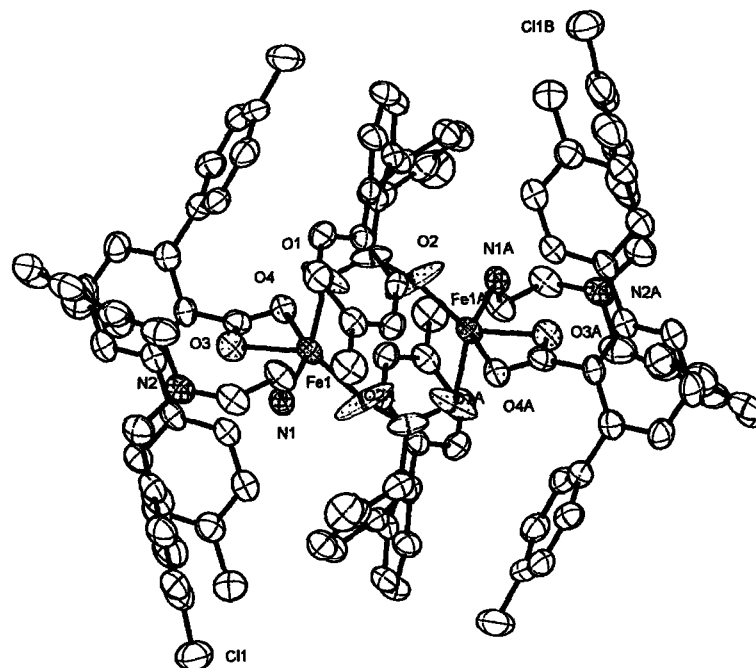


**Figure 2.1.** ORTEP drawing of  $[\text{Fe}_2(\mu\text{-O}_2\text{CAr}^{\text{Tol}})_2(\text{O}_2\text{CAr}^{\text{Tol}})_2(\text{N,N}\text{-}(4\text{-Cl-Bn})\text{Bnen})_2]$  (**2**) showing 50 % probability thermal ellipsoids. The solvent molecules and hydrogen atoms are omitted for clarity.

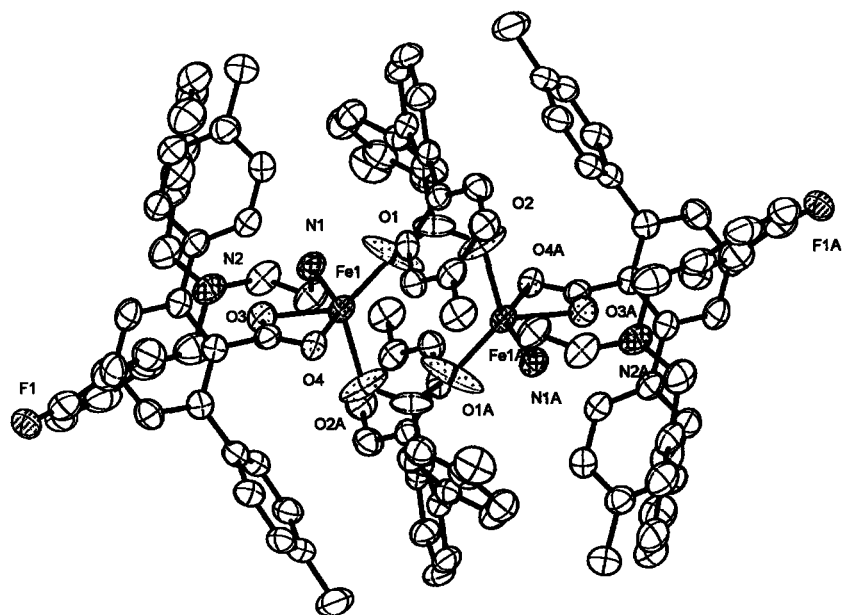


**Figure 2.2.** ORTEP drawing of  $[\text{Fe}_2(\mu\text{-O}_2\text{CAr}^{\text{Tol}})_2(\text{O}_2\text{CAr}^{\text{Tol}})_2(\text{N,N}\text{-}(4\text{-F-Bn})\text{Bnen})_2]$  (**3**) showing 50 % probability thermal ellipsoids. The solvent molecules and hydrogen atoms are omitted for clarity.

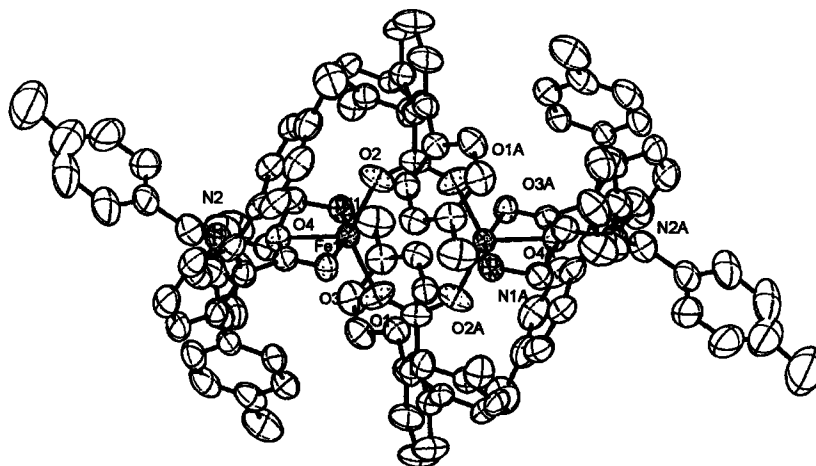


**Figure 2.3.** ORTEP drawing of  $[\text{Fe}_2(\mu\text{-O}_2\text{CAr}^{\text{Tol}})_2(\text{O}_2\text{CAr}^{\text{Tol}})_2(\text{N,N}\text{-}(4\text{-Me-Bn})\text{Bnen})_2]$  (**4**) showing 50 % probability thermal ellipsoids. The solvent molecules and hydrogen atoms are omitted for clarity.

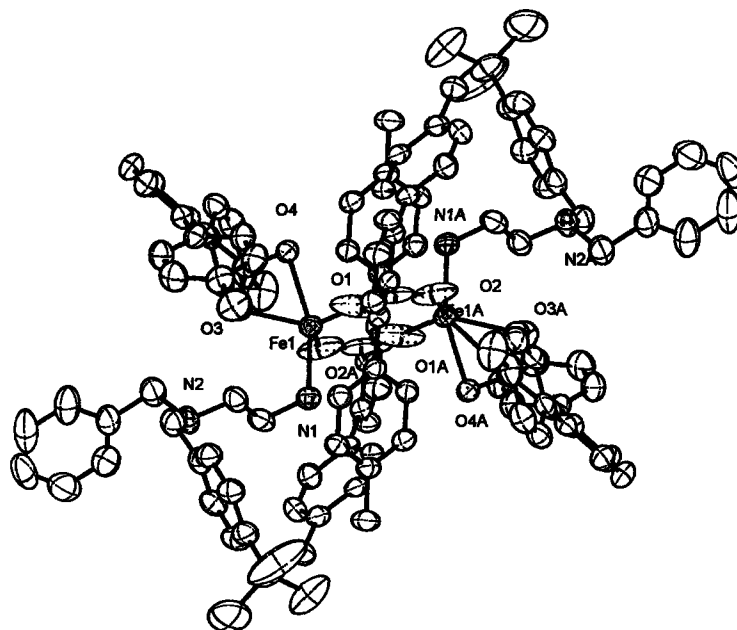


**Figure 2.4.** ORTEP drawing of  $[\text{Fe}_2(\mu\text{-O}_2\text{CAr}^{\text{Tol}})_2(\text{O}_2\text{CAr}^{\text{Tol}})_2(\text{N,N}\text{-}(4\text{-}^t\text{Bu-Bn})\text{Bnen})_2]$  (5) showing 50 % probability thermal ellipsoids. The solvent molecules and hydrogen atoms are omitted for clarity.

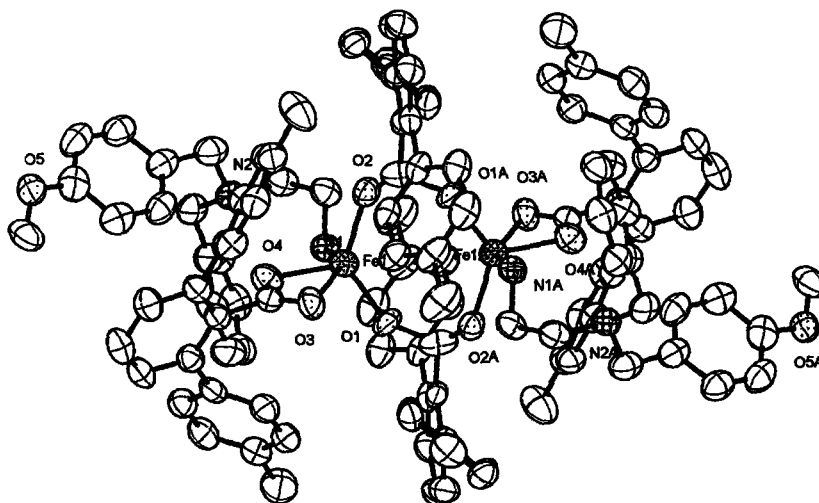


**Figure 2.5.** ORTEP drawing of  $[\text{Fe}_2(\mu\text{-O}_2\text{CAr}^{\text{Tol}})_2(\text{O}_2\text{CAr}^{\text{Tol}})_2(\text{N,N}\text{-}(4\text{-OMe-Bn})\text{Bnen})_2]$  (**6**) showing 50 % probability thermal ellipsoids. The solvent molecules and hydrogen atoms are omitted for clarity.

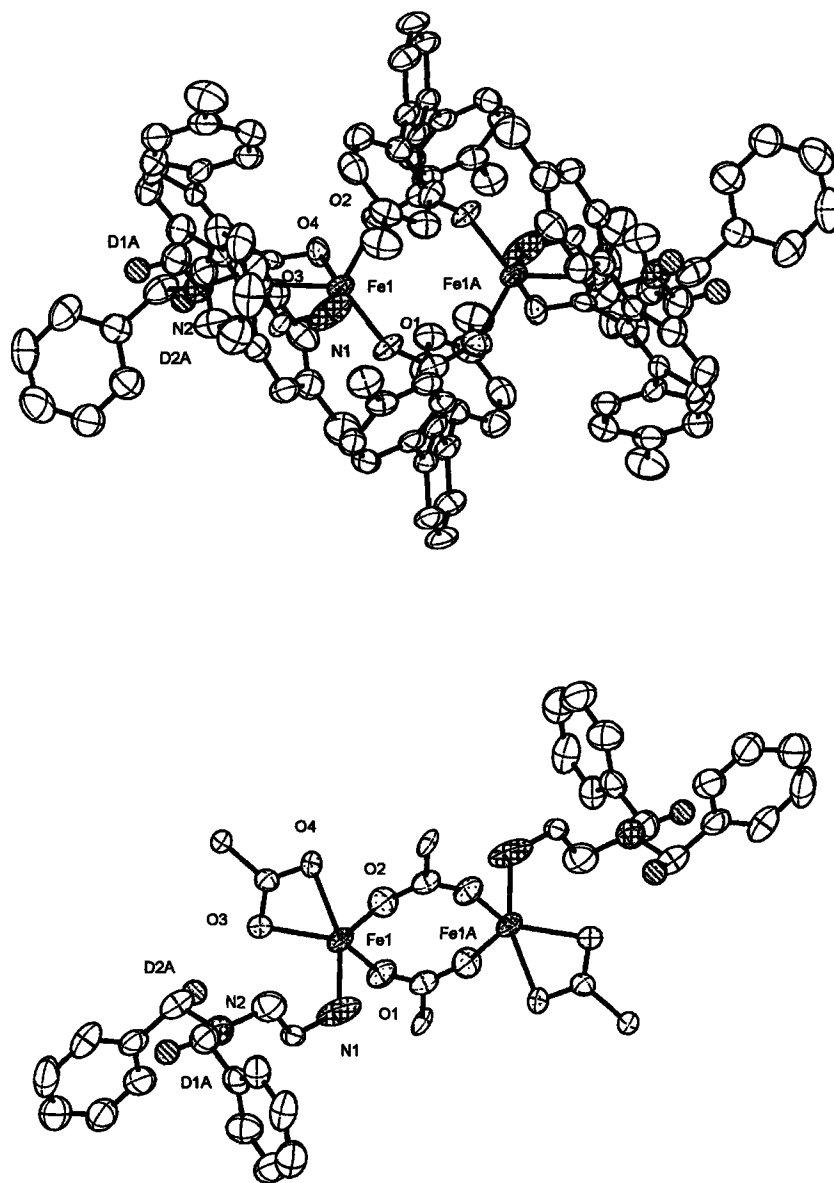


**Figure 2.6.** ORTEP drawings of  $[\text{Fe}_2(\mu\text{-O}_2\text{CAr}^{\text{Tol}})_2(\text{O}_2\text{CAr}^{\text{Tol}})_2((\text{C}_6\text{H}_5\text{CDH})_2\text{en})_2]$  (7) (Top) showing 50 % probability thermal ellipsoids. The solvent molecules and hydrogen atoms are omitted for clarity. (Bottom) All atoms of  $\text{Ar}^{\text{Tol}}\text{CO}_2^-$  ligands in 7, except for the carboxylate groups and the  $\alpha$ -carbon atoms, were omitted for clarity.



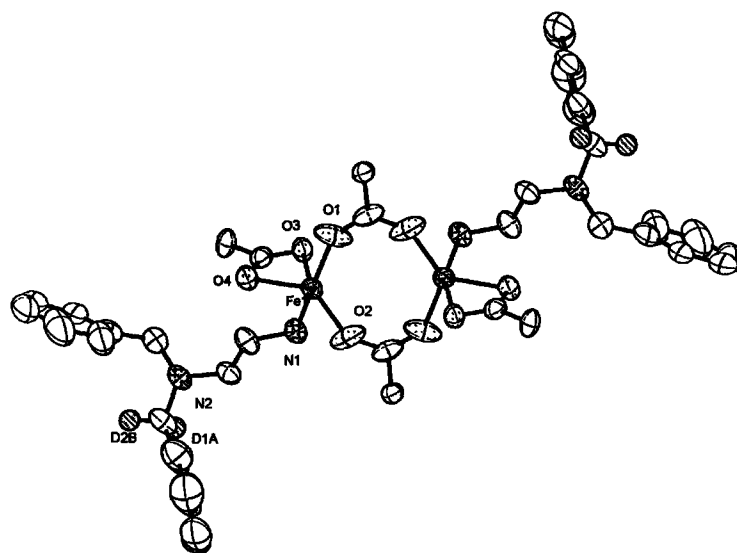
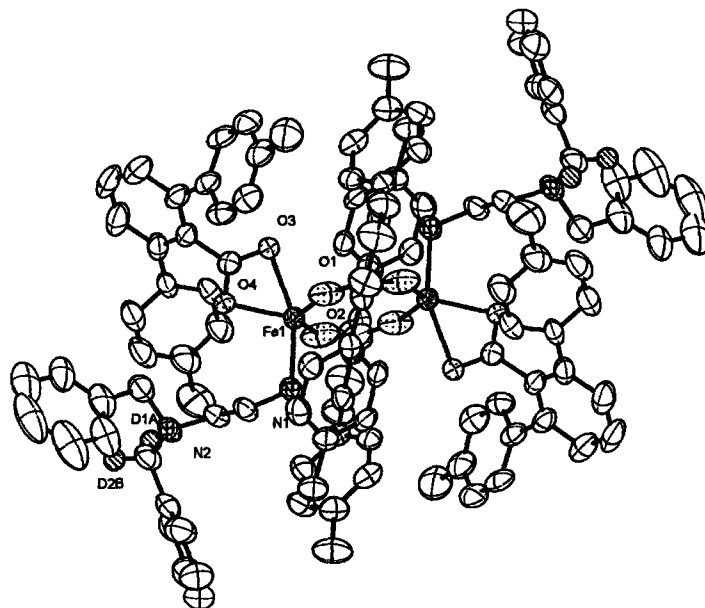


**Figure 2.7.** ORTEP drawing of  $[\text{Fe}_2(\mu\text{-O}_2\text{CAr}^{\text{Tol}})_2(\text{O}_2\text{CAr}^{\text{Tol}})((\text{D}_2\text{-Bn})\text{Bnen})_2]$  (**8**) (Top) showing 50 % probability thermal ellipsoids. The solvent molecules and hydrogen atoms are omitted for clarity. (Bottom) all atoms of  $\text{Ar}^{\text{Tol}}\text{CO}_2^-$  ligands in **8**, except for the carboxylate groups and the  $\alpha$ -carbon atoms, were omitted for clarity.

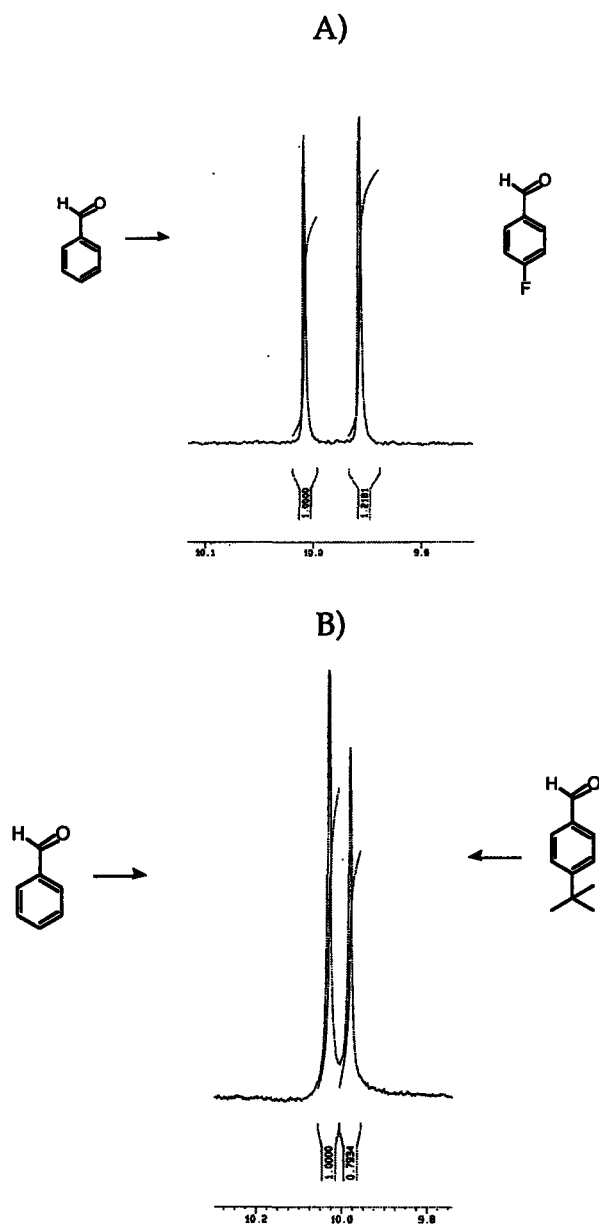


**Figure 2.8.** The oxygenation product distributions of  $[\text{Fe}_2(\mu\text{-O}_2\text{CAr}^{\text{Tol}})_2(\text{O}_2\text{CAr}^{\text{Tol}})_2(\text{N},\text{N}\text{-}(4\text{-F-Bn})\text{Bnen})_2]$  (3) and  $[\text{Fe}_2(\mu\text{-O}_2\text{CAr}^{\text{Tol}})_2(\text{O}_2\text{CAr}^{\text{Tol}})(\text{N},\text{N}\text{-}(4\text{-}^t\text{Bu-Bn})\text{Bnen})_2]$  (5) at 23 °C, determined  $^1\text{H}$  NMR spectroscopy, are shown in A) and B), respectively.

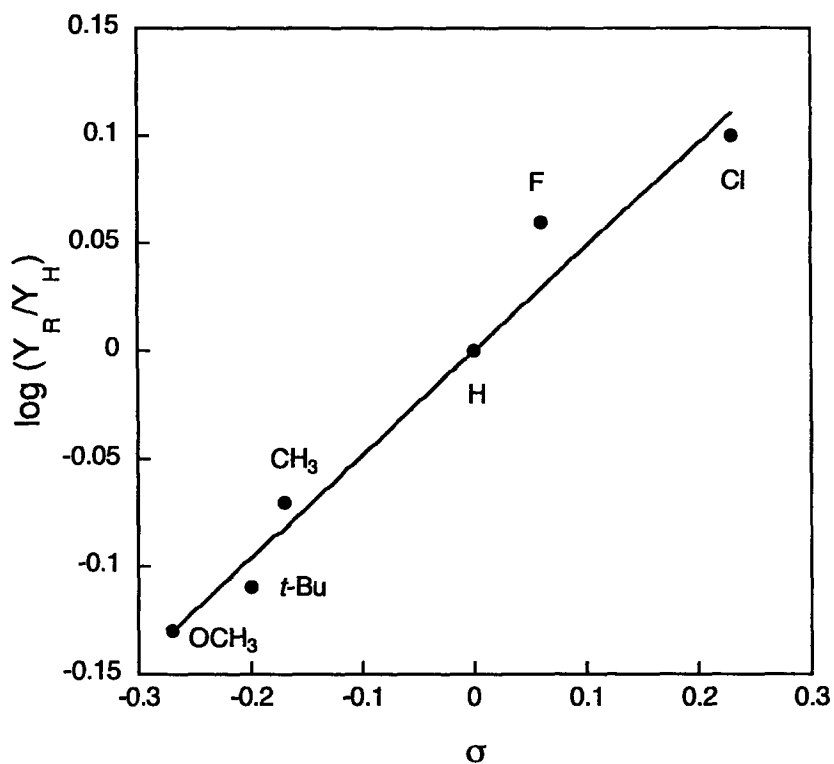


**Figure 2.9.** Hammett plot for the oxygenation of  $[\text{Fe}_2(\mu\text{-O}_2\text{CAr}^{\text{Tol}})_2(\text{O}_2\text{CAr}^{\text{Tol}})_2(4\text{-}^{\text{R}}\text{BnBnen})_2]$  ( $\text{R} = \text{Cl}, \text{F}, \text{H}, \text{Me}, t\text{-Bu}, \text{and OCH}_3$ ) in  $\text{CH}_2\text{Cl}_2$  at 23 °C.  $Y_{\text{H}}$  and  $Y_{\text{R}}$  stand for the product yields of PhCHO and 4-R-PhCHO, respectively. The line represents a least squares fit to the data with the slope  $\rho = 0.48$  ( $R = 0.98$ ).

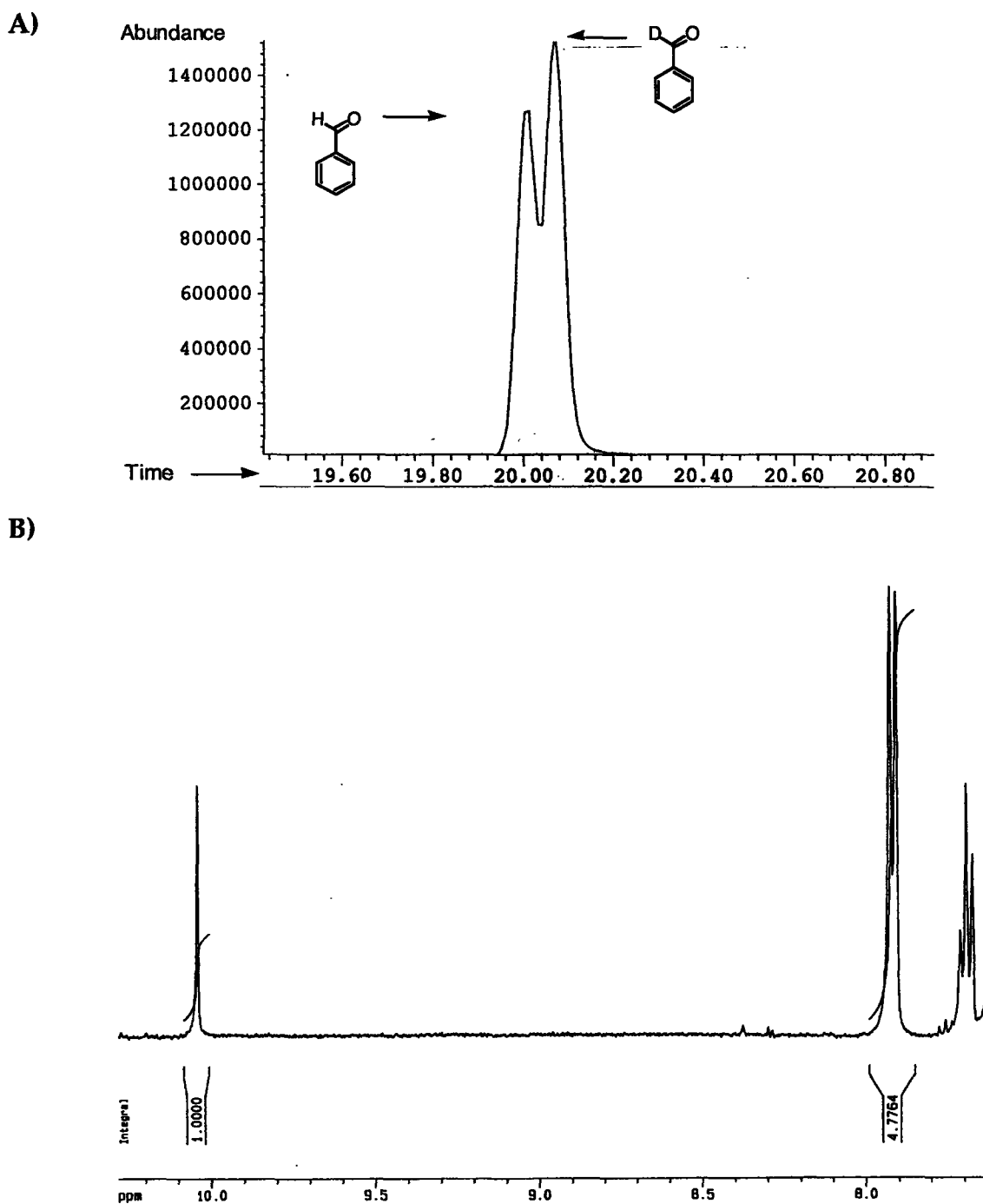
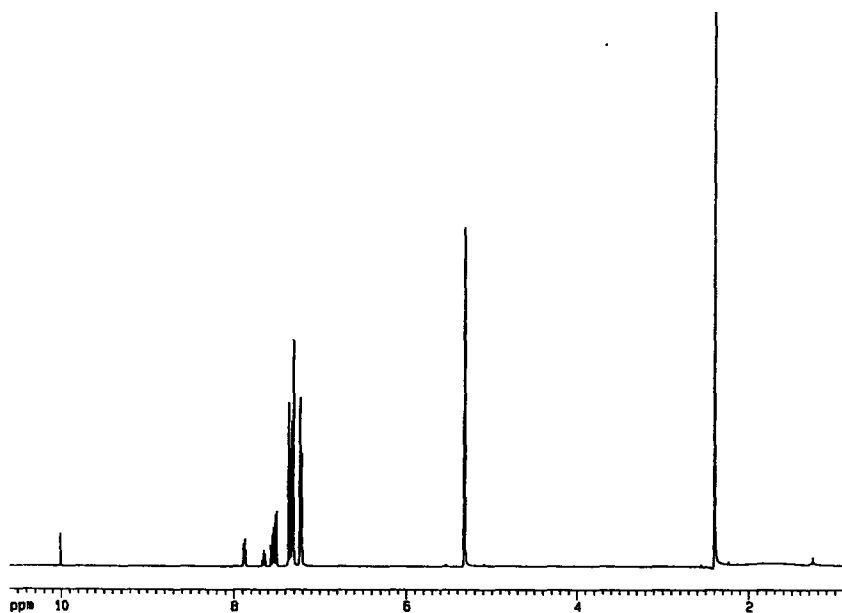


**Figure 2.10.** The oxygenation product distribution of  $[\text{Fe}_2(\mu\text{-O}_2\text{CAr}^{\text{Tol}})_2(\text{O}_2\text{CAr}^{\text{Tol}})_2((\text{C}_6\text{H}_5\text{CDH})_2\text{en})_2]$  (**7**) at 23 °C. A) GC-MS: 20.011 min, PhCHO ( $M^+ = 106$ ); 20.08 min, PhCDO ( $M^+ = 107$ ) B)  $^1\text{H}$  NMR spectrum: 10.01, (s, 1H from PhCHO), 7.88, (d, 2H from the combination of PhCHO and PhCDO).

A)



B)

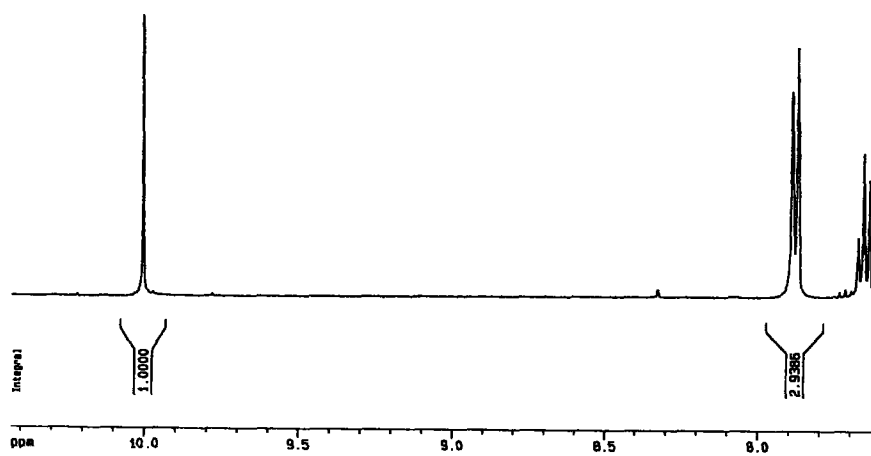


**Figure 2.11.** The oxygenation product distribution of  $[\text{Fe}_2(\mu\text{-O}_2\text{CAr}^{\text{Tol}})_2(\text{O}_2\text{CAr}^{\text{Tol}})_2((\text{C}_6\text{H}_5\text{CD}_2)\text{Bnen})_2]$  (**8**) at 23 °C. A) and B) <sup>1</sup>H NMR spectrum: 10.01, (s, 1H from PhCHO), 7.88, (d, 2H from the combination of PhCHO and PhCDO).

## **Chapter 3**

# **Synthesis, Characterization, and Dioxygen Reactivity of Tetracarboxylate-Bridged Diiron(II) Complexes with Coordinated Substrates**

---

## Introduction

Dioxygen activation and O-atom transfer reactions promoted by iron-containing metalloenzymes are of considerable interest. Monooxygenases,<sup>1-3</sup> which catalyze the hydroxylation of unactivated hydrocarbons, are of particular interest because of their ability to hydroxylate methyl groups bearing a range of substituents.<sup>4</sup> The hydroxylase component of soluble methane monooxygenase (sMMOH) performs this function by first activating dioxygen to afford reactive intermediate(s).<sup>5</sup> The resulting oxidant can insert one oxygen atom selectively into a C–H bond. Understanding this bio-catalytic process in molecular detail is an important objective which, if accomplished, could both reveal how the metalloproteins work and facilitate the design of catalysts for O<sub>2</sub> activation and selective hydrocarbon oxidation.

In pursuit of our goal to prepare diiron(II) complexes that mimic the functional chemistry of sMMOH, we reported the carboxylate-bridged diiron(II) complex,  $[\text{Fe}_2(\mu\text{-O}_2\text{CAr}^{\text{Tol}})_2(\text{O}_2\text{CAr}^{\text{Tol}})_2(\text{N,N-Bn}_2\text{en})_2]$ , where  $\text{Ar}^{\text{Tol}}\text{CO}_2^-$  is 2,6-di(*p*-tolyl)benzoate and *N,N*-Bn<sub>2</sub>en is *N,N*-dibenzylethylenediamine, which oxidatively *N*-dealkylates a tethered *N*-benzylamino functionality upon reaction with dioxygen. Based on Hammett and kinetic isotope effect (KIE) studies, it was proposed that *N*-dealkylation occurs through sequential one-electron oxidation of the nitrogen atom by a putative iron(IV) oxo intermediate, followed by  $\alpha$ -proton abstraction and oxygen rebound (Scheme 3.1).<sup>6</sup> The proximity of the lone pair electrons on the uncoordinated nitrogen atom of the Bn<sub>2</sub>en ligand to the proposed high-valent intermediate may be the major reason for this pathway. The oxidative *N*-dealkylation reactions effected by {Cu<sub>2</sub>O<sub>2</sub>} and {Ni<sub>2</sub>O<sub>2</sub>} model complexes with coordinated benzylamine ligands, however, were proposed to occur through a hydrogen atom abstraction pathway.<sup>7-9</sup> The difference between these {Cu<sub>2</sub>O<sub>2</sub>} or {Ni<sub>2</sub>O<sub>2</sub>} systems<sup>7-9</sup> and  $[\text{Fe}_2(\mu\text{-O}_2\text{CAr}^{\text{Tol}})_2(\text{O}_2\text{CAr}^{\text{Tol}})_2(\text{N,N-Bn}_2\text{en})_2]$  is the existence of a

non-bonding electron pair within benzylamine substrates of *N,N*-Bn<sub>2</sub>en ligands; the benzylamine ligands in the {Cu<sub>2</sub>O<sub>2</sub>} or {Ni<sub>2</sub>O<sub>2</sub>} species<sup>7-9</sup> are coordinated to metal sites and thus have no free non-bonding electron pair. In order to test the possibility that *N*-dealkylation might occur for diiron(II) benzylamine complexes having no available non-bonded electron pairs, we designed a system that lacks this feature, in which the benzylamine groups are directly coordinated to the diiron(II) sites.

In this chapter, we describe the synthesis and characterization of [Fe<sub>2</sub>(μ-O<sub>2</sub>CAr<sup>Tol</sup>)<sub>4</sub>L<sub>2</sub>] complexes, where L is benzylamine (BA) or 4-methoxybenzylamine (BA<sup>OMe</sup>), and their oxygenation chemistry. Various methods, including resonance Raman (rR) and electron paramagnetic resonance (EPR) spectroscopy, were applied to understand the mechanism and the intermediates involved. In addition, upon dissolution of the tetracarboxylate bridged diiron(II) benzylamine complex in methanol, an asymmetric cubane tetrairon(II) complex was identified and structurally characterized. A preliminary communication of a portion of this work has appeared elsewhere.

## Experimental Section

**General Considerations.** All reagents were obtained from commercial suppliers and used as received unless otherwise noted. Dichloromethane, pentane, and toluene were saturated with argon and purified by passage through activated Al<sub>2</sub>O<sub>3</sub> columns under argon.<sup>10</sup> Dioxygen (99.994%, BOC Gases) was dried by passing the gas stream through Drierite. The compound [Fe<sub>2</sub>(μ-O<sub>2</sub>CAr<sup>Tol</sup>)<sub>2</sub>(O<sub>2</sub>CAr<sup>Tol</sup>)<sub>2</sub>(THF)<sub>2</sub>] was prepared as described in the literature.<sup>11</sup> Air-sensitive manipulations were carried out under nitrogen in an MBraun glovebox. <sup>1</sup>H-NMR spectra were recorded on a Bruker 400 MHz spectrometer housed in the Massachusetts Institute of Technology Department of



Chemistry Instrument Facility (MIT DCIF); chemical shifts were referenced to residual solvent peaks. FT-IR spectra were recorded with both a Bio-Rad FTS 135 spectrometer and a Thermo Nicolet Avatar 360 spectrometer. UV-vis spectra were recorded on a Hewlett-Packard 8453 diode array spectrophotometer.

$[\text{Fe}_2(\mu\text{-O}_2\text{CAr}^{\text{Tol}})_4(\text{BA})_2]$  (**1**). To a rapidly stirred  $\text{CH}_2\text{Cl}_2$  (10 mL) solution of  $[\text{Fe}_2(\mu\text{-O}_2\text{CAr}^{\text{Tol}})_2(\text{O}_2\text{CAr}^{\text{Tol}})_2(\text{THF})_2]$  (86.8 mg, 0.0615 mmol) was added benzylamine (BA) (14.1 mg, 2 equiv), to afford a greenish yellow precipitate (70.1 mg, 76 %). This solid dissolved to THF (10 mL) upon gentle heating. Light green blocks of **1** suitable for X-ray crystallography were obtained by vapor diffusion of pentane into the THF solution. FT-IR (KBr,  $\text{cm}^{-1}$ ) 3324 (w), 3271 (w), 3024 (w), 2919 (w), 1607 (s), 1585 (m), 1550 (w), 1514 (m), 1452 (m), 1404 (s), 1384 (s), 1303 (w), 1210 (w), 1187 (w), 1150 (w), 1109 (w), 1074 (w), 1036 (w), 1020 (w), 996 (w), 843 (w), 814 (m), 790 (m), 763 (w), 727 (w), 706 (m), 584 (w), 526 (m), 463 (w). Anal. Calcd. for  $\text{C}_{98}\text{H}_{86}\text{N}_2\text{Fe}_2\text{O}_8$  : C, 76.86; H, 5.66; N, 1.83. Found: C, 76.81; H, 5.61; N, 1.87.

$[\text{Fe}_2(\mu\text{-O}_2\text{CAr}^{\text{Tol}})_4(\text{BA}^{\text{p-OMe}})_2]$  (**2**). To a rapidly stirred yellow  $\text{CH}_2\text{Cl}_2$  (10 mL) solution of  $[\text{Fe}_2(\mu\text{-O}_2\text{CAr}^{\text{Tol}})_2(\text{O}_2\text{CAr}^{\text{Tol}})_2(\text{THF})_2]$  (94.8 mg, 0.064 mmol) was added dropwise neat 4-methoxybenzylamine ( $\text{BA}^{\text{p-OMe}}$ ) (17.1 mg, 2 equiv). The resulting light greenish yellow solution was stirred for 10 min and filtered through Celite. Light green blocks of **2** (87.4 mg, 83 %) suitable for X-ray crystallography were obtained by layering pentanes over the filtrate. FT-IR (KBr,  $\text{cm}^{-1}$ ) 3332(w), 3274(w), 3021(w), 2918(w), 2863(w), 2833(w), 1607(s), 1586(m), 1550(w), 1514(s), 1453(m), 1404 (m), 1303 (s), 1248 (s), 1178 (w), 1110 (w), 1073 (w), 1035 (m), 1020 (w), 997 (w), 842 (w), 814 (m), 791 (m), 763 (w), 726 (w), 706 (m), 643 (w), 584 (w), 558 (w), 526 (m), 462 (w). Anal. Calcd. for  $\text{C}_{100}\text{H}_{90}\text{N}_2\text{Fe}_2\text{O}_{10}$  : C, 75.47; H, 5.70; N, 1.76. Found: C, 75.11; H, 5.39; N, 1.92.

**[Fe<sub>4</sub>(μ-OMe)<sub>4</sub>(O<sub>2</sub>CAr<sup>Tol</sup>)<sub>4</sub>(HOMe)<sub>6</sub>](HOMe) (3).** **Method A.** Rapid stirring of a suspension of **2** in methanol (10 mL) for 30 min effected dissolution. Light green blocks of **[Fe<sub>4</sub>(μ-OMe)<sub>4</sub>(O<sub>2</sub>CAr<sup>Tol</sup>)<sub>4</sub>(OMe)<sub>6</sub>](HOMe) (3)** suitable for X-ray crystallography were obtained by layering pentanes over the light greenish solution. **Method B.** A portion of the NaO<sub>2</sub>CAr<sup>Tol</sup> (0.597 g, 1.84 mmol) was mixed with Fe(OTf)<sub>2</sub>·2CH<sub>3</sub>CN (0.802 g, 1.84 mmol) in 20 mL of methanol, affording a pale yellow solution. After 1 h stirring, triethylamine (0.186 g, 1 equiv) was added and colorless block crystals (0.2010 g, yield 25 %) were isolated after 2 days. FT-IR (KBr, cm<sup>-1</sup>) 3053 (w), 3021 (w), 2918 (w), 2871 (w), 1609 (s), 1590 (s), 1517 (w), 1482 (m), 1444 (m), 1400 (s), 1283 (w), 1266 (w), 1154 (w), 1101 (w), 1035 (m), 1005 (w), 845 (w), 818 (m), 761 (s), 733 (m), 718 (m), 711 (m), 658 (m), 639 (w), 567 (w), 549 (w), 512 (m), 475 (w). Anal. Calcd. for C<sub>94</sub>H<sub>104</sub>Fe<sub>4</sub>O<sub>18</sub> : C, 64.69; H, 6.01. Found: C, 64.63; H, 5.79.

**α-d<sub>1</sub>-4-Methoxybenzylamine (α-d<sub>1</sub>-BA<sup>p-OMe</sup>).** To a stirred anhydrous THF (25 mL) suspension of lithium aluminum deuteride (2.6 g, 62 mmol), a solution of anisaldehyde oxime (3.0 g, 24 mmol) was slowly added at -78 °C. The mixture was warmed to room temperature and stirred for 2 days. The mixture was carefully hydrolyzed by addition of 2.6 g of water, 2.6 g of 15 % NaOH (aq), and 3 × 2.6 g of water. Inorganic salts were removed by filtration and washed with ethylacetate (200 mL). The solution was dried (MgSO<sub>4</sub>), filtered through Celite, and concentrated to give 1.6 g (61 %) of the product. <sup>1</sup>H NMR (CDCl<sub>3</sub>, 400 MHz): δ 7.22 (d, *J* = 8.5 Hz, 2 H), 6.87 (d, *J* = 8.6 Hz, 2 H), 3.79 (s, 3 H), 3.77 (t, *J* = 0.05 Hz, 1 H).

**[Fe<sub>2</sub>(μ-O<sub>2</sub>CAr<sup>Tol</sup>)<sub>4</sub>(α-d<sub>1</sub>-BA<sup>p-OMe</sup>)<sub>2</sub>].** This compound was prepared as described above for **2**. FT-IR (KBr, cm<sup>-1</sup>) 3332 (w), 3275 (w), 3051 (w), 3022 (w), 2918 (m), 2862 (w), 2299 (w), 1607 (s), 1545 (s), 1514 (s), 1454 (s), 1405 (s), 1385 (s), 1304 (w), 1287 (w), 1247 (s), 1178 (m), 1154 (w), 1110 (w), 1071 (w), 1032 (m), 942 (w), 914 (w), 858 (w), 843 (m),

816 (s), 800 (s), 787 (m), 764 (m), 736 (w), 727 (w), 713 (m), 705 (m), 638 (w), 585 (m), 546 (w), 525 (m), 461 (w).

**[Fe<sub>2</sub>(μ-O<sub>2</sub>CAr<sup>Tol</sup>)<sub>4</sub>(BA<sup>p-OMe</sup>)<sub>2</sub>](PF<sub>6</sub>) (4).** To a rapidly stirred yellow CH<sub>2</sub>Cl<sub>2</sub> (7 mL) solution of [Fe<sub>2</sub>(μ-O<sub>2</sub>CAr<sup>Tol</sup>)<sub>4</sub>(BA<sup>p-OMe</sup>)<sub>2</sub>] (151.5 mg, 0.095 mmol) was added dropwise a CH<sub>2</sub>Cl<sub>2</sub> (3 mL) solution of AgPF<sub>6</sub> (24.0 mg, 0.095 mmol). The resulting dark-forest green solution was stirred for 2 h and filtered through Celite. Dichroic brown-green blocks of [Fe<sub>2</sub>(μ-O<sub>2</sub>CAr<sup>Tol</sup>)<sub>4</sub>(BA<sup>p-OMe</sup>)<sub>2</sub>](PF<sub>6</sub>) (43.2 mg, yield 26%) were obtained by layering pentanes over the filtrate. FT-IR (KBr, cm<sup>-1</sup>) 3300 (w), 3243 (w), 2919 (w), 1613 (w), 1583 (m), 1514 (s), 1441 (s), 1405 (s), 1386 (s), 1304 (w), 1252 (m), 1182 (w), 1155 (w), 1110 (w), 1074 (w), 1034 (w), 973 (w), 847 (s), 814 (s), 793 (m), 762 (w), 727 (w), 713 (w), 705 (m), 586 (m), 557 (w), 529 (m), 491 (w). Anal. Calcd. for C<sub>100</sub>H<sub>90</sub>N<sub>2</sub>Fe<sub>2</sub>O<sub>10</sub>F<sub>6</sub>P : C, 69.17; H, 5.22; N, 1.61. Found: C, 69.17; H, 5.16; N, 1.55.

**X-ray Crystallographic Studies.** Intensity data were collected on a Bruker (formerly Siemens) and APEX CCD diffractometer with graphite-monochromatized Mo Kα radiation (λ = 0.71073 Å), controlled by a Pentium-based PC running the SMART software package. Single crystals were mounted at room temperature on the tips of quartz fibers, coated with Paratone-N oil, and cooled to 173 K under a stream of cold nitrogen maintained by a Bruker LT-2A nitrogen cryostat. Data collection and reduction protocols are described elsewhere.<sup>12</sup> The structures were solved by Patterson and direct methods and refined on F<sup>2</sup> by using the SHELXTL software package.<sup>13</sup> Empirical absorption corrections were applied with SADABS<sup>14</sup>, part of the SHELXTL program package, and the structures were checked for higher symmetry by the program PLATON.<sup>15</sup> All non-hydrogen atoms were refined anisotropically unless otherwise noted. In general, hydrogen atoms were assigned idealized positions and given thermal parameters equivalent to either 1.5 (methyl hydrogen atoms and NH<sub>2</sub> hydrogen atoms)

or 1.2 (all other hydrogen atoms) times the thermal parameter of the carbon atom to which they were attached. The hydrogen atoms of O–H groups in six coordinated methanol molecules in compound **3** were assigned from electron-density map. In the structure of **3**, one methanol molecule was found in the crystal lattice. Detailed crystallographic information is provided in Table 3.1. Selected interatomic distances and angles are listed in Table 3.2 for compounds **1** and **2** and Table 3.3 for compound **3**.

**<sup>57</sup>Fe Mössbauer Spectroscopy.** Zero-field Mössbauer spectra were obtained on an MS1 spectrometer (WEB Research Co.) with a <sup>57</sup>Co source in a Rh matrix maintained at room temperature in the DCIF. Solid samples were prepared by suspending ca 0.015 mmol of the powdered material in Apeizon N grease and packing the mixture into a nylon sample holder. All data were collected at 4.2 K and the isomer shift ( $\delta$ ) values are reported with respect to natural iron foil that was used for velocity calibration at room temperature. The spectra were fit to Lorentzian lines by using the WMOSS plot and fit program.<sup>16</sup>

**Magnetic Susceptibility Measurement.** Magnetic susceptibility data for powdered solid for **1** were measured between 5 and 300 K with applied magnetic fields of 0.1 T and multifield saturated magnetic susceptibility data for powdered solid **2** were measured between 2 and 300 K with applied magnetic fields of 0.5, 1, 2.5, and 5 T using a Quantum design MPMS SQUID susceptometer. The samples were loaded in a gel capsule and suspended in a plastic straw. The susceptibilities of the straw and gel capsule were independently determined over the same temperature range and field to correct for their contribution to the total measured susceptibility. Underlying diamagnetism of the samples was calculated from Pascal's constants.<sup>17</sup> The saturation magnetization difference data of **2** were fit using the simplex method to find the spin Hamiltonian parameter set, yielding the minimum in the standard quality of the fit

parameter,  $\chi^2$ .<sup>2</sup> The uncertainties were calculated by averaging the parameters from the best fits obtained from two independently prepared samples. The detailed data handling and fitting processes are described in the literature.<sup>18-21</sup> The software package (WMAG) used to carry out the data analysis is a product of WEB Research Co., Edina, MN, U.S.A

**Electrochemistry.** Cyclic voltammetric measurements with an EG&G model 263 potentiostat were performed in an MBraun glovebox under nitrogen. A three-electrode configuration consisting a platinum working electrode, a AgNO<sub>3</sub>/Ag (0.1 M in acetonitrile with 0.5 M (Bu<sub>4</sub>N)PF<sub>6</sub>) reference electrode, and a platinum mesh auxiliary electrode was used. The supporting electrode was 0.5 M (Bu<sub>4</sub>N)PF<sub>6</sub> in CH<sub>2</sub>Cl<sub>2</sub>. All cyclic voltammograms were externally referenced to the Cp<sub>2</sub>Fe/Cp<sub>2</sub>Fe<sup>+</sup> couple.

**Resonance Raman Spectroscopy.** Resonance Raman spectra of frozen solutions of 2 oxygenated with either <sup>16</sup>O<sub>2</sub> or <sup>18</sup>O<sub>2</sub> at -78 °C were obtained by using a Kr<sup>+</sup> ion laser with excitation provided at 647.1 nm and 8 milliwatt of power at the sample. A monochromator (1200 grooves/nm grating) with an entrance slit of 18 microns and a TE-CCD-1100-PB-VISAR detector cooled to -30 °C with a circulating water bath was employed in a standard backscattering configuration. Data were collected at -196 °C in dichloromethane using a glass cryostat, similar in design to one described previously, that incorporates a copper cold finger.<sup>24</sup> The sample concentration was 5 mM. Each measurement was made on more than one freshly prepared sample and the measurements were made in triplicate to ensure the authenticity of the results. The dichloromethane bands at 1156 cm<sup>-1</sup>, 897 cm<sup>-1</sup>, 704 cm<sup>-1</sup>, and 286 cm<sup>-1</sup> were used as an internal calibration standard. Data were processed using WinSpec 3.2.1 (Princeton Instruments, Inc.) and were further manipulated with Kaleidagraph.

**EPR Measurements.** X-band EPR spectra were recorded on a Bruker EMX EPR spectrometer (9.37 GHz) running WinEPR software. Temperature control was achieved with an Oxford Instruments ESR900 liquid-helium cryostat and an ITC503 controller. Dry O<sub>2</sub> gas was directly bubbled into an 0.50 mM CH<sub>2</sub>Cl<sub>2</sub> solution of [Fe<sub>2</sub>(μ-O<sub>2</sub>CAr<sup>Tol</sup>)<sub>4</sub>(BA<sup>p-OMe</sup>)<sub>2</sub>] for 1 min at -78 °C, resulting in a color change from light yellow to dark forest green, indicating the formation of a mixed-valent Fe(II)Fe(III) intermediate. The solution was then frozen at liquid N<sub>2</sub>.

**Stopped-flow Kinetics.** Kinetic experiments were performed by using a double-mixing Canterbury Stopped-Flow SF-40 and MG-6000 Rapid Diode array System (Hi-Tech Scientific). A CH<sub>2</sub>Cl<sub>2</sub> solution of **2** prepared in a glove box under a nitrogen atmosphere and stored in a gas-tight syringe prior to loading into the stopped-flow apparatus. Dioxygen was introduced to the system as a saturated solution in solvent, generated by bubbling in dried O<sub>2</sub> gas for 30 min at 20 °C.

**GC/MS Studies.** GC/MS analyses were carried out with an HP-5890 gas chromatograph connected to a HP-5971 mass analyzer. Alltech Econo-cap EC-WAX capillary columns of dimensions (30 m × 0.25 mm × 0.25 μm) were used for GC/MS studies. The following method was used to effect all separations: initial temperature = 100 °C; initial time = 5 min; temperature ramp = 100 – 250 °C at 25 deg/min. The products were identified by comparing their retention times and mass spectral patterns to those of authentic standards. Response calibrations were measured by running calibration curves with authentic samples and an internal standard of 1,2-dichlorobenzene. A 7.1 mM CH<sub>2</sub>Cl<sub>2</sub> solution (1 mL) of compound **2** was loaded into a vessel fitted with a rubber septum. Dioxygen was bubbled into the solution for one minute at room temperature and the resulting yellow solution was filtered through a 1

cm silica column. 63.5 mM toluene solution (0.15 mL) of dichlorobenzene was added. All samples were prepared in an anaerobic glove box prior to introduction of dried O<sub>2</sub>.

**Kinetic Isotope Effect Measurement.** A 7.8 mM CH<sub>2</sub>Cl<sub>2</sub> solution of [Fe<sub>2</sub>(μ-O<sub>2</sub>CAr<sup>Tol</sup>)<sub>4</sub>(α-*d*<sub>1</sub>-BA<sup>*p*-OMe</sup>)<sub>2</sub>] was bubbled with dry O<sub>2</sub> gas at -78 °C for 1 h, warmed to room temperature, and filtered through a 1 cm (diameter, 0.6 cm) dry silica column. <sup>1</sup>H-NMR spectroscopy (CD<sub>2</sub>Cl<sub>2</sub>) was used to determine the product distribution by comparing the integration of 9.85 ppm (s, 1H) and 7.83 ppm (d, *J* = 8.5 Hz, 2H) peaks.

## Results and Discussion

**Synthesis and Structural Characterization of Compounds [Fe<sub>2</sub>(μ-O<sub>2</sub>CAr<sup>Tol</sup>)<sub>4</sub>(BA)<sub>2</sub>] (1) and [Fe<sub>2</sub>(μ-O<sub>2</sub>CAr<sup>Tol</sup>)<sub>4</sub>(BA<sup>*p*-OMe</sup>)<sub>2</sub>] (2).** Addition of 2 equiv of BA to [Fe<sub>2</sub>(μ-O<sub>2</sub>CAr<sup>Tol</sup>)<sub>2</sub>(O<sub>2</sub>CAr<sup>Tol</sup>)<sub>2</sub>(THF)<sub>2</sub>] in CH<sub>2</sub>Cl<sub>2</sub> afforded the tetracarboxylate-bridged diiron(II) compound [Fe<sub>2</sub>(μ-O<sub>2</sub>CAr<sup>Tol</sup>)<sub>4</sub>(BA)<sub>2</sub>] (1) in good yield (Scheme 3.2). The structure of 1 is depicted in Figure 3.1 and Table 3.2 lists selected bond lengths and angles. Two crystallographically inequivalent iron(II) centers have square pyramidal geometry with an NO<sub>4</sub> coordination environment and are linked by four terphenyl-based carboxylates. These geometric parameters closely resemble those of previously reported paddlewheel type diiron(II) complexes.<sup>25,26</sup> Interestingly, the Fe...Fe distance (2.7937(6) Å) of 1 is comparatively shorter than that of the compound [Fe<sub>2</sub>(μ-O<sub>2</sub>CAr<sup>Tol</sup>)<sub>4</sub>(4-<sup>*t*</sup>BuC<sub>5</sub>H<sub>4</sub>N)<sub>2</sub>], 2.8229(9) Å, where 4-<sup>*t*</sup>BuC<sub>5</sub>H<sub>4</sub>N is 4-*tert*-butylpyridine.<sup>25</sup> Using BA<sup>*p*-OMe</sup> in place of BA, the compound [Fe<sub>2</sub>(μ-O<sub>2</sub>CAr<sup>Tol</sup>)<sub>4</sub>(BA<sup>*p*-OMe</sup>)<sub>2</sub>] (2) was synthesized and the structure determined. Selected bond lengths and angles for 2 (Figure 3.2) are listed in Table 3.2, revealing very close similarities with compound 1. The Fe...Fe distance is 2.7638(17) Å. The closest intermolecular separation between the centers of the diiron(II) unit of 2 are 11.631 Å (Figure 3.2, bottom right), a value

indicating that the diiron(II) sites in **2** are magnetically isolated. Since **1** is not very soluble in most aprotic organic solvents, further studies were performed exclusively with compound **2**.

#### Synthesis and Structural Analysis of $[\text{Fe}_4(\mu\text{-OMe})_4(\text{O}_2\text{CAr}^{\text{Tol}})_4(\text{HOMe})_6](\text{HOMe})$

(**3**). The methoxide-bridged cubane-type tetrairon(II) cluster **3** was initially isolated when the solubility of compound **2** in methanol was tested. The crystal structure of **3** is shown in Figure 3.3 and selected bond lengths and angles are listed in Table 3.3. Compound **3** has a distorted cubic  $\{\text{Fe}_4(\mu\text{-OMe})_4\}^{4+}$  unit, in which  $\text{Fe}_4$  and  $(\text{OMe})_4$  disphenoids are interpenetrating. Three iron(II) sites (Fe1, Fe2, and Fe3) have slightly distorted octahedral geometries with an  $\text{O}_6$  donor atom set. By contrast, the Fe4 site has a distorted trigonal bipyramidal  $\text{O}_5$  coordination environment, resulting in overall  $\text{C}_1$  point group symmetry for compound **3**. Unlike the monodentate carboxylates coordinated to the three octahedral Fe(II) sites, the carboxylate ligand at the Fe4 site is chelating, with Fe–O separations of 2.0957(17) Å and 2.2101(19) Å. The Fe–O(methoxide) average distance is 2.116(56) Å and the Fe–O–Fe angles are closely distributed, ranging from 92.20 (6)° to 98.24 (7)°. The average Fe···Fe separation is 3.134(33) Å. The other coordination sites in three octahedral iron(II) sites are filled by 3 × 2 methanol molecules. The assignment of methanol over methoxide is supported by overall charge balance considerations as well as by the location and refinement of the associated hydrogen atoms from the difference electron density maps. The coordinated methanols and terminal monodentated carboxylates generate a tight intracuster network of hydrogen bonds with an average O···O separation of 2.675(44) Å. Such hydrogen bonding interactions may help the assembly of the  $\{\text{Fe}_4(\mu\text{-OMe})_4\}^{4+}$  core.

Both the absence of  $\text{BA}^{p\text{-OMe}}$  ligands and the presence of deprotonated methoxide in the structure of **3** suggest that the basic amine ligand ( $\text{BA}^{p\text{-OMe}}$ ) may deprotonate



methanol to form the methoxide anion. The methoxide ions so generated react with the metal ion to afford the isolated cubane-type tetrairon(II) complex. This hypothesis was tested by treating a methanol solution of a mixture of  $\text{NaO}_2\text{CAr}^{\text{Tol}}$  and  $\text{Fe}(\text{OTf})_2 \cdot 2\text{CH}_3\text{CN}$  with 1 equiv of triethylamine (Method B), affording compound **3**. The chemistry discussed here limits the range of solvents that can be used to characterize the physical properties and study the reactivity of these carboxylate rich diiron(II) complexes.

**Mössbauer Spectroscopy.** The zero-field Mössbauer spectra of solid samples of **1**, **2** and **3** at 4.2 K are displayed in Figures 3.4. and 3.5. The corresponding parameters derived from fits of the spectra are provided in Table 3.4. Both compound **1** and **2** displays a broad and asymmetric signal that was best fit as two overlapping quadrupole doublets. The crystallographically inequivalent iron(II) sites may be distinguished in the Mössbauer spectra. The isomer shifts and quadrupole splittings are typical of high-spin iron(II) centers and comparable to those reported for related tetracarboxylate bridged diiron(II) complexes.

Two distinct quadrupole doublets with 1:3 intensity ratio are observed in the Mössbauer spectrum of **3** at 4.2 K (Figures 3.5). This result is in accord with the two types of iron(II) sites with different geometries revealed by X-ray crystallography. The Mössbauer fit parameters are listed in Table 3.4. It is noteworthy that the iron(II) sites with  $\text{O}_6$  coordination environments have a larger isomer shift of 1.30(2) mm/s than the iron(II) site with  $\text{O}_5$  geometry (1.17(2) mm/s).

**Magnetochemistry.** The effective magnetic moments ( $\mu_{\text{eff}}$ ) of **1**, measured at 0.1 Tesla, steadily increase from 8.0  $\mu_B$  at 300 K to a maximum of 8.6  $\mu_B$  at 80 K, before decreasing to 7.7  $\mu_B$  at 5 K (Figure 3.6). This behavior indicates weak ferromagnetic exchange coupling between the two high-spin iron(II) centers of the tetracarboxylate-

bridged dimer. The measured value of  $8.0 \mu_B$  at 300 K is consistent with the presence of two uncoupled  $S = 2$  centers with  $g = 2.3$  (expected  $\mu_{eff}$  value of 7.967).

One complicating feature of diiron(II) complexes in elucidating their exchange coupling interaction is the large zero-field splitting (ZFS) effect, up to  $\sim |20 \text{ cm}^{-1}|$ , which can affect the magnetic behavior even at fairly high temperatures.<sup>27</sup> In the case of  $|D| \geq J$  (where  $D$  and  $J$  are axial ZFS and exchange coupling parameters, respectively), the solutions from single field magnetic data are not often unique. In order to address the ZFS effect, multifold saturated magnetic susceptibilities of 2 from 2K to 300K were measured (Figure 3.7). A Curie magnetization law plot of the data set at 0.5 T has a near zero intercept, -0.015 with  $R = 0.99$ , indicating no significant intermolecular interaction (Figure 3.8). This result is in agreement with the very long intermolecular distance observed in the crystal lattice. Thus, the observed magnetic data were considered to reflect only the intramolecular interactions.

The energy levels of the system formed by two exchange coupled high-spin ferrous ( $S = 2$ ) sites can be described by the spin Hamiltonian, given in eq 1, where  $J$  is the isotropic exchange coupling constant,  $D_i$  and  $E_i$  are the axial and rhombic zero-field splitting parameters, and  $g_i$  are the  $g$  tensors of the uncoupled site ( $i = 1, 2$ ).

$$H = -2JS_1 \cdot S_2 + \sum_i [D_i(S_{zi}^2 - 2) + E_i(S_{xi}^2 - S_{yi}^2) + \beta S_i \cdot g_i \cdot H] \quad i = 1, 2 \quad (1)$$

We assumed two identical high spin Fe(II) sites to prevent over-parameterization. In Figure 3.7 (Top) the data are presented as magnetic moment versus temperature at all four fields. In Figure 3.7 (Bottom) the data are presented as susceptibility versus temperature. The solid lines in Figure 3.7 were calculated by diagonalization of the full  $25 \times 25$  spin Hamiltonian of eq 1 with  $J = 9.2(0.8) \text{ cm}^{-1}$ ,  $D_1 = D_2$

= -5(0.2) cm<sup>-1</sup>,  $E_1/D_1 = E_2/D_2 = 0.14(0.3)$ , and  $g_1 = g_2 = 2.23(0.8)$ . The small positive  $J$  value indicate that the high-spin diiron(II) sites are weakly but ferromagnetically exchange coupled. The significant difference between the magnetic behavior of **1** and **2** compared to the previously reported strong antiferromagnetic exchange coupling interaction for the paddlewheel complex [Fe<sub>2</sub>(μ-O<sub>2</sub>CAr<sup>Tol</sup>)<sub>4</sub>(4-<sup>t</sup>BuC<sub>5</sub>H<sub>4</sub>N)<sub>2</sub>] must reflect small differences (~0.03-0.06 Å) in Fe...Fe distance as well as the electronic character of the axial ligands. Theoretical studies are required for further insight.

**Electrochemistry.** The electrochemical properties of **2** were investigated to evaluate the one-electron oxidation potential and to probe the possibility of outer-sphere redox chemistry with dioxygen. Cyclic voltammograms of a CH<sub>2</sub>Cl<sub>2</sub> solution of **2** revealed a quasi-reversible, one-electron oxidation at  $E_{1/2} = 69$  mV vs. Cp<sub>2</sub>Fe/Cp<sub>2</sub>Fe<sup>+</sup> ( $\Delta E_p = 114$  mV, scan rate = 25 mV/s) (Figure 3.8). This potential can be converted to +772 mV vs. NHE. Conversion from Cp<sub>2</sub>Fe/Cp<sub>2</sub>Fe<sup>+</sup> scale to NHE scale was based on following values: Cp<sub>2</sub>Fe/Cp<sub>2</sub>Fe<sup>+</sup> = 460 mV vs. SCE (in CH<sub>2</sub>Cl<sub>2</sub> with (Bu<sub>4</sub>N)PF<sub>6</sub> supporting electrolyte),<sup>22</sup> SCE = +242 mV vs. NHE.<sup>23</sup> Based on the measured  $E_{1/2}$  value for oxidation of **2**, outer-sphere electron transfer upon reaction with dioxygen to form {Fe<sub>2</sub><sup>III</sup> + O<sub>2</sub><sup>-</sup>} is unlikely to occur, due to the low reduction potential of dioxygen (O<sub>2</sub>/O<sub>2</sub><sup>-</sup> = -550 mV vs. NHE) in CH<sub>2</sub>Cl<sub>2</sub>.

**Reactivity with Dioxygen and Characterization of Intermediates.** When a CH<sub>2</sub>Cl<sub>2</sub> solution of **2** was allowed to react with dioxygen at -78 °C, a green color developed ( $\lambda_{max} = 645$  nm) over a period of 200 sec. This metastable solution decayed within ~6 h at -78 °C to form a yellow species (Figure 3.9 a). Clues to the identity of the observed green intermediate were provided by resonance Raman (rR) and EPR spectroscopic measurements. The frozen solution rR spectrum was measured, revealing an enhanced peak at 844 cm<sup>-1</sup> (Figure 3.10). This peak is not <sup>18</sup>O-sensitive, which

indicates that the chromophore does not contain an Fe–O bond derived from dioxygen. A rR peak with similar characteristics has been previously reported for the intermediate formed by oxygenation of  $[\text{Fe}_2(\mu\text{-O}_2\text{CAr}^{\text{Tol}})_4(4\text{-}^t\text{BuC}_5\text{H}_4\text{N})_2]$ .<sup>25,28,29</sup>

The X-band EPR spectra of the green intermediate measured at 5 K exhibited two distinct signals at  $g = 12$  and  $g = 2.0$  (Figure 3.11). The broad  $g = 12$  signal may originate from a ferromagnetically coupled high spin Fe(II)Fe(III) unit with an  $S = 9/2$  ground state. This assignment was confirmed by comparison to the UV-vis and EPR spectra of the chemically synthesized, mixed-valent  $[\text{Fe}_2(\mu\text{-O}_2\text{CAr}^{\text{Tol}})_4(\text{BA}^{p\text{-OMe}})_2](\text{PF}_6)$  complex (Figures 3.10b and 3.11b). The  $g = 2.0$  signal (Figure 3.11) must then arise from an antiferromagnetically coupled Fe(III)Fe(IV) unit with an  $S = 1/2$  ground state. These observations are identical to the reported behavior of the tetracarboxylate bridged diiron(II) complex  $[\text{Fe}_2(\mu\text{-O}_2\text{CAr}^{\text{Tol}})_4(4\text{-}^t\text{BuC}_5\text{H}_4\text{N})_2]$  in the presence of dioxygen.

**Oxygenation Product and Kinetic Isotope Effect (KIE) Analyses.** The products formed upon exposure of a  $\text{CH}_2\text{Cl}_2$  solution of **2** to dioxygen at ambient temperature as analyzed by GC-MS include anisaldehyde, with an average yield of 26(7) % per  $\text{Fe}^{\text{II}}_2$  unit. This product corresponds to *N*-dealkylation following putative hydroxylation at the benzylic position. This supposition was confirmed by the reaction of  $[\text{Fe}_2(\mu\text{-O}_2\text{CAr}^{\text{Tol}})_4(\alpha\text{-}d_1\text{-BA}^{p\text{-OMe}})_2]$  in  $\text{CH}_2\text{Cl}_2$  solution with dioxygen at  $-78\text{ }^\circ\text{C}$ , which afforded anisaldehyde and  $d_1$ -anisaldehyde in a ratio of ~1:3 (Figure 3.12). This kinetic isotope effect is consistent with C–H bond cleavage in the product-determining step of the reaction. The benzyl substituent in **2** being positioned such that the C–H bonds to be activated are  $\alpha$  to the metal-bound nitrogen atom.

## Summary

Generation of the mixed valence intermediates and *N*-dealkylation might occur via the following scenario. Reaction of **2** with dioxygen affords a transient adduct [2-O<sub>2</sub>] that never accumulates, possibilities for which are as Fe<sub>2</sub><sup>II,III</sup>(O<sub>2</sub><sup>-</sup>), Fe<sub>2</sub><sup>III</sup>(O<sub>2</sub><sup>2-</sup>), or Fe<sub>2</sub><sup>IV</sup>(O<sup>2-</sup>)<sub>2</sub>. Based on the E<sub>1/2</sub> value for oxidation of **2** measured electrochemically, outer-sphere electron transfer upon reaction with dioxygen to form {Fe<sub>2</sub><sup>II,III</sup> + O<sub>2</sub>} is unlikely to occur, due to the low reduction potential of dioxygen in dichloromethane. We therefore conclude that a transient [2-O<sub>2</sub>] adduct forms, but before it can accumulate to any spectroscopically detectable concentration, it reacts rapidly with unreacted **2** to afford an equimolar mixture of the green mixed-valent Fe<sup>II</sup>Fe<sup>III</sup> and Fe<sup>III</sup>Fe<sup>IV</sup> complexes. A similar sequence of reactions was proposed for the chemistry of [Fe<sub>2</sub>(μ-O<sub>2</sub>CAr<sup>Tol</sup>)<sub>4</sub>(4-<sup>t</sup>BuC<sub>5</sub>H<sub>4</sub>N)<sub>2</sub>] with dioxygen.

Oxidative *N*-dealkylation of compound **2** may proceed by one-electron oxidation at the nitrogen atom followed by proton transfer and rebound (Scheme 3.1), stepwise oxygen recoil/rebound, or by a concerted mechanism. The absence of a lone pair of electrons in the coordinated BA<sup>*p*-OMe</sup> ligand eliminates the first of these possibilities for the present reaction. The involvement of electron transfer between the intermediate and starting diiron(II) complex to generate mixed-valent species does not allow us to determine the reaction mechanism for this step.

**References**

- (1) Solomon, E. I.; Brunold, T. C.; Davis, M. I.; Kemsley, J. N.; Lee, S.-K.; Lehnert, N.; Neese, F.; Skulan, A. J.; Yang, Y.-S.; Zhou, J. *Chem. Rev.* **2000**, *100*, 235 - 349.
- (2) Feig, A. L.; Lippard, S. J. *Chem. Rev.* **1994**, *94*, 759-805.
- (3) Solomon, E. I.; Sundaram, U. M.; Machonkin, T. E. *Chem. Rev.* **1996**, *96*, 2563 - 2605.
- (4) Ambundo, E. A.; Friesner, R. A.; Lippard, S. J. *J. Am. Chem. Soc.* **2002**, *124*, 8770-8771.
- (5) Merckx, M.; Kopp, D. A.; Sazinsky, M. H.; Blazyk, J. L.; Müller, J.; Lippard, S. J. *Angew. Chem., Int. Ed.* **2001**, *40*, 2782-2807.
- (6) Yoon, S. **2004**.
- (7) Mahapatra, S.; Halfen, J. A.; Tolman, W. B. *J. Am. Chem. Soc.* **1996**, *118*, 11575-11586.
- (8) Itoh, S.; Bando, H.; Nagatomo, S.; Kitagawa, T.; Fukuzumi, S. *J. Am. Chem. Soc.* **1999**, *121*, 8945-8946.
- (9) Itoh, S.; Nakao, H.; Berreau, L. M.; Kondo, T.; Komatsu, M.; Fukuzumi, S. *J. Am. Chem. Soc.* **1998**, *120*, 2890-2899.
- (10) Pangborn, A. B.; Giardello, M. A.; Grubbs, R. H.; Rosen, R. K.; Timmers, F. J. *Organometallics* **1996**, *15*, 1518-1520.
- (11) Lee, D.; Lippard, S. J. *J. Am. Chem. Soc.* **1998**, *120*, 12153-12154.
- (12) Kuzelka, J.; Mukhopadhyay, S.; Spingler, B.; Lippard, S. J. *Inorg. Chem.* **2004**, *43*, 1751-1761.
- (13) Sheldrick, G. M.; University of Göttingen: Göttingen, Germany, 1997.
- (14) Sheldrick, G. M.; University of Göttingen: Göttingen, Germany, 1996.
- (15) Spek, A. L.; Utrecht University: Utrecht, The Netherlands, 1998.

- (16) Kent, T. A.; v2.5 ed.: Minneapolis, 1998.
- (17) Carlin, R. L. *magnetochemistry*; Springer-Verlag: New York, 1986.
- (18) Day, E. P. *Methods in Enzymology* **1993**, *227*, 437-463.
- (19) Hendrich, M. P.; Day, E. P.; Wang, C.-P.; Synder, B. S.; Holm, R. H.; Münck, E. *Inorg. Chem.* **1994**, *33*, 2848-2856.
- (20) Hendrich, M. P.; Pearce, L. L.; Que, L., Jr.; Chasteen, N. D.; Day, E. P. *J. Am. Chem. Soc.* **1991**, *113*, 3039-3044.
- (21) Karlin, K. D.; Nanthakumar, A.; Fox, S.; Murthy, N. N.; Ravi, N.; Huynh, B. H.; Orosz, R. D.; Day, E. P. *J. Am. Chem. Soc.* **1994**, *116*, 4753-4763.
- (22) Connelly, N. G.; Geiger, W. E. *Chem. Rev.* **1996**, *96*, 877-910.
- (23) Bard, A. J.; Faulkner, L. R. *Electrochemical Methods Fundamentals and Applications*; John Wiley & Sons: New York, 1980.
- (24) Feig, A. L.; Bautista, M. T.; Lippard, S. J. *Inorg. Chem.* **1996**, *35*, 6892-6898.
- (25) Lee, D.; Du Bois, J.; Petasis, D.; Hendrich, M. P.; Krebs, C.; Huynh, B. H.; Lippard, S. J. *J. Am. Chem. Soc.* **1999**, *121*, 9893-9894.
- (26) Chavez, F. A.; Ho, R. Y. N.; Pink, M.; Young, V. G., Jr.; Kryatov, S. V.; Rybak-Akomova, E. V.; Andres, H.; Münck, E.; Que, L., Jr.; Tolman, W. B. *Angew. Chem., Int. Ed.* **2002**, *41*, 149-152.
- (27) Reem, R. C.; Solomon, E. I. *J. Am. Chem. Soc.* **1987**, *109*, 1216-1226.
- (28) Lee, D.; DuBois, J. L.; Pierce, B.; Hedman, B.; Hodgson, K. O.; Hendrich, M. P.; Lippard, S. J. *Inorg. Chem.* **2002**, *41*, 3172-3182.
- (29) Lee, D.; Pierce, B.; Krebs, C.; Hendrich, M. P.; Huynh, B. H.; Lippard, S. J. *J. Am. Chem. Soc.* **2002**, *124*, 3993-4007.

**Table 3.1.** Summary of X-ray Crystallographic Information for [Fe<sub>2</sub>(μ-O<sub>2</sub>CAr<sup>Tol</sup>)<sub>4</sub>(BA)<sub>2</sub>] (1), [Fe<sub>2</sub>(μ-O<sub>2</sub>CAr<sup>Tol</sup>)<sub>4</sub>(BA<sup>p-OMe</sup>)<sub>2</sub>] (2) and [Fe<sub>4</sub>(μ-OMe)<sub>2</sub>(O<sub>2</sub>CAr<sup>Tol</sup>)<sub>4</sub>(HOMe)<sub>6</sub>] (3)

Compound	1	2·0.5CH <sub>2</sub> Cl <sub>2</sub>	3·MeOH
Empirical formula	Fe <sub>2</sub> C <sub>98</sub> H <sub>86</sub> O <sub>8</sub> N <sub>2</sub>	Fe <sub>2</sub> C <sub>92</sub> H <sub>88</sub> O <sub>12</sub>	Fe <sub>4</sub> C <sub>95</sub> H <sub>108</sub> O <sub>19</sub>
Formula weight	1531.39	1633.90	1777.21
Space group	P2 <sub>1</sub> /n	P $\bar{1}$	P2 <sub>1</sub> /c
<i>a</i> , Å	14.6583(18)	14.353(9)	17.421(3)
<i>b</i> , Å	19.801(3)	16.211(9)	14.762(2)
<i>c</i> , Å	27.365(4)	19.993(12)	36.701(6)
α, deg		70.78(3)	
β, deg	91.968(2)	89.83(3)	102.017(3)
γ, deg		76.08(3)	
<i>V</i> , Å <sup>3</sup>	7938.2(17)	4249(4)	9232(3)
<i>Z</i>	4	2	4
ρ <sub>calc</sub> , g/cm <sup>3</sup>	1.281	1.277	1.279
<i>T</i> , °C	-80	-133	-100
μ(Mo Kα), mm <sup>-1</sup>	0.426	0.435	0.682
total no. of data	57047	26166	46880
no. of unique data	18357	18658	16172
no. of params	1007	1064	1127
R1 (%) <sup>a</sup>	5.38	5.78	3.78
wR <sub>2</sub> (%) <sup>b</sup>	10.31	15.83	11.84
Largest diff. peak and hole	0.508 -0.615	1.184 -0.318	0.816 -0.493

<sup>a</sup> R1 =  $\Sigma||F_o| - |F_c||/\Sigma|F_o|$ . <sup>b</sup> wR2 =  $\{\Sigma[w(F_o^2 - F_c^2)^2]/\Sigma[w(F_o^2)^2]\}^{1/2}$



**Table 3.2.** Selected interatomic bond lengths (Å) and angles (deg) for [Fe<sub>2</sub>(μ-O<sub>2</sub>CAr<sup>Tol</sup>)<sub>4</sub>(BA)<sub>2</sub>] (1) and [Fe<sub>2</sub>(μ-O<sub>2</sub>CAr<sup>Tol</sup>)<sub>4</sub>(BA<sup>*p*-OMe</sup>)<sub>2</sub>] (2)<sup>a</sup>

Compound	1	2·0.5CH <sub>2</sub> Cl <sub>2</sub>
Fe1···Fe2	2.79379(8)	2.7638(17)
Fe1–O1	2.0953(13)	2.102(2)
Fe1–O3	2.1256(19)	2.044(2)
Fe1–O5	2.046(2)	2.120(2)
Fe1–O7	2.0831(19)	2.039(2)
Fe2–O2	2.074(2)	2.049(2)
Fe2–O4	2.0372(19)	2.067(2)
Fe2–O6	2.1754(19)	2.036(2)
Fe2–O8	2.0512(19)	2.143(2)
Fe1–N2	2.119(3)	2.105(3)
Fe2–N2	2.130(3)	2.119(3)
O1–Fe1–N1	86.71(10)	100.63(12)
O3–Fe1–N1	90.30(11)	103.96(13)
O5–Fe1–N1	110.51(10)	96.30(12)
O7–Fe1–N1	106.29(11)	91.45(13)
O2–Fe2–N2	116.15(10)	101.23(11)
O4–Fe2–N2	99.26(12)	116.05(11)
O6–Fe2–N2	81.61(10)	95.36(11)
O8–Fe2–N2	97.18(12)	83.77(11)
O1–Fe1–O3	87.31(7)	86.72(9)
O1–Fe1–O5	162.40(8)	163.08(8)
O1–Fe1–O7	86.80(8)	90.63(9)
O3–Fe1–O5	88.95(8)	89.22(9)
O3–Fe1–O7	162.03(7)	164.59(8)
O5–Fe1–O7	91.56(8)	88.93(9)
O2–Fe2–O4	91.79(8)	90.59(9)
O2–Fe2–O6	162.15(7)	162.11(9)
O2–Fe2–O8	88.38(8)	88.14(9)
O4–Fe2–O6	86.76(7)	88.06(9)
O4–Fe2–O8	161.57(8)	159.96(8)
O6–Fe2–O8	87.46(7)	87.06(9)

<sup>a</sup>Numbers in parentheses are estimated standard deviations of the last significant figure. Atoms are labeled as indicated Figure 3.1 and 3.2.

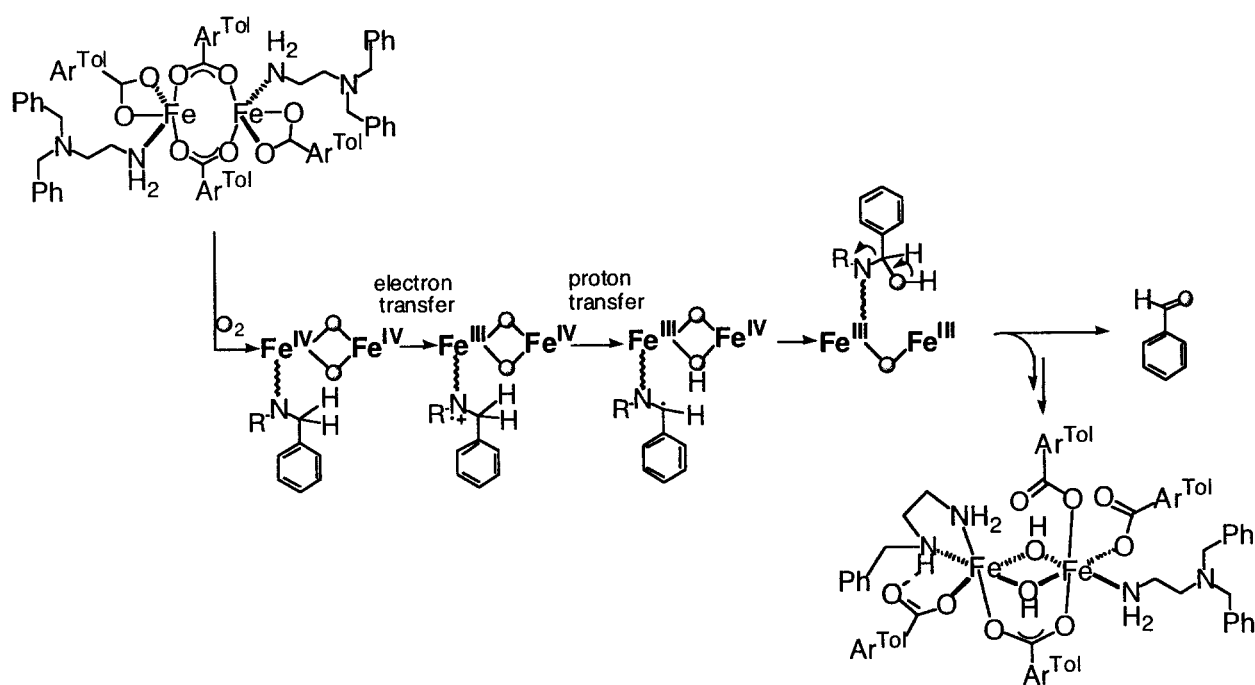
**Table 3.3.** Selected interatomic bond lengths (Å) and angles (deg) for [Fe<sub>4</sub>(μ-O<sub>2</sub>CAr<sup>Tol</sup>)<sub>4</sub>(HOMe)<sub>6</sub>](HOMe) (3)<sup>a</sup>

Fe1...Fe2	3.1680(6)	Fe1-O1-Fe2	97.90(7)
Fe1...Fe3	3.1453(6)	Fe1-O1-Fe3	97.32(7)
Fe1...Fe4	3.1580(6)	Fe1-O2-Fe2	94.15(6)
Fe2...Fe3	3.1435(6)	Fe1-O2-Fe4	97.02(7)
Fe2...Fe4	3.0907(6)	Fe1-O3-Fe3	92.20(6)
Fe3...Fe4	3.0956(7)	Fe1-O3-Fe4	98.24(7)
Fe1-O1	2.0972(17)	Fe2-O1-Fe3	97.04(7)
Fe1-O2	2.1715(17)	Fe2-O2-Fe4	94.79(7)
Fe1-O3	2.1406(17)	Fe2-O4-Fe3	94.79(6)
Fe2-O1	2.1037(16)	Fe2-O4-Fe4	94.16(6)
Fe2-O2	2.1550(17)	Fe3-O3-Fe4	93.14(7)
Fe2-O4	2.1582(16)	O1-Fe1-O2	83.24(6)
Fe3-O1	2.0920(16)	O1-Fe1-O3	85.46(6)
Fe3-O3	2.2237(17)	O1-Fe2-O2	83.49(6)
Fe3-O4	2.1123(16)	O1-Fe2-O4	83.01(6)
Fe4-O2	2.0429(17)	O1-Fe3-O3	83.51(6)
Fe4-O3	2.0353(17)	O1-Fe3-O4	84.41(6)
Fe4-O4	2.0611(16)	O2-Fe1-O3	79.57(6)
O5...O15	2.646(3)	O2-Fe2-O4	82.64(6)
O6...O14	2.718(3)	O2-Fe4-O3	85.16(7)
O7...O18	2.743(3)	O3-Fe3-O4	82.38(6)
O8...O16	2.654(3)	O3-Fe4-O4	88.43(7)
O9...O13	2.640(3)	O4-Fe4-O12	154.33(7)
O10...O17	2.647(3)	O4-Fe4-O11	94.32(7)
Fe4-O11	2.0957(19)	O11-Fe4-O12	60.27(7)
Fe4-O12	2.2101(19)	O2-Fe4-O11	131.75(8)
		O2-Fe4-O12	111.21(7)
		O3-Fe4-O11	143.02(8)
		O3-Fe4-O12	109.45(7)

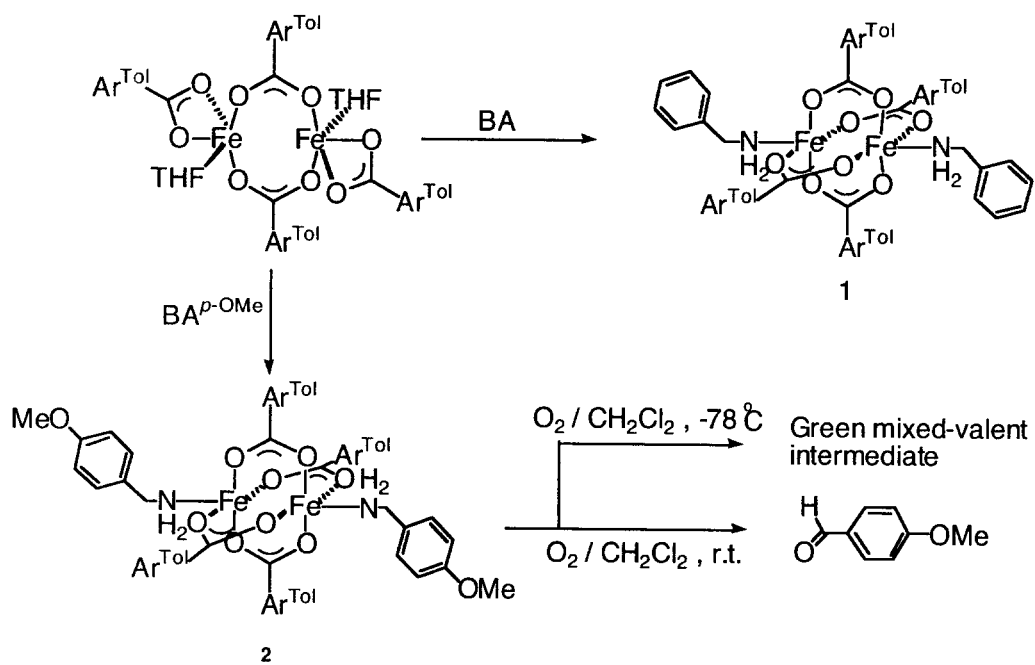
<sup>a</sup>Numbers in parentheses are estimated standard deviations of the last significant figure. Atoms are labeled as indicated Figure 3.3.

**Table 3.4.** Summary of Mössbauer parameters for  $[\text{Fe}_2(\mu\text{-O}_2\text{CAr}^{\text{Tol}})_4(\text{BA})_2]$  (1),  $[\text{Fe}_2(\mu\text{-O}_2\text{CAr}^{\text{Tol}})_4(\text{BA}^{p\text{-OMe}})_2]$  (2), and  $[\text{Fe}_4(\mu\text{-OMe})_2(\text{O}_2\text{CAr}^{\text{Tol}})_4(\text{HOMe})_6]$  (3)

	1		2		3	
$\delta$ (mm/s)	1.08(2)	1.12(2)	1.06(2)	1.14(2)	1.17(2)	1.30 (2)
$\Delta E_Q$ (mm/s)	2.12(2)	2.58(2)	2.12(2)	2.44(2)	2.35(2)	3.53(2)
$\Gamma$	0.29(2)	0.22(2)	0.25(2)	0.33(2)	0.28 (2)	0.28(2)
Area	1	1	1	1	1	3



Scheme 3.1.



Scheme 3.2.

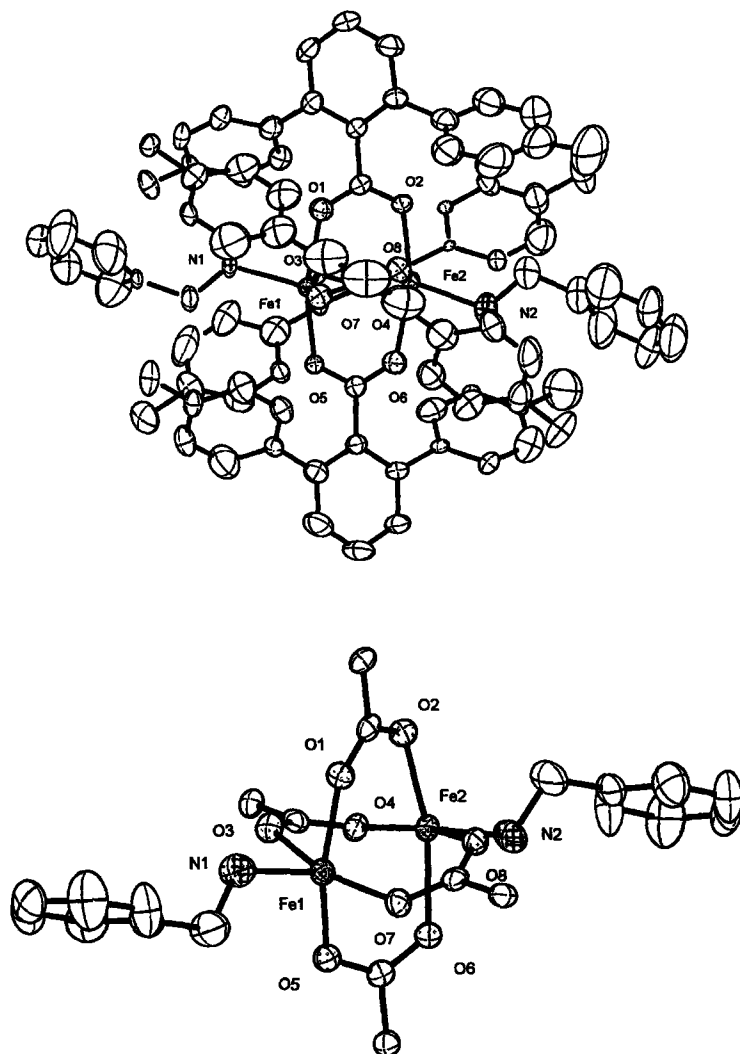


**Figure 3.1.** Top: ORTEP diagram of  $[\text{Fe}_2(\mu\text{-O}_2\text{CAr}^{\text{Tol}})_4(\text{BA})_2]$  (1) showing 50 % probability thermal ellipsoids for all non-hydrogen atoms. Bottom: The aromatic rings of  $\text{Ar}^{\text{Tol}}\text{CO}_2^-$  ligands are omitted for clarity.

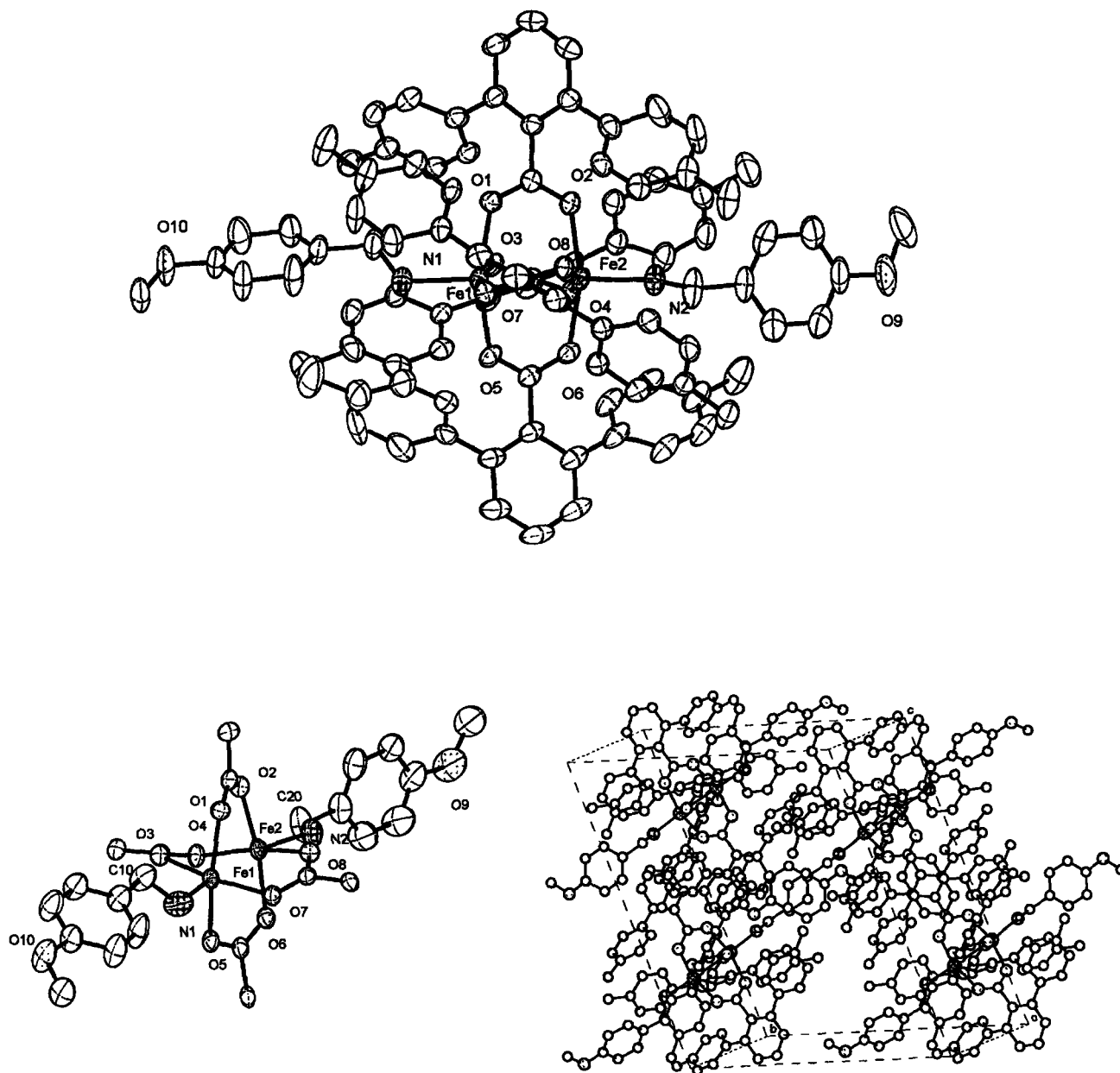


**Figure 3.2.** Top: ORTEP diagram of  $[\text{Fe}_2(\mu\text{-O}_2\text{CAR}^{\text{Tol}})_4(\text{BA}^{p\text{-OMe}})_2]$  (2) showing 50% probability thermal ellipsoids for all non-hydrogen atoms. Bottom left: The aromatic rings of  $\text{Ar}^{\text{Tol}}\text{CO}_2^-$  ligands are omitted for clarity. Bottom right: Crystal packing diagram of 2.

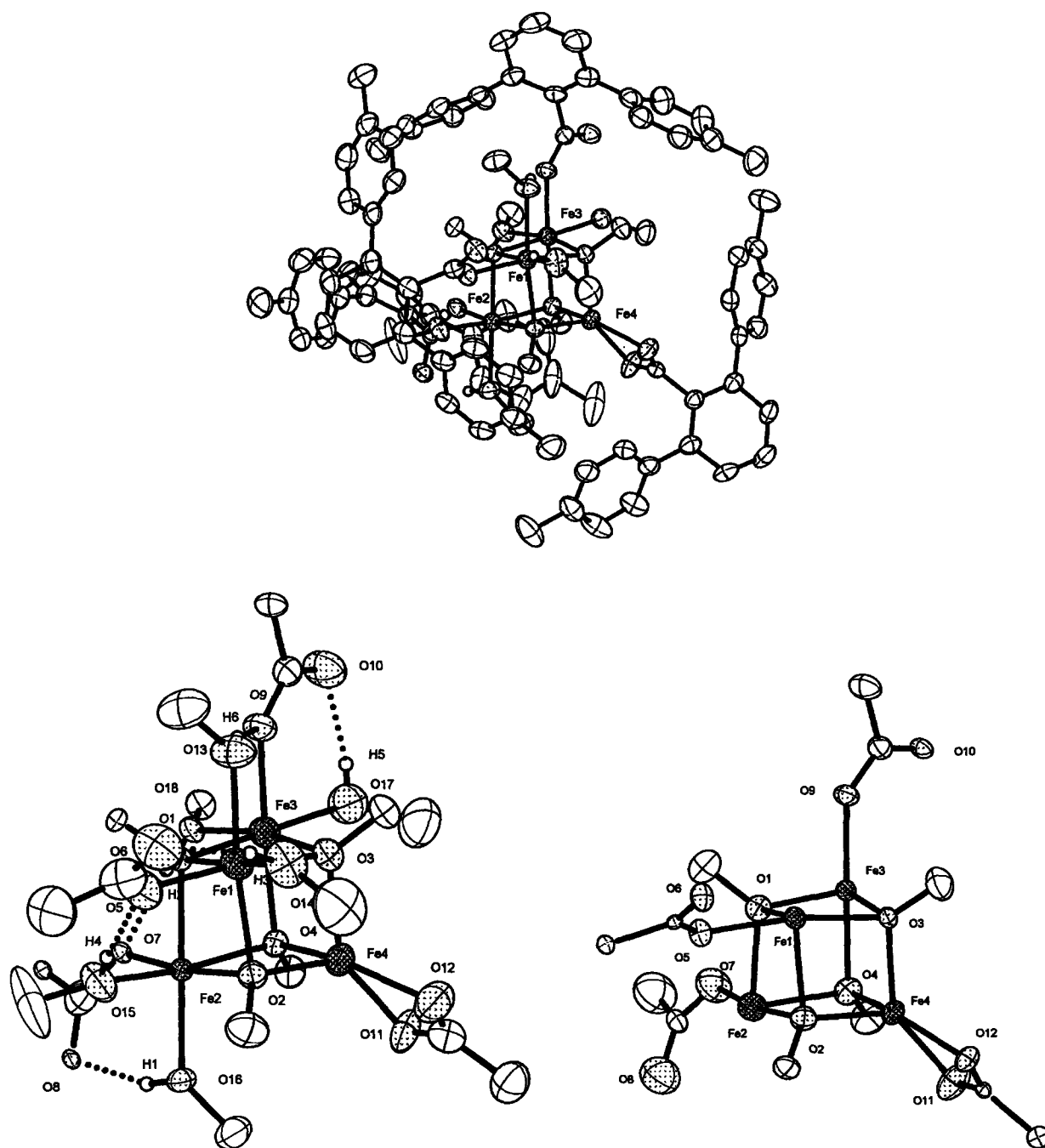


**Figure 3.3.** Top: ORTEP diagram of  $[\text{Fe}_4(\mu\text{-OMe})_4(\text{O}_2\text{CAr}^{\text{Tol}})_4(\text{HOMe})_6]$  (**3**) showing 50 % probability thermal ellipsoids for all non-hydrogen atoms. Bottom left: The aromatic rings of  $\text{Ar}^{\text{Tol}}\text{CO}_2^-$  ligands are omitted for clarity and hydrogen-bonding interactions are depicted with dot lines. Bottom right: The cubane core diagram with carboxylates and bridging methoxides.



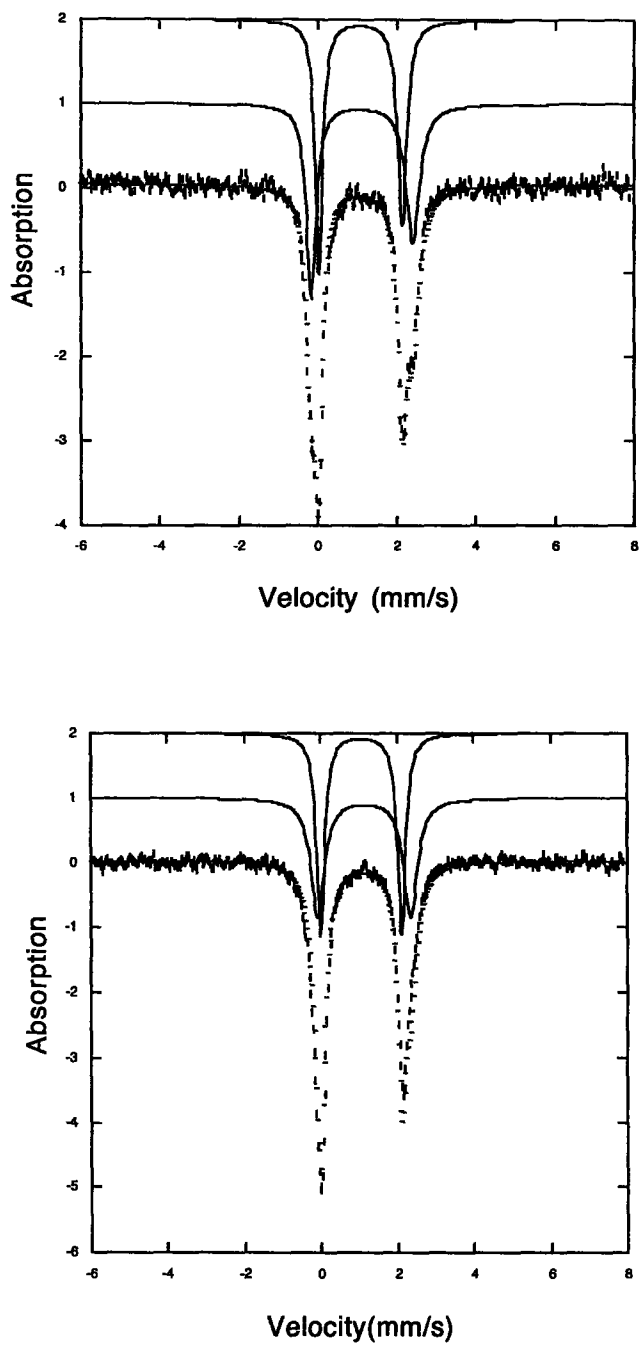


**Figure 3.4.** Zero-field Mössbauer spectrum (experimental data (|), calculated fit (—)) recorded at 4.2 K of the solid sample of  $[\text{Fe}_2(\mu\text{-O}_2\text{CAr}^{\text{Tol}})_4(\text{BA})_2]$  (1) and  $[\text{Fe}_2(\mu\text{-O}_2\text{CAr}^{\text{Tol}})_4(\text{BA}^{\text{p-OMe}})_2]$  (2), top and bottom, respectively.

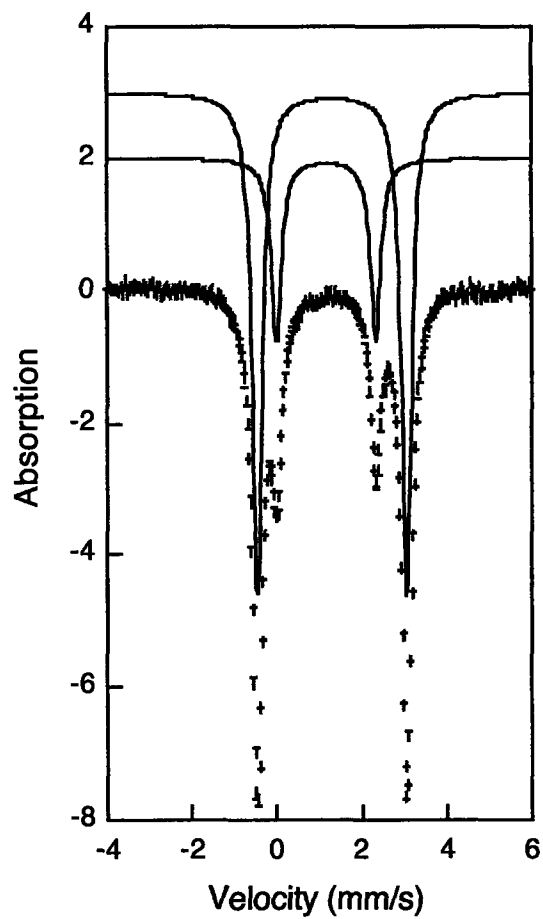


**Figure 3.5.** Zero-field Mössbauer spectrum (experimental data (|), calculated fit (—)) recorded at 4.2 K of the solid sample of  $[\text{Fe}_4(\mu\text{-OMe})_4(\text{O}_2\text{CAr}^{\text{Tol}})_4(\text{HOMe})_6]$  (3).

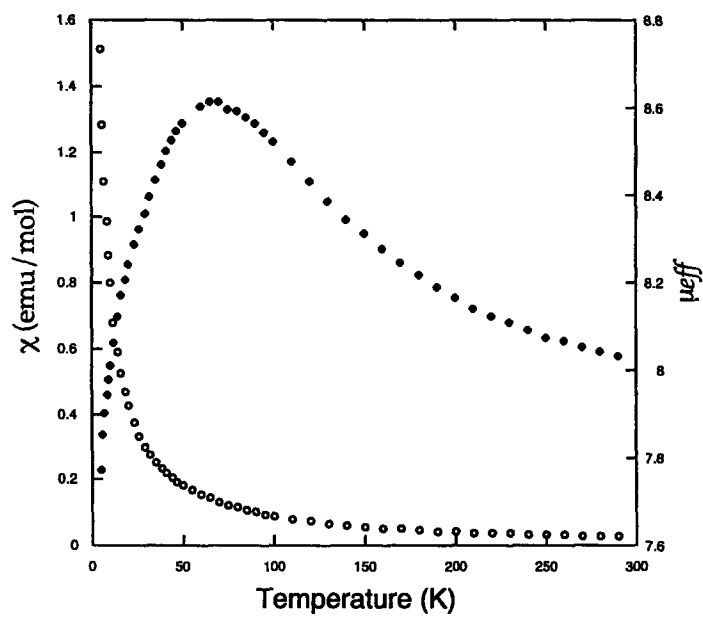


**Figure 3.6.** Plots of the effective magnetic moment ( $\mu_{\text{eff}}$ ) per molecule versus temperature (filled circles) and molar susceptibility ( $\chi_M$ ) versus temperature (unfilled circles) for  $[\text{Fe}_2(\mu\text{-O}_2\text{CAr}^{\text{Tol}})_4(\text{BA})_2]$  (1).

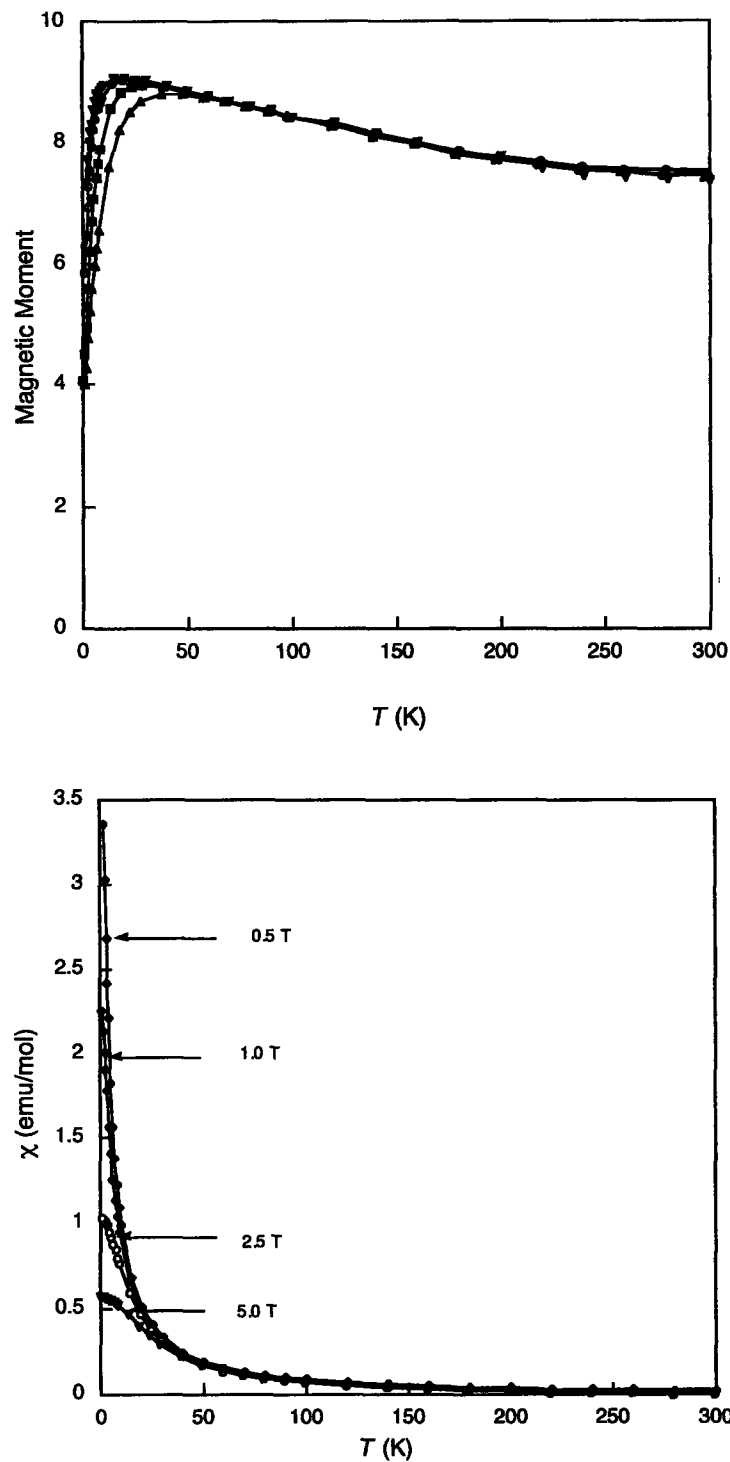


**Figure 3.7.** Plots of the effective magnetic moment ( $\mu_{eff}$ ) per molecule versus temperature (Top) and molar susceptibility ( $\chi_M$ ) versus temperature (Bottom) for  $[\text{Fe}_2(\mu\text{-O}_2\text{CAr}^{\text{Tol}})_4(\text{BA}^{\text{p-OMe}})_2]$  (**2**). The line represents the fit.

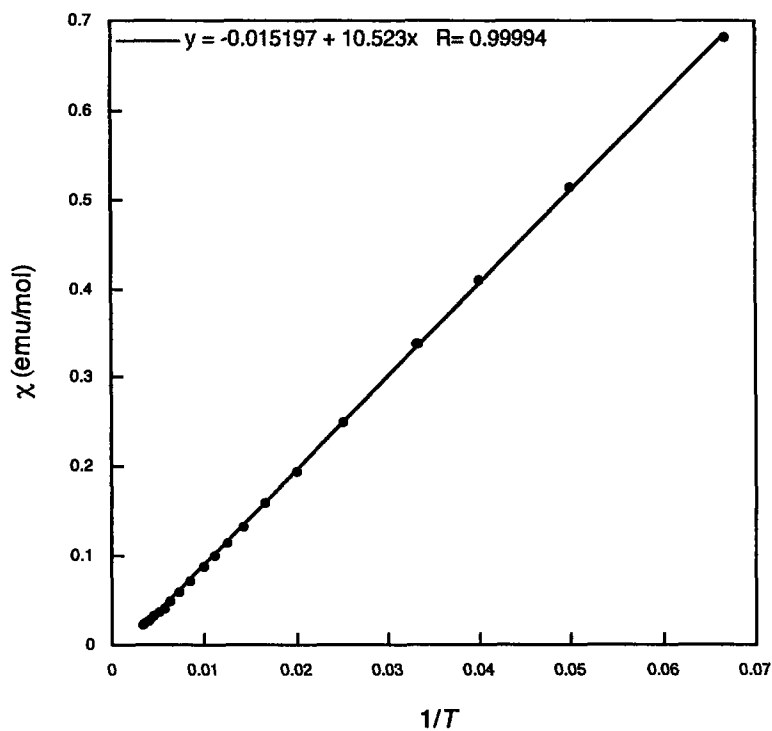


**Figure 3.8.** Plots of molar susceptibility ( $\chi_M$ ) versus inverse temperature for  $[\text{Fe}_2(\mu\text{-O}_2\text{CAr}^{\text{Tol}})_4(\text{BA}^{\text{p-OMe}})_2]$  (**2**), measured at 0.5 T.

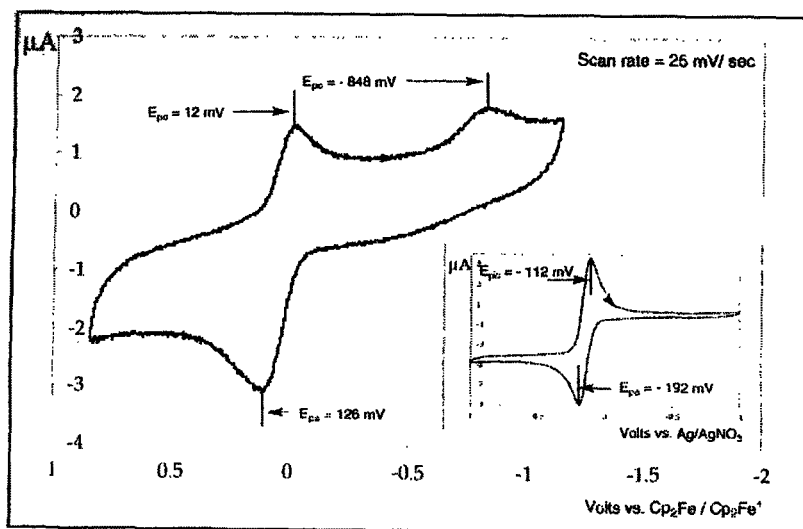


**Figure 3.9.** Cyclic voltammogram of  $[\text{Fe}_2(\mu\text{-O}_2\text{CAr}^{\text{Tol}})_4(\text{BA}^{\text{p-OMe}})_2]$  (2) in  $\text{CH}_2\text{Cl}_2$  with  $0.5 \text{ M } (\text{Bu}_4\text{N})\text{PF}_6$  as supporting electrolyte and a scan rate of  $25 \text{ mV/s}$ . The inset is a cyclic voltammogram of  $\text{Cp}_2\text{Fe}^+ / \text{Cp}_2\text{Fe}$ .

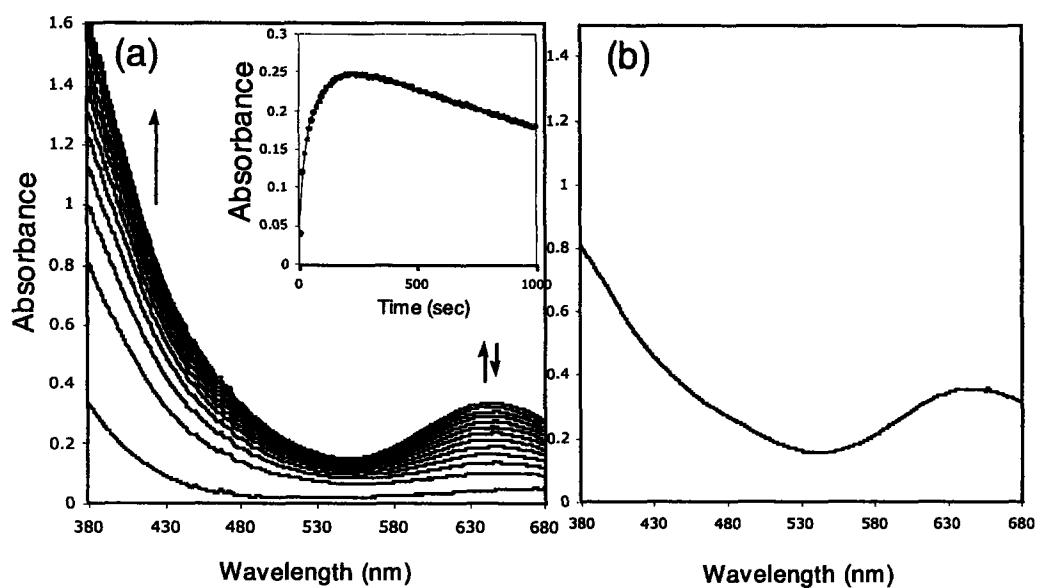


**Figure 3.10.** (a) Spectral changes that occur during the reaction of **2** ( $1.46 \times 10^{-4}$  M) with dioxygen in  $\text{CH}_2\text{Cl}_2$  at  $-78$  °C. (Inset) Kinetic trace for the development and decay of the intermediate recorded at 645 nm. (b) UV-vis spectrum of  $[\text{Fe}_2(\mu\text{-O}_2\text{CAr}^{\text{Tol}})_4(\text{BA}^{\text{p-OMe}})_2](\text{PF}_6)$  in  $\text{CH}_2\text{Cl}_2$ .

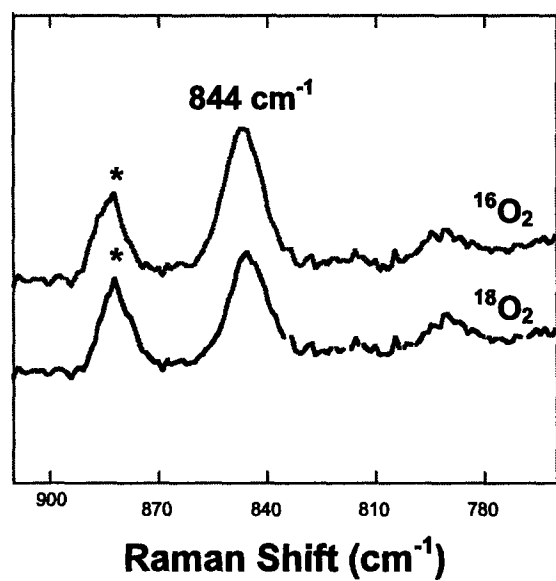


**Figure 3.11.** Resonance Raman spectra of the frozen solution of intermediates derived from the oxygenation of  $[\text{Fe}_2(\mu\text{-O}_2\text{CAR}^{\text{Tol}})_4(\text{BA}^{p\text{-OMe}})_2]$  (**2**) with  $^{16}\text{O}_2$  (top spectrum) and  $^{18}\text{O}_2$  (bottom spectrum) at  $-78\text{ }^\circ\text{C}$ . The asterisk indicates a solvent band.



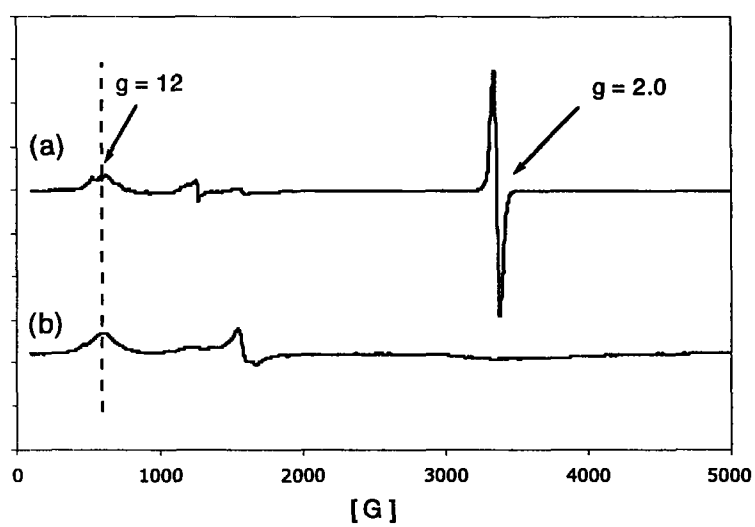
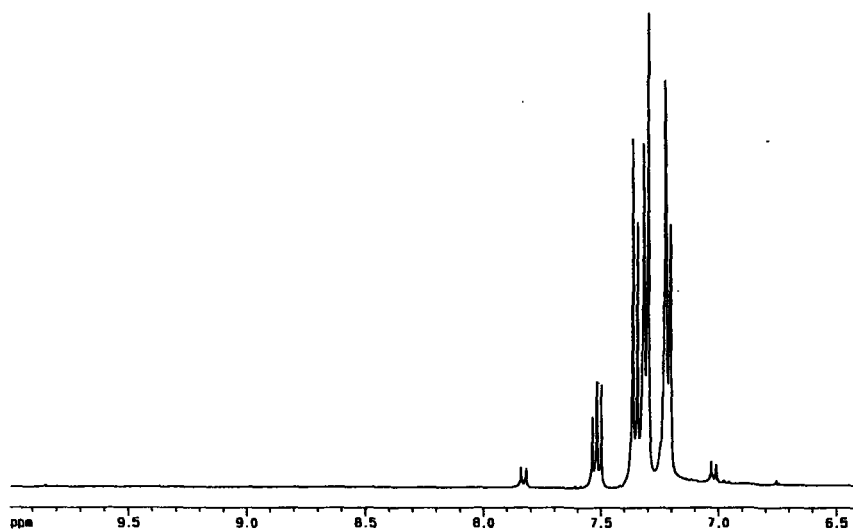


**Figure 3.12.** X-band EPR spectra of a frozen  $\text{CH}_2\text{Cl}_2$  solution sample of (a) intermediate species generated by the oxygenation of **2** at  $-78\text{ }^\circ\text{C}$ , (b)  $[\text{Fe}_2(\mu\text{-O}_2\text{CAr}^{\text{Tol}})_4(\text{BA}^{p\text{-OMe}})_2](\text{PF}_6)$ , measured at 5 K.

a)



b)

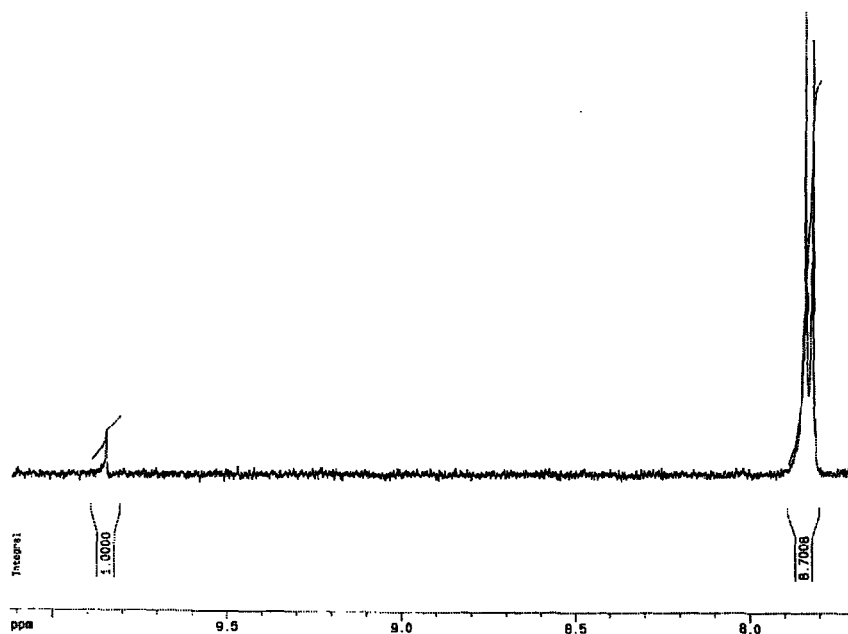


**Figure 3.13.** The oxygenation product distribution of  $[\text{Fe}_2(\mu\text{-O}_2\text{CAr}^{\text{Tol}})_4(\alpha\text{-}d_1\text{-BA}^{p\text{-OMe}})_2]$  (**4**) at  $-78\text{ }^\circ\text{C}$ . a) and b)  $^1\text{H}$  NMR spectrum: 9.85 ppm (s, 1H from anisaldehyde), 7.83 ppm (d, 2H from the combination of anisaldehyde and  $d_1$ -anisaldehyde).

## Chapter 4

**Synthesis and Characterization of  $\{\text{Fe}_2(\mu\text{-OH})_2(\mu\text{-O}_2\text{CR})\}^{3+}$  and  $\{\text{Fe}_2(\mu\text{-O})(\mu\text{-O}_2\text{CR})\}^{3+}$  Complexes with Carboxylate-Rich Metal Coordination Environment as Models for Diiron Centers in Oxygen-Dependent Non-Heme Enzymes\***

## Introduction

Carboxylate-bridged diiron clusters are frequently found among dioxygen-dependent non-heme enzymes, including the R2 subunit of ribonucleotide reductases (RNR-R2), soluble methane monooxygenase (sMMOH), and  $\Delta^9$  desaturase ( $\Delta^9$ D).<sup>1-5</sup> The diiron active sites within these enzymes include four carboxylates and two histidine ligands derived from the amino acid residues. This structural motif is effectively utilized to achieve diverse functions, such as the generation of a stable tyrosyl radical, methane oxidation, and the insertion of a 9,10 *cis*-double bond into a bound fatty acid. Subtle changes in the universal structure of the diiron core might have been necessary for these enzymes to accomplish their diverse physiological roles. One distinct difference occurs in the structure of the oxidized forms of the diiron center, which is  $\{\text{Fe}_2(\mu\text{-OH})_2(\mu\text{-O}_2\text{CR})\}^{3+}$  in sMMOH<sub>ox</sub><sup>6,7</sup> and  $\{\text{Fe}_2(\mu\text{-O})(\mu\text{-O}_2\text{CR})\}^{3+}$  in RNR-R2<sup>8</sup> (Chart 4.1). A ( $\mu$ -oxo)diiron(III) core has been proposed as the structure of the oxidized form of  $\Delta^9$ D, based on spectroscopic informations.<sup>9</sup> Changes in the bridging ligand at these diiron(III) sites are reflected not only in their functions but also in their spectroscopic and magnetic properties.<sup>1</sup>

To unravel the relationships among the structural, functional, and physical properties of diiron sites in these enzymes, small model complexes have been prepared and studied concurrently with direct investigations of the natural systems. For examples, a number of symmetric diiron complexes employing nitrogen and phenolic oxygen ligands have been reported as mimics for the asymmetric diiron sites in enzymes with carboxylate-rich metal coordination environment.<sup>10-12</sup> Studies of these complexes contributed to an initial understanding of the native enzymes. The model complexes with N-rich metal coordination environments, however, have limitations in

reproducing the structural and physical properties of diiron cores in enzymes having O-rich ligand sets. The synthesis of asymmetric model complexes with a carboxylate-rich coordination environment is required to elucidate the close relationship between structure and function or physical properties of diiron sites in this series of related enzymes.

The synthesis of complexes with  $\{\text{Fe}_2(\mu\text{-OH})_2(\mu\text{-O}_2\text{CR})\}^{3+}$  or  $\{\text{Fe}_2(\mu\text{-O})(\mu\text{-O}_2\text{CR})\}^{3+}$  cores in a carboxylate-rich coordination environment, however, is often challenging due to the propensity of iron(III) salts to form oligo- or polynuclear iron(III) complexes. Along with hydrolysis of ferric salts in the presence of a chelating ligand, a commonly used strategy to prepare diiron(III) model complexes is direct oxygenation of carboxylate-bridged diiron(II) complexes. This route mimics the oxidation process of the enzymes and results in the isolation of diiron(III) complexes with coordination geometries similar to those of the enzymes.<sup>1,13,14</sup> The first synthetic analogue of the  $\{\text{Fe}_2(\mu\text{-OH})_2(\mu\text{-O}_2\text{CR})\}^{3+}$  core of sMMOH<sub>ox</sub> was synthesized by direct oxygenation of the diiron(II) complex  $[\text{Fe}_2(\mu\text{-O}_2\text{CAr}^{\text{Tol}})_2(\text{O}_2\text{CAr}^{\text{Tol}})_2(\text{N},\text{N}\text{-Bn}_2\text{en})_2]$ , where  $\text{Ar}^{\text{Tol}}\text{CO}_2^-$  is 2,6-di(*p*-tolyl)benzoate and *N,N*-Bn<sub>2</sub>en is *N,N*-dibenzylethylenediamine.<sup>13,15</sup>

An alternative strategy is to decompose a carboxylate-bridged diiron(II) complex into its mononuclear components and, upon oxygenation, bimolecular combination can generate a diiron(III) product via a possible  $\text{Fe}_2(\text{O}_2)$  intermediate adduct (Scheme 4.1). In this chapter, we describe such an approach, namely, the synthesis of carboxylate-rich, asymmetric  $\{\text{Fe}_2(\mu\text{-OH})_2(\mu\text{-O}_2\text{CR})\}^{3+}$  and  $\{\text{Fe}_2(\mu\text{-O})(\mu\text{-O}_2\text{CR})\}^{3+}$  cores from direct oxygenation of mononuclear iron(II) complexes. Their physical properties, including electronic transitions, Mössbauer spectra, and magnetic data, have been characterized and are compared with those of the diiron sites of the related enzymes.

## Experimental Section

**General.** All reagents were obtained from commercial suppliers and used as received unless otherwise noted. Dichloromethane, pentane, THF, and toluene were saturated with argon and purified by passage through activated Al<sub>2</sub>O<sub>3</sub> columns under argon.<sup>16</sup> Dioxygen (99.994%, BOC Gases) was dried by passing the gas stream through Drierite. The compounds [Fe<sub>2</sub>(μ-O<sub>2</sub>CAr<sup>Tol</sup>)<sub>2</sub>(O<sub>2</sub>CAr<sup>Tol</sup>)<sub>2</sub>(THF)<sub>2</sub>] and [Fe<sub>2</sub>(μ-O<sub>2</sub>CAr<sup>4F-Ph</sup>)<sub>2</sub>(O<sub>2</sub>CAr<sup>4F-Ph</sup>)<sub>2</sub>(THF)<sub>2</sub>], where <sup>-</sup>O<sub>2</sub>CAr<sup>Tol</sup> is 2,6-di(*p*-tolyl)benzoate and <sup>-</sup>O<sub>2</sub>CAr<sup>4F-Ph</sup> is 2,6-di(*p*-fluorophenyl)benzoate, were prepared as described in the literature.<sup>14</sup> Air-sensitive manipulations were carried out under nitrogen in an MBraun glovebox. FT-IR spectra were recorded with a Thermo Nicolet Avatar 360 spectrometer. UV-vis spectra were recorded on a Hewlett-Packard 8453 diode array spectrophotometer.

[Fe(O<sub>2</sub>CAr<sup>Tol</sup>)<sub>2</sub>(Hdmpz)<sub>2</sub>] (**1**). To a rapidly stirring light yellow CH<sub>2</sub>Cl<sub>2</sub> (6 mL) solution of [Fe<sub>2</sub>(μ-O<sub>2</sub>CAr<sup>Tol</sup>)<sub>2</sub>(O<sub>2</sub>CAr<sup>Tol</sup>)<sub>2</sub>(THF)<sub>2</sub>] (92 mg, 0.062 mmol) was added Hdmpz (23 mg, 4.0 equiv) to afford a light yellow homogeneous solution. After 2 h of stirring, the solution was filtered through Celite and reduced to 3 mL under reduced pressure. Light violet block crystals of **1** were isolated in 91 % yield upon vapor diffusion of pentane into the solution. The structure was determined by X-ray crystallography. FT-IR (KBr, cm<sup>-1</sup>) 3356(w, br), 3050 (w), 3022 (w), 2919 (w), 2862 (w), 1618 (w), 1612 (w), 1585 (s), 1577 (s), 1571 (s), 1560 (s), 1542 (s), 1514 (s), 1405 (w), 1384 (m), 811 (s), 789 (s), 705 (s), 585 (w), 524 (m). Anal. Calcd. for C<sub>52</sub>H<sub>50</sub>FeN<sub>4</sub>O<sub>4</sub>: C, 73.41; H, 5.92; N, 6.58. Found: C, 73.88; H, 6.14; N, 6.59.

[Fe(O<sub>2</sub>CAr<sup>4F-Ph</sup>)<sub>2</sub>(Hdmpz)<sub>2</sub>] (**2**). This compound was prepared as described above for **1** (yield 85 %) using [Fe<sub>2</sub>(μ-O<sub>2</sub>CAr<sup>4F-Ph</sup>)<sub>2</sub>(O<sub>2</sub>CAr<sup>4F-Ph</sup>)<sub>2</sub>(THF)<sub>2</sub>] as the precursor. The

structure was determined by X-ray crystallography. FT-IR (KBr,  $\text{cm}^{-1}$ ) 3200 (w, br), 3041 (w), 2928 (w), 2863 (w), 1599 (s), 1562 (s), 1511 (s), 1475 (m), 1454 (m), 1403 (w), 1370 (m), 1288 (w), 1216 (s), 1158 (m), 1096 (w), 1037 (m), 1014 (w), 845 (s), 815 (s), 791 (s), 772 (m), 740 (w), 718 (w), 706 (s), 598 (w), 584 (w), 555 (m), 531 (m), 469 (w), 421 (w). Anal. Calcd. for  $\text{C}_{48}\text{H}_{38}\text{F}_4\text{FeN}_4\text{O}_4$ : C, 66.52; H, 4.42; N, 6.46. Found: C, 66.06; H, 4.32; N, 6.74.

**$[\text{Fe}_2(\mu\text{-OH})_2(\mu\text{-O}_2\text{CAr}^{\text{Tol}})(\text{O}_2\text{CAr}^{\text{Tol}})_3(\text{OH}_2)(\text{Hdmpz})_2]$  (3).** A colorless toluene (10 mL) solution of **1** (15 mg, 0.017 mmol) was saturated with dry dioxygen by bubbling over a period of 10 min, resulting in a golden yellow solution. The solvent was evaporated under reduced pressure and the resulting yellow powder was dissolved in 3 mL of  $\text{CH}_2\text{Cl}_2$ . The solution was filtered through Celite and pentane was diffused into it. Yellow needle crystals of **3** (11 mg, 70 %) were obtained after several days and analyzed by X-ray crystallography. FT-IR (KBr,  $\text{cm}^{-1}$ ) 3572 (w, br), 3386 (w), 3283 (w, br), 3053 (w), 3023 (w), 2920 (w), 2864 (w), 1609 (m), 1574 (s), 1539 (s), 1515 (s), 1542 (s), 1408 (m), 1348 (w), 1305 (m), 1145 (w), 1110 (w), 1070 (w), 1045 (w), 818 (s), 800 (s), 785 (s), 765 (m), 714 (m), 699 (m), 585 (m), 543 (m), 522 (m). Anal. Calcd. for  $\text{C}_{94}\text{H}_{88}\text{Fe}_2\text{N}_4\text{O}_{11}$ : C, 72.31; H, 5.68; N, 3.59. Found: C, 71.81; H, 5.52; N, 3.55.

**$[\text{Fe}_2(\mu\text{-O})(\mu\text{-O}_2\text{CAr}^{\text{AF-Ph}})(\text{O}_2\text{CAr}^{\text{AF-Ph}})_3(\text{Hdmpz})_3](\text{CH}_2\text{Cl}_2)$  (4).** A colorless toluene (20 mL) solution of **2** (126 mg, 0.145 mmol) was saturated with dry dioxygen by bubbling over a period of 10 min. The yellow brown solution was filtered through Celite and the volatile portion evaporated under reduced pressure. The brown powder was dissolved in 3 mL of  $\text{CH}_2\text{Cl}_2$  and pentane was diffused into it. Brown block crystals of **4** (98.3 mg, 78 %) were obtained overnight and analyzed by X-ray crystallography. FT-IR (KBr,  $\text{cm}^{-1}$ ) 3369 (w), 3206 (w), 2929 (w), 1607 (w), 1574 (w), 1539 (m), 1511 (s), 1452 (m), 1411 (m), 1375 (m), 1281 (w), 1223 (s), 1159 (m), 1043 (w), 865 (w), 833 (m), 817

(m), 771 (w), 712 (m), 701 (w), 555 (w), 531 (w). Anal. Calcd. For  $C_{92}H_{70}Cl_2F_8Fe_2N_6O_9$ : C, 63.57; H, 4.06; N, 4.83. Found: C, 63.45; H, 4.27; N, 4.87.

**Physical Measurements.** Mössbauer spectra were obtained on an MS1 spectrometer (WEB Research Co.) with a  $^{57}Co$  source in a Rh matrix maintained at room temperature in the Massachusetts Institute of Technology Department of Chemistry Instrument Facility (MIT DCIF). Solid samples were prepared by suspending ca 30 mg, 25 mg and 80 mg of the powdered material **2**, **3** and **4**, respectively, in Apeizon N grease and packing the mixture into a nylon sample holder. Data were collected at 4.2 K and the isomer shift ( $\delta$ ) values are reported with respect to natural iron foil that was used for velocity calibration at room temperature. The spectra were fit to Lorentzian lines by using the WMOSS plot and fit program.<sup>17</sup>

Magnetic susceptibility data for powdered solid were measured between 5 and 300 K with applied magnetic fields of 0.1 T using a Quantum design MPMS SQUID susceptometer. The sample was embedded in a gel capsule using the parafilm and suspended in a plastic straw. The susceptibilities of the straw and gel capsule with parafilm were independently determined over the same temperature range and field for correction of their contribution to the total measured susceptibility. Underlying diamagnetism of the sample was calculated from Pascal's constants.<sup>18</sup> The molar magnetic susceptibility data were fit to the expression derived from the general isotropic exchange Hamiltonian,  $H = -2JS_1 \cdot S_2$ , where  $S_1 = S_2 = 5/2$ . This expression is given in eq 1, where  $x = J/kT$  and  $p$  is the mole fraction of a paramagnetic impurity with  $S = 5/2$ . The uncertainties in spin Hamiltonian parameters are derived from the results of fitting data collected from two independently prepared samples.



$$\chi_M = \frac{Ng^2\mu_B^2}{kT} \frac{2e^{2x} + 10e^{6x} + 28e^{12x} + 60e^{20x} + 110e^{30x}}{1 + 3e^{2x} + 5e^{6x} + 7e^{12x} + 9e^{20x} + 11e^{30x}} + 4.4p/T \quad (1)$$

**X-ray Crystallographic Studies.** Intensity data were collected on a Bruker (formerly Siemens) CCD diffractometer with graphite-monochromatized Mo K $\alpha$  radiation ( $\lambda = 0.71073 \text{ \AA}$ ), controlled by a Pentium-based PC running the SMART software package. Single crystals were mounted at room temperature on the tips of quartz fibers, coated with Paratone-N oil, and cooled under a stream of cold nitrogen maintained by a Bruker LT-2A nitrogen cryostat. Data collection and reduction protocols are described elsewhere.<sup>19</sup> The structures were solved by both direct and Patterson methods and refined on  $F^2$  by using the SHELXTL software package.<sup>20</sup> Empirical absorption corrections were applied with SADABS<sup>21</sup>, part of the SHELXTL program package, and the structures were checked for higher symmetry by the program PLATON.<sup>22</sup> All non-hydrogen atoms were refined anisotropically. In general, hydrogen atoms were assigned idealized positions and given thermal parameters equivalent to either 1.5 (methyl hydrogen atoms) or 1.2 (all other hydrogen atoms) times the thermal parameter of the carbon atom to which they were attached. Hydrogen atoms of N–H of Hdmpz, O–H of bridging hydroxides, and water molecule were assigned using difference Fourier electronic density maps. Hydrogen atoms of disordered CH<sub>2</sub>Cl<sub>2</sub> molecules were not included in the refinement. In the structure of **1**, one CH<sub>2</sub>Cl<sub>2</sub> solvent molecule was assigned in the lattice. The structure of **3** contains 3.25 CH<sub>2</sub>Cl<sub>2</sub> molecules that were distributed over four positions at occupancies of 0.75, 0.75, 0.75, and 1.00. In the structure of **4**, one Hdmpz ligand coordinated to Fe2 is disordered over two positions. They were split over two conformations with 0.5 occupancy factors.

One lattice  $\text{CH}_2\text{Cl}_2$  molecule was found in compound **4** in two positions with 0.5 occupancy factors.

## Results and Discussion

**Rationale for the synthetic approach.** The observation of a green peroxodiiron(III) species during the oxygenation of  $[\text{Fe}(\text{O}_2\text{CR})\{\text{HB}(\text{pz}')_3\}]$ ,  $\text{pz}' = 3,5$ -bis(isopropyl)pyrazoyl, provided an early validation of the strategy for bimolecular combination of mononuclear iron(II) complexes to generate a diiron(III) product by oxygenation.<sup>23,24</sup> Upon warming to ambient temperature, however, the structural integrity of the spectroscopically characterized,  $[\text{Fe}_2(\mu\text{-O}_2)(\text{O}_2\text{CR})_2\{\text{HB}(\text{pz}')_3\}_2]$  complex was lost, resulting in a trinuclear iron(III) product. This example suggested to us that oxygenation of mononuclear iron(II) complexes would be a good route to di( $\mu$ -hydroxo)diiron(III) species if ligand framework were able to stabilize the dinuclear entity.

Previous work in our group demonstrated that *m*-terphenyl-based carboxylates can provide such a framework. Diiron(II) complexes were synthesized using bulky carboxylates, and  $\{\text{Fe}_2(\mu\text{-OH})_2(\mu\text{-O}_2\text{CR})_{n=1,2}\}$  species were isolated from oxygenation of these diiron(II) precursors.<sup>13,14</sup> Mononuclear iron complexes with these sterically bulky carboxylates have also been previously synthesized. The mononuclear iron(II) precursors to assemble interesting diiron(III) complexes upon oxygenation, however, had not been reported yet.

**Synthesis.** The reaction of  $[\text{Fe}_2(\mu\text{-O}_2\text{CAr}^{\text{Tol}})_2(\text{O}_2\text{CAr}^{\text{Tol}})_2(\text{THF})_2]$ , where  $\text{O}_2\text{CAr}^{\text{Tol}}$  is 2,6-di(*p*-tolyl)benzoate, with 4 equiv of Hdmpz quantitatively yielded the mononuclear iron(II) compound **1** (Scheme 4.2). Oxygenation of a solution of **1** afforded crystalline **3**,

containing the  $\{\text{Fe}_2(\mu\text{-OH})_2(\mu\text{-O}_2\text{CR})\}^{3+}$  core. Compound **2**, the analogue of **1**, was prepared using  $[\text{Fe}_2(\mu\text{-O}_2\text{CAR}^{4\text{F-Ph}})_2(\text{O}_2\text{CAR}^{4\text{F-Ph}})_2(\text{THF})_2]$  ( $\text{O}_2\text{CAR}^{4\text{F-Ph}} = 2,6\text{-di}(p\text{-fluorophenyl})\text{benzoate}$ ). A colorless toluene solution of **2** reacts with dioxygen, resulting in a green brown solution. Compound **4**, which has a  $\{\text{Fe}_2(\mu\text{-O})(\mu\text{-O}_2\text{CR})\}^{3+}$  core, was exclusively isolated as a final oxygenation product.

**Description of the Structures.** A summary of crystal parameters and refinement results is given in Table 4.1, and selected interatomic distances and angles are summarized in Table 4.2, and 4.3. Compounds **3** and **4** crystallize as a racemic mixture of enantiomers.

$[\text{Fe}(\text{O}_2\text{CAR}^{\text{Tol}})_2(\text{Hdmpz})_2]$  (**1**). An ORTEP diagram of the X-ray structure, shown in Figure 4.1, depicts a pseudo-tetrahedral iron(II) center bound to two carboxylates, each in monodentate fashion with Fe–O distances of 1.9559(16) and 1.9569(16) Å (Table 4.2). Other coordination sites are occupied by two Hdmpz ligands with Fe–N distances of 2.042(2) and 2.057(2) Å. The comparatively short Fe-to-ligand distances are a consequence from the low coordination number of the Fe atom. The L–Fe–L angles are distributed around 109.46° with the largest deviation being 7.29°. Two hydrogen bonding interactions are observed between the  $\text{Ar}^{\text{Tol}}\text{CO}_2^-$  and Hdmpz ligands, the O···H–N distances being 2.743 and 2.783 Å. A space filling model conveys the steric wall imposed by two  $\text{Ar}^{\text{Tol}}\text{CO}_2^-$  and two Hdmpz ligands. The combined influence of the sterically hindered carboxylate ligands and the intramolecular hydrogen-bonding interactions changes the binding mode of the carboxylate ligands from monodentate to bidentate and stabilizes **1** with the low coordination number of 4.

$[\text{Fe}(\text{O}_2\text{CAR}^{4\text{F-Ph}})_2(\text{Hdmpz})_2]$  (**2**). Compound **2** is isostructural with **1** (Figure 4.2). The less acidic and less sterically hindered nature of  $\text{HO}_2\text{CAR}^{4\text{F-Ph}}$  ligand, compared with

HO<sub>2</sub>CAr<sup>Tol</sup>, does not appear to affect the structure. Although **2** is less soluble than **1** in toluene and THF solvents.

[Fe<sub>2</sub>(μ-OH)<sub>2</sub>(μ-O<sub>2</sub>CAr<sup>Tol</sup>)(O<sub>2</sub>CAr<sup>Tol</sup>)<sub>3</sub>(OH<sub>2</sub>)(Hdmpz)<sub>2</sub>] (**3**). The structure of **3** is depicted in Figure 4.3. The two iron atoms are pseudo-octahedral unit bridged by one carboxylate and two hydroxo groups. The Fe1–O1–Fe2 unit has Fe2–O1 and Fe1–O(2) distances of 1.958(5) and 1.944(5) Å, respectively, and a 100.3(3)° bridging angle. The Fe–O bond lengths in the Fe1–O2–Fe2 unit are longer, but the angle is sharper, the separation values having 2.012(5) and 1.953(5) Å, and 98.1(2)° for the bridging angle. The torsion angle is 153.2°, for Fe1–O1–Fe2–O2, reflecting that the Fe<sub>2</sub>(OH)<sub>2</sub> ring is bent upward, away from the bridging carboxylate. The Fe⋯Fe distance is 2.996(2) Å, similar to those of previously reported bis(μ-hydroxo)(μ-carboxylato)diiron(III) cores. Values of 2.9788(6) and 2.99–3.14 Å were reported for the [Fe<sub>2</sub>(μ-OH)<sub>2</sub>(μ-O<sub>2</sub>CAr<sup>Tol</sup>)(O<sub>2</sub>CAr<sup>Tol</sup>)<sub>3</sub>(Bn<sub>2</sub>en)(Bnen)] model complex<sup>15</sup> and the diiron cores in MMOH<sub>ox</sub><sup>6,7</sup> respectively.

In addition to the bridging ligands, the coordination sites of Fe1 include one monodentate carboxylate and two Hdmpz ligands, completing a N<sub>2</sub>O<sub>4</sub> donor set. The other site, Fe2, is octahedral with a O<sub>6</sub> set, completed by two monodentate carboxylates and one water molecule. The largest deviations from ideal 90° interbond angles are 12.5(2)° and 13.6(2)° for Fe1 and Fe2, respectively, and occur at the O–Fe–O angle of the bent four-membered Fe<sub>2</sub>(μ-OH)<sub>2</sub> ring. Two hydrogen bonding interactions occur between the carboxylate and bridging hydroxo groups, with O(1)⋯O(8) and O(2)⋯O(6) interatomic distances of 2.768(2) and 2.898(3) Å, respectively. The carboxylate and water molecule coordinated to Fe2 generate a hydrogen-bonding interaction at a distance of the 2.662(3) Å between O(10)⋯O(11). The combined effect of sterically hindered

carboxylates and three hydrogen bonding interactions stabilizes the diiron(III) core, allowing its isolation and characterization.

The closest intermetallic distance between diiron in the crystal lattice is 13.776 Å. The large separation suggests that there are no significant interactions between  $[\text{Fe}_2(\mu\text{-OH})_2(\mu\text{-O}_2\text{CAr}^{\text{Tol}})(\text{O}_2\text{CAr}^{\text{Tol}})_3(\text{OH}_2)(\text{Hdmpz})_2]$  molecules in the lattice, and the major magnetic coupling interaction originates from intramolecular exchange coupling between two iron(III) sites (see Magnetism section).

$[\text{Fe}_2(\mu\text{-O})(\mu\text{-O}_2\text{CAR}^{\text{AF-Ph}})(\text{O}_2\text{CAR}^{\text{AF-Ph}})_3(\text{Hdmpz})_3]$  (**4**). The structure of **4** is depicted in Figure 4.4. The two iron atoms have a distorted octahedral geometry and are linked by one carboxylate and one oxo group. The Fe1–O(1) and Fe2–O(1) distances, composing the bridging connection of Fe1–O(1)–Fe2, are 1.7882(2) and 1.771(2) Å, respectively. The Fe1–O1–Fe2 angle of 139.85(12)° is larger than those in  $[\text{Fe}_2(\mu\text{-O})(\mu\text{-HCO}_2)(\text{N-MeIm})_8]^{3+}$  (131.3(2)°)<sup>25</sup> and  $[\text{Fe}_2(\mu\text{-O})(\mu\text{-HCO}_2)(\text{TPA})_2]^{3+}$  (128.6(3)°)<sup>8</sup>, for which the Fe–O distances are *ca* 1.78 Å, a value almost identical to those observed in **4**. Because of the larger angle, the Fe···Fe distance in **4** (3.3425(8) Å) is longer than those of  $[\text{Fe}_2(\mu\text{-O})(\mu\text{-HCO}_2)(\text{N-MeIm})_8]^{3+}$  (3.285(5) Å)<sup>25</sup> and of  $[\text{Fe}_2(\mu\text{-O})(\mu\text{-HCO}_2)(\text{TPA})_2]^{3+}$  (3.231(5) Å)<sup>8</sup>. Interestingly, the Fe···Fe separation of 3.4 Å in the (μ-oxo)(μ-carboxylato)diiron(III) core of RNR-R2 is close to that of **4**.

The coordination sites of Fe1 are occupied by one monodentate carboxylate and two Hdmpz ligands, while those of Fe2 are completed with two carboxylates (one monodentate and one chelating) and one Hdmpz ligand. The bond lengths and angles in **4** fall within the typical range of those observed in published (μ-oxo)diiron(III) complexes. The closest intermetallic distance in the lattice is between Fe1 and Fe2 is 12.992 Å.

The N–H groups of the Hdmpz ligands generate hydrogen bonding interactions with either the carboxylate ligands or the bridging oxo group. Three hydrogen bonding interactions were identified, O(1)⋯H–N(4), O(6)⋯H–N(2), and O(9)⋯H–N(6) with O⋯N distances of 2.743, 2.783, and 2.888 Å, respectively. One interesting feature is that the O1⋯H–N4 hydrogen bonding interaction generates a five membered Fe1–N–N–H⋯O(oxo) ring which is similar to the five membered Fe–O–O–H⋯O(oxo) ring plane in oxyhemerythrin (Chart 4.2).<sup>4,26</sup> It has been proposed that the Fe–O(oxo) strength decreases as a result of this hydrogen bonding interaction and reduces the magnetic exchange coupling interaction ( $J = -77 \text{ cm}^{-1}$ ) in oxyhemerythrin, compared to methemerythrin ( $J = -134 \text{ cm}^{-1}$ ).<sup>27,28</sup> However, the hydrogen bond interaction of O1⋯H–N4 in compound **4** perturbed neither the Fe1–O1–Fe2 angle nor the Fe1–O1 distance compared to the range typical of those found in ( $\mu$ -oxo)( $\mu$ -carboxylato)diiron(III) complexes. Consistent with these structural features, the magnetic exchange coupling interaction for oxo-bridged diiron(III) center in **4** is not unusual (see Magnetism section). Our results these suggest that the reported exchange coupling in oxyHr is worthy of a re-examination.

**Electronic Absorption Spectral Properties.** No UV-vis transition, as expected for a complex with two bridging hydroxide ligands, was observed for a CH<sub>2</sub>Cl<sub>2</sub> solution of **3** (Figure 4.5). The electronic absorption properties are changed by converting to a ( $\mu$ -oxo) moiety. The optical spectrum of **4** in CH<sub>2</sub>Cl<sub>2</sub> has bands at 470 (sh,  $\epsilon = 900 \text{ M}^{-1}\text{cm}^{-1}$ ) and 580 ( $\epsilon = 400 \text{ M}^{-1}\text{cm}^{-1}$ ) nm, which are characteristic for ( $\mu$ -oxo)diiron(III) complexes. These transitions were also observed in the oxidized form of RNR-R2, at 500 ( $\epsilon = 800 \text{ M}^{-1}\text{cm}^{-1}$ ) and 600 ( $\epsilon = 300 \text{ M}^{-1}\text{cm}^{-1}$ ) nm.<sup>29</sup>

**Mössbauer Spectroscopy.** The  $^{57}\text{Fe}$  Mössbauer spectrum, measured at 4.2 K, consists of a single quadrupole doublet of compound **2** (Figure 4.6). The resulting parameters are shown in Table 4.4. The Mössbauer spectra of both **3** and **4** consist of a single quadrupole doublet (Figure 4.7). Although the two iron(III) sites differ in both cases, there is no evidence for two overlapping doublets in either spectrum. The line widths are reasonably close to natural line widths indicating that the two iron(III) atoms in **3** and **4** are indistinguishable by Mössbauer spectroscopy.

Compound **3** with the  $\{\text{Fe}_2(\mu\text{-OH})_2(\mu\text{-O}_2\text{CR})\}^{3+}$  core exhibits a quadrupole doublet with  $\delta = 0.45(2)$  mm/s and  $\Delta E_Q = 1.21(2)$  mm/s at 4.2 K. The isomer shift falls in the range of the high-spin Fe(III) complexes.<sup>1,30</sup> The significantly different  $\Delta E_Q$  values obtained for **3** and the structurally related  $[\text{Fe}_2(\mu\text{-OH})_2(\mu\text{-O}_2\text{CAR}^{\text{Tol}})(\text{O}_2\text{CAR}^{\text{Tol}})_3(\text{Bn}_2\text{en})(\text{Bnen})]$  complex ( $\Delta E_Q = 0.61(2)$  mm/s) are somewhat unexpected due to the similar octahedral coordination geometry around the iron(III) sites.<sup>15</sup> Notably, compound **3** has a more O-rich coordination environment than  $[\text{Fe}_2(\mu\text{-OH})_2(\mu\text{-O}_2\text{CAR}^{\text{Tol}})(\text{O}_2\text{CAR}^{\text{Tol}})_3(\text{Bn}_2\text{en})(\text{Bnen})]$ , with a  $\text{H}_2\text{O}$  (O-donor) ligand instead of the Bnen (N-donor) ligand. It is quite interesting that the  $\{\text{Fe}_2(\mu\text{-OH})_2(\mu\text{-O}_2\text{CR})\}^{3+}$  core in sMMOH<sub>ox</sub> which also has one water molecule, displays the similar  $\Delta E_Q$  values (0.87 and 1.16 mm/s).<sup>31</sup> The O-rich metal coordination environment may result in the similar  $\Delta E_Q$  ( $\sim 1$  mm/s) values both for compound **3** and the diiron sites of sMMOH<sub>ox</sub>.

Compound **4**, with the  $\{\text{Fe}_2(\mu\text{-O})(\mu\text{-O}_2\text{CR})\}^{3+}$  core, has  $\delta = 0.51(2)$  mm/s indicating a high-spin diiron(III) site. The small  $\Delta E_Q$  value (1.256(2) mm/s) is at the lower end of the range ( $> 1$  mm/s) found for most oxo-bridged diiron(III) complexes.<sup>1</sup> The value is close to that measured for **3**, indicating a similar electronic field gradient at the iron(III) nuclei. Deprotonation of the hydroxo-bridge may be accompanied by a decrease in the

Fe–O distance in the crystal structure of **4**. The coordination environment perturbed by the presence of an oxo bridge may be compensated by a carboxylate shift of the monodentate carboxylate, which results in similar electronic field gradient to compound **3**.

**Magnetism.** Variable-temperature magnetic susceptibility plots for **3** and **4** are depicted in Figures 4.8 and Figure 4.9, respectively. The effective magnetic moment of **3** at 300 K is  $7.4 \mu_B$ , which is lower than the calculated value of  $8.37 \mu_B$  for a high spin diiron(III) center with  $g = 2.0$ . Upon lowering the temperature, the magnetic moment decreases to  $0.01 \mu_B$  at 5 K. The best fit was obtained with  $J = -7.2(2) \text{ cm}^{-1}$  and  $g = 2.0$  (fixed), implying a weak antiferromagnetic exchange coupling interaction in di( $\mu$ -hydroxo)diiron centers. This result is the first measured spin exchange integral for a  $\{\text{Fe}_2(\mu\text{-OH})_2(\mu\text{-O}_2\text{CR})\}^{3+}$  core in any small molecule complex. The observed  $J$  values for the diiron(III) sites of  $\text{sMMOH}_{\text{ox}}$  and **3** are identical, consistent with the observed close similarity in the structure and Mössbauer spectrum.<sup>31</sup>

The effective magnetic moment of **4** at 300 K is  $4.3 \mu_B$ , indicating a stronger antiferromagnetic exchange interaction at the diiron(III) site even at high temperature. The best fit was obtained with  $J = -117.2(1) \text{ cm}^{-1}$ , with  $g = 2.0$  (fixed), which in the range of values ( $J = -90 - -120 \text{ cm}^{-1}$ ) reported for ( $\mu$ -oxo)( $\mu$ -carboxylate)diiron(III) complexes.<sup>10</sup> The effect of hydrogen bonding between the N–H group of Hdmpz and bridging oxo group (Chart 4.2) does not significantly perturb exchange interactions in the ground states of ( $\mu$ -oxo)( $\mu$ -carboxylate)diiron(III) molecules.



**Summary.**

Utilizing hydrogen bonding interaction and sterically bulky carboxylates, synthetic routes were developed to prepare mononuclear iron(II) complexes with vacant coordination sites for O<sub>2</sub> binding. Reaction of such compounds with O<sub>2</sub> resulted in rare asymmetric complexes having the {Fe<sub>2</sub>(μ-O)(μ-O<sub>2</sub>CR)}<sup>3+</sup> and {Fe<sub>2</sub>(μ-OH)<sub>2</sub>(μ-O<sub>2</sub>CR)}<sup>3+</sup> units. These diiron(III) complexes mimic the carboxylate-rich metal coordination environments of metal cores housed in four-helix bundles in nature. Interestingly, compound **3** which replicates the {Fe<sub>2</sub>(μ-OH)<sub>2</sub>(μ-O<sub>2</sub>CR)} core of sMMOH<sub>ov</sub>, shares several physical properties including electronic transitions, Mössbauer spectra, and magnetic properties with the enzyme. On the other hand, the structure of **4**, which can be defined as a (μ-oxo)(μ-carboxylato)diiron(III) species, mimics the diiron(III) site of RNR-R2. The electronic transitions and Mössbauer spectra of **4** are typical of such diiron(III) complexes having an Fe-O-Fe moiety. The magnetic exchange coupling interaction in **4** is within the expected range for oxo-bridged diiron(III) sites. These results demonstrate how the diiron(III) structures in different metalloproteins, namely, the μ-oxo cores of RNR-R2 and Δ9D the di(μ-hydroxo) unit in MMOH and ToMOH can be accessed by the appropriate differences in ligand compositions

**References**

- (1) Kurtz, Jr., D. M. *Chem. Rev.* **1990**, *90*, 585-606.
- (2) Feig, A. L.; Bautista, M. T.; Lippard, S. J. *Inorg. Chem.* **1996**, *35*, 6892-6898.
- (3) Wallar, B. J.; Lipscomb, J. D. *Chem. Rev.* **1996**, *96*, 2625-2657.
- (4) Solomon, E. I.; Brunold, T. C.; Davis, M. I.; Kemsley, J. N.; Lee, S.-K.; Lehnert, N.; Neese, F.; Skulan, A. J.; Yang, Y.-S.; Zhou, J. *Chem. Rev.* **2000**, *100*, 235-349.
- (5) Merckx, M.; Kopp, D. A.; Sazinsky, M. H.; Blazyk, J. L.; Müller, J.; Lippard, S. J. *Angew. Chem., Int. Ed.* **2001**, *40*, 2782-2807.
- (6) Elango, N.; Radhakrishnan, R.; Froland, W. A.; Wallar, B. J.; Earhart, C. A.; Lipscomb, J. D.; Ohlendorf, D. H. *Protein Sci* **1997**, *6*, 556-568.
- (7) Whittington, D. A.; Lippard, S. J. *J. Am. Chem. Soc.* **2001**, *123*, 827-838.
- (8) Norman, R. E.; Leising, R. A.; Yan, S.; Que, L., Jr. *Inorg. Chim. Acta* **1998**, *273*, 393-396.
- (9) Fox, B. G.; Shanklin, J.; Ai, J.; Loehr, T. M.; Sanders-Loehr, J. *Biochemistry* **1994**, *33*, 12776-12786.
- (10) Hartman, J. R.; Rardin, R. L.; Chaudhuri, P.; Pohl, K.; Wieghardt, K.; Nuber, B.; Weiss, J.; Papaefthymiou, G. C.; Frankel, R. B.; Lippard, S. J. *J. Am. Chem. Soc.* **1987**, *109*, 7387-7396.
- (11) Holz, R. C.; Elgren, T. E.; Pearce, L. L.; Zhang, J. H.; O'Connor, C. J.; Que, L., Jr. *Inorg. Chem.* **1993**, *32*, 5844-5850.
- (12) Dong, Y.; Ménage, S.; Brennan, B. A.; Elgren, T. E.; Jang, H. G.; Pearce, L. L.; Que, L., Jr. *J. Am. Chem. Soc.* **1993**, *115*, 1851-1859.
- (13) Lee, D.; Lippard, S. J. *Inorg. Chem.* **2002**, *41*, 827-837.
- (14) Lee, D.; Lippard, S. J. *Inorg. Chem.* **2002**, *41*, 2704-2719.
- (15) Lee, D.; Lippard, S. J. *J. Am. Chem. Soc.* **2001**, *123*, 4611-4612.

- (16) Pangborn, A. B.; Giardello, M. A.; Grubbs, R. H.; Rosen, R. K.; Timmers, F. J. *Organometallics* **1996**, 1518-1520.
- (17) Kent, T. A.; v2.5 ed.: Minneapolis, 1998.
- (18) Carlin, R. L. *Magnetochemistry*; Springer-Verlag: New York, 1986.
- (19) Kuzelka, J.; Mukhopadhyay, S.; Spingler, B.; Lippard, S. J. *Inorg. Chem.* **2004**, 43, 1751-1761.
- (20) Sheldrick, G. M.; University of Göttingen: Göttingen, Germany, 1997.
- (21) Sheldrick, G. M.; University of Göttingen: Göttingen, Germany, 1996.
- (22) Spek, A. L.; Utrecht University: Utrecht, The Netherlands, 1998.
- (23) Kitajima, N.; Fukui, H.; Moro-oka, Y. *J. Am. Chem. Soc.* **1990**, 112, 6402-6403.
- (24) Kitajima, N.; Tamura, N.; Amagai, H.; Fukui, H.; Moro-oka, Y.; Mizutani, Y.; Kitagawa, T.; Mathur, R.; Heerwegh, K.; Reed, C. A.; Randall, C. R.; Que, L., Jr.; Tatsumi, K. *J. Am. Chem. Soc.* **1994**, 116, 9071-9085.
- (25) Colby, J.; Stirling, D. I.; Dalton, H. *Biochem. J.* **1977**, 165, 395-402.
- (26) Brunold, T. C.; Solomon, E. I. *J. Am. Chem. Soc.* **1999**, 121, 8277-8287.
- (27) Dawson, J. W.; Gray, H. B.; Hoenig, H. E.; Rossman, G. R.; Schredder, J. M.; Wang, R.-H. *Biochemistry* **1972**, 11, 461-465.
- (28) Shiemke, A. K.; Loehr, T. M.; Sanders-Loehr, J. *J. Am. Chem. Soc.* **1986**, 108, 2437-2443.
- (29) J., J. B.; Edmondson, D. E.; Huynh, B. H.; Filley, J.; Norton, J. R.; Stebbe, J. *Science* **1991**, 253, 292-298.
- (30) Liu, T.; Lovell, T.; Han, W.-G.; Noodleman, L. *Inorg. Chem.* **2003**, 42, 5244-5251.
- (31) Fox, B. G.; Hendrich, M. P.; Surerus, K. K.; Andersson, K. K.; Froland, W. A.; Lipscomb, J. D.; Münck, E. *J. Am. Chem. Soc.* **1993**, 115, 3688-3701.

**Table 4.1.** Summary of X-ray Crystallographic Data for Compounds  $[\text{Fe}(\text{O}_2\text{CAr}^{\text{Iol}})_2(\text{Hdmpz})_2]$  (1),  $[\text{Fe}(\text{O}_2\text{CAr}^{4\text{F-Ph}})_2(\text{Hdmpz})_2]$  (2),  $[\text{Fe}_2(\mu\text{-OH})_2(\mu\text{-O}_2\text{CAr}^{\text{Iol}})(\text{O}_2\text{CAr}^{\text{Iol}})_3(\text{OH}_2)(\text{Hdmpz})_2]$  (3), and  $[\text{Fe}_2(\mu\text{-O})(\mu\text{-O}_2\text{CAr}^{4\text{F-Ph}})(\text{O}_2\text{CAr}^{4\text{F-Ph}})_3(\text{Hdmpz})_3]$  (4).

Compound	1·0.5(CH <sub>2</sub> Cl <sub>2</sub> )	2	3·3.25(CH <sub>2</sub> Cl <sub>2</sub> )	4·(CH <sub>2</sub> Cl <sub>2</sub> )
Empirical Formula	C <sub>52.50</sub> H <sub>51</sub> ClFeN <sub>4</sub> O <sub>4</sub>	C <sub>48</sub> H <sub>38</sub> F <sub>4</sub> FeN <sub>4</sub> O <sub>4</sub>	C <sub>97.25</sub> H <sub>94.5</sub> Cl <sub>6.5</sub> Fe <sub>2</sub> N <sub>4</sub> O <sub>11</sub>	C <sub>92</sub> H <sub>70</sub> Cl <sub>2</sub> F <sub>8</sub> Fe <sub>2</sub> N <sub>6</sub> O <sub>9</sub>
Weight	893.27	866.67	1837.39	1738.14
Color	pale violet block	pale violet block	yellow needle	brown block
T, K	203(2)	203(2)	173(2)	173(2)
space group	P2 <sub>1</sub> /c	P $\bar{1}$	P2 <sub>1</sub> /n	P $\bar{1}$
a, Å	11.306(3)	11.0012(16)	15.385(9)	13.920(2)
b, Å	10.404(3)	13.702(2)	28.695(17)	15.434(2)
c, Å	39.541(10)	15.552(2)	21.194(12)	19.559(3)
$\alpha$ , deg		68.884(2)		88.767(2)
$\beta$ , deg	93.282(5)	88.421(2)	91.151(12)	88.313(2)
$\gamma$ , deg		77.728(2)		84.813(2)
V, Å <sup>3</sup>	4643(2)	2133.9(6)	9355(9)	4182.3(11)
Z	4	2	4	2
$\rho$ (calcd), g cm <sup>-3</sup>	1.278	1.349	1.305	1.380
abs coeff, mm <sup>-1</sup>	0.432	0.420	0.556	0.491
R1, <sup>a</sup> %	5.39	3.60	9.36	6.61
wR2, <sup>b</sup> %	12.71	9.82	22.79	20.76

$$^a \text{R1} = \Sigma ||F_o| - |F_c|| / \Sigma |F_o|, \quad ^b \text{wR2} = \{\Sigma [w(F_o^2 - F_c^2)^2] / \Sigma [w(F_o^2)]\}^{1/2}$$

**Table 4.2.** Selected Interatomic Distances (Å) and Angles (deg) for [Fe(O<sub>2</sub>CAr<sup>Tol</sup>)<sub>2</sub>(Hdmpz)<sub>2</sub>] (1) and [Fe(O<sub>2</sub>CAr<sup>4F-Ph</sup>)<sub>2</sub>(Hdmpz)<sub>2</sub>] (2).

	1·0.5(CH <sub>2</sub> Cl <sub>2</sub> )	2
Fe – N1	2.042(2)	2.0907(14)
Fe – N3	2.057(2)	2.0578(14)
Fe – O1	1.9560(16)	1.9968(11)
Fe – O3	1.9570(16)	1.9691(11)
N1 – Fe – N3	103.05(8)	108.41(6)
N1 – Fe – O1	104.33(8)	99.99(5)
N1 – Fe – O3	116.75(8)	116.55(5)
N3 – Fe – O1	113.54(7)	110.18(5)
N3 – Fe – O3	108.89(7)	104.91(5)
O1 – Fe – O3	110.22(7)	116.67(5)
N2 ... O4	2.783(3)	2.711(2)
N4 ... O2	2.743(3)	2.8019(19)

<sup>a</sup> Number in parentheses are estimated standard deviations of the last significant figure. Atoms are labeled as indicated in Figures 4.1 and 4.2.

**Table 4.3.** Selected Interatomic Distances (Å) and Angles (deg) for  $[\text{Fe}_2(\mu\text{-OH})_2(\mu\text{-O}_2\text{CAr}^{\text{Tol}})(\text{O}_2\text{CAr}^{\text{Tol}})_3(\text{OH}_2)(\text{Hdmpz})_2]$  (3) and  $[\text{Fe}_2(\mu\text{-O})(\mu\text{-O}_2\text{CAr}^{4\text{F-Ph}})(\text{O}_2\text{CAr}^{4\text{F-Ph}})_3(\text{Hdmpz})_3]$  (4).

	3·3.25(CH <sub>2</sub> Cl <sub>2</sub> )		4·(CH <sub>2</sub> Cl <sub>2</sub> )
Fe1 ... Fe2	2.996(2)	Fe1 ... Fe2	3.3425(8)
Fe1 – O(1)	1.953(5)	Fe1 – O(1)	1.772(3)
Fe1 – O(2)	1.958(5)	Fe1 – O(2)	2.062(2)
Fe1 – O(3)	2.073(5)	Fe1 – O(4)	2.067(2)
Fe1 – O(5)	1.980(5)	Fe1 – O(5)	2.295(3)
Fe1 – N(1)	2.139(6)	Fe1 – N(1)	2.135(3)
Fe1 – N(3)	2.106(6)	Fe1 – N(3)	2.087(3)
Fe2 – O(1)	1.944(5)	Fe2 – O(1)	1.786(3)
Fe2 – O(2)	2.012(4)	Fe2 – O(3)	2.117(2)
Fe2 – O(4)	2.027(4)	Fe2 – O(6)	2.068(2)
Fe2 – O(7)	1.986(4)	Fe2 – O(7)	2.309(3)
Fe2 – O(9)	2.059(4)	Fe2 – O(8)	2.017(2)
Fe2 – O(11)	2.016(6)	Fe2 – N(5)	2.076(3)
Fe1–O(1)–Fe2	100.3(3)	Fe1–O1–Fe2	139.94(14)
Fe1–O(2)–Fe2	98.1(2)		

<sup>a</sup> Number in parentheses are estimated standard deviations of the last significant figure. Atoms are labeled as indicated in Figures 4.3 and 4.4.

**Table 4.4.** Summary of Pertinent Spectroscopic Data for **3**, **4**, sMMOH<sub>ox</sub> and RNR-R2

	<b>3</b>	sMMOH <sub>ox</sub> (OB3b)		sMMOH <sub>ox</sub> (Bath)		<b>4</b>	RNR-R2 <sub>act</sub>	
Optical								
$\lambda_{max}$ nm		282				470(sh,900)	500 (800),	
( $\epsilon$ , M <sup>-1</sup> cm <sup>-1</sup> )						580 (400)	600 (300)	
Mössbauer		Fe1	Fe2	Fe1	Fe2		Fe1	Fe2
$\delta$ , mm s <sup>-1</sup>	0.454 (2)	0.51	0.50	0.51	0.50	0.508(2)	0.53	0.44
$\Delta E_Q$ , mm s <sup>-1</sup>	1.206 (2)	1.16	0.87	1.16	0.87	1.256(2)	1.66	2.45
$\Gamma_{L,R}$ , mm s <sup>-1</sup>	0.357 (2)					0.303(2)		
Magnetics								
$J$ , cm <sup>-1</sup>	-7.2 (2)	-7 ± 3				-117.4 (1)	-110	
$g$ (fixed)	2.0					2.0		
Reference	This work	31				This work		

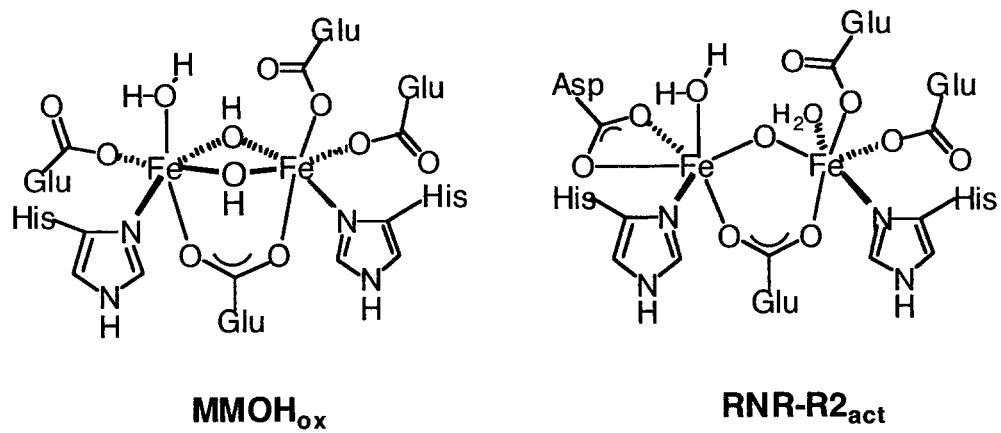


Chart 4.1.



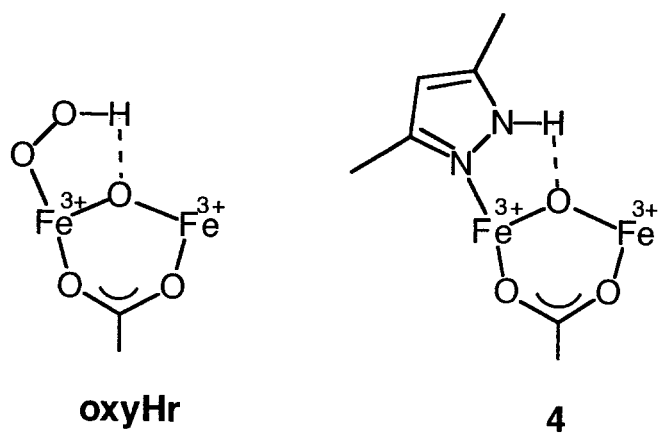
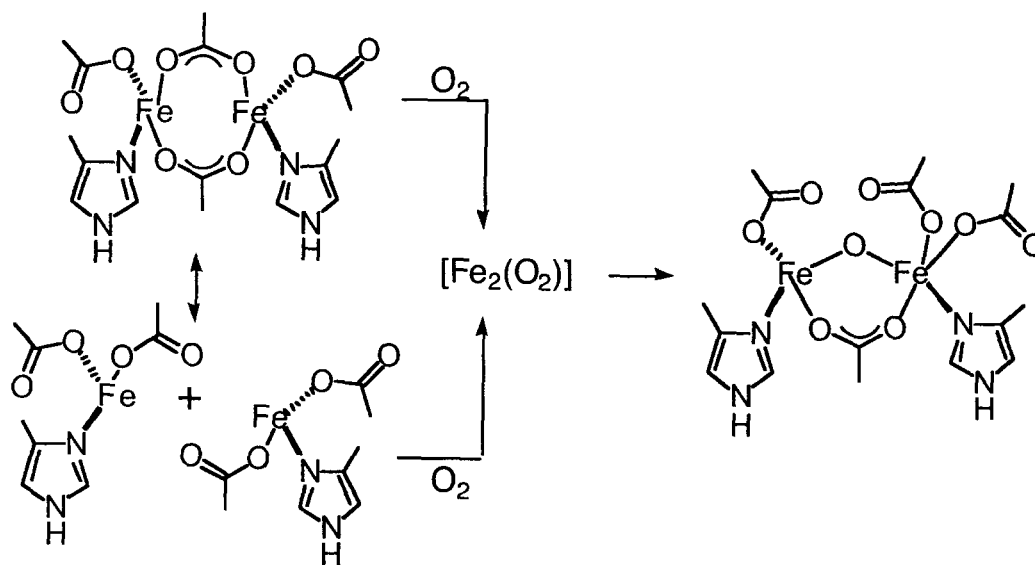
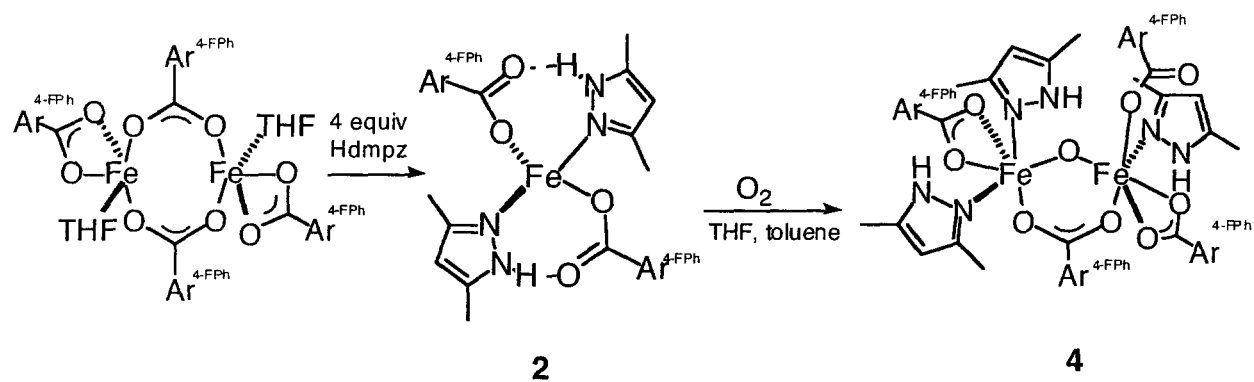
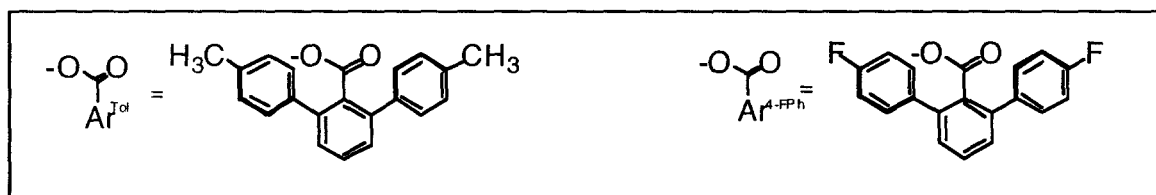
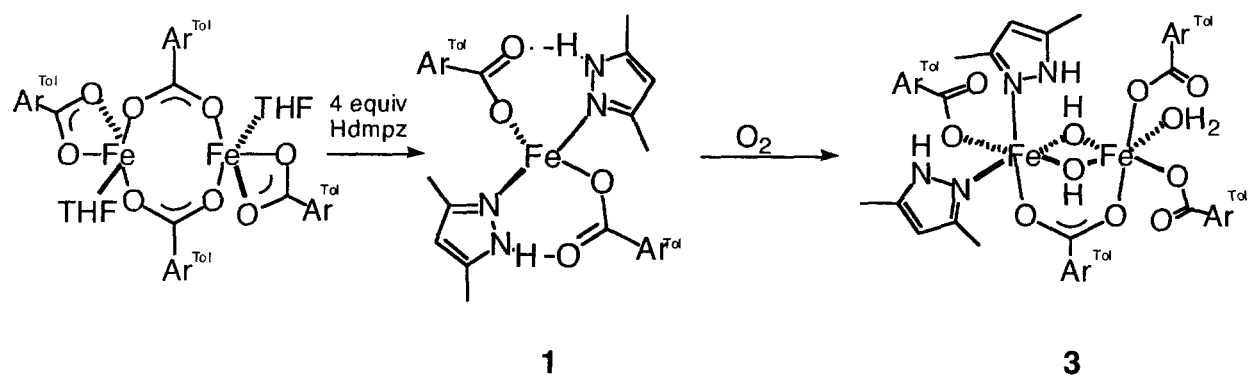


Chart 4.2.



Scheme 4.1.



Scheme 4.2.

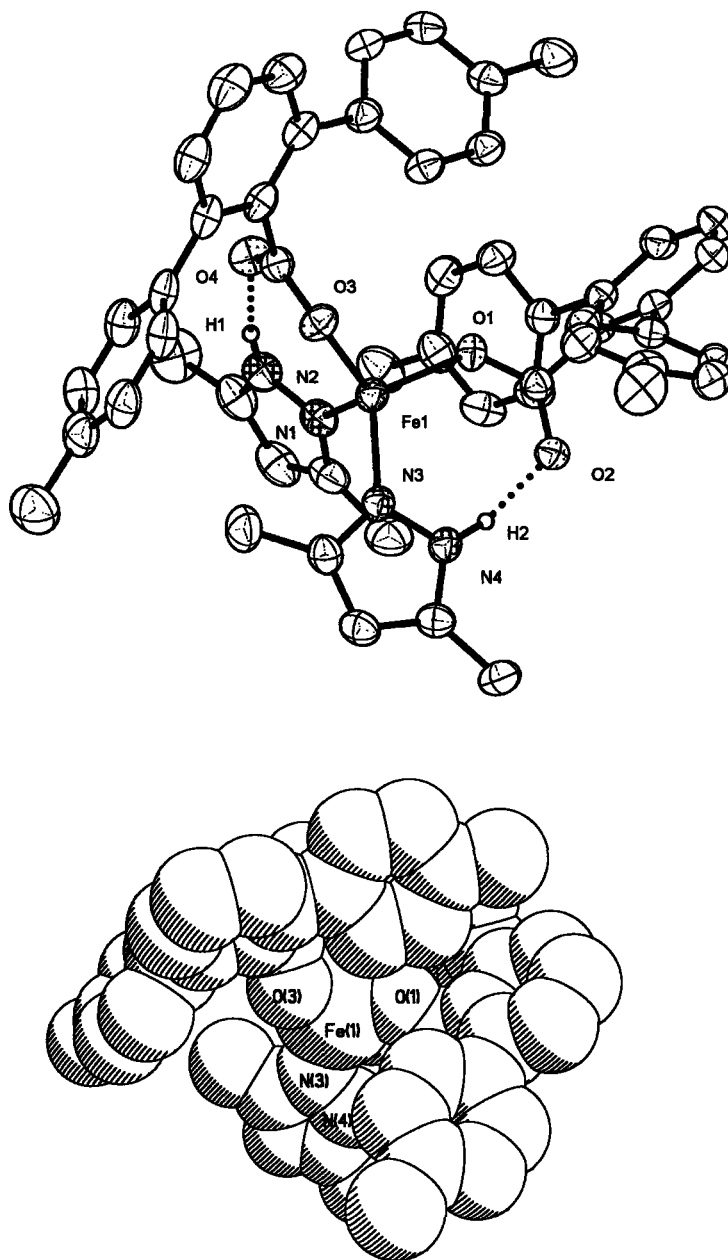


**Figure 4.1.** Top: ORTEP diagram of  $[\text{Fe}(\text{O}_2\text{CAr}^{\text{Tol}})_2(\text{Hdmpz})_2]$  (**1**) showing 50% probability thermal ellipsoids for all non-hydrogen atoms. The hydrogen atoms of the N–H group of the Hdmpz ligands are added to show the hydrogen bonding interaction. Bottom: Space-filling representation of **1**.

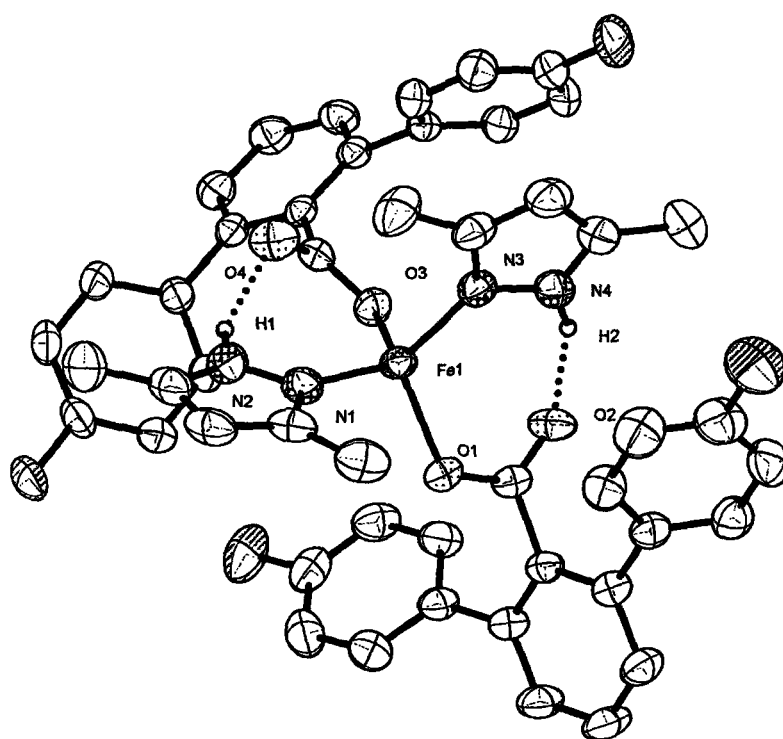


**Figure 4.2.** ORTEP diagram of  $[\text{Fe}(\text{O}_2\text{CAr}^{4\text{F-Ph}})_2(\text{Hdmpz})_2]$  (**2**) showing 50% probability thermal ellipsoids for all non-hydrogen atoms. The hydrogen atoms in the N-H group of Hdmpz ligands are added to show hydrogen bonding interactions.

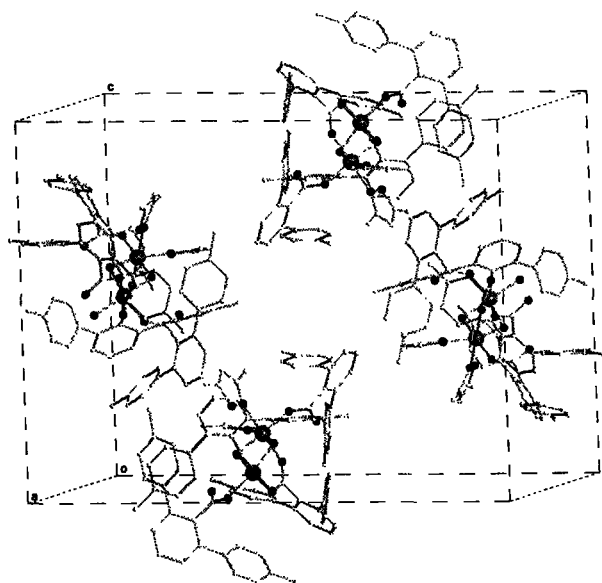
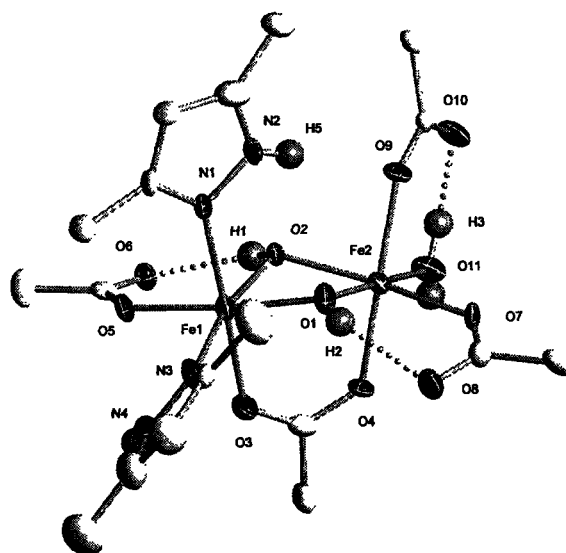


**Figure 4.3.** Top: ORTEP diagram of  $[\text{Fe}_2(\mu\text{-OH})_2(\mu\text{-O}_2\text{CAr}^{\text{Tol}})(\text{O}_2\text{CAr}^{\text{Tol}})_3(\text{OH}_2)(\text{Hdmpz})_2]$  (**3**) showing 50% probability thermal ellipsoids for all non-hydrogen atoms. The hydrogen atoms in the N–H group of Hdmpz, the bridging O–H group, and water ligands are included. The aromatic rings of  $\text{Ar}^{\text{Tol}}\text{CO}_2^-$  ligands are omitted for clarity. Bottom: Crystal packing diagram of **3**.

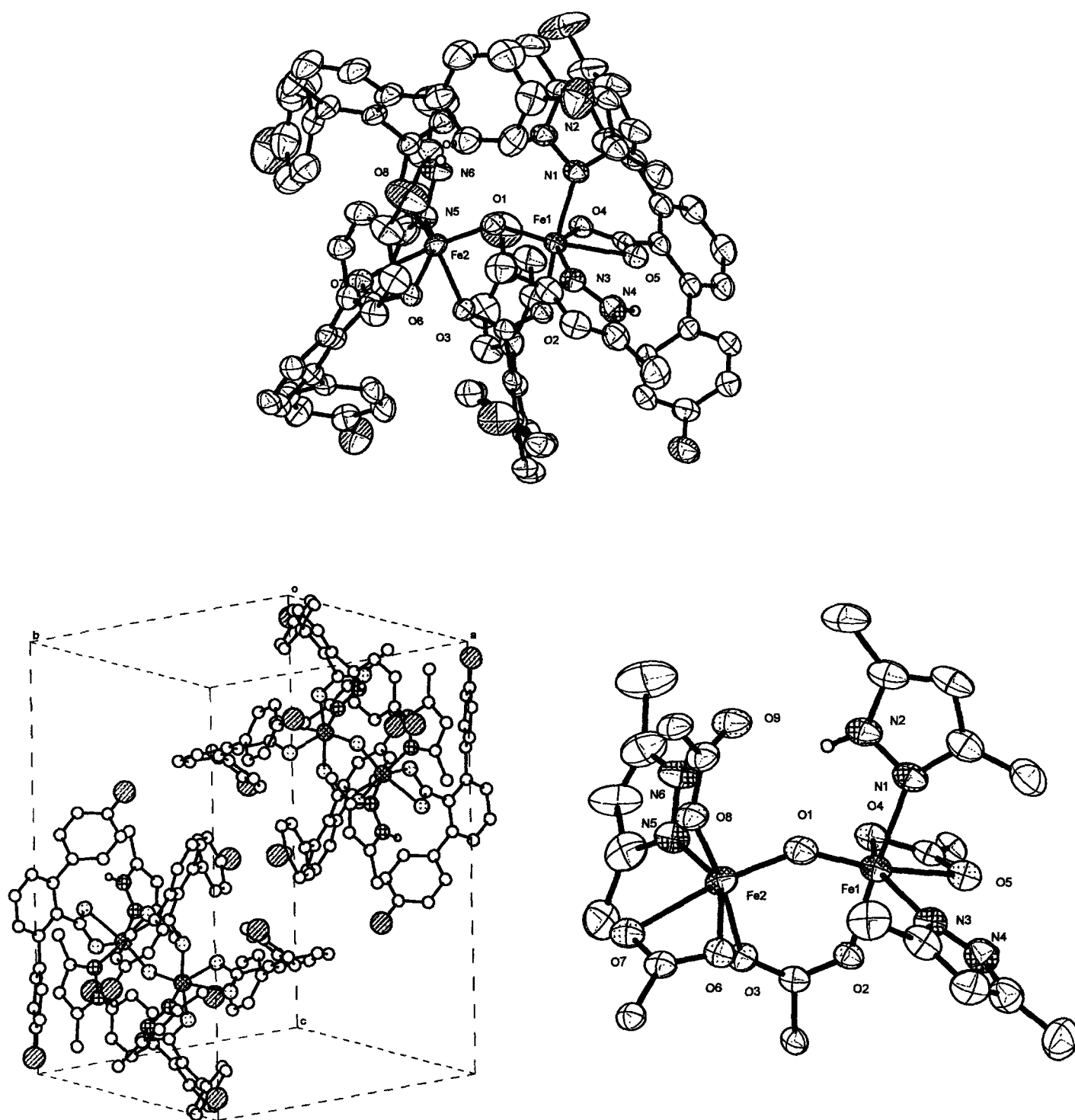


**Figure 4.4.** Top: ORTEP diagrams of  $[\text{Fe}_2(\mu\text{-O})(\mu\text{-O}_2\text{CAR}^{4\text{F-Ph}})(\text{O}_2\text{CAR}^{4\text{F-Ph}})_3(\text{Hdmpz})_3]$  (**4**) showing 50 % probability thermal ellipsoids for all non-hydrogen atoms. The hydrogen atoms in the N–H group of Hdmpz ligands are added. Bottom: The phenyl rings of  $\text{Ar}^{4\text{-FPh}}\text{CO}_2^-$  ligands are omitted for clarity. Bottom left: Crystal packing diagram of **4**.

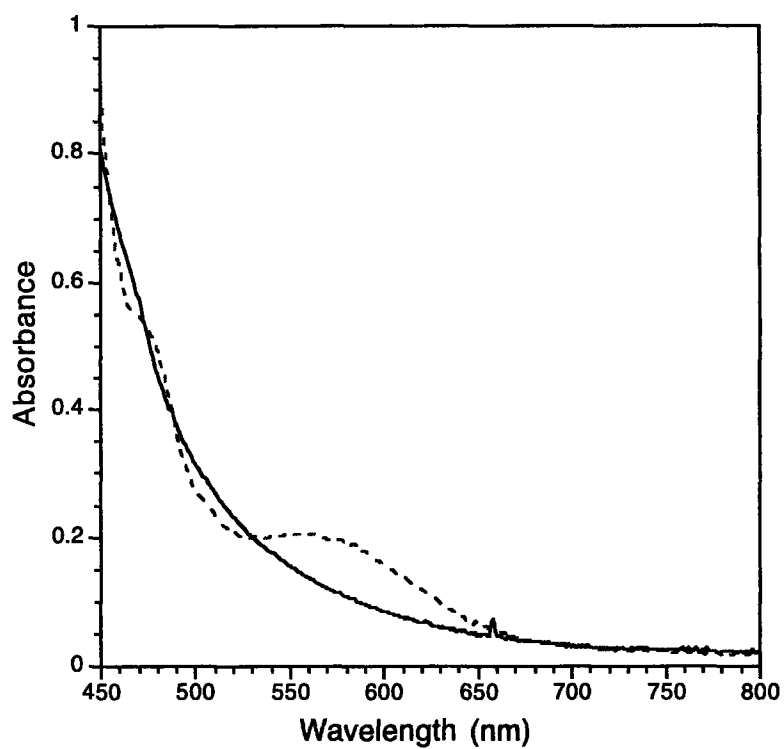


**Figure 4.5.** UV-vis spectra of  $[\text{Fe}_2(\mu\text{-OH})_2(\mu\text{-O}_2\text{CAr}^{\text{Tol}})(\text{O}_2\text{CAr}^{\text{Tol}})_3(\text{OH}_2)(\text{Hdmpz})_2]$  (**3**) (solid line) and  $[\text{Fe}_2(\mu\text{-O})(\mu\text{-O}_2\text{CAr}^{\text{4F-Ph}})(\text{O}_2\text{CAr}^{\text{4F-Ph}})_3(\text{Hdmpz})_3]$  (**4**) (dashed line) in  $\text{CH}_2\text{Cl}_2$ .



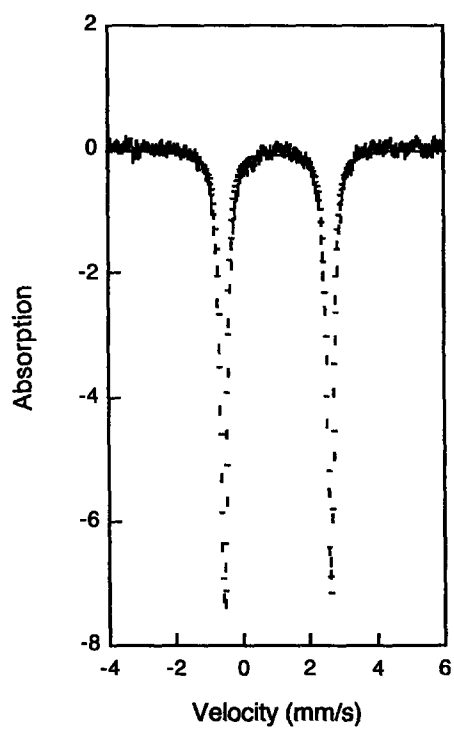


**Figure 4.6.** Mössbauer spectrum (experimental data (1), calculated fit (-)) recorded at 4.2 K for a solid sample of  $[\text{Fe}(\text{O}_2\text{CAr}^{4\text{F-Ph}})_2(\text{Hdmpz})_2]$  (2).

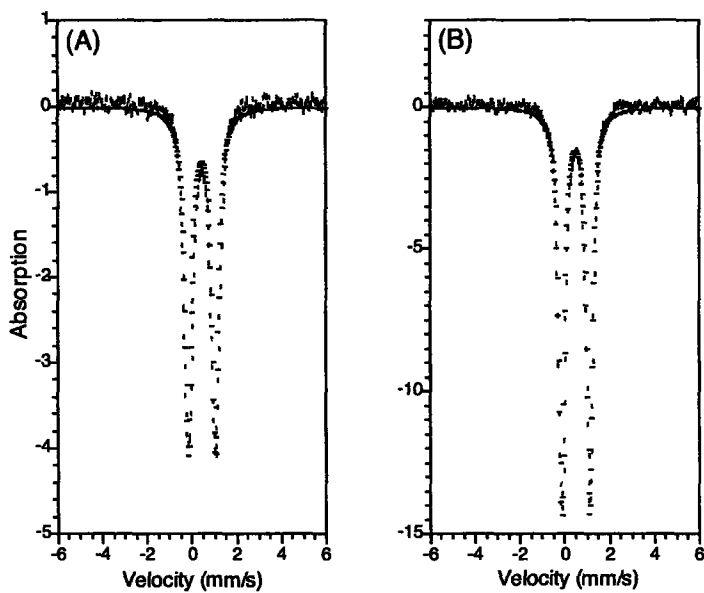


**Figure 4.7.** Mössbauer spectra (experimental data (|), calculated fit (—)) recorded at 4.2 K for a solid sample of  $[\text{Fe}_2(\mu\text{-OH})_2(\mu\text{-O}_2\text{CAr}^{\text{Toi}})(\text{O}_2\text{CAr}^{\text{Toi}})_3(\text{OH}_2)(\text{Hdmpz})_2]$  (3) (A) and  $[\text{Fe}_2(\mu\text{-O})(\mu\text{-O}_2\text{CAr}^{4\text{-FPH}})(\text{O}_2\text{CAr}^{4\text{-FPH}})_3(\text{Hdmpz})_3]$  (4) (B).

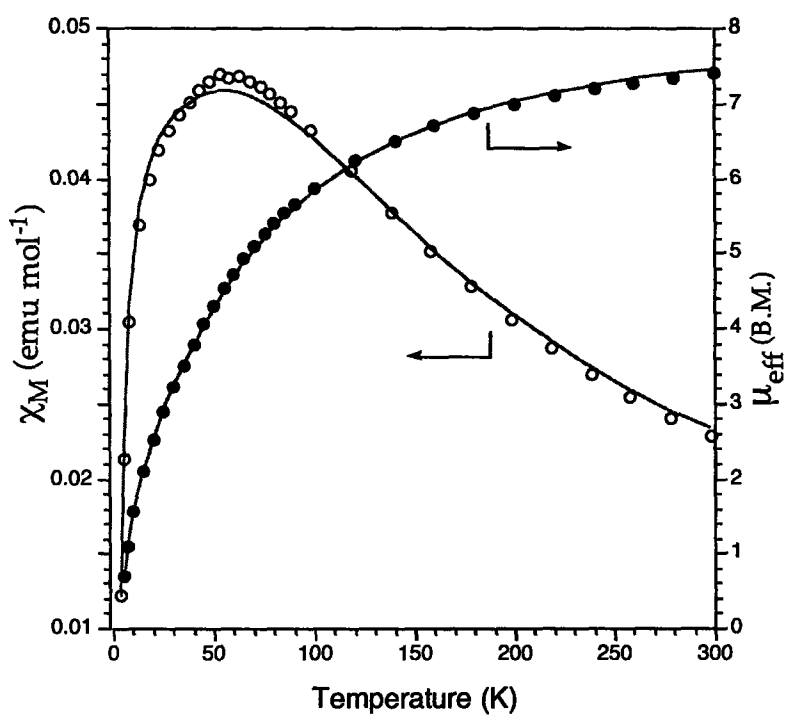


**Figure 4.8.** Plots of  $\chi_M$  (o) and  $\mu_{\text{eff}}$  (•) vs  $T$  for solid 3. The solid lines represents the best least-squares fit of eq 1 (see text) to the experimental susceptibility data.

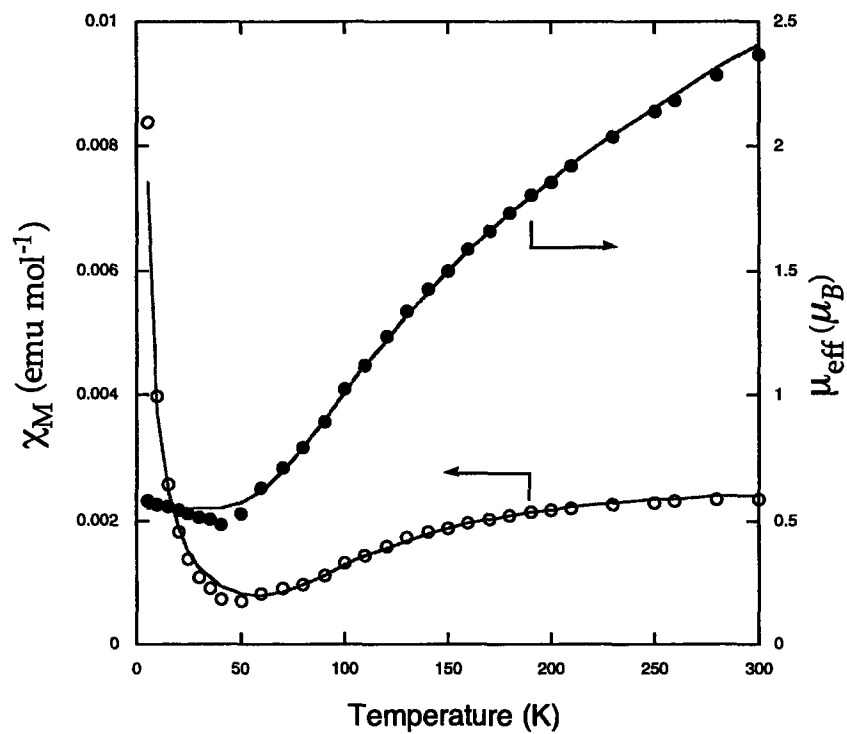


**Figure 4.9.** Plots of  $\chi_M$  (o) and  $\mu_{\text{eff}}$  (•) vs  $T$  for solid 4. The solid lines represents the best least-squares fit of eq 1 (see text) to the experimental susceptibility data.

## **Chapter 5**

# **Synthesis and Characterization of Dinuclear Iron Complexes Having Proton Donors in the Ligand Framework**

## Introduction

The R2 subunit of ribonucleotide reductase (RNR-R2),<sup>1,2</sup>  $\Delta$ 9-desaturase,<sup>3</sup> and the hydroxylase components of soluble methane monooxygenase (sMMOH)<sup>4</sup> and toluene monooxygenase (ToMOH)<sup>5</sup> are examples of well-known dioxygen-dependent non-heme enzymes. Despite their diverse biological functions, however, a common structural motif is shared between these enzymes. In their reduced states, they all have four carboxylates and two imidazoles as the endogenous ligands derived from amino acid side chains (Chart 5.1). A universal mechanism for oxygenation of these diiron sites, involving (peroxo)diiron(III) intermediates and high-valent oxo species, is proposed due to their close structural similarity. The reactivity of such generated high-valent oxo species toward substrate varies accordingly to their required physiological roles. The high-valent intermediate in sMMOH hydroxylates methane to methanol, whereas that in RNR-R2 generates a tyrosyl radical. Subtle variations, including the existence of water in the first and second coordination sphere of the diiron sites, the binding mode of carboxylates, and the different amino acid side chains arranged outside the diiron core, contribute to the differences in reactivity. Proton donors in the proximity of diiron sites may influence the conversion of intermediates and modify their characteristics. Such proton donors could be water or amino acid side chain residues.

The first deliberate efforts to position such proton donors in proximity to the diiron(II) sites in model complexes are described here. We employed pyrazole derivatives for this purpose. The hydrogen-bonding interaction between pyrazole and sterically hindered *m*-terphenyl-derived benzoate analogues directs of the N-H group in proximity to the diiron center.

## Experimental Section

**General Considerations.** All reagents, including pyrazole (pz) and 3,5-dimethyl pyrazole (Hdmpz), were obtained from commercial suppliers and used as received unless otherwise noted. Dichloromethane, pentane, ethylether (OEt<sub>2</sub>) and toluene were saturated with argon and purified by passage through activated Al<sub>2</sub>O<sub>3</sub> columns under argon.<sup>6</sup> The precursor complex [Fe<sub>2</sub>(μ-O<sub>2</sub>CAr<sup>Tol</sup>)<sub>2</sub>(O<sub>2</sub>CAr<sup>Tol</sup>)<sub>2</sub>(THF)<sub>2</sub>] was prepared as described in the literature.<sup>7,8</sup> All syntheses and air-sensitive manipulations were carried out under nitrogen in an MBraun glovebox. FT-IR spectra were recorded with a Thermo Nicolet Avatar 360 spectrometer or Perkin Elmer FTIR model 2000.

[Fe<sub>2</sub>(μ-O<sub>2</sub>CAr<sup>Tol</sup>)<sub>4</sub>(pz)<sub>2</sub>] (1) and [Fe<sub>2</sub>(μ-O<sub>2</sub>CAr<sup>Tol</sup>)<sub>2</sub>(O<sub>2</sub>CAr<sup>Tol</sup>)<sub>2</sub>(pz)<sub>2</sub>] (2). To a rapidly stirred light yellow CH<sub>2</sub>Cl<sub>2</sub> (3 mL) solution of [Fe<sub>2</sub>(μ-O<sub>2</sub>CAr<sup>Tol</sup>)<sub>2</sub>(O<sub>2</sub>CAr<sup>Tol</sup>)<sub>2</sub>(THF)<sub>2</sub>] (39 mg, 0.027 mmol) was added pz (3.6 mg, 2 equiv) to afford a gray-yellow homogeneous solution. After 2 h stirring, the solution was divided into equal parts into which pentane or OEt<sub>2</sub> was diffused. Colorless block crystals of 1 were separated from the CH<sub>2</sub>Cl<sub>2</sub>/diethylether solution. Light yellow block crystals of 2 precipitated from the CH<sub>2</sub>Cl<sub>2</sub>/pentane solution. They were both analyzed by X-ray crystallography. The yields were 75 % for 1 and 52% for 2. FT-IR (KBr, cm<sup>-1</sup>) for 1 3360 (m, br), 3048 (w), 3022 (w), 2918 (m), 2860 (w), 1616 (s), 1585 (s), 1575 (s), 1571 (s), 1550 (s), 1513 (s), 1439 (s), 1405 (s), 1385 (s), 1131 (w), 1109 (w), 1055 (m), 1044 (m), 843 (s), 813 (s), 789 (s), 753 (s), 705 (m), 584 (m), 524 (s). Anal. Calcd. For C<sub>90</sub>H<sub>76</sub>Fe<sub>2</sub>N<sub>4</sub>O<sub>8</sub>: C, 74.38; H, 5.27; N, 3.86. Found: C, 74.09; H, 5.12; N, 3.79.

FT-IR (KBr, cm<sup>-1</sup>) for 2 3378 (m), 3134 (w), 3119 (w), 3022 (w), 2915 (w), 1604 (s), 1556 (s), 1514 (s), 1456 (s), 1409 (s), 1379 (s), 1353 (m), 1126 (w), 1111 (w), 1058 (m), 1045 (m), 856 (m), 847 (w), 816 (m), 801 (m), 785 (m), 772 (m), 736 (m), 712 (m), 698 (m), 686 (m), 593 (w), 585 (w), 544 (w), 541 (w), 521 (m). Anal. Calcd. For C<sub>90</sub>H<sub>76</sub>Fe<sub>2</sub>N<sub>4</sub>O<sub>8</sub>: C, 74.38; H, 5.27; N, 3.86. Found: C, 74.78; H, 5.14; N, 4.12.

**[Fe<sub>2</sub>(μ-O<sub>2</sub>CAr<sup>Tol</sup>)<sub>2</sub>(O<sub>2</sub>CAr<sup>Tol</sup>)<sub>2</sub>(Hdmpz)<sub>2</sub>] (3).** A 5 mL CH<sub>2</sub>Cl<sub>2</sub> solution of Hdmpz (33.4 mg, 2 equiv) was added dropwise to a stirred light yellow CH<sub>2</sub>Cl<sub>2</sub> solution (15 mL) of [Fe<sub>2</sub>(μ-O<sub>2</sub>CAr<sup>Tol</sup>)<sub>2</sub>(O<sub>2</sub>CAr<sup>Tol</sup>)<sub>2</sub>(THF)<sub>2</sub>] (260 mg, 0.178 mmol). After stirring overnight, the solution was concentrated under reduced pressure and the resulting light yellow powder was dissolved in 5 mL of benzene. Pentane diffusion afforded colorless block crystals that were analyzed by X-ray crystallography. Yield, 71 %. FT-IR (KBr, cm<sup>-1</sup>) 3332 (w, br), 3053 (w), 3024 (w), 2920 (w), 2861 (w), 2562 (s), 1513 (s), 1454 (s), 1408 (m), 1381 (s), 1305 (w), 1186 (w), 1146 (w), 1109 (w), 1069 (w), 1045 (w), 1021 (w), 851 (m), 817 (m), 800 (s), 785 (m), 765 (m), 737 (w), 711 (w), 651 (w), 584 (w), 542 (w), 521 (w), 462 (w). Anal. Calcd. For C<sub>94</sub>H<sub>84</sub>Fe<sub>2</sub>N<sub>4</sub>O<sub>8</sub>: C, 74.80; H, 5.61; N, 3.71. Found: C, 74.61; H, 5.81; N, 3.80.

**[Fe<sub>2</sub>(μ-O)(O<sub>2</sub>CAr<sup>Tol</sup>)<sub>4</sub>(Hdmpz)<sub>2</sub>] (4).** A toluene (5 mL) solution of 3 (63.9 mg, mmol) was purged with dioxygen for 10 min, generating a brownish yellow solution. After 1 h, anhydrous pentane was diffused into the solution, affording red brown block crystals that were analyzed by X-ray crystallography. Yield, 81 %. FT-IR (KBr, cm<sup>-1</sup>) 3298 (w), 3130 (w), 3026 (w), 2920 (m), 2868 (w), 1623 (m), 1578 (m), 1515 (s), 1455 (s), 1410 (s), 1385 (s), 1343 (s), 1305 (w), 1186 (w), 1109 (w), 1053 (w), 1019 (w), 882 (w), 870 (w), 854 (m), 817 (s), 800 (s), 785 (s), 765 (w), 714 (m), 678 (w), 586 (w), 542 (w), 520 9m), 459 (w). Anal. Calcd. For C<sub>94</sub>H<sub>84</sub>Fe<sub>2</sub>N<sub>4</sub>O<sub>9</sub>: C, 74.01; H, 5.55; N, 3.67. Found: C, 73.72; H, 5.68; N, 3.75.

**X-ray Crystallography.** Single crystals were mounted at room temperature on the tips of quartz fibers, coated with Paratone-N oil, and cooled under a stream of cold nitrogen. Intensity data were collected on a Bruker (formerly Siemens) APEX CCD diffractometer running the SMART software package, with Mo Kα radiation (λ = 0.71073 Å). Data collection and reduction protocols are described in detail elsewhere.<sup>9</sup> The structures were solved by the Patterson method and refined on F<sup>2</sup> by using the



SHELXTL software package.<sup>10</sup> Empirical absorption corrections were applied with SADABS<sup>11</sup>, part of the SHELXTL program package, and the structures were checked for higher symmetry by the program PLATON.<sup>12</sup> All non-hydrogen atoms were refined anisotropically. In general, hydrogen atoms were assigned idealized positions and given thermal parameters equivalent to either 1.5 (methyl hydrogen atoms) or 1.2 (all other hydrogen atoms) times the thermal parameter of the carbon atom to which they were attached. Hydrogen atoms of N-H of the pyrazole derivatives were identified from difference Fourier maps. In the structure of **1**, one diethylether molecule was assigned in the lattice. The structure of **3** contains one benzene and 0.5 pentane molecules, the latter having disordered over two positions with equal occupancies. In the structure of **4**, one pentane and two benzene molecules were located and isotropically refined. Data collection and experimental details for the complexes are summarized in Table 5.1. Relevant interatomic distances and angles for **1** – **2**, **3** and **4** are listed in Table 5.2, 5.3, and 5.4, respectively.

**Mössbauer Spectroscopy.** Mössbauer spectra (4.2 K) were recorded in the MIT department of Chemistry Instrument Facility on an MS1 spectrometer (WEB Research Co.) with a <sup>57</sup>Co source in a Rh matrix kept at room temperature. Spectra were fit to Lorentzian line shapes by using the WMOSS plot and fit program<sup>13</sup> and isomer shifts were referenced to natural abundance Fe at room temperature. Solid samples were prepared by suspending powdered material (~0.04 mmol) in Apeiezon N grease and placing the mixture in a nylon sample holder.

**EPR Measurements.** X-band EPR spectra were recorded on a Bruker EMX EPR spectrometer (9.37 GHz) running WinEPR software. Temperature control was achieved with an Oxford Instruments ESR900 liquid-helium cryostat and an ITC503 controller. Dry O<sub>2</sub> gas was directly bubbled into an 0.50 mM toluene solution of [Fe<sub>2</sub>(μ-

$\text{O}_2\text{CAr}^{\text{Tol}})_2(\text{O}_2\text{CAr}^{\text{Tol}})_2(\text{Hdmpz})_2]$  for 10 sec at  $-78\text{ }^\circ\text{C}$ , and the solution was then freeze-quenched within 10 sec with liquid  $\text{N}_2$ .

## Results

**Synthesis and Structural Characterization of the Isomeric Compounds**  $[\text{Fe}_2(\mu\text{-O}_2\text{CAr}^{\text{Tol}})_4(\text{pz})_2]$  (1) and  $[\text{Fe}_2(\mu\text{-O}_2\text{CAr}^{\text{Tol}})_2(\text{O}_2\text{CAr}^{\text{Tol}})_2(\text{pz})_2]$  (2). The reaction  $[\text{Fe}_2(\mu\text{-O}_2\text{CAr}^{\text{Tol}})_2(\text{O}_2\text{CAr}^{\text{Tol}})_2(\text{THF})_2]^{7,8}$  with 2 equiv of pz afforded both compounds 1 and 2, depending on the crystallization conditions (Scheme 5.1). The tetracarboxylate bridged, paddle-wheel diiron(II) compound 1, was exclusively isolated as colorless block crystals upon diethylether vapor diffusion into the  $\text{CH}_2\text{Cl}_2$  reaction mixture. Figure 5.1 shows its structure and Table 5.2 lists selected interatomic distances and angles. The crystallographically inequivalent iron(II) centers have identical square pyramidal geometries with an  $\text{NO}_4$  donor atom set and are linked by four terphenyl-based carboxylates with an  $\text{Fe}\cdots\text{Fe}$  separation of  $2.7886(7)\text{ \AA}$ . There is a virtual  $\text{C}_2$  axis along the  $\text{Fe}\text{--}\text{Fe}$  vector and the four *p*-tolyl groups flanking the bimetallic center are disposed nearly orthogonal to each other along that axis. The pz ligands are coordinated through the resulting pockets, each with a diameter of  $\sim 9\text{ \AA}$  (Figure 5.1 top left). The two pz ring planes have a nearly orthogonal orientation, the dihedral angle of  $96.6^\circ$ . The  $2.793\text{ \AA}$  distance between the N4 atom in pz and the O7 atom of the carboxylate ligand indicates the presence of a hydrogen-bonding interaction. A broad infrared peak at  $3360\text{ cm}^{-1}$  further corroborates this feature. The hydrogen-bond may cause the elongation of the  $\text{Fe1}\text{--}\text{O5}$  distance to  $2.1568(19)\text{ \AA}$ . The  $\text{Fe1}\text{--}\text{O1}$  bond, located *trans* to the  $\text{Fe1}\text{--}\text{O5}$  bond, is shortened to  $2.0677(19)\text{ \AA}$ , an exemplification of the *trans*-influence. Typical  $\text{Fe1}\cdots\text{O}$  distances of  $2.0301(18)\text{ \AA}$  and  $2.0335(19)\text{ \AA}$  were measured for the  $\text{Fe1}\text{--}\text{O3}$  and  $\text{Fe1}\text{--}\text{O8}$  bonds, respectively.

The dicarboxylate-bridged diiron(II) windmill isomer **2** was obtained when pentane was diffused into the CH<sub>2</sub>Cl<sub>2</sub> solution. The structure and a list of selected distances and angles are shown in Figure 5.2 and Table 5.2, respectively. The crystallographically equivalent iron(II) centers in **2** have a distorted trigonal bipyramidal geometry with NO<sub>4</sub> coordination environments. The diiron(II) core undergoes a dramatic shift from four bridging (in **1**) to two bridging and two terminal carboxylates in **2**, with concomitant elongation of the Fe...Fe distance to 4.326(2) Å. The 1.537 Å difference in Fe...Fe distance between **1** and **2** illustrates the flexible nature of diiron(II) complexes with the four terphenyl based-carboxylate ligand framework.

Together with the crystal structures of the two isomers, [Fe<sub>2</sub>(μ-O<sub>2</sub>CAr<sup>4F-Ph</sup>)<sub>4</sub>(THF)<sub>2</sub>] and [Fe<sub>2</sub>(μ-O<sub>2</sub>CAr<sup>4F-Ph</sup>)<sub>2</sub>(O<sub>2</sub>CAr<sup>4F-Ph</sup>)<sub>2</sub>(THF)<sub>2</sub>], the isolation of isomers **1** and **2** from the same solution reinforced the contention that the di- and tetracarboxylate bridged diiron(II) complexes are nearly isoenergetic.<sup>14</sup> The energy states of these two isomers can be differentiated by using a more sterically hindered N-donor ligand, because the small pocket size affording by in the structure of **1** cannot accommodate bulkier groups.

**Synthesis and Crystallographic Analysis of the Dicarboxylate-Bridged Compound [Fe<sub>2</sub>(μ-O<sub>2</sub>CAr<sup>Tol</sup>)<sub>2</sub>(O<sub>2</sub>CAr<sup>Tol</sup>)<sub>2</sub>(Hdmpz)<sub>2</sub>] (**3**).** The previous argument is illustrated by compound **3**, which forms exclusively by substituting methyl groups at the 3- and 5-positions of the pz unit. The reaction of [Fe<sub>2</sub>(μ-O<sub>2</sub>CAr<sup>Tol</sup>)<sub>2</sub>(O<sub>2</sub>CAr<sup>Tol</sup>)<sub>2</sub>(THF)<sub>2</sub>] with 2 equiv of Hdmpz afforded the colorless diiron(II) compound [Fe<sub>2</sub>(μ-O<sub>2</sub>CAr<sup>Tol</sup>)<sub>2</sub>(O<sub>2</sub>CAr<sup>Tol</sup>)<sub>2</sub>(Hdmpz)<sub>2</sub>] (**3**). The structure of **3** is presented in Figure 5.3 and selected interatomic distances and angles are in Table 5.3. Two crystallographically independent, centrosymmetric diiron(II) units are located in one unit cell. Each has two equivalent iron(II) centers with NO<sub>3</sub> coordination geometry bridged by two carboxylate ligands. The Fe...Fe separations are 4.153 and 4.192 Å, comparable to the 4.326(2) Å value of the windmill isomer **2** but longer than the 2.7886(7) Å distance of the paddle

wheel isomer 1. An average distance of 1.995(48) was observed for the Fe–O bonds, comparable to those of other high-spin iron(II) complexes.

**Oxygenation of Compound 3 and Crystallographic Analysis of the Resembling Oxo-bridged Diiron(III) Compound  $[\text{Fe}_2(\mu\text{-O})(\text{O}_2\text{CAr}^{\text{Tol}})_4(\text{Hdmpz})_2]$  (4).** Oxygenation of a toluene solution of 3 at  $-78\text{ }^\circ\text{C}$  did not generate any optically distinguishable intermediates. The initial solution had a very weak  $g = 16$  signal in the X-band EPR spectrum at 5 K (Figure 5.4 A). Two signals, at  $g = 1.99$  and  $4.28$ , formed upon oxygenation of 3 at  $-78\text{ }^\circ\text{C}$  (Figure 5.4 B), which decayed together at higher temperature (Figure 5.4 C). The signal at  $g = 2.0$  completely disappeared and only a trace signal remained at  $g = 4.3$ . These results indicate that intermediates with half-integer spin develop in the course of the oxygenation of 3 and that an EPR-silent species is generated as the final product. The possibility of solvent oxidation by this characterized intermediate was checked, but only trace amounts of benzaldehyde and benzyl alcohol were detected from an oxygenated toluene solution of 3. When the oxygenation was performed in the presence of a potential substrate, including propylene, cyclohexene, or 2,4-di-*tert*-butylphenol, no corresponding oxidation product was observed. This result suggests that the EPR-active intermediate is unable to oxidize the added species. From the oxygenation reaction was crystallized the oxo-bridged diiron(III) complex  $[\text{Fe}_2(\mu\text{-O})(\text{O}_2\text{CAr}^{\text{Tol}})_4(\text{Hdmpz})_2]$  (4) in over 80 % yield by layering on pentane, suggesting that ligand oxidation also does not occur. Although autooxidation is one of the possible reaction pathways, a reasonable explanation for all of the observed results is currently not available.

The best crystal for X-ray analysis was obtained from oxygenation of 3 in benzene solution followed by pentane vapor diffusion. The structure of 4 is depicted in Figure 5.5 and the selected interatomic distances and angles are reported in Table 5.4. Two iron(III) atoms are linked by a single oxo ligand with an Fe...Fe separation of 3.493

Å. The assignment of a bridging oxo versus hydroxo unit is based on the short observed distances of 1.781(3) Å and 1.760(2) Å between O1 and the Fe(III) sites. The overall charge balance also supports this assignment. The Fe1–O1–Fe2 angle is 160.5(2)°. Both iron(III) sites are coordinated by one Hdmpz and two terminal carboxylate units, but they have different coordination environments. One has a pseudooctahedral NO<sub>5</sub> coordination environment and the other site has distorted trigonal bipyramidal NO<sub>4</sub> geometry. The small separation of 2.576 Å and the orientation of the N9 atom in Hdmpz and O4 of one of the carboxylates indicates the existence of a hydrogen bonding interaction while further links the two iron(III) centers.

**Mössbauer Spectroscopic Properties of Compounds 3 and 4.** The zero-field <sup>57</sup>Fe Mössbauer spectrum of **3**, measured at 4.2 K, consists of a single quadrupole doublet with  $\delta = 1.11(2)$  mm/s,  $\Delta E_Q = 3.00(2)$  mm/s and  $\Gamma = 0.25(2)$  mm/s (Figure 5.6. left). The isomer shift and quadrupole splitting are typical of high-spin iron(II) sites and comparable to those reported for related dicarboxylate bridged diiron(II) complexes with a NO<sub>3</sub> coordination environment.<sup>7,8,15,16</sup> The Mössbauer parameters obtained for **4** at 4.2 K are  $\delta = 0.49(2)$  mm/s and  $\Delta E_Q = 0.70(2)$  mm/s with a natural line width ( $\Gamma = 0.26(2)$  mm/s) (Figure 5.6. right). The isomer shift is in the range typical of high-spin iron(III) sites.<sup>7,17-19</sup> The  $\Delta E_Q$  value for **4** is not in this range, however, the diiron(III) sites, despite the crystallographically inequivalent five- and six-coordination environments, were not distinguished by Mössbauer spectroscopy.

## Summary

It was possible to synthesize carboxylate-rich diiron(II) complexes having proton donors in the proximity to the diiron(II) sites. Two isomers, windmill and paddlewheel type diiron(II) complexes **1** and **2**, were isolated from the same reaction mixture, attesting to the facile interconversion of the two isomers by carboxylate shifts. Using a

sterically bulkier N-donor ligand (Hdmpz) than the pz moieties in **1**, the dicarboxylate bridged diiron(II) windmill complex **3** was exclusively formed.

**References**

- (1) Nordlund, P.; Sjoberg, B.-M.; Eklund, H. *Nature* **1990**, *345*, 593-598.
- (2) Stubbe, J.; van der Donk, W. A. *Chem. Rev.* **1998**, *98*, 705-762.
- (3) Lindqvist, Y.; Hung, W.; Schneider, G.; Shanklin, J. *EMBO J.* **1996**, *15*, 4081-4092.
- (4) Merkx, M.; Kopp, D. A.; Sazinsky, M. H.; Blazyk, J. L.; Müller, J.; Lippard, S. J. *Angew. Chem., Int. Ed.* **2001**, *40*, 2782-2807.
- (5) Sazinsky, M. H.; Bard, J.; Di Donato, A.; Lippard, S. J. *J. Biol. Chem.* **2004**, in press.
- (6) Pangborn, A. B.; Giardello, M. A.; Grubbs, R. H.; Rosen, R. K.; Timmers, F. J. *Organometallics* **1996**, 1518-1520.
- (7) Lee, D.; Lippard, S. J. *Inorg. Chem.* **2002**, *41*, 2704-2719.
- (8) Lee, D.; Du Bois, J.; Petasis, D.; Hendrich, M. P.; Krebs, C.; Huynh, B. H.; Lippard, S. J. *J. Am. Chem. Soc.* **1999**, *121*, 9893-9894.
- (9) Kuzelka, J.; Mukhopadhyay, S.; Spingler, B.; Lippard, S. J. *Inorg. Chem.* **2004**, *43*, 1751-1761.
- (10) Sheldrick, G. M.; University of Göttingen: Göttingen, Germany, 1997.
- (11) Sheldrick, G. M.; University of Göttingen: Göttingen, Germany, 1996.
- (12) Spek, A. L.; Utrecht University: Utrecht, The Netherlands, 1998.
- (13) Kent, T. A.; v2.5 ed.: Minneapolis, 1998.
- (14) Lee, D.; DuBois, J. L.; Pierce, B.; Hedman, B.; Hodgson, K. O.; Hendrich, M. P.; Lippard, S. J. *Inorg. Chem.* **2002**, *41*, 3172-3182.
- (15) Lee, D.; Lippard, S. J. *Inorganica Chimica Acta* **2002**, *341*, 1-11.
- (16) Yoon, S.; Lippard, S. J. *Inorg. Chem.* **2003**, *42*, 8606-8608.
- (17) Kurtz, Jr., D. M. *Chem. Rev.* **1990**, *90*, 585-606.
- (18) Lee, D.; Lippard, S. J. *Inorg. Chem.* **2002**, *41*, 827-837.
- (19) Yoon, S.; Lippard, S. J. *J. Am. Chem. Soc.* **2004**, *126*, 2666-2667.

**Table 4.1.** Summary of X-ray Crystallographic Data for  $[\text{Fe}_2(\mu\text{-O}_2\text{CAr}^{\text{Tot}})_4(\text{pz})_2]$  (1),  $[\text{Fe}_2(\mu\text{-O}_2\text{CAr}^{\text{Tot}})_2(\text{O}_2\text{CAr}^{\text{Tot}})_2(\text{pz})_2]$  (2),  $[\text{Fe}_2(\mu\text{-O}_2\text{CAr}^{\text{Tot}})_2(\text{O}_2\text{CAr}^{\text{Tot}})_2(\text{Hdmpz})_2]$  (3), and  $[\text{Fe}_2(\mu\text{-O})(\text{O}_2\text{CAr}^{\text{Tot}})_4(\text{Hdmpz})_2]$  (4).

	1·OEt <sub>2</sub>	2	3·C <sub>6</sub> H <sub>6</sub> :pentane	4·C <sub>6</sub> H <sub>6</sub> :0.5pentane
Empirical formula	Fe <sub>2</sub> C <sub>94</sub> H <sub>86</sub> N <sub>4</sub> O <sub>9</sub>	Fe <sub>2</sub> C <sub>90</sub> H <sub>76</sub> N <sub>4</sub> O <sub>8</sub>	Fe <sub>2</sub> C <sub>122</sub> H <sub>117</sub> N <sub>4</sub> O <sub>9</sub>	Fe <sub>2</sub> C <sub>102.5</sub> H <sub>96</sub> N <sub>4</sub> O <sub>9</sub>
weight	1527.37	1453.25	1608.20	1639.53
space group	P $\bar{1}$	P $\bar{1}$	P $\bar{1}$	Pna2 <sub>1</sub>
<i>a</i> , Å	14.215(3)	10.484(3)	13.1403(17)	38.583(8)
<i>b</i> , Å	14.635(3)	13.386(3)	16.257(2)	19.546(4)
<i>c</i> , Å	19.763(4)	14.837(4)	20.497(3)	12.115(2)
$\alpha$ , deg	90.367(3)	70.099(5)	79.511(2)	
$\beta$ , deg	108.581(3)	73.338(5)	82.256(2)	
$\gamma$ , deg	90.328(3)	79.834(6)	79.961(2)	
<i>V</i> , Å <sup>3</sup>	3897.0(13)	1868.4(8)	4215.5(9)	9136(3)
<i>Z</i>	2	1	2	4
$\rho_{\text{calc}}$ , g/cm <sup>3</sup>	1.302	1.292	1.267	1.192
<i>T</i> , °C	-100	-80	-85	-100
$\mu$ (Mo K $\alpha$ ), mm <sup>-1</sup>	0.435	0.450	0.406	0.376
total no. of data	28819	8567	31667	68016
no. of unique data points	13590	5366	15143	16569
no. of parameters	1000	477	1053	1073
R1 (%) <sup>a</sup>	5.31	6.66	7.30	6.90
wR2 (%) <sup>b</sup>	13.10	15.83	18.15	18.37
max, min peaks, e/Å <sup>3</sup>	0.914, -0.381	0.472, -0.949	0.544, -0.441	0.759, -0.469

<sup>a</sup> R1 =  $\Sigma||F_o| - |F_c||/\Sigma|F_o|$ . <sup>b</sup> wR2 =  $\{\Sigma[w(F_o^2 - F_c^2)^2]/\Sigma[w(F_o^2)]\}^{1/2}$



**Table 5.2.** Selected interatomic distances (Å) and angles (deg) for  $[\text{Fe}_2(\mu\text{-O}_2\text{CAr}^{\text{Tol}})_4(\text{pz})_2]$  (1) and  $[\text{Fe}_2(\mu\text{-O}_2\text{CAr}^{\text{Tol}})_2(\text{O}_2\text{CAr}^{\text{Tol}})_2(\text{pz})_2]$  (2).<sup>a</sup>

	1		2
Fe1...Fe2	2.7886(7)	Fe1...Fe2	4.326(2)
Fe1–O1	2.0677(19)	Fe1–O1	2.001(4)
Fe1–O3	2.0301(18)	Fe1–O2	1.975(4)
Fe1–O5	2.1568(19)	Fe1–O3	2.039(4)
Fe1–O8	2.0335(18)	Fe1–O4	2.380(5)
Fe1–N1	2.064(2)	Fe1–N1	2.119(5)
Fe2–O2	2.0471(19)	O1–Fe1–N1	90.0(2)
Fe2–O4	2.114(2)	O1–Fe1–O2	112.09(18)
Fe2–O6	2.037(2)	O1–Fe1–O3	121.38(18)
Fe2–O7	2.1377(19)	O1–Fe1–O4	107.98(16)
Fe2–N3	2.053(2)	O2–Fe1–N1	103.83(19)
O1–Fe1–N1	106.95(8)	O2–Fe1–O3	123.54(19)
O3–Fe1–N1	102.11(8)	O2–Fe1–O4	89.70(17)
O5–Fe1–N1	85.91(8)	O3–Fe1–O4	58.77(16)
O8–Fe1–N1	101.56(8)	O3–Fe1–N1	93.36(19)
O1–Fe1–O3	91.23(7)	O4–Fe1–N1	151.72(19)
O1–Fe1–O5	166.89(7)	O1...N2	2.973(7)
O1–Fe1–O8	90.27(7)		
O3–Fe1–O5	88.49(7)		
O3–Fe1–O8	154.71(8)		
O5–Fe1–O8	84.46(7)		
O2–Fe2–N3	101.67(9)		
O4–Fe2–N3	97.57(9)		
O6–Fe2–N3	101.65(9)		
O7–Fe2–N3	92.70(9)		
O2–Fe2–O4	89.43(8)		
O2–Fe2–O6	156.59(8)		
O2–Fe2–O7	87.37(7)		
O4–Fe2–O6	87.59(7)		
O4–Fe2–O7	169.67(7)		
O6–Fe2–O7	89.46(7)		
N2...O5	3.104		
N4...O7	2.793		

<sup>a</sup>Numbers in parentheses are estimated standard deviations of the last significant figures.

**Table 5.3.** Selected interatomic distances (Å) and angles (deg) for  $[\text{Fe}_2(\mu\text{-O}_2\text{CAr}^{\text{Tol}})_2(\text{O}_2\text{CAr}^{\text{Tol}})_2(\text{Hdmpz})_2]$  (3).<sup>a</sup>

Fe1...Fe1A	4.1909(14)	Fe2...Fe2A	4.153(2)
Fe1-O2	1.927(3)	Fe2-O1	2.032(3)
Fe1-O3	2.020(3)	Fe2-O4	1.940(3)
Fe1-O7	2.023(3)	Fe2-O5	2.038(3)
Fe1-N3	2.093(4)	Fe2-N1	2.178(3)
O2-Fe1-O3	116.67(16)	O1-Fe2-O4	117.20(15)
O2-Fe1-O7	126.15(15)	O1-Fe2-O5	108.59(13)
O2-Fe1-N3	106.32(15)	O1-Fe2-N1	98.16(14)
O3-Fe1-O7	111.46(14)	O4-Fe2-O5	130.22(14)
O3-Fe1-N3	95.73(14)	O4-Fe2-N1	101.58(14)
O7-Fe1-N3	91.10(13)	O5-Fe2-N1	89.84(13)

<sup>a</sup>Numbers in parentheses are estimated standard deviations of the last significant figure

**Table 5.4.** Selected interatomic distances (Å) and angles (deg) for  $[\text{Fe}_2(\mu\text{-O})(\text{O}_2\text{CAr}^{\text{Tot}})_4(\text{Hdmpz})_2]$  (**4**).<sup>a</sup>

Fe1...Fe2	3.493(3)	O3-Fe1-N3	88.85(16)
Fe1-O1	1.781(3)	O4-Fe1-O5	61.69(12)
Fe2-O1	1.760(3)	O4-Fe1-N3	85.49(12)
Fe1-O1-Fe2	160.5(2)	O5-Fe1-N3	98.15(15)
Fe1-O2	2.071(3)	Fe2-O6	2.036(3)
Fe1-O3	2.211(3)	Fe2-O7	2.178(3)
Fe1-O4	2.172(3)	Fe2-O8	1.924(3)
Fe1-O5	2.057(3)	Fe2-N1	2.069(4)
Fe1-N3	2.055(4)	O1-Fe2-O6	118.66(15)
O1-Fe1-O2	98.13(14)	O1-Fe2-O7	102.93(14)
O1-Fe1-O3	158.99(13)	O1-Fe2-O8	121.82(16)
O1-Fe1-O4	96.39(14)	O1-Fe2-N1	98.12(16)
O1-Fe1-O5	106.31(14)	O6-Fe2-O7	62.08(13)
O1-Fe1-N3	96.25(17)	O6-Fe2-O8	117.29(15)
O2-Fe1-O3	60.90(12)	O6-Fe2-N1	91.50(14)
O2-Fe1-O4	89.69(13)	O7-Fe2-O8	89.45(14)
O2-Fe1-O5	143.74(14)	O7-Fe2-N1	151.89(14)
O2-Fe1-N3	105.47(16)	O8-Fe2-N1	95.14(16)
O3-Fe1-O4	158.63(14)	O4...N2	2.964(18)
O3-Fe1-O5	93.05(12)	O9...N4	2.710(18)

<sup>a</sup>Numbers in parentheses are estimated standard deviations of the last significant figures

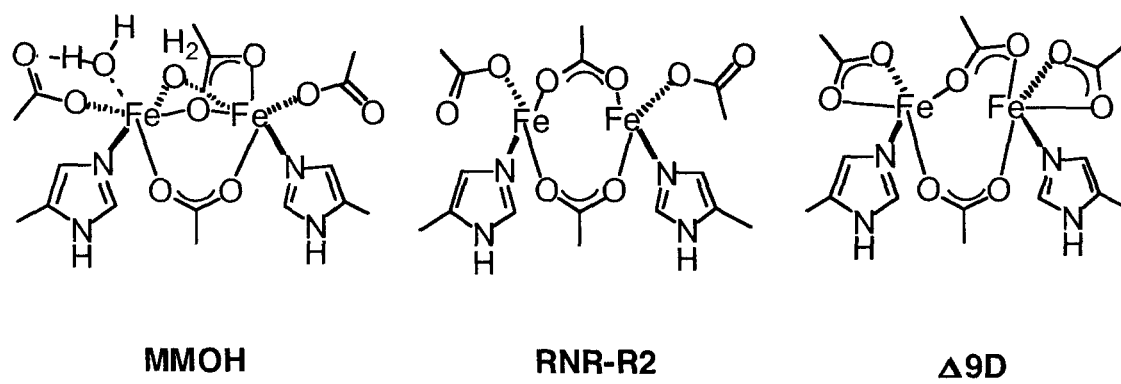
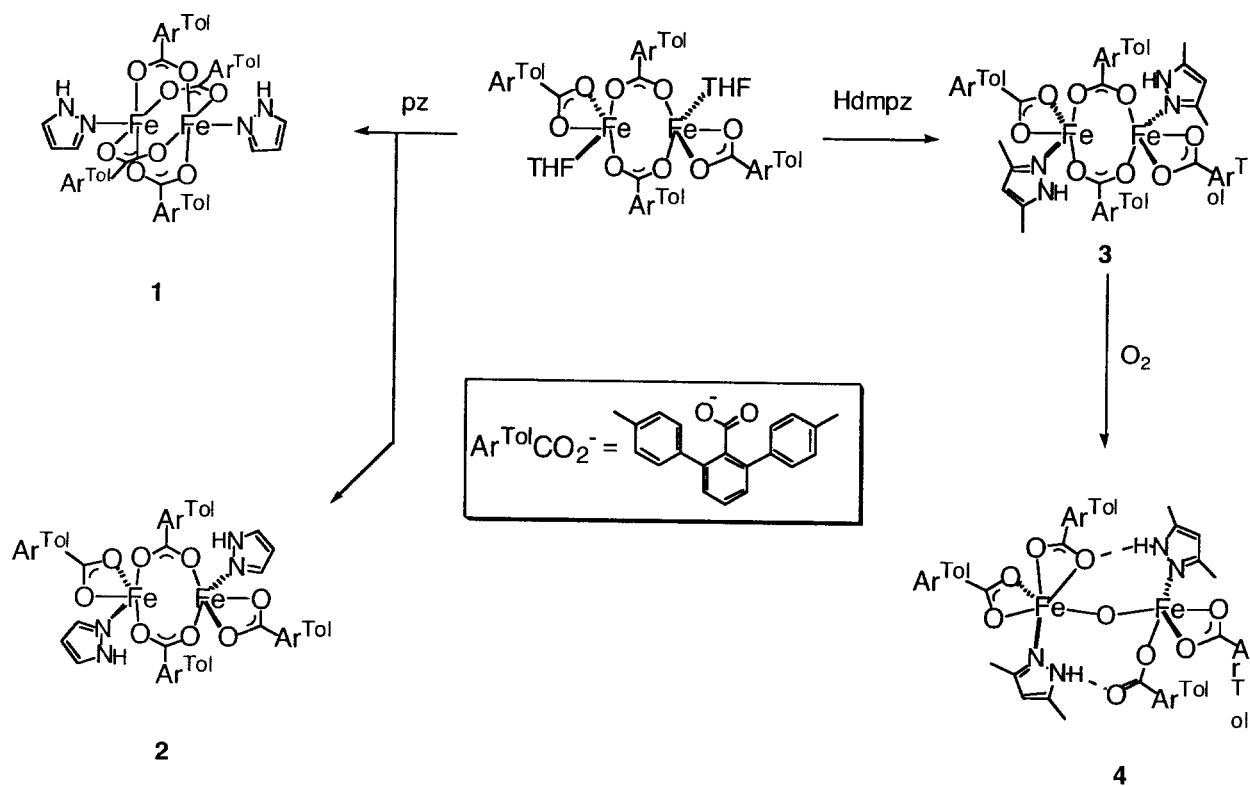
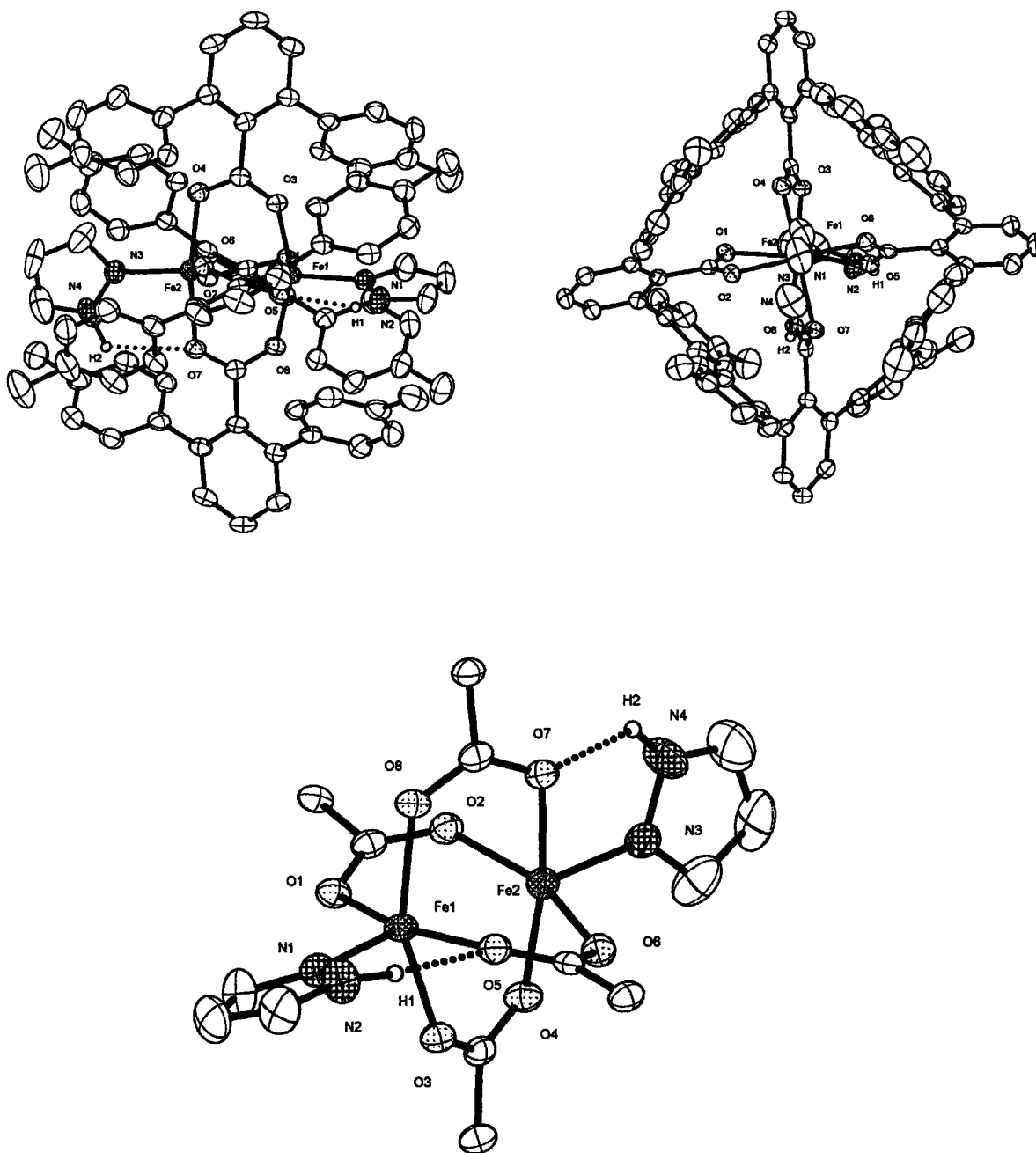


Chart 5.1



Scheme 5.1



**Figure 5.1.** ORTEP drawing of  $[\text{Fe}_2(\mu\text{-O}_2\text{CAr}^{\text{Tol}})_4(\text{pz})_2]$  (1) showing 50% probability thermal ellipsoids. (Top, Left) The hydrogen atoms are omitted for clarity. (Top, Right) Side on view showing pocket generated by four carboxylates. (Bottom) Drawing with the aromatic rings of  $\text{Ar}^{\text{Tol}}\text{CO}_2^-$  ligands omitted for clarity.

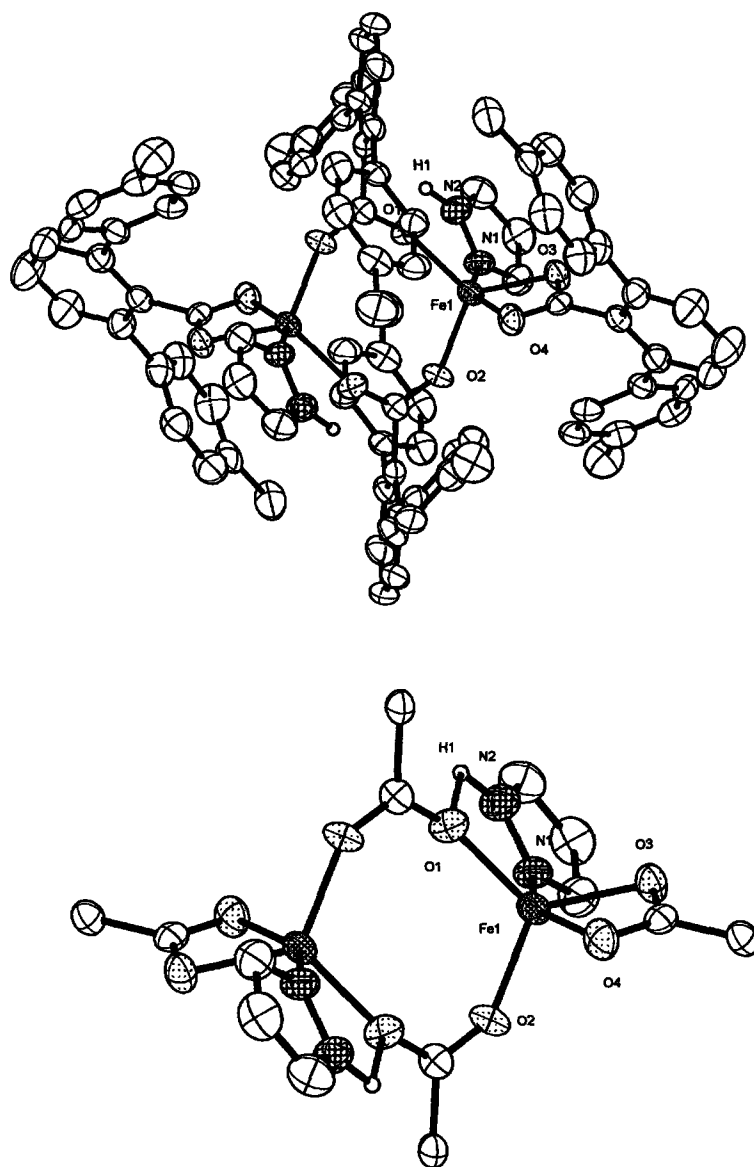


**Figure 5.2.** ORTEP drawing of  $[\text{Fe}_2(\mu\text{-O}_2\text{CAr}^{\text{Tol}})_2(\text{O}_2\text{CAr}^{\text{Tol}})(\text{pz})_2]$  (2) showing 50% probability thermal ellipsoids. (Top) The solvent molecules and hydrogen atoms are omitted for clarity. (Bottom) The aromatic rings of  $\text{Ar}^{\text{Tol}}\text{CO}_2^-$  ligands were omitted for additional clarity.

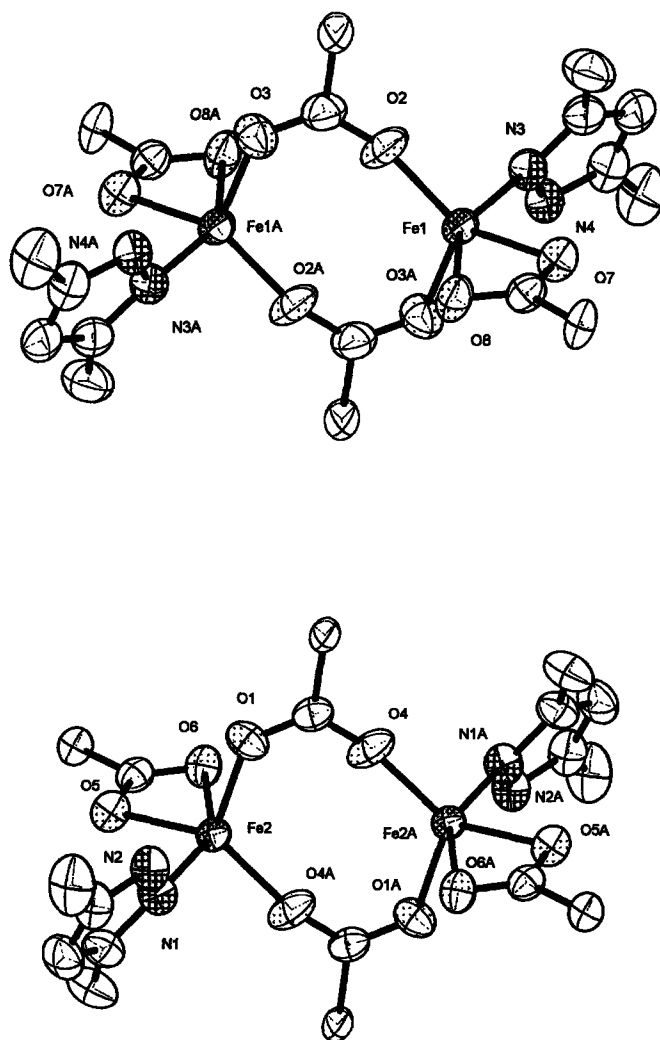


**Figure 5.3.** ORTEP drawing of  $[\text{Fe}_2(\mu\text{-O}_2\text{CAr}^{\text{Tol}})_2(\text{O}_2\text{CAr}^{\text{Tol}})_2(\text{Hdmpz})_2]$  (3) showing 50% probability thermal ellipsoids. The solvent molecules, hydrogen atoms, and aromatic rings of  $\text{Ar}^{\text{Tol}}\text{CO}_2^-$  ligands are omitted for clarity. The top and bottom views display the two crystallographically independent dimers.



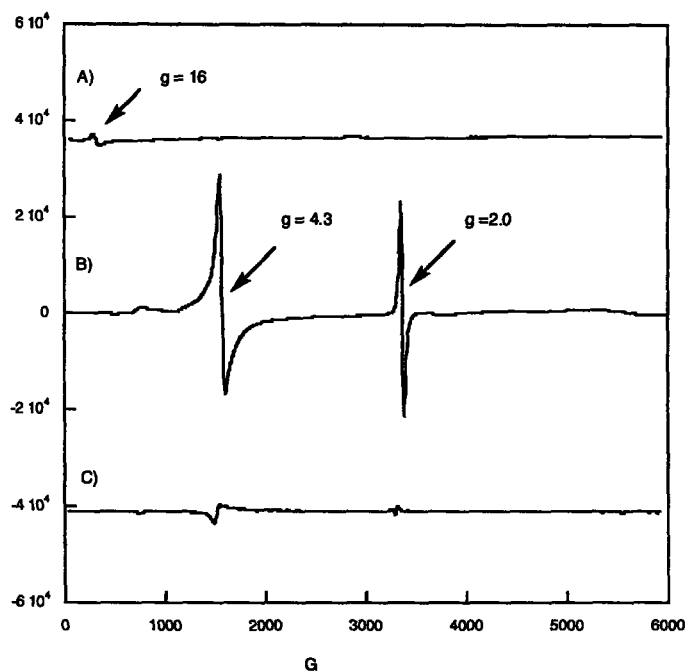


**Figure 5.4.** X-band EPR spectra collected at 5 K. A) The toluene solution of **3** B) Samples were prepared by exposing a toluene solution of **3** to  $O_2$  at  $-78\text{ }^\circ\text{C}$  and freeze-quenching after 10 sec in liquid  $N_2$ . C) The fully oxidized toluene solution of **3** at the room temperature.

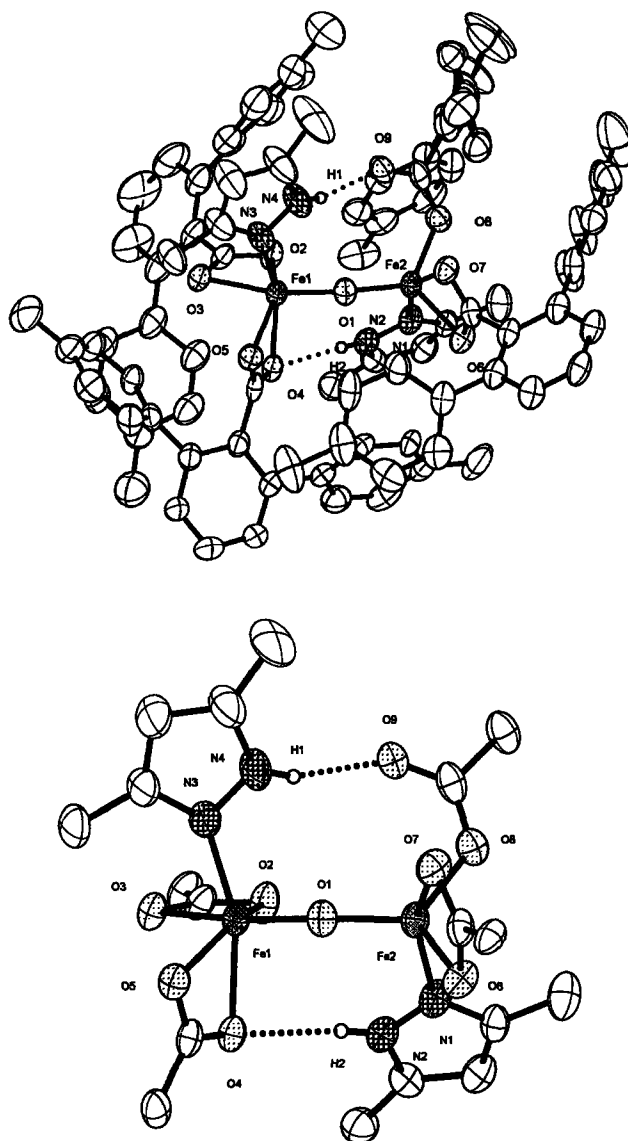


**Figure 5.5.** ORTEP drawing of  $[\text{Fe}_2(\mu\text{-O})(\text{O}_2\text{CAr}^{\text{Tol}})_4(\text{Hdmpz})_2]$  (**4**) showing 50 % probability thermal ellipsoids. (Top) The solvent molecules and hydrogen atoms are omitted for clarity. (Bottom) The aromatic rings of  $\text{Ar}^{\text{Tol}}\text{CO}_2^-$  ligands were omitted for clarity.

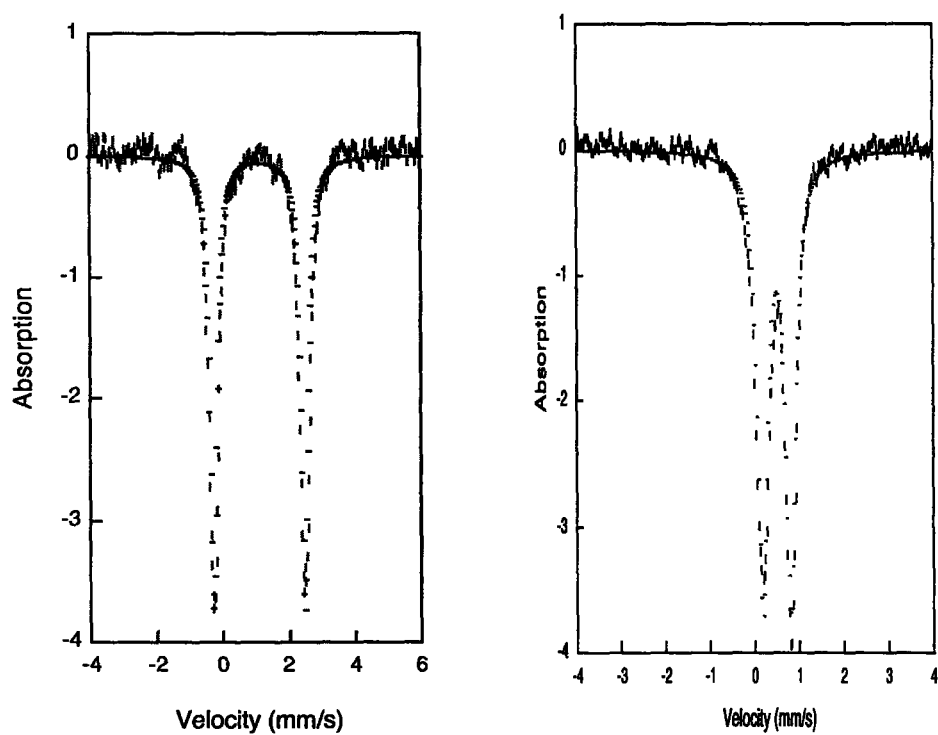


**Figure 5.6.** Mössbauer spectra (experimental data (|), calculated fit (–)) recorded at 4.2 K for a solid sample of  $[\text{Fe}_2(\mu\text{-O}_2\text{CAr}^{\text{Tot}})_2(\text{O}_2\text{CAr}^{\text{Tot}})_2(\text{Hdmpz})_2]$  (3) (Left) and  $[\text{Fe}_2(\mu\text{-O})(\text{O}_2\text{CAr}^{\text{Tot}})_4(\text{Hdmpz})_2]$  (4) (Right).

## **Chapter 6**

### **Di- and Tetra-Bridged Diiron(II) Complexes with Four Terphenyl- Derived Carboxylates and Two Water Molecules**

## Introduction

The activation of triplet ground state dioxygen and the hydroxylation of unactivated C–H bonds under ambient conditions by non-heme diiron enzymes are topics of much current interest.<sup>1-3</sup> The hydroxylase component of soluble methane monooxygenase (sMMOH), which utilizes dioxygen to convert CH<sub>4</sub> into CH<sub>3</sub>OH, is a well-studied member of this class of enzymes.<sup>4</sup> The enzyme active site contains a diiron core coordinated by four glutamate carboxylate groups and two histidine imidazole ligands.<sup>5</sup> This diiron unit with a carboxylate-rich coordination environment is effectively utilized to bind, activate and transfer an oxygen atom from O<sub>2</sub> to the substrate. Similar diiron cores occur in related multicomponent dioxygen-dependent enzymes, including toluene monooxygenase,<sup>6</sup> the R2 subunit of ribonucleotide reductase,<sup>7,8</sup> and stearyl-ACP  $\Delta^9$  desaturase.<sup>9</sup>

To help understand how these enzymes achieve their physiological roles of O<sub>2</sub> activation and utilization at carboxylate-rich diiron cores, much effort has been devoted to reproducing the structures and functions of their active sites by small model complexes. Recently, our group and others have reproduced the carboxylate-rich composition of these diiron sites with the use of sterically hindered terphenyl-derived carboxylate ligands.<sup>10-13</sup> Although these model complexes are able to hydroxylate benzylic C–H bonds and to oxidize phosphine and sulfide moieties,<sup>13-17</sup> the activation of strong C–H bonds, such as that in methane, has not yet been achieved. This situation directed us to revisit the diiron sites in the enzymes to identify features that had not been adequately incorporated into the model complexes. One compositional difference between most of the reported model complexes and the diiron(II) core at the active site of MMOH is the presence of two water molecules in the first and second coordination spheres (Chart 5.1). In recently published DFT calculations, the utilization of a

coordinated H<sub>2</sub>O molecule as a hydrogen-bond donor was considered to be a key component in the formation of reactive intermediate(s) upon oxygenation of the diiron(II) site.<sup>18-20</sup> The computational results strongly suggest that the ligated water molecules may be required to reproduce the function of the enzyme in model systems. Accordingly, we have undertaken the synthesis of model complexes containing water molecules in the coordination spheres of their carboxylate-bridged diiron(II) sites. Here, we report the result of our first efforts in this area, in which the synthesis and characterization of diiron(II) complexes with two ligated water molecules and sterically hindered terphenyl-based carboxylates are described.

## Experimental

**General Considerations.** All reagents, including 4-*tert*-butylpyridine (4-<sup>t</sup>BuC<sub>5</sub>H<sub>4</sub>N), were obtained from commercial suppliers and used as received unless otherwise noted. Dichloromethane, pentane, and THF were saturated with argon and purified by passage through activated Al<sub>2</sub>O<sub>3</sub> columns under argon.<sup>21</sup> Sodium 2,6-di-(*p*-tolyl)benzoate (NaO<sub>2</sub>CAr<sup>Tol</sup>),<sup>22,23</sup> sodium 2,6-di-(*p*-fluorophenyl)benzoate (NaO<sub>2</sub>CAr<sup>4F-Ph</sup>),<sup>23</sup> [Fe<sub>2</sub>(μ-O<sub>2</sub>CAr<sup>Tol</sup>)<sub>2</sub>(O<sub>2</sub>CAr<sup>Tol</sup>)<sub>2</sub>(THF)<sub>2</sub>],<sup>11</sup> and [Fe<sub>2</sub>(μ-O<sub>2</sub>CAr<sup>Tol</sup>)<sub>4</sub>(4-<sup>t</sup>BuC<sub>5</sub>H<sub>4</sub>N)<sub>2</sub>]<sup>11</sup> were prepared as described in the literature. All syntheses and air-sensitive manipulations were carried out under nitrogen in an MBraun glovebox. FT-IR spectra were recorded with a Thermo Nicolet Avatar 360 spectrometer.

[Fe<sub>2</sub>(μ-O<sub>2</sub>CAr<sup>4F-Ph</sup>)<sub>2</sub>(O<sub>2</sub>CAr<sup>4F-Ph</sup>)<sub>2</sub>(THF)<sub>2</sub>(OH<sub>2</sub>)<sub>2</sub>] (**1**). To a CH<sub>2</sub>Cl<sub>2</sub> solution (15 mL) of NaO<sub>2</sub>CAr<sup>4F-Ph</sup> (528 mg, 1.59 mmol) was added Fe(BF<sub>4</sub>)<sub>2</sub>·6H<sub>2</sub>O (268 mg, 0.794 mmol) in THF (5 mL). The resulting suspension was stirred under reflux for 2 days, affording a white precipitate that was filtered through Celite. Colorless blocks of **1** (231 mg, 34 % yield) were obtained by layering pentane onto the filtrate, followed by slow evaporation

and analyzed by X-ray crystallography. FT-IR (KBr,  $\text{cm}^{-1}$ ) 3600 (w,  $\nu_{\text{O-H}}$ ), 3443 (m, br,  $\nu_{\text{O-H}}$ ), 3059 (w), 2979 (w), 1606 (s), 1511 (s), 1455 (s), 1412 (s), 1382 (s), 1300 (w), 1221 (s), 1159 (s), 1095 (m), 1071 (w), 1036 (m), 1013 (w), 845 (m), 835 (m), 808 (s), 792 (m), 772 (m), 738 (w), 714 (m), 700 (m), 554 (s), 529 (s), 463 (m). Anal. Calcd for 1·0.5( $\text{CH}_2\text{Cl}_2$ ) or  $\text{C}_{84.5}\text{H}_{65}\text{Fe}_2\text{F}_8\text{O}_{12}\text{Cl}$ : C, 64.58; H, 4.17. Found: C, 64.85; H, 4.26.

$[\text{Fe}_2(\mu\text{-OH})_2(\mu\text{-O}_2\text{CAr}^{\text{Tol}})_2(\text{O}_2\text{CAr}^{\text{Tol}})_2(\text{THF})_2]$  (**2**). *Method A.* To a  $\text{CH}_2\text{Cl}_2$  solution (9 mL) of  $\text{NaO}_2\text{CAr}^{\text{Tol}}$  (100 mg, 308  $\mu\text{mol}$ ) was added  $\text{Fe}(\text{BF}_4)_2 \cdot 6\text{H}_2\text{O}$  (52 mg, 0.15 mmol) in THF (3 mL). The resulting suspension was stirred for a day. The white precipitate was filtered through Celite. Colorless blocks of **2** were obtained by pentane vapor diffusion (7 mg, 6 % yield) and analyzed by X-ray crystallography.

*Method B.* To a portion (45.4 mg, 32.3  $\mu\text{mol}$ ) of  $[\text{Fe}_2(\mu\text{-O}_2\text{CAr}^{\text{Tol}})_2(\text{O}_2\text{CAr}^{\text{Tol}})_2(\text{THF})_2]$ <sup>11</sup> was added a THF solution (1 mL) containing 10  $\mu\text{L}$  (0.56 mmol) of  $\text{H}_2\text{O}$ . The reaction mixture was stirred for 30 min. Colorless blocks of **2** (34.9 mg, 72 % yield), obtained after 2 days by diffusing pentane into the solution, were analyzed by X-ray crystallography. FT-IR (KBr,  $\text{cm}^{-1}$ ) 3555 (m,  $\nu_{\text{O-H}}$ ), 3400 (w, br,  $\nu_{\text{O-H}}$ ), 3051 (w), 3022 (m), 2918 (m), 1588 (s), 1571 (s), 1514 (s), 1454 (s), 1408 (s), 1381 (s), 1305 (w), 1211 (w), 1145 (w), 1070 (w), 1042 (m), 1019 (w), 914 (w), 890 (w), 853 (w), 835 (m), 822 (s), 802 (s), 787 (m), 765 (m), 736 (m), 714 (w), 701 (m), 584 (m), 547 (m), 523 (m). Anal. Calcd for  $\text{C}_{92}\text{H}_{88}\text{Fe}_2\text{O}_{12}$ : C, 73.80; H, 5.92. Found: C, 72.98; H, 5.98.

$[\text{Fe}_2(\mu\text{-OH})_2(\mu\text{-O}_2\text{CAr}^{\text{Tol}})_2(\text{O}_2\text{CAr}^{\text{Tol}})_2(4\text{-}^t\text{BuC}_5\text{H}_4\text{N})_2]$  (**3**). A portion (50.5 mg, 31.8  $\mu\text{mol}$ ) of  $[\text{Fe}_2(\mu\text{-O}_2\text{CAr}^{\text{Tol}})_4(4\text{-}^t\text{BuC}_5\text{H}_4\text{N})_2]$ <sup>11</sup> was added to THF (1 mL) containing 10  $\mu\text{L}$  (0.56 mmol) of  $\text{H}_2\text{O}$ . Stirring effected dissolution within 30 min to yield a light yellow solution. Light yellow blocks of **3** (41.6 mg, 76 % yield), obtained by layering pentane onto the solution, were analyzed by X-ray crystallography. FT-IR (KBr,  $\text{cm}^{-1}$ ) 3537 (s,  $\nu_{\text{O-H}}$ ), 3425 (w, br,  $\nu_{\text{O-H}}$ ), 3052 (m), 3020 (m), 2964 (s), 2919 (s), 2866 (m), 1613 (s), 1587 (s),

1514 (s), 1501 (w), 1451 (s), 1383 (s), 1273 (w), 1071 (m), 1021 (w), 909 (w), 842 (w), 830 (m), 813 (m), 786 (m), 764 (m), 726 (w), 706 (m), 584 (m), 568 (w), 526 (m), 459 (w). Anal. Calcd for  $C_{102}H_{98}Fe_2N_2O_{10}$ : C, 75.46; H, 6.08; N, 1.73. Found: C, 75.26; H, 6.14; N, 1.70.

**X-ray Crystallography.** Single crystals were mounted at room temperature on the tips of quartz fibers, coated with Paratone-N oil, and cooled under a stream of cold nitrogen. Intensity data were collected on a Bruker (formerly Siemens) APEX CCD diffractometer running the SMART software package, with Mo  $K\alpha$  radiation ( $\lambda = 0.71073 \text{ \AA}$ ). Data collection and reduction protocols are described in detail elsewhere.<sup>24</sup> The structures were solved by Patterson methods and refined on  $F^2$  by using the SHELXTL software package.<sup>25</sup> Empirical absorption corrections were applied with SADABS,<sup>26</sup> part of the SHELXTL program package, and the structures were checked for higher symmetry by the program PLATON.<sup>27</sup> All non-hydrogen atoms were refined anisotropically. In general, hydrogen atoms were assigned idealized positions and given thermal parameters equivalent to either 1.5 (methyl hydrogen atoms) or 1.2 (all other hydrogen atoms) times the thermal parameter of the carbon atom to which they were attached. Hydrogen atoms of O–H of the coordinated water molecule were identified from difference electron maps. In the structure of **1**, two  $CH_2Cl_2$  solvent molecules were assigned in the lattice. The structure of **3** contains one THF and 0.5 pentane molecules. Data collection and experimental details for the complexes are summarized in Table 6.1 and relevant interatomic bond lengths and angles are listed in 6.2.

**Electrochemistry.** Cyclic voltammetric measurements were performed in an MBraun glovebox under nitrogen with an EG&G model 263 potentiostat. A three-electrode configuration consisting of a platinum working electrode, a  $AgNO_3/Ag$  (0.1 M in acetonitrile with 0.5 M  $Bu_4N(PF_6)$ ) reference electrode, and a platinum mesh auxiliary



electrode was used. The supporting electrolyte was 0.5 M Bu<sub>4</sub>N(PF<sub>6</sub>) in CH<sub>2</sub>Cl<sub>2</sub>. All cyclic voltammograms were externally referenced to the Cp<sub>2</sub>Fe/Cp<sub>2</sub>Fe<sup>+</sup> couple.

## Results and Discussion

**Synthesis and Characterization of the Doubly Bridged Diiron(II) Complex [Fe<sub>2</sub>(OH<sub>2</sub>)<sub>2</sub>(μ-O<sub>2</sub>CAr<sup>4F-Ph</sup>)<sub>2</sub>(O<sub>2</sub>CAr<sup>4F-Ph</sup>)<sub>2</sub>(THF)<sub>2</sub>] (1).** Compound 1 was prepared from a reaction between Fe(BF<sub>4</sub>)<sub>2</sub>·6H<sub>2</sub>O and 2 equiv of NaO<sub>2</sub>CAr<sup>4F-Ph</sup> in a THF/CH<sub>2</sub>Cl<sub>2</sub> solution. The structure comprises two distorted trigonal bipyramidal iron(II) centers straddling a crystallographic inversion center with an Fe...Fe separation of 3.4433(8) Å (Figure 6.1). The coordination sites are occupied by two bridging Ar<sup>4F-Ph</sup>CO<sub>2</sub><sup>-</sup> ligands and the oxygen atoms of THF, water, and monodentate terminal carboxylate group. The water molecule coordinated to Fe(1) with a Fe–O bond length of 2.157(2) Å is 3.107(2) Å from Fe(1A) and thus not bridging the two iron atoms in this structure. A THF molecule is located trans to the water ligand. Strong intramolecular hydrogen bonding interactions occur between terminal metal-bound carboxylates and water molecules, with O...O distances of 2.608(3) Å.

**Synthesis and Characterization of the Diaqua-bridged Diiron(II) Complex [Fe<sub>2</sub>(μ-OH<sub>2</sub>)<sub>2</sub>(μ-O<sub>2</sub>CAr<sup>Tol</sup>)<sub>2</sub>(O<sub>2</sub>CAr<sup>Tol</sup>)<sub>2</sub>(THF)<sub>2</sub>] (2).** Although the syntheses of related diaqua-bridged dinickel(II) and dicobalt(II) complexes have been described<sup>28</sup>, an iron(II) analogue has not previously been reported. Only monoqua-bridged diiron(II) complexes, including [Fe<sub>2</sub>(μ-OH<sub>2</sub>)(O<sub>2</sub>CR)<sub>4</sub>(tmen)<sub>2</sub>] [tmen = tetramethylethylenediamine, R = CH<sub>3</sub> and C<sub>6</sub>H<sub>5</sub>]<sup>29</sup> and [Fe<sub>2</sub>(μ-OH<sub>2</sub>)(O<sub>2</sub>Ac)<sub>5</sub>(pyridine)<sub>2</sub>]<sup>30,31</sup> have been characterized. The synthesis of compound 2 was initially achieved by self-assembly from Fe(BF<sub>4</sub>)<sub>2</sub>·6H<sub>2</sub>O and 2 equiv of NaO<sub>2</sub>CAr<sup>Tol</sup> in poor yield, as described in Method A in the experimental section. The water molecules in 2 must derive from the iron(II) salt,

$\text{Fe}(\text{BF}_4)_2 \cdot 6\text{H}_2\text{O}$ , used in the synthesis. The reaction may proceed through the intermediate formation of  $[\text{Fe}_2(\mu\text{-O}_2\text{CAr}^{\text{Tol}})_2(\text{O}_2\text{CAr}^{\text{Tol}})_2(\text{THF})_2]$  in the reaction. This hypothesis was tested by treating independently synthesized  $[\text{Fe}_2(\mu\text{-O}_2\text{CAr}^{\text{Tol}})_2(\text{O}_2\text{CAr}^{\text{Tol}})_2(\text{THF})_2]$  with  $\sim 17$  equiv of water (Method B), resulting in the isolation of compound **2** in excellent yield.

The structure, displayed in Figure 2, reveals two pseudo-octahedral iron(II) centers bridged by two carboxylate ligands and two water molecules. The Fe...Fe separation of 3.073(4) Å is shorter by  $\sim 0.37$  Å than that in **1**, owing to the presence of two additional water bridges. The assignment of these ligands as water rather than hydroxo groups is based on the Fe1–O(aqua) distances, which are 2.2903(11) and 2.3161(12) Å, by the location and refinement of the associated hydrogen atoms in the X-ray structure determination (O–H, 0.789 and 0.958 Å) and by charge considerations. This assignment is further supported by two O–H stretching bands at 3400 and 3555  $\text{cm}^{-1}$  in the IR spectrum of **2**. The remaining coordination sites are occupied by THF and monodentate terminal carboxylate ligands. Strong intramolecular hydrogen bonding interactions occur between terminal metal-bound carboxylates and water molecules, with O...O distances of 2.543(2) Å.

**Synthesis and Characterization of the Diaqua-bridged Diiron(II) Complex**  $[\text{Fe}_2(\mu\text{-OH}_2)_2(\mu\text{-O}_2\text{CAr}^{\text{Tol}})_2(\text{O}_2\text{CAr}^{\text{Tol}})_2(4\text{-}^t\text{BuC}_5\text{H}_4\text{N})_2]$  (**3**). The compound  $[\text{Fe}_2(\mu\text{-O}_2\text{CAr}^{\text{Tol}})_4(4\text{-}^t\text{BuC}_5\text{H}_4\text{N})_2]$ ,<sup>11</sup> which has a composition close to those of MMOH,<sup>5</sup> RNR-R2,<sup>8</sup> and ToMOH,<sup>6</sup> is one of the better studied model complexes. To address how water in the coordination sphere might affect the properties of this complex, we synthesized a water-containing analogue. Compound **3** was prepared in excellent yield by addition of excess  $\text{H}_2\text{O}$  to  $[\text{Fe}_2(\mu\text{-O}_2\text{CAr}^{\text{Tol}})_4(4\text{-}^t\text{BuC}_5\text{H}_4\text{N})_2]$ . The pseudo-octahedrally coordinated iron(II) atoms in **3** are related by a crystallographic inversion center and bridged by two

water molecules and two carboxylates, resulting in an Fe...Fe distance of 3.0548(10) Å (Figure 6.3). Additionally, two hydrogen bonding interactions between terminal carboxylates and bridging water groups further compact the diiron(II) sites. The O...O distance of 2.5519 (36) Å indicates a strong interaction. A broad IR band at 3434 cm<sup>-1</sup> in the spectrum of **3** is consistent with strongly hydrogen-bonded water, and a relatively sharp O–H stretching band at 3573 cm<sup>-1</sup> originates from the remaining proton on the ligand.

Although the structures of a series of Fe<sub>2</sub>(II,II),<sup>32</sup> Fe<sub>2</sub>(III,III)<sup>33</sup> and Fe<sub>2</sub>(III,IV)<sup>34</sup> complexes having neutral polypyridine ligands and a central 2Fe2O quadrilateral are currently available, only recently have related units with biologically more relevant O-rich metal coordination environments become available (Chart 6.2).<sup>10</sup> Compounds **2** and **3** complete one end of the series of diamond cores with O-rich metal coordination environments. As indicated in Chart 6.2, there are several noteworthy differences between members of the two series. The N-rich diiron complexes tend to have O-atom bridges with fewer protons. Thus, the diiron(II) sites in the neutral O-rich complex **3** are bridged by H<sub>2</sub>O molecules, in contrast to the hydroxo bridges in the dicationic diiron(II) complex **A**. Similarly, hydroxo bridges occur in the neutral O-rich diiron(III) compound **E**, compared to the oxo bridges in the N-rich diiron(III) complex **C**, which is a dication. The aqua bridges that occur in the diiron(II) complexes [Fe<sub>2</sub>(μ-OH<sub>2</sub>)(O<sub>2</sub>CR)<sub>4</sub>(tmen)<sub>2</sub>]<sup>29</sup> (R= CH<sub>3</sub> and C<sub>6</sub>H<sub>5</sub>) and [Fe<sub>2</sub>(μ-OH<sub>2</sub>)(O<sub>2</sub>Ac)<sub>5</sub>(pyridine)<sub>2</sub>]<sup>30,31</sup> further substantiate this observation. It is now generally accepted that the diiron(II) sites in deoxyhemerythrin,<sup>3</sup> which has a N-rich metal coordination environment, are bridged by a hydroxo moiety rather than water. Bridging H<sub>2</sub>O molecule(s) are therefore anticipated in the diiron(II) site ligated by four carboxylates and two histidines in reduced ToMOH, as in MMOH. A second difference noted is the small variation in Fe...Fe distance through the O-rich

series compared to the N-rich one. The difference among diiron sites from 3 to E is only 0.171 Å, compared to the 0.471 Å spread from A to C. This property may be attributed to the presence of two additional bridging carboxylates in the O-rich series of compounds.

**Vibrational and Electrochemical Properties.** Figure 6.4 displays the infrared spectra of compound 3 before and after heating at 100 °C under a nitrogen atmosphere. The disappearance of bands at 3573 and 3434  $\text{cm}^{-1}$  after heating is attributed to the loss of coordinated water molecules in the solid state. The spectrum of 3 after heating matches that of the known compound  $[\text{Fe}_2(\mu\text{-O}_2\text{CAr}^{\text{Tol}})_4(4\text{-}^t\text{BuC}_5\text{H}_4\text{N})_2]$ .<sup>11</sup>

The electrochemical properties of 3 were investigated by cyclic voltammetry (Figure 6.5). One irreversible oxidation at  $E_{1/2} = -210$  mV ( $\Delta E_p = 140$  mV;  $i_{pa}/i_{pc} = 5.9$ , scan rate = 50 mV/s) accompanied by a broad reduction wave at ca. -890 mV vs.  $\text{Cp}_2\text{Fe}^+/\text{Cp}_2\text{Fe}$  was observed in  $\text{CH}_2\text{Cl}_2$  solution. When the voltammogram was scanned only cathodically between -343 mV and -1143 mV and recorded, the reduction wave at -890 mV was no longer present (Figure 6.5B). Similar voltammograms (Figure 6.6) were produced by addition of 0, 1, 2, and 3 equiv of  $\text{H}_2\text{O}$  to a  $\text{CH}_2\text{Cl}_2$  solution of the compound  $[\text{Fe}_2(\mu\text{-O}_2\text{CAr}^{\text{Tol}})_4(4\text{-}^t\text{BuC}_5\text{H}_4\text{N})_2]$ . Combined with the IR spectroscopic data, these results can be rationalized in the following manner (Scheme 6.1). Dehydration of 3 in  $\text{CH}_2\text{Cl}_2$  can occur to afford two molecules of water and  $[\text{Fe}_2(\mu\text{-O}_2\text{CAr}^{\text{Tol}})_4(4\text{-}^t\text{BuC}_5\text{H}_4\text{N})_2]$ ,<sup>11</sup> which has a reversible  $\text{Fe}_2(\text{II,II})/\text{Fe}_2(\text{II,III})$  couple at  $E_{1/2} = -216$  mV.<sup>35</sup> Oxidation of  $[\text{Fe}_2(\mu\text{-O}_2\text{CAr}^{\text{Tol}})_4(4\text{-}^t\text{BuC}_5\text{H}_4\text{N})_2]$  provides the mixed-valent cation,  $[\text{Fe}_2(\mu\text{-O}_2\text{CAr}^{\text{Tol}})_4(4\text{-}^t\text{BuC}_5\text{H}_4\text{N})_2]^+$ , which is stable in the absence of water.<sup>35</sup> In presence of water molecules, however, an aquated  $[\text{Fe}_2(\text{O}_2\text{CAr}^{\text{Tol}})_4(4\text{-}^t\text{BuC}_5\text{H}_4\text{N})_2(\text{OH}_2)_x]^+$  species may form, in which  $x$  can be one or two. This complex will exhibit different electrochemical behavior, and its reduction may give rise to the wave at ca -890 mV. The complex

$[\text{Fe}_2(\text{O}_2\text{CAr}^{\text{Tot}})_4(4\text{-}^t\text{BuC}_5\text{H}_4\text{N})_2(\text{OH}_2)_x]$ , generated in this manner, would quickly lose water molecules to form  $[\text{Fe}_2(\mu\text{-O}_2\text{CAr}^{\text{Tot}})_4(4\text{-}^t\text{BuC}_5\text{H}_4\text{N})_2]$ , resulting in no oxidation wave on the reverse sweep until a potential greater than  $-300$  mV is attained. Uptake of water thus appears to lower the reduction potential of the diiron(II) core by  $\sim 610$  mV, as might be expected from the addition of good  $\sigma$  donors to the dimetallic center. Both the reported dissociation of water from  $[\text{Fe}_2(\mu\text{-OH}_2)(\text{O}_2\text{CR})_4(\text{tmen})_2]$  in solution by NMR studies<sup>29</sup> and the association/dissociation of water molecules of  $(\text{Co}_2(\mu\text{-OH}_2)_2)^{4+}$  in solid state<sup>28</sup> are consistent with our observations of reversible water loss from **3** in both the solid and solution states.

The diiron sites in **3** and MMOH both contain four carboxylates, two N-donor ligands, and two water molecules. The two water molecules in the first and second coordination spheres of the kinetically labile diiron(II) sites in MMOH may also be in an equilibrium between bound and free forms, like **3**. Dissociation of water molecules in  $\text{MMOH}_{\text{red}}$ , together with a carboxylate shift, may generate the open coordination site(s) needed for dioxygen binding and activation.<sup>36</sup> In this respect it is noteworthy that, in the presence of the coupling and reductase components, MMOB and MMOR, the redox potential of the diiron center in MMOH changes significantly.<sup>37,38</sup> The present results suggest that this change may reflect loss of coordinated water molecules. On the other hand, DFT calculations of the MMOH reaction cycle identify an associated water molecule as a key component for generating oxygenated intermediate(s).<sup>18-20</sup> A more complete understanding of the effects of water association and dissociation at carboxylate-bridged diiron sites, before and after the introduction of dioxygen, is clearly desirable. Although we now have clear evidence that the water molecules in **3** are reversibly bound, exactly when and how they may influence the oxygenation reactivity of diiron(II) sites remains to be determined. Efforts are underway to clarify the effect of

water in the oxygenation pathways of model complexes with composition similar to that of MMOH.

### Summary

The existence of water molecules at the diiron(II) active sites of carboxylate-bridged diiron enzymes directed us to explore water as a ligand in related complexes supported by sterically hindered carboxylate groups. The first carboxylate rich di(aqua)-bridged diiron(II) complexes have been characterized, completing one end of this series of O-rich diamond core structures. Chemical, IR spectroscopic and electrochemical experiments indicate the reversible generation of the quadruply bridged diiron(II) complex  $[\text{Fe}_2(\mu\text{-O}_2\text{CAr}^{\text{Tol}})_4(4\text{-}^t\text{BuC}_5\text{H}_4\text{N})_2]$  by loss of two water molecules from compound  $[\text{Fe}_2(\mu\text{-OH}_2)_2(\mu\text{-O}_2\text{CAr}^{\text{Tol}})_2(\text{O}_2\text{CAr}^{\text{Tol}})_2(4\text{-}^t\text{BuC}_5\text{H}_4\text{N})_2]$ .

**References**

- \* This work has appeared previously in Yoon, S.; Kelly, A. E.; Lippard, S. J. *Polyhedron* 2004 in press.
- (1) Tshuva, E. Y.; Lippard, S. J. *Chem. Rev.* 2004, 104, 987-1012.
  - (2) Costas, M.; Mehn, M. P.; Jensen, M. P.; Que, L., Jr. *Chem. Rev.* 2004, 104, 939-986.
  - (3) Solomon, E. I.; Brunold, T. C.; Davis, M. I.; Kemsley, J. N.; Lee, S.-K.; Lehnert, N.; Neese, F.; Skulan, A. J.; Yang, Y.-S.; Zhou, J. *Chem. Rev.* 2000, 100, 235-349.
  - (4) Merckx, M.; Kopp, D. A.; Sazinsky, M. H.; Blazyk, J. L.; Müller, J.; Lippard, S. J. *Angew. Chem. Int. Ed.* 2001, 40, 2782-2807.
  - (5) Whittington, D. A.; Lippard, S. J. *J. Am. Chem. Soc.* 2001, 123, 827-838.
  - (6) Sazinsky, M. H.; Bard, J.; Di Donato, A.; Lippard, S. J. *J. Biol. Chem.* 2004, 279, 30600-30610.
  - (7) Stubbe, J.; Donk, W. A. v. d. *Chem. Rev.* 1998, 98, 705-762.
  - (8) Nordlund, P.; Eklund, H. J. *Mol. Biol.* 1993, 232, 123-164.
  - (9) Lindqvist, Y.; Huang, W.; Schneider, G.; Shanklin, J. *EMBO J.* 1996, 15, 4081-4092.
  - (10) Lee, D.; Pierce, B.; Krebs, C.; Hendrich, M. P.; Huynh, B. H.; Lippard, S. J. *J. Am. Chem. Soc.* 2002, 124, 3993-4007.
  - (11) Lee, D.; Lippard, S. J. *Inorg. Chem.* 2002, 41, 2704-2719.
  - (12) Hagadorn, J. R.; Que, L., Jr.; Tolman, W. B. *J. Am. Chem. Soc.* 1998, 120, 13531-13532.
  - (13) Kryatov, S. V.; Chavez, F. A.; Reynolds, A. M.; Rybak-Akimova, E. V.; Que, L., Jr.; Tolman, W. B. *Inorg. Chem.* 2004, 43, 2141-2150.
  - (14) Lee, D.; Lippard, S. J. *J. Am. Chem. Soc.* 2001, 123, 4611-4612.
  - (15) Lee, D.; Lippard, S. J. *Inorg. Chem.* 2002, 41, 827-837.
  - (16) Yoon, S.; Lippard, S. J. *Inorg. Chem.* 2003, 42, 8606-8608.

- (17) Carson, E. C.; Lippard, S. J. *J. Am. Chem. Soc.* 2004, *126*, 3412-3413.
- (18) Dunietz, B. D.; Beachy, M. D.; Cao, Y.; Whittington, D. A.; Lippard, S. J.; Friesner, R. A. *J. Am. Chem. Soc.* 2000, *122*, 2828-2839.
- (19) Gherman, B. F.; Dunietz, B. D.; Whittington, D. A.; Lippard, S. J.; Friesner, R. A. *J. Am. Chem. Soc.* 2001, *123*, 3836-3837.
- (20) Gherman, B. F.; Baik, M.-H.; Lippard, S. J.; Friesner, R. A. *J. Am. Chem. Soc.* 2004, *126*, 2978-2990.
- (21) Pangborn, A. B.; Giardello, M. A.; Grubbs, R. H.; Rosen, R. K.; Timmers, F. J. *Organometallics* 1996, *15*, 1518-1520.
- (22) Du, C.-J. F.; Hart, H.; Ng, K.-K. D. *J. Org. Chem.* 1986, *51*, 3162-3165.
- (23) Chen, C.-T.; Siegel, J. S. *J. Am. Chem. Soc.* 1994, *116*, 5959-5960.
- (24) Kuzelka, J.; Mukhopadhyay, S.; Springler, B.; Lippard, S. J. *Inorg. Chem.* 2004, *43*, 1751-1761.
- (25) Sheldrick, G. M.; University of Göttingen: Göttingen, Germany, 1997.
- (26) Sheldrick, G. M.; University of Göttingen: Göttingen, Germany, 1996.
- (27) Spek, A. L.; Utrecht University: Utrecht, The Netherlands, 1998.
- (28) Lee, D.; Hung, P.-L.; Spingler, B.; Lippard, S. J. *Inorg. Chem.* 2002, *41*, 521-531.
- (29) Hagen, K. S.; Lachicotte, R. *J. Am. Chem. Soc.* 1992, *114*, 8741-8742.
- (30) Coucouvanis, D.; III, R. A. R.; Dunham, W. R. *J. Am. Chem. Soc.* 1995, *117*, 7570-7571.
- (31) III, R. A. R.; Dunham, W. R.; Coucouvanis, D. *Inorg. Chem.* 1998, *37*, 1232-1241.
- (32) MacMurdo, V. L.; Zheng, H.; Que, L., Jr. *Inorg. Chem.* 2000, *39*, 2254-2255.
- (33) Zheng, H.; Zang, Y.; Dong, Y.; Young, V. G., Jr.; Que, L., Jr. *J. Am. Chem. Soc.* 1999, *121*, 2226-2235.



- (34) Hsu, H.-F.; Dong, Y.; Shu, L.; Young, V. G., Jr.; Que, L., Jr. *J. Am. Chem. Soc.* 1999, 121, 5230-5237.
- (35) Lee, D.; DuBois, J. L.; Pierce, B.; Hedman, B.; Hodgson, K. O.; Hendrich, M. P.; Lippard, S. J. *Inorg. Chem.* 2002, 41, 3172-3182.
- (36) Rosenzweig, A. C.; Nordlund, P.; Takahara, P. M.; Frederick, C. A.; Lippard, S. J. *Chem. Biol.* 1995, 2, 409-418.
- (37) Liu, K. E.; Lippard, S. J. *J. Biol. Chem.* 1991, 266, 12836-12839.
- (38) Liu, Y.; Nesheim, J. C.; Paulsen, K. E.; Stankovich, M. T.; Lipscomb, J. D. *Biochemistry* 1997, 36, 5223-5233.

**Table 6.1.** Summary of X-ray crystallographic information for  $[\text{Fe}_2(\text{OH})_2(\mu\text{-O}_2\text{CAr}^{\text{4F-Ph}})_2(\text{THF})_2]$  (1),  $[\text{Fe}_2(\mu\text{-OH})_2(\mu\text{-O}_2\text{CAr}^{\text{Tol}})_2(\text{O}_2\text{CAr}^{\text{Tol}})_2(\text{THF})_2]$  (2) and  $[\text{Fe}_2(\mu\text{-OH})_2(\mu\text{-O}_2\text{CAr}^{\text{Tol}})_2(\text{O}_2\text{CAr}^{\text{Tol}})_2(4\text{-}^t\text{BuC}_5\text{H}_4\text{N})_2]$  (3).

Compound	1·2CH <sub>2</sub> Cl <sub>2</sub>	2	3·THF·1 / 2Pentane
empirical formula	Fe <sub>2</sub> C <sub>86</sub> H <sub>68</sub> O <sub>12</sub> F <sub>8</sub> Cl <sub>4</sub>	Fe <sub>2</sub> C <sub>92</sub> H <sub>88</sub> O <sub>12</sub>	Fe <sub>2</sub> C <sub>108.5</sub> H <sub>112</sub> N <sub>2</sub> O <sub>11</sub>
weight	1698.90	1497.33	1731.70
space group	P $\bar{1}$	P21/c	C2/c
<i>a</i> , Å	12.3562(11)	13.509(3)	23.880(6)
<i>b</i> , Å	13.9639(13)	14.260(3)	17.100(4)
<i>c</i> , Å	14.0539(13)	20.278(4)	27.078(7)
$\alpha$ , deg	97.189(2)		
$\beta$ , deg	114.862(2)	104.707(3)	112.139(4)
$\gamma$ , deg	111.331(2)		
<i>V</i> , Å <sup>3</sup>	1935.3(3)	3778.6(13)	10208(4)
<i>Z</i>	1	2	4
$\rho_{\text{calc}}$ , g/cm <sup>3</sup>	1.458	1.316	1.127
<i>T</i> , °C	-100	-100	-100
$\mu$ (Mo K $\alpha$ ), mm <sup>-1</sup>	0.596	0.449	0.341
total no. of data	14443	31708	37188
no. of unique data	6755	8571	9008
no. of params	651	490	616
<i>R</i> (%) <sup>a</sup>	4.55	4.02	6.49
<i>R</i> <sub>w</sub> <sup>2</sup> (%) <sup>b</sup>	11.81	10.76	20.84
max, min peaks, e/Å <sup>3</sup>	0.370, -0.349	0.544, -0.232	0.768, -0.365

<sup>a</sup>  $R = \frac{\sum ||F_o| - |F_c||}{\sum |F_o|}$ . <sup>b</sup>  $R_w^2 = \left\{ \frac{\sum [w(F_o^2 - F_c^2)^2]}{\sum [w(F_o^2)^2]} \right\}^{1/2}$

**Table 6.2.** Selected interatomic bond lengths (Å) and angles (deg) for [Fe<sub>2</sub>(OH<sub>2</sub>)<sub>2</sub>(μ-O<sub>2</sub>CAr<sup>4F-Ph</sup>)<sub>2</sub>(O<sub>2</sub>CAr<sup>4F-Ph</sup>)<sub>2</sub>(THF)<sub>2</sub>] (1), [Fe<sub>2</sub>(μ-OH<sub>2</sub>)<sub>2</sub>(μ-O<sub>2</sub>CAr<sup>Tol</sup>)<sub>2</sub>(O<sub>2</sub>CAr<sup>Tol</sup>)<sub>2</sub>(THF)<sub>2</sub>] (2) and [Fe<sub>2</sub>(μ-OH<sub>2</sub>)<sub>2</sub>(μ-O<sub>2</sub>CAr<sup>Tol</sup>)<sub>2</sub>(O<sub>2</sub>CAr<sup>Tol</sup>)<sub>2</sub>(4-<sup>t</sup>BuC<sub>5</sub>H<sub>4</sub>N)<sub>2</sub>] (3).

Compound	1·2CH <sub>2</sub> Cl <sub>2</sub>	2	3·THF·1/2Pentane
Fe1...Fe1A	3.4433(8)	3.073(4)	3.0548(10)
Fe1-O1	2.157(2)	2.2903(11)	2.292(3)
Fe1A-O1	3.1070(21)	2.3161(12)	2.306(3)
Fe1-O2	2.0391(18)	2.0806(11)	2.043(2)
Fe1-O3	2.0099(18)	2.0334(11)	2.085(2)
Fe1-O4	2.0298(18)	2.0536(11)	2.060(2)
Fe1-L <sup>a</sup>	2.1012(18)	2.1014(11)	2.132(3)
Fe1-O1-Fe1A	N/A	83.68(4)	83.26(9)
O1-Fe1-O1A	N/A	96.32(4)	96.74(9)
O2-Fe1-O3	138.60(7)	156.40(4)	156.85(9)
O1-Fe1-O4	92.12(8)	89.30(4)	89.06(9)
O1-Fe1-L <sup>a</sup>	176.07(8)	176.85(4)	177.84(11)
O2-Fe1-O4	108.55(7)	105.85(6)	105.68(9)
O3-Fe1-O4	112.85(7)	105.60(4)	93.73(9)
O2-Fe1-L <sup>a</sup>	90.39(7)	94.36(5)	96.02(10)
O3-Fe1-L <sup>a</sup>	89.08(8)	96.29(5)	96.90(10)
O4-Fe1-L <sup>a</sup>	91.46(8)	87.59(4)	88.79(10)
O2-Fe1-O1	90.02(8)	83.75(5)	84.81(10)
O3-Fe1-O1	88.02(8)	84.04(5)	82.99(9)
O2-Fe1-O1A	N/A	77.65(4)	83.60(10)
O3-Fe1-O1A	N/A	83.72(5)	78.40(9)
O4-Fe1-O1A	N/A	169.62(4)	169.52(10)
L <sup>a</sup> -Fe1-O1A	N/A	86.83(4)	85.34(10)
O5...O1	2.608(2)	2.543(2)	2.5519(36)

Numbers in parentheses are estimated standard deviations of the last significant figures.

<sup>a</sup> L is the O-atom of THF in 1 and 2, the N-atom of 4-<sup>t</sup>BuC<sub>5</sub>H<sub>4</sub>N in 3, respectively.

Chart 1

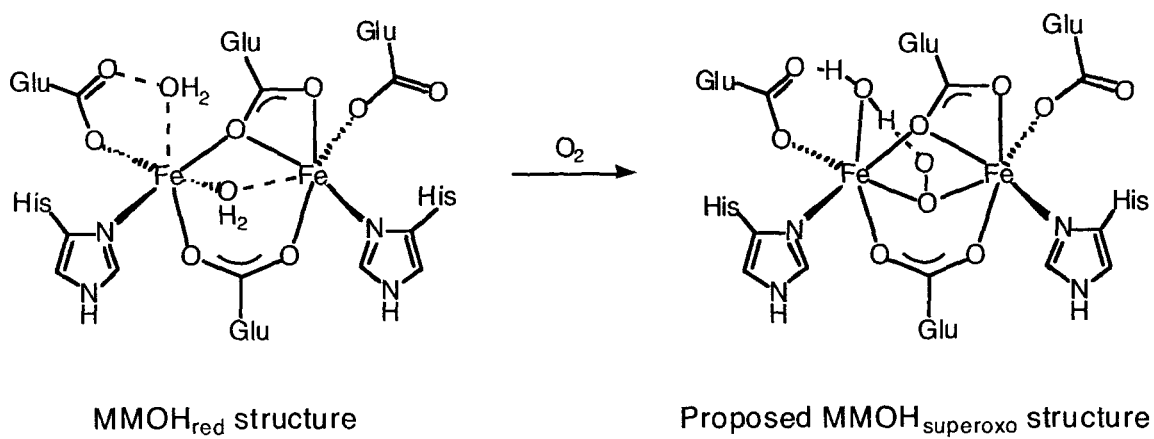
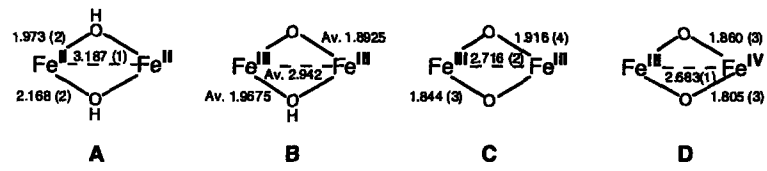


Chart 6.1.

Chart 2

## N-rich metal coordination environment



## O-rich metal coordination environment

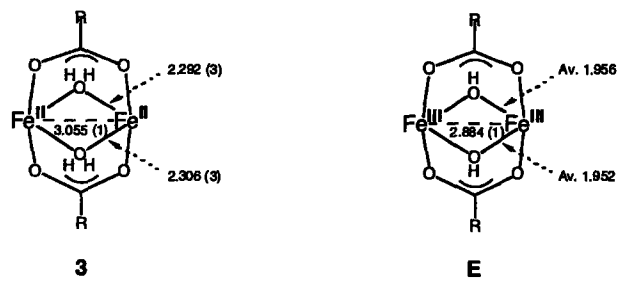
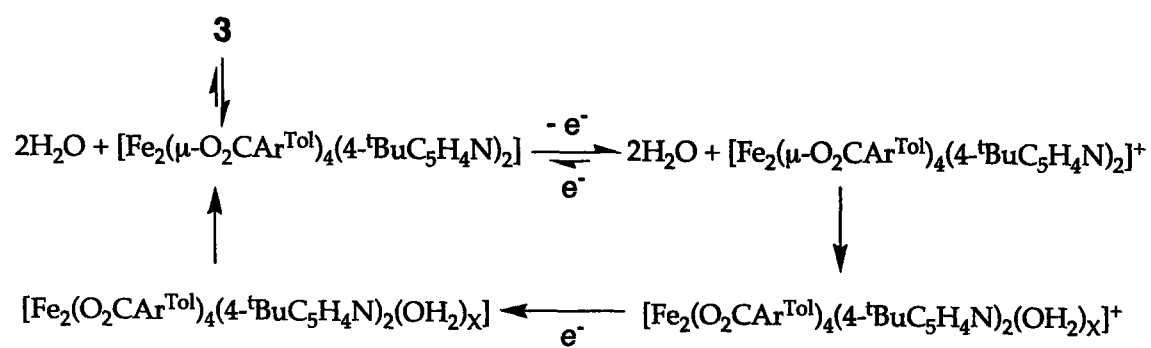
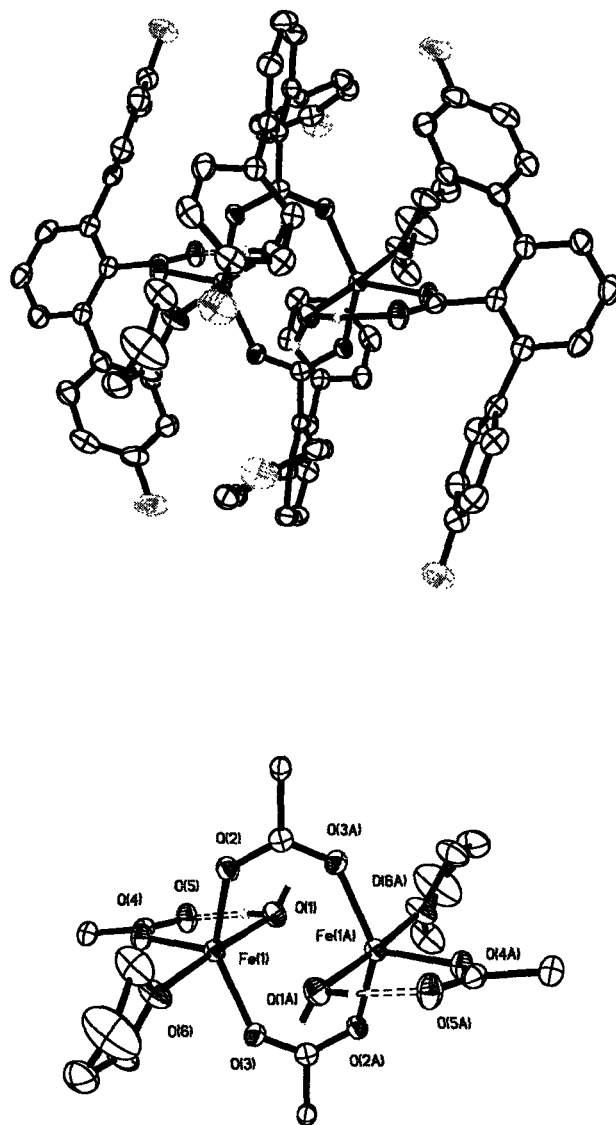


Chart 6.2.

Scheme 1



Scheme 6.1.



**Figure 6.1.** Top: ORTEP diagrams of  $[\text{Fe}_2(\text{OH})_2(\mu\text{-O}_2\text{CAr}^{4\text{F-Ph}})_2(\text{O}_2\text{CAr}^{4\text{F-Ph}})_2(\text{THF})_2]$  (1) showing 50 % probability thermal ellipsoids for all non-hydrogen atoms. Bottom: Drawing with the aromatic rings of  $\text{Ar}^{4\text{F-Ph}}\text{CO}_2^-$  ligands omitted for clarity.

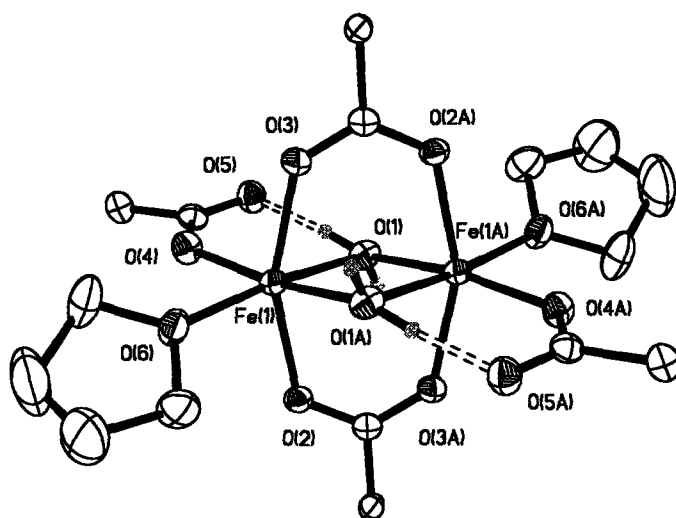


**Figure 6.2.** ORTEP diagram of  $[\text{Fe}_2(\mu\text{-OH})_2(\mu\text{-O}_2\text{CAR}^{\text{Tol}})_2(\text{O}_2\text{CAR}^{\text{Tol}})_2(\text{THF})_2]$  (**2**) showing 50 % probability thermal ellipsoids for all non-hydrogen atoms. The aromatic rings of  $\text{Ar}^{\text{Tol}}\text{CO}_2^-$  ligands are omitted for clarity.



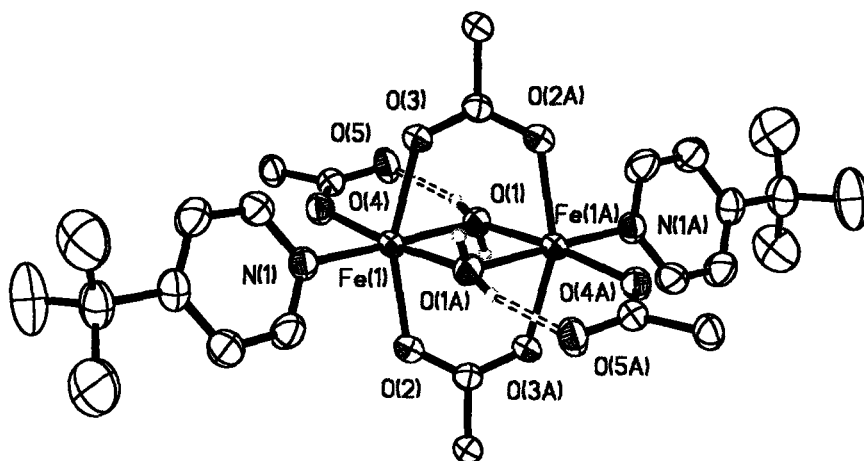


**Figure 6.3.** ORTEP diagrams of  $[\text{Fe}_2(\mu\text{-OH})_2(\mu\text{-O}_2\text{CAr}^{\text{Tol}})_2(\text{O}_2\text{CAr}^{\text{Tol}})_2(4\text{-}^t\text{BuC}_5\text{H}_4\text{N})_2]$  (**3**) showing 50 % probability thermal ellipsoids for all non-hydrogen atoms. Drawing with the aromatic rings of  $\text{Ar}^{\text{Tol}}\text{CO}_2^-$  ligands omitted for clarity.

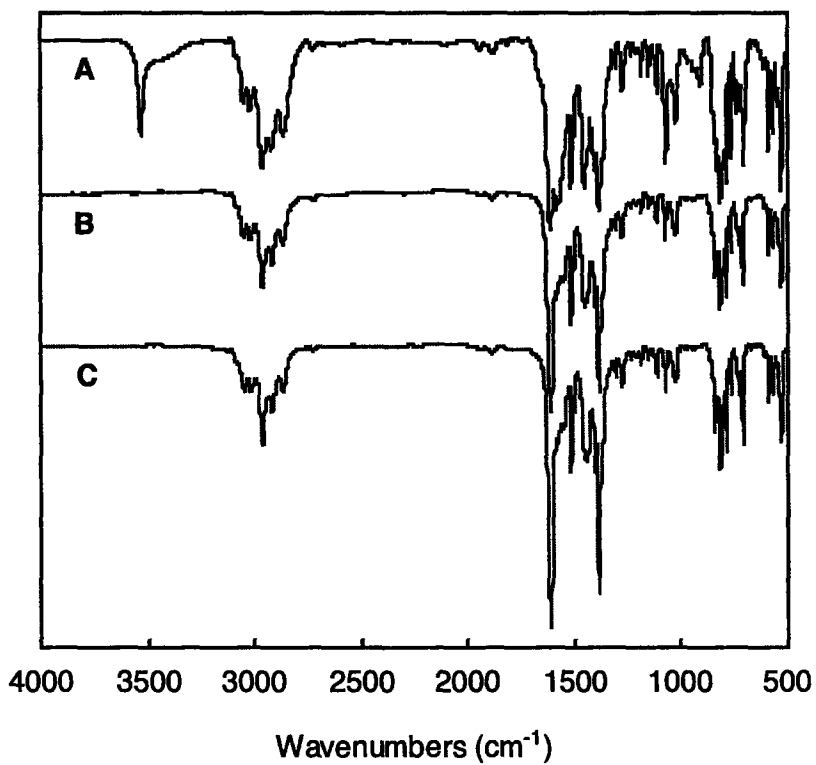


**Figure 6.4.** IR spectra of (A, B)  $[\text{Fe}_2(\mu\text{-OH}_2)_2(\mu\text{-O}_2\text{CAr}^{\text{Tol}})_2(\text{O}_2\text{CAr}^{\text{Tol}})_2(4\text{-}^t\text{BuC}_5\text{H}_4\text{N})_2]$  (**3**), before and after heating, and (C)  $[\text{Fe}_2(\mu\text{-O}_2\text{CAr}^{\text{Tol}})_4(4\text{-}^t\text{BuC}_5\text{H}_4\text{N})_2]$ .

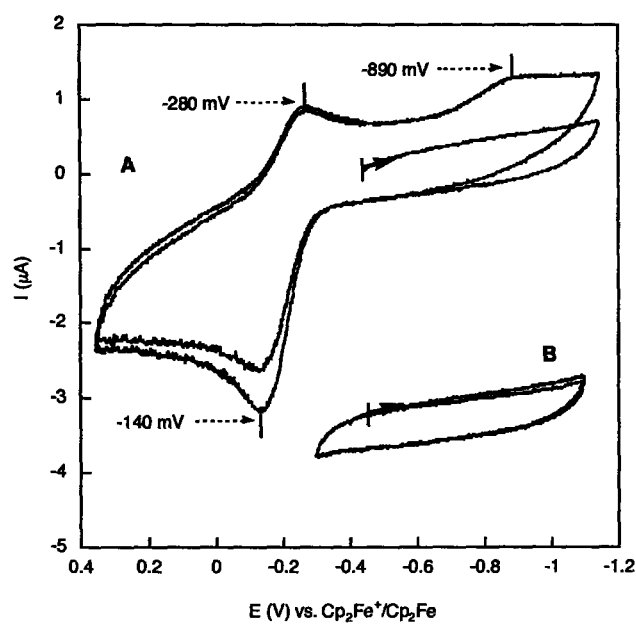


**Figure 6.5.** Cyclic voltammograms of (A and B)  $[\text{Fe}_2(\mu\text{-OH})_2(\mu\text{-O}_2\text{CAr}^{\text{Tol}})_2(\text{O}_2\text{CAr}^{\text{Tol}})_2(4\text{-}^t\text{BuC}_5\text{H}_4\text{N})_2]$  (**3**) in  $\text{CH}_2\text{Cl}_2$  with 0.5 M  $(\text{Bu}_4\text{N})\text{PF}_6$  as supporting electrolyte and a scan rate of 50 mV/s.

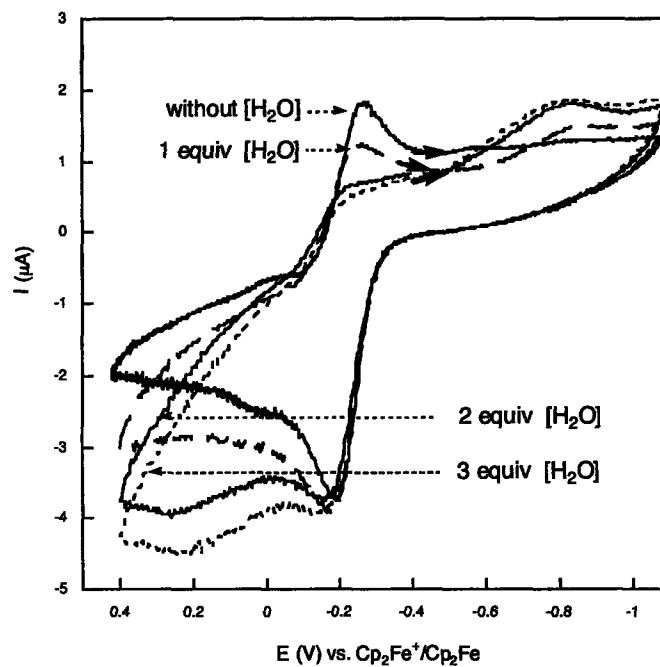


**Figure 6.6.** Cyclic voltammograms of  $[\text{Fe}_2(\mu\text{-O}_2\text{CAr}^{\text{Tol}})_4(4\text{-}^t\text{BuC}_5\text{H}_4\text{N})_2]$  with variable amounts of  $\text{H}_2\text{O}$  in  $\text{CH}_2\text{Cl}_2$  with 0.5 M  $(\text{Bu}_4\text{N})\text{PF}_6$  as supporting electrolyte and a scan rate of 50 mV/s.

## **Chapter 7**

### **Water-Dependent Reactions of Diiron(II) Carboxylate Complexes**

## Introduction

Carboxylate-bridged diiron(II) cores, housed in the four-helix bundles, occur frequently in the active sites of dioxygen-dependent non-heme diiron(II) enzymes.<sup>1-3</sup> The R2 subunit of ribonucleotide reductase (RNR-R2),  $\Delta$ -9-desaturase ( $\Delta$ 9D), and the hydroxylase component of soluble methane monooxygenase (sMMOH) are important members of this metalloprotein family. A common diiron structural unit, in O-donor ligand, is utilized to achieve the diverse, physiologically related roles of these enzymes. Much effort has been devoted to reproducing the structures and functions of these active sites by synthetic model complexes.<sup>14</sup> Studies of the oxygenation reactions of these system have contributed to our understanding of the chemistry in the oxygenation cycle of enzymes. Few of the models, however, address the role of water in determining the reactivity of the carboxylate-rich diiron(II) sites. Recently we reported the designed synthesis of the water-containing diiron(II) complexes as our initial effort to address this issue.<sup>5</sup> Our result suggested the existence of the water-dependent equilibria as an important factor in directing the chemistry.

In the present chapter we describe the isolation and characterization of diiron(II) complexes with varying numbers of ligated water molecules and supporting 2,6-di-(*p*-fluorophenyl)benzoate ( $\text{O}_2\text{CAr}^{4\text{F-Ph}}$ )<sup>6</sup> ligands. X-ray crystallographically determined structures, clearly delineate a series of water-induced conversions, which may reflect transformations that occur at the diiron(II) sites of related metalloproteins in an aqueous environment. The physical properties of novel water-bridged diiron(II) complexes are also described.

## Experimental

**General Considerations.** All reagents were obtained from commercial suppliers and used as received unless otherwise noted. Pentane and THF were saturated with argon and purified by passage through activated  $\text{Al}_2\text{O}_3$  columns under argon.<sup>7</sup> The compound  $[\text{Fe}_2(\mu\text{-O}_2\text{CAr}^{4\text{F-Ph}})_2(\text{O}_2\text{CAr}^{4\text{F-Ph}})_2(\text{THF})_2]$  was prepared as described in the literature.<sup>9</sup> All syntheses and air-sensitive manipulations were carried out under nitrogen in an MBraun glovebox. FT-IR spectra were recorded with a Thermo Nicolet Avatar 360 spectrometer.

$[\text{Fe}(\text{H}_2\text{O})_6](\text{O}_2\text{CAr}^{4\text{F-Ph}})_2 \cdot 2\text{THF}$  (**1**). To a portion (45.4 mg, 32.3  $\mu\text{mol}$ ) of  $[\text{Fe}_2(\mu\text{-O}_2\text{CAr}^{4\text{F-Ph}})_2(\text{O}_2\text{CAr}^{4\text{F-Ph}})_2(\text{THF})_2]$  was added a THF solution (0.7 mL) containing 20  $\mu\text{L}$  (1.11 mmol) of  $\text{H}_2\text{O}$ . Dissolution occurred within 30 min to yield a light green solution. Colorless needles of **1**, obtained within 2 days of pentane diffusion into the solution, were analyzed by X-ray crystallography. The quantity of needles diminishes if crystals are allowed to be stored without isolation.

$[\text{Fe}_2(\mu\text{-OH}_2)_2(\mu\text{-O}_2\text{CAr}^{4\text{FPh}})(\text{O}_2\text{CAr}^{4\text{FPh}})_3(\text{THF})_2(\text{OH}_2)]$  (**2**). To a portion (45.4 mg, 32.3  $\mu\text{mol}$ ) of  $[\text{Fe}_2(\mu\text{-O}_2\text{CAr}^{4\text{F-Ph}})_2(\text{O}_2\text{CAr}^{4\text{F-Ph}})_2(\text{THF})_2]$  was added a THF solution (0.7 mL) containing 10  $\mu\text{L}$  (0.56 mmol) of  $\text{H}_2\text{O}$ . Dissolution within 30 min occurs without stirring to yield a light green solution. Colorless multifaceted blocks of **2** (19.9 mg, 41 % yield) were obtained within 2 days by diffusing pentane into the solution and were analyzed by X-ray crystallography. FT-IR (KBr,  $\text{cm}^{-1}$ ) 3601 (w,  $\nu_{\text{O-H}}$ ), 3434 (w, br,  $\nu_{\text{O-H}}$ ), 3064 (w), 2957 (w), 1605 (s), 1546 (w), 1510 (s), 1455 (m), 1408 (w), 1380 (m), 1299 (w), 1225 (m), 1095 (w), 1071 (w), 1036 (w), 1014 (w), 914 (w), 880 (w), 853 (w), 838 (m), 808 (s), 789 (w), 774 (w), 737 (w), 712 (w), 700 (w), 582 (w), 554 (m), 529 (m). Anal. Calcd for  $2 \cdot 2\text{THF}$  or  $\text{C}_{92}\text{H}_{82}\text{Fe}_2\text{O}_{15}\text{F}_8$ : C, 65.33; H, 4.89. Found: C, 65.13; H, 5.31.

$[\text{Fe}_2(\text{OH})_2(\mu\text{-O}_2\text{CAr}^{\text{4F-Ph}})_2(\text{O}_2\text{CAr}^{\text{4F-Ph}})_2(\text{THF})_2][\text{Fe}_2(\mu\text{-O}_2\text{CAr}^{\text{4F-Ph}})_2(\text{O}_2\text{CAr}^{\text{4F-Ph}})_2(\text{THF})_2]$  (3). A portion (50.5 mg, 31.8  $\mu\text{mol}$ ) of 2 was added to THF (1 mL). Stirring effected dissolution within 30 min to yield a colorless solution. A cluster of colorless square blocks of 3 developed upon layering pentane onto the solution. The composition was revealed by X-ray crystallography.

**X-ray Crystallography.** Single crystals were mounted at room temperature on the tips of quartz fibers, coated with Paratone-N oil, and cooled under a stream of cold nitrogen. Intensity data were collected on a Bruker (formerly Siemens) APEX CCD diffractometer running the SMART software package, with Mo K $\alpha$  radiation ( $\lambda = 0.71073$  Å). Data collection and reduction protocols are described in detail elsewhere.<sup>11</sup> The structures were solved by Patterson methods and refined on  $F^2$  by using the SHELXTL software package.<sup>12</sup> Empirical absorption corrections were applied with SADABS<sup>13</sup>, part of the SHELXTL program package, and the structures were checked for higher symmetry by the program PLATON.<sup>14</sup> All non-hydrogen atoms were refined anisotropically. In general, hydrogen atoms were assigned idealized positions and given thermal parameters equivalent to either 1.5 (methyl hydrogen atoms) or 1.2 (all other hydrogen atoms) times the thermal parameter of the carbon atom to which they were attached. Hydrogen atoms of the coordinated water molecules were identified from difference Fourier maps. In the structure of 1, an oxygen atom in one of the THF solvent molecules was disordered in two positions and refined as such with half occupancy factors. The structure of 2 contains 2.5 THF molecules over three positions in the lattice with 1, 0.75, and 0.75 occupancies. The structure of 2 also contains 0.75 H<sub>2</sub>O molecule in the lattice. The structure of 3 contains 1 pentane molecule in lattice. Data collection and experimental details for the complexes are summarized in Table 7.1 and



relevant interatomic bond lengths and angles for **1** and **2** are listed in Tables 7.2 and 7.3, respectively.

**<sup>57</sup>Fe Mössbauer Spectroscopy.** Mössbauer spectra were obtained on an MS1 spectrometer (WEB Research Co.) with a <sup>57</sup>Co source in a Rh matrix maintained at room temperature in the DCIF. Solid samples were prepared by suspending ca 0.015 mmol of the powdered material in Apeizon N grease and packing the mixture into a nylon sample holder. All data were collected at 4.2 K and the isomer shift ( $\delta$ ) values are reported with respect to natural iron foil that was used for velocity calibration at room temperature. The spectra were fit to Lorentzian lines by using the WMOSS plot and fit program.<sup>15</sup>

**Magnetic Susceptibility.** Multifield saturation magnetic susceptibility data for powdered solid **2** were measured between 2 and 300 K with applied magnetic fields of 0.1, 1, 2.5, and 5 T using a Quantum design MPMS SQUID susceptometer. The finely powdered sample was loaded in a gel capsule and suspended in a plastic straw. The susceptibilities of the straw and gel capsule were independently determined over the same temperature range and fields in order to correct for their contribution to the total measured susceptibility. The saturation magnetization data of **2** were fit by using the simplex method to determine the spin Hamiltonian parameter set that yielded the minimum standard quality of fit parameter,  $\chi^2$ .<sup>16-18</sup> The software package (WMAG) used to carry out the data analysis is a product of WEB Research Co., Edina, MN, U.S.A.

## Results and Discussion

**Synthesis and Structural Characterization of the HexaaquaIron(II) Complex [Fe(H<sub>2</sub>O)<sub>6</sub>](O<sub>2</sub>CAr<sup>4-FPh</sup>)<sub>2</sub>·2(THF) (**1**).** The dissolution of [Fe<sub>2</sub>( $\mu$ -O<sub>2</sub>CAr<sup>4F-Ph</sup>)<sub>2</sub>(O<sub>2</sub>CAr<sup>4F-Ph</sup>)<sub>2</sub>(THF)<sub>2</sub>] in THF with 20 equiv of water, followed by pentane diffusion, results in

colorless long needles. The structure of **1** is depicted in Figure 7.1 and selected interatomic distances and angles are listed in Table 7.2. Two octahedral hexaqua iron(II) units are housed in the unit cell, with Fe–O bond length ranging from 2.1055(17) to 2.1673(16) Å. The charge of hexairon(II) unit is balanced by two carboxylate units, and there are also two THF molecules in the asymmetric unit. The CO<sub>2</sub><sup>-</sup> moieties of the carboxylates are oriented perpendicular to each other (Figure 7.1 Top), with C–O bond length of 2.247(2) Å, 2.253(2) Å, 2.255(2) Å, and 2.259(2) Å. These values indicate them to be deprotonated. The average O···O distance between the carboxylate and coordinated water O-atoms is 2.737(23) Å, indicating the presence of hydrogen bonding interactions. The oxygen atom in THF is also near the oxygen atoms of coordinated water molecules at O···O separations of 2.643 and 2.690 Å. Hydrogen bonding interactions also occur between water molecules on adjacent iron(II) sites, with O···O separations of 2.955 and 3.129 Å (Figure 7.2). The adjacent iron(II) octahedral are twisted by 45 degrees relative to each other and propagate in one dimension. All 12 hydrogen atoms in the six water molecules are involved a tight hydrogen bonding network along the one dimensional iron(II) channel. Two modes of carboxylate orientations, parallel and perpendicular to the direction of the channel, repeat along this channel. The sterically hindered carboxylates separate one channel from another by ~ 14 Å, as shown in Figure 7.1 bottom. Unfortunately, the colorless needles quickly lose their identity when removed from solution, as evidenced by a change in color possibly indication of decomposition. This instability hindered further physical characterizations of compound **1**.

**Synthesis and Structural Characterization of [Fe<sub>2</sub>(μ-OH<sub>2</sub>)<sub>2</sub>(μ-O<sub>2</sub>CAr<sup>AF-Ph</sup>)-(O<sub>2</sub>CAr<sup>AF-Ph</sup>)<sub>3</sub>(THF)<sub>2</sub>(OH<sub>2</sub>)] (2) and [Fe<sub>2</sub>(OH<sub>2</sub>)<sub>2</sub>(μ-O<sub>2</sub>CAr<sup>AF-Ph</sup>)<sub>2</sub>(O<sub>2</sub>CAr<sup>AF-Ph</sup>)<sub>2</sub>(THF)<sub>2</sub>][Fe<sub>2</sub>(μ-O<sub>2</sub>CAr<sup>AF-Ph</sup>)<sub>2</sub>(O<sub>2</sub>CAr<sup>AF-Ph</sup>)<sub>2</sub>(THF)<sub>2</sub>] (3).** Colorless block crystals of **2** were initially observed

to form in the reaction of  $[\text{Fe}_2(\mu\text{-O}_2\text{CAr}^{4\text{F-Ph}})_2(\text{O}_2\text{CAr}^{4\text{F-Ph}})_2(\text{THF})_2]^9$  with 34 equiv of water, after separation of compound 1 from the solution. Since 2 has fewer water molecules than 1, this result suggested that formation of 1 may diminish the water content in the solution leading to diiron(II) complexes containing fewer water molecules. This hypothesis was confirmed by the synthesis of complex 2 through reaction of  $[\text{Fe}_2(\mu\text{-O}_2\text{CAr}^{4\text{F-Ph}})_2(\text{O}_2\text{CAr}^{4\text{F-Ph}})_2(\text{THF})_2]^9$  with 17 equiv of water. Colorless multifaceted crystals of 2 were obtained upon vapor diffusion of pentane. The structure of 2 is shown in Figure 7.3 and selected interatomic distance and angles are provided in Table 7.3. Two iron(II) atoms having a pseudo-octahedral coordination geometry are bridged by one carboxylate and two water molecules. The Fe1–O1–Fe2 unit has Fe2–O1 and Fe1–O1 distances of 2.233(2) and 2.294(2) Å, respectively, and a 93.18(8)° bridging angle. For Fe1–O2–Fe2 the values are Fe2–O2 and Fe1–O2 distances of 2.234(2) and 2.152(2) Å, respectively, and a 97.14(8)° for the angle. The  $\text{Fe}_2(\text{OH}_2)_2$  unit is bent up and away from the bridging carboxylate. The Fe...Fe distance is 3.289(3) Å. This diiron(II) core has not been previously reported in structures of either small molecules or metalloproteins, The bent motif occurs in the  $\{\text{Fe}_2(\mu\text{-OH})_2(\mu\text{-O}_2\text{CR})(\text{OH}_2)\}^{3+}$  cores of the diiron(III) sites in the enzymes.<sup>22,23</sup> Each iron(II) center contains one terminal carboxylate, which makes a hydrogen bonding interaction with the bridging water molecule at O...O distances of 2.587 and 2.546 Å. The position of the Fe1 site trans to the bridging carboxylate is occupied by a terminal carboxylate, which is hydrogen-bonded to the bridging water molecule O<sub>2</sub>. A terminal water molecule occupies the corresponding site on the Fe2 and is strongly hydrogen-bonded to the terminal carboxylate on Fe1 at an O...O distance of 2.721 Å. This interaction stabilizes a  $\{\text{Fe}_2(\mu\text{-OH}_2)_2\}^{4+}$  core fragment. The hydrogen atom on the axial water interacts with a THF molecule in the crystal lattice at an O...O

distance of 2.644 Å. The closest intermolecular separation in the lattice between the centers of the diiron units is 13.22 Å, indicating that solid **2** is magnetically dilute.

The dissolution of **2** in THF, followed by re-crystallization, affords **3**. The structure, displayed in Figure 7.4, reveals two different diiron(II) units, with composition  $[\text{Fe}_2(\mu\text{-O}_2\text{CAr}^{4\text{F-Ph}})_2(\text{O}_2\text{CAr}^{4\text{F-Ph}})_2(\text{THF})_2]$ <sup>9</sup> and  $[\text{Fe}_2(\text{OH})_2(\mu\text{-O}_2\text{CAr}^{4\text{F-Ph}})_2(\text{O}_2\text{CAr}^{4\text{F-Ph}})_2(\text{THF})_2]$ .<sup>5</sup> Both of these compounds were previously reported from our laboratory. The isolation of these water-containing **3** is in accord with our working hypothesis, that these water-containing carboxylate-rich diiron(II) complexes are in dynamic equilibrium with one another.

Only one species,  $[\text{Fe}_2(\mu\text{-OH})_2(\mu\text{-O}_2\text{CAr}^{\text{Tol}})_2(\text{O}_2\text{CAr}^{\text{Tol}})_2(\text{THF})_2]$ <sup>5</sup> has been detected in the reaction of  $[\text{Fe}_2(\mu\text{-O}_2\text{CAr}^{\text{Tol}})_2(\text{O}_2\text{CAr}^{\text{Tol}})_2(\text{THF})_2]$  with water. This finding is interesting considering to the variety of water-containing diiron(II) complexes containing  $\text{O}_2\text{CAr}^{4\text{F-Ph}}$  ligands. The difference may be related to the solubility considerations. Iron(II) complexes with  $\text{O}_2\text{CAr}^{4\text{F-Ph}}$  ligands are often less soluble in aprotic solvents than those of 2,6-di-(*p*-tolyl)benzoate ( $\text{O}_2\text{CAr}^{\text{Tol}}$ ).<sup>6</sup> Thus, the complexes isolated may reflect kinetic products.

**Mössbauer Spectroscopic Properties of Complex 2.** The zero-field Mössbauer spectrum of **2** was recorded at 4.2 K to address the influence of water coordination on the Mössbauer parameters (Figure 7.5). The symmetric quadrupole doublet indicates that the two different iron sites are indistinguishable under Mössbauer conditions. The isomer shift ( $\delta = 1.35(2) \text{ mm s}^{-1}$ ), quadrupole splitting ( $\Delta E_{\text{Q}} = 3.26(2) \text{ mm s}^{-1}$ ), and linewidth  $\Gamma = 0.25(2) \text{ mm s}^{-1}$  are comparable to with those of other high-spin iron(II) complexes.

**Multifield Saturated Magnetic Susceptibility Properties of Compound 2.** A ferromagnetic exchange coupling interaction of the two iron(II) sites in sMMOH has

temperature. The solid lines in Figure 7.5 were calculated by diagonalization of the full  $25 \times 25$  spin Hamiltonian of eq 1 with  $J = 0.02 \text{ cm}^{-1}$ ,  $D_1 = D_2 = -5.3 \text{ cm}^{-1}$ ,  $E_1/D_1 = E_2/D_2 = 0.13$ , and  $g_1 = g_2 = 2.02$  and  $\chi^2 = 11.5$ . The  $J$  value close to zero indicates that there is no significant exchange coupling interaction between two high-spin diiron(II) sites. When compared to the previously described ferromagnetically coupled dibridged diiron(II) complexes, this result suggests that the magnetic interaction in these systems may also depend on the planarity of the  $\text{Fe}_2(\text{X})_2$  site, where X is the bridging atom.

### Conclusions and Summary

Use of the sterically-hindered 2,6-di-(*p*-fluorophenyl)benzoate ( $\text{O}_2\text{CAr}^{4\text{F-Ph}}$ ) ligand, which has moderate solubility in organic solvents, afforded iron(II) complexes with a diverse number of water molecules. The synthetic pathway, shown in Scheme 7.1, reveals the existence of water-dependent equilibria. The complete disruption of the  $[\text{Fe}_2(\mu\text{-O}_2\text{CAr}^{4\text{F-Ph}})_2(\text{O}_2\text{CAr}^{4\text{F-Ph}})_2(\text{THF})_2]$  complex by the addition of 34 equiv of water reveals that the polymeric hydrated ferrous ion is very stable and that the carboxylate ligands provide further electrostatic and hydrogen bonding interactions contributions to this stability. When less water is added, diiron(II) complex 2, with three water molecules, two in the bridging position and one in the terminal position is generated. The related and previously known complex  $[\text{Fe}_2(\text{OH}_2)_2(\mu\text{-O}_2\text{CAr}^{4\text{F-Ph}})_2(\text{O}_2\text{CAr}^{4\text{F-Ph}})_2(\text{THF})_2]$  contains just two water molecules, both in bridging positions. Even an average of fewer water molecules occur in  $[\text{Fe}_2(\text{OH}_2)_2(\mu\text{-O}_2\text{CAr}^{4\text{F-Ph}})_2(\text{O}_2\text{CAr}^{4\text{F-Ph}})_2(\text{THF})_2] \cdot [\text{Fe}_2(\mu\text{-O}_2\text{CAr}^{4\text{F-Ph}})_2(\text{O}_2\text{CAr}^{4\text{F-Ph}})_2(\text{THF})_2]$ . The isolation of these five diiron(II) compounds strongly support the occurrence of water-dependent equilibria in the solution. Carboxylate-rich diiron units apparently can accommodate diverse geometries depending on the amount of water available. The diiron(II) sites in sMMOH,<sup>22</sup> RNR-

been revealed by resonance techniques.<sup>24</sup> Such ferromagnetic coupling very rare, even among synthetic diiron(II) molecules.<sup>18,25,26</sup> Only the dihalide,<sup>25</sup> diphenoxide,<sup>18,26</sup> and recently observed diaqua<sup>27</sup> bridged diiron(II) complexes have displayed ferromagnetic exchange coupling between the two iron(II) sites. These observations suggest that two single atom bridges are required for such coupling, suggesting the diiron(II) site in reduced sMMOH may contain two single atom bridges.<sup>18,26</sup> The previously reported ferromagnetically coupled diiron(II) complexes have another common feature, namely, that two single atom bridges are all in the plane defined by the two iron(II) atoms and the two bridging atoms. It was therefore of interest to see whether complex 2 which has two single-atom bridges but a non-planar core, exhibit a ferromagnetic exchange coupling interaction.

In order to address this issue, multifold saturated magnetic susceptibility measurements of 2 were made (Figure 7.6). The effective magnetic moment ( $\mu_{eff}$ ) of 2 steadily decreases from 7.2  $\mu_B$  at 300 K to 6.6  $\mu_B$  at 2 K. This behavior signals weak exchange coupling between the two high-spin iron(II) centers of the triply-bridged dimer. The energy levels of the system formed by two exchange coupled high-spin ferrous ( $S = 2$ ) sites can be described by the spin Hamiltonian given in eq 1, where  $J$  is the isotropic exchange coupling constant,  $D_i$  and  $E_i$  are the axial and rhombic zero-field splitting parameters, and  $\mathbf{g}_i$  is the  $\mathbf{g}$  tensors of the uncoupled site ( $i = 1, 2$ ). We assumed two identical, collinear high spin diiron(II) sites to prevent overparameterization.

$$H = -2JS_1 \cdot S_2 + \sum_i [D_i(S_{zi}^2 - 2) + E_i(S_{xi}^2 - S_{yi}^2) + \beta S_i \cdot \mathbf{g}_i \cdot \mathbf{H}] \quad i = 1, 2 \quad (1)$$

In Figure 7.6 Top the data are presented as magnetic moment versus temperature at all four fields. In Figure 7.5 Bottom the data are presented as susceptibility versus

R2,<sup>28</sup>  $\Delta$ -9-deasturase,<sup>29</sup> and ToMOH<sup>23</sup> contain variable numbers of water molecules in the coordination sphere of their diiron sites. Each is housed near a hydrophobic pocket that limits water access in the X-ray crystal structure of the reduced form of sMMOH,<sup>22</sup> the diiron sites have two water molecules compared with no water molecules at all in the diiron(II) core of RNR-R2.<sup>28</sup> Perhaps, the accessible amount water in non-heme diiron(II) sites is important and must be controlled. Although our study clearly demonstrates that water is involved in equilibria with carboxylate-rich diiron(II) complexes, a quantitative treatment and understanding of its influence on the oxygenation events remains for future work.

**References**

- (1) Tshuva, E. Y.; Lippard, S. J. *Chem. Rev.* **2004**, *104*, 987-1012.
- (2) Costas, M.; Mehn, M. P.; Jensen, M. P.; Que, L., Jr. *Chem. Rev.* **2004**, *104*, 939-986.
- (3) Solomon, E. I.; Brunold, T. C.; Davis, M. I.; Kemsley, J. N.; Lee, S.-K.; Lehnert, N.; Neese, F.; Skulan, A. J.; Yang, Y.-S.; Zhou, J. *Chem. Rev.* **2000**, *100*, 235-349.
- (4) Du Bois, J.; Mizoguchi, T. J.; Lippard, S. J. *Coord. Chem. Rev.* **2000**, *200-202*, 443-485.
- (5) Yoon, S.; Kelly, A. M.; Lippard, S. J. *Polyhedron* **2004**, in press.
- (6) Du, C.-J. F.; Hart, H.; Ng, K.-K. D. *J. Org. Chem.* **1986**, *51*, 3162-3165.
- (7) Pangborn, A. B.; Giardello, M. A.; Grubbs, R. H.; Rosen, R. K.; Timmers, F. J. *Organometallics* **1996**, *15*, 1518-1520.
- (8) Lee, D.; Lippard, S. J. *Inorg. Chem.* **2002**, *41*, 827-837.
- (9) Lee, D.; Lippard, S. J. *Inorg. Chem.* **2002**, *41*, 2704-2719.
- (10) Lee, D.; Pierce, B.; Krebs, C.; Hendrich, M. P.; Huynh, B. H.; Lippard, S. J. *J. Am. Chem. Soc.* **2002**, *124*, 3993-4007.
- (11) Kuzelka, J.; Mukhopadhyay, S.; Spingler, B.; Lippard, S. J. *Inorg. Chem.* **2004**, *43*, 1751-1761.
- (12) Sheldrick, G. M.; University of Göttingen: Göttingen, Germany, 1997.
- (13) Sheldrick, G. M.; University of Göttingen: Göttingen, Germany, 1996.
- (14) Spek, A. L.; Utrecht University: Utrecht, The Netherlands, 1998.
- (15) Kent, T. A.; v2.5 ed.: Minneapolis, 1998.
- (16) Day, E. P. *Methods in Enzymology* **1993**, *227*, 437-463.
- (17) Hendrich, M. P.; Pearce, L. L.; Que, L., Jr.; Chasteen, N. D.; Day, E. P. *J. Am. Chem. Soc.* **1991**, *113*, 3039-3044.



- (18) Hendrich, M. P.; Day E. P.; Wang, C.-P.; Synder, B. S.; Holm, R. H.; Münck, E. *Inorg. Chem.* **1994**, *33*, 2848-2856.
- (19) Coucouvanis, D.; Reynolds, III, R. A.; Dunham, W. R. *J. Am. Chem. Soc.* **1995**, *117*, 7570-7571.
- (20) Hagen, K. S.; Lachicotte, R. *J. Am. Chem. Soc.* **1992**, *114*, 8741-8742.
- (21) Lachicotte, R.; Kitaygorodskiy, A.; Hagen, K. S. *J. Am. Chem. Soc.* **1993**, *115*, 8883-8884.
- (22) Whittington, D. A.; Lippard, S. J. *J. Am. Chem. Soc.* **2001**, *123*, 827-838.
- (23) Sazinsky, M. H.; Bard, J.; Di Donato, A.; Lippard, S. J. *J. Biol. Chem.* **2004**, in press.
- (24) Hendrich, M. P.; Münck, E.; Fox, B. G.; Lipscomb, J. D. *J. Am. Chem. Soc.* **1990**, *112*, 5861-5865.
- (25) Zang, Y.; Jang, H. G.; Chiou, Y.-M.; Hendrich, M. P.; Que, L., Jr. *Inorg. Chim. Acta* **1993**, *213*, 41-48.
- (26) Stassinopoulos, A.; Schulte, G.; Papaefthymiou, G. C.; Caradonna, J. P. *J. Am. Chem. Soc.* **1991**, *113*, 8686-8697.
- (27) Kelly, A. M.; Lippard, S. J., unpublished result.
- (28) Nordlund, P.; Eklund, H. *J. Mol. Biol.* **1993**, *232*, 123-164.
- (29) Lindqvist, Y.; Huang, W.; Schneider, G.; Shanklin, J. *EMBO J.* **1996**, *15*, 4081-4092.

**Table 7.1.** Summary of X-ray Crystallographic Information for  $[\text{Fe}(\text{H}_2\text{O})_6(\text{O}_2\text{CAr}^{4\text{F-Ph}})_2(\text{THF})_2]_2$  (1),  $[\text{Fe}_2(\mu\text{-OH}_2)_2(\mu\text{-O}_2\text{CAr}^{4\text{F-Ph}})(\text{O}_2\text{CAr}^{4\text{F-Ph}})_3(\text{THF})_2(\text{OH}_2)]$  (2) and  $[\text{Fe}_2(\text{OH}_2)_2(\mu\text{-O}_2\text{CAr}^{4\text{F-Ph}})_2(\text{O}_2\text{CAr}^{4\text{F-Ph}})_2(\text{THF})_2][\text{Fe}_2(\mu\text{-O}_2\text{CAr}^{4\text{F-Ph}})_2(\text{O}_2\text{CAr}^{4\text{F-Ph}})_2(\text{THF})_2]$  (3).

Compound	1	2·2THF	3·C <sub>5</sub> H <sub>10</sub>
Empirical formula	Fe <sub>1</sub> C <sub>46</sub> H <sub>53</sub> O <sub>12</sub> F <sub>4</sub>	Fe <sub>2</sub> C <sub>94</sub> H <sub>87.5</sub> O <sub>16.5</sub> F <sub>8</sub>	Fe <sub>4</sub> C <sub>173</sub> H <sub>136</sub> O <sub>22</sub> F <sub>16</sub>
Formula weight	929.74	1744.84	3094.22
space group	P $\bar{1}$	P $\bar{1}$	P $\bar{1}$
<i>a</i> Å	11.244(3)	14.537(3)	13.645(2)
<i>b</i> Å	13.777(3)	15.812(3)	16.523(3)
<i>c</i> Å	15.447(3)	20.001(4)	16.777(3)
$\alpha$ , deg	69.953(3)	92.153(3)	93.187(3)
$\beta$ , deg	89.780(4)	109.997(3)	107.174(3)
$\gamma$ , deg	79.225(4)	98.874(3)	95.246(3)
<i>V</i> , Å <sup>3</sup>	2203.6(8)	4248.1(13)	3585.0(10)
<i>Z</i>	2	2	1
$\rho_{\text{calc}}$ , g/cm <sup>3</sup>	1.401	1.364	1.433
<i>T</i> , °C	-100	-100	-100
$\mu(\text{Mo K}\alpha)$ , mm <sup>-1</sup>	0.422	0.427	0.490
total no. of data	19290	32795	31330
no. of unique data	9707	15649	15822
no. of params	717	1087	981
R1 (%) <sup>a</sup>	5.11	5.35	5.54
wR <sub>2</sub> (%) <sup>b</sup>	14.06	17.90	13.79
Largest diff. peak and hole	0.586 -0.294	0.631 -0.586	0.576 -0.320

<sup>a</sup>  $R1 = \Sigma||F_o| - |F_c||/\Sigma|F_o|$ . <sup>b</sup>  $wR2 = \{\Sigma[w(F_o^2 - F_c^2)^2]/\Sigma[w(F_o^2)^2]\}^{1/2}$

**Table 7.2.** Selected interatomic distances (Å) and angles (deg) for  $[\text{Fe}(\text{H}_2\text{O})_6(\text{O}_2\text{CAr}^{\text{Ph}})_2(\text{THF})_2]_2$  (1).<sup>a</sup>

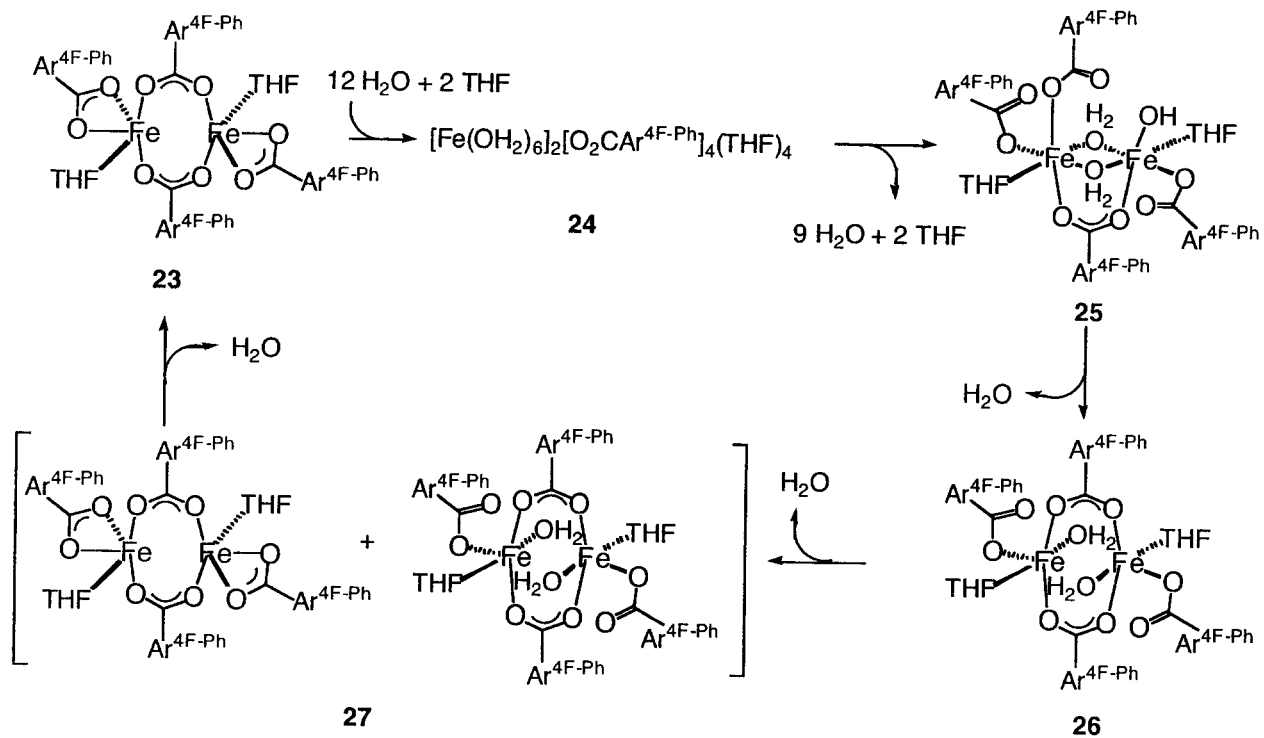
Fe1–O1	2.1158(15)	Fe2–O1–Fe3	97.04(7)
Fe1–O2	2.1279(17)	Fe2–O2–Fe4	94.79(7)
Fe1–O3	2.1531(15)	Fe2–O4–Fe3	94.79(6)
Fe2–O4	2.1673(16)	Fe2–O4–Fe4	94.16(6)
Fe2–O5	2.1248(15)	Fe3–O3–Fe4	93.14(7)
Fe2–O6	2.1055(17)	O1–Fe1–O2	83.24(6)
C100–O7	2.247(2)	O1–Fe1–O3	85.46(6)
C100–O8	2.253(2)	O1–Fe2–O2	83.49(6)
C200–O9	2.255(2)	O1–Fe2–O4	83.01(6)
C200–O10	2.259(2)	O1–Fe3–O3	83.51(6)
O1–Fe1–O2	92.23(6)	O1–Fe3–O4	84.41(6)
O1–Fe1–O3	88.32(6)	O2–Fe1–O3	79.57(6)
O2–Fe1–O3	91.91(7)	O2–Fe2–O4	82.64(6)
O4–Fe1–O5	93.18(6)	O2–Fe4–O3	85.16(7)
O4–Fe1–O6	91.62(7)	O3–Fe3–O4	82.38(6)
O5–Fe1–O6	90.94(7)	O3–Fe4–O4	88.43(7)
Fe1–O1–Fe2	97.90(7)	O4–Fe4–O12	154.33(7)
Fe1–O1–Fe3	97.32(7)	O4–Fe4–O11	94.32(7)
Fe1–O2–Fe2	94.15(6)	O11–Fe4–O12	60.27(7)
Fe1–O2–Fe4	97.02(7)	O2–Fe4–O11	131.75(8)
Fe1–O3–Fe3	92.20(6)	O2–Fe4–O12	111.21(7)
Fe1–O3–Fe4	98.24(7)	O3–Fe4–O11	143.02(8)
		O3–Fe4–O12	109.45(7)

<sup>a</sup>Numbers in parentheses are estimated standard deviations of the last significant figures.

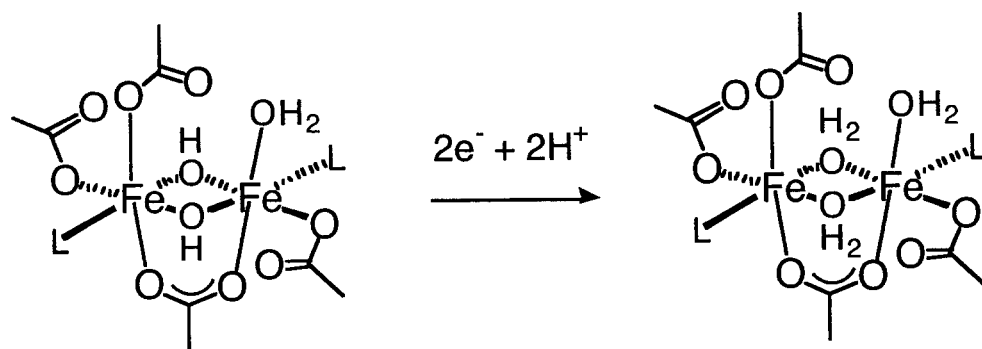
**Table 7.3.** Selected interatomic distances (Å) and angles (deg) for  $[\text{Fe}_2(\mu\text{-OH}_2)_2(\mu\text{-O}_2\text{CAr}^{\text{4F-Ph}})^3(\text{THF})_2(\text{OH}_2)]$  (**2**)<sup>a</sup>

Fe1...Fe2	3.289(3)	O2-Fe1-O4	89.50(8)
Fe1-O1	2.294(2)	O2-Fe1-O6	171.10(8)
Fe1-O2	2.152(2)	O2-Fe1-O10	85.52(8)
Fe1-O4	2.1251(19)	O2-Fe1-O12	95.31(9)
Fe1-O6	2.0413(19)	O4-Fe1-O6	93.07(8)
Fe1-O10	2.1416(19)	O4-Fe1-O10	174.11(7)
Fe1-O12	2.082(2)	O4-Fe1-O12	89.98(8)
Fe2-O1	2.233(2)	O6-Fe1-O10	91.40(8)
Fe2-O2	2.234(2)	O6-Fe1-O12	93.21(8)
Fe2-O3	2.116(2)	O10-Fe1-O12	93.61(8)
Fe2-O5	2.0190(19)	O1-Fe2-O2	81.28(8)
Fe2-O8	2.0594(19)	O1-Fe2-O3	80.97(9)
Fe2-O13	2.097(2)	O1-Fe2-O5	88.41(8)
O1...O7	2.547(3)	O1-Fe2-O8	169.08(8)
O2...O9	2.587(3)	O1-Fe2-O13	100.09(8)
O2...O11	2.617(3)	O2-Fe2-O3	88.52(9)
O3...O11	2.720(3)	O2-Fe2-O5	91.74(8)
O3...O1S	2.644(3)	O2-Fe2-O8	89.24(8)
Fe1-O1-Fe2	93.18(8)	O2-Fe2-O13	174.83(8)
Fe1-O2-Fe2	97.14(8)	O3-Fe2-O5	169.22(8)
O1-Fe1-O2	81.68(8)	O3-Fe2-O8	93.44(8)
O1-Fe1-O4	85.30(8)	O3-Fe2-O13	86.78(9)
O1-Fe1-O6	90.03(8)	O5-Fe2-O8	97.34(8)
O1-Fe1-O10	90.86(8)	O5-Fe2-O13	93.29(8)
O1-Fe1-O12	174.41(8)	O8-Fe2-O13	88.89(8)

<sup>a</sup>Numbers in parentheses are estimated standard deviations of the last significant figures.



Scheme 7.1



Scheme 7.2

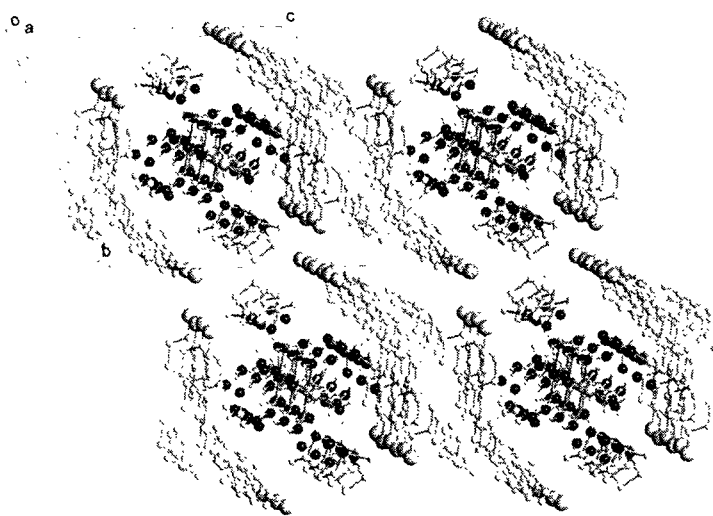
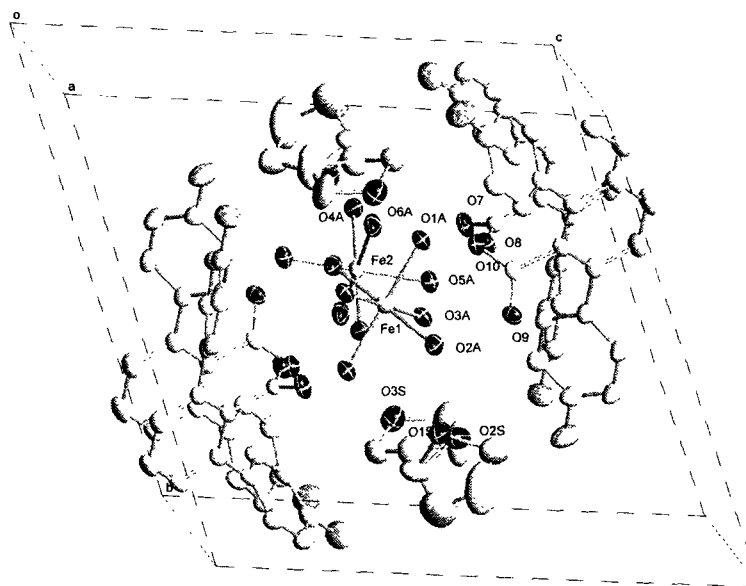


**Figure 7.1.** Top: ORTEP diagrams of  $[\text{Fe}(\text{H}_2\text{O})_6(\text{O}_2\text{CAr}^{4\text{F-Ph}})_2(\text{THF})_2]_2$  (**1**), showing 50 % probability thermal ellipsoids for all non-hydrogen atoms in one unit cell. Bottom: Ball and stick diagrams of 8 unit cells.

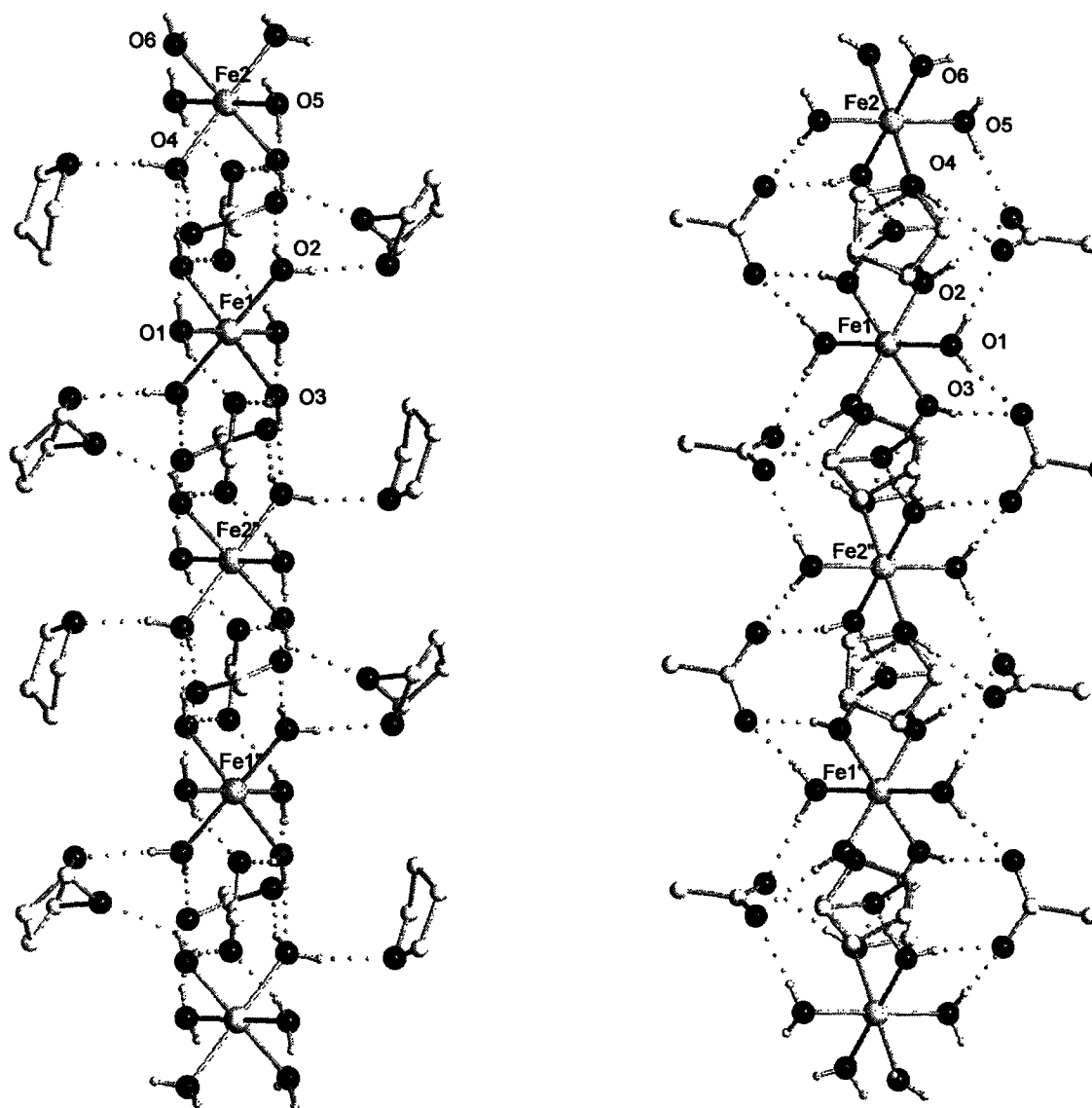


**Figure 7.2.** Ball and stick diagram of  $[\text{Fe}(\text{H}_2\text{O})_6(\text{O}_2\text{CAr}^{4\text{F-Ph}})_2(\text{THF})_2]_2$  (1) The aromatic rings of  $\text{Ar}^{4\text{F-Ph}}\text{CO}_2^-$  ligands and hydrogen atoms in THF molecules are omitted for clarity. Left and Right are the side on views to each other.



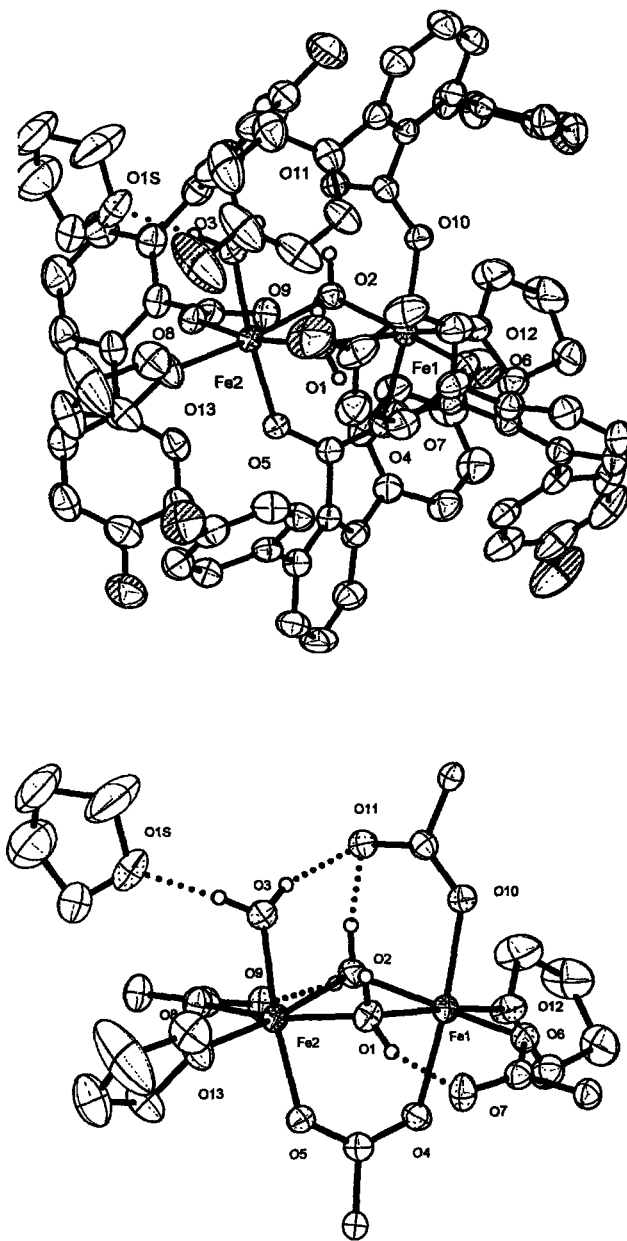


**Figure 7.3.** (Top) ORTEP diagrams of  $[\text{Fe}_2(\mu\text{-OH}_2)_2(\mu\text{-O}_2\text{CAr}^{4\text{F-Ph}})(\text{O}_2\text{CAr}^{4\text{F-Ph}})_3(\text{THF})_2(\text{OH}_2)]$  (**2**) showing 50 % probability thermal ellipsoids for all non-hydrogen atoms in one unit cell. (Bottom) The aromatic rings of  $\text{Ar}^{4\text{F-Ph}}\text{CO}_2^-$  ligands and hydrogen atoms in THF molecules are omitted for clarity

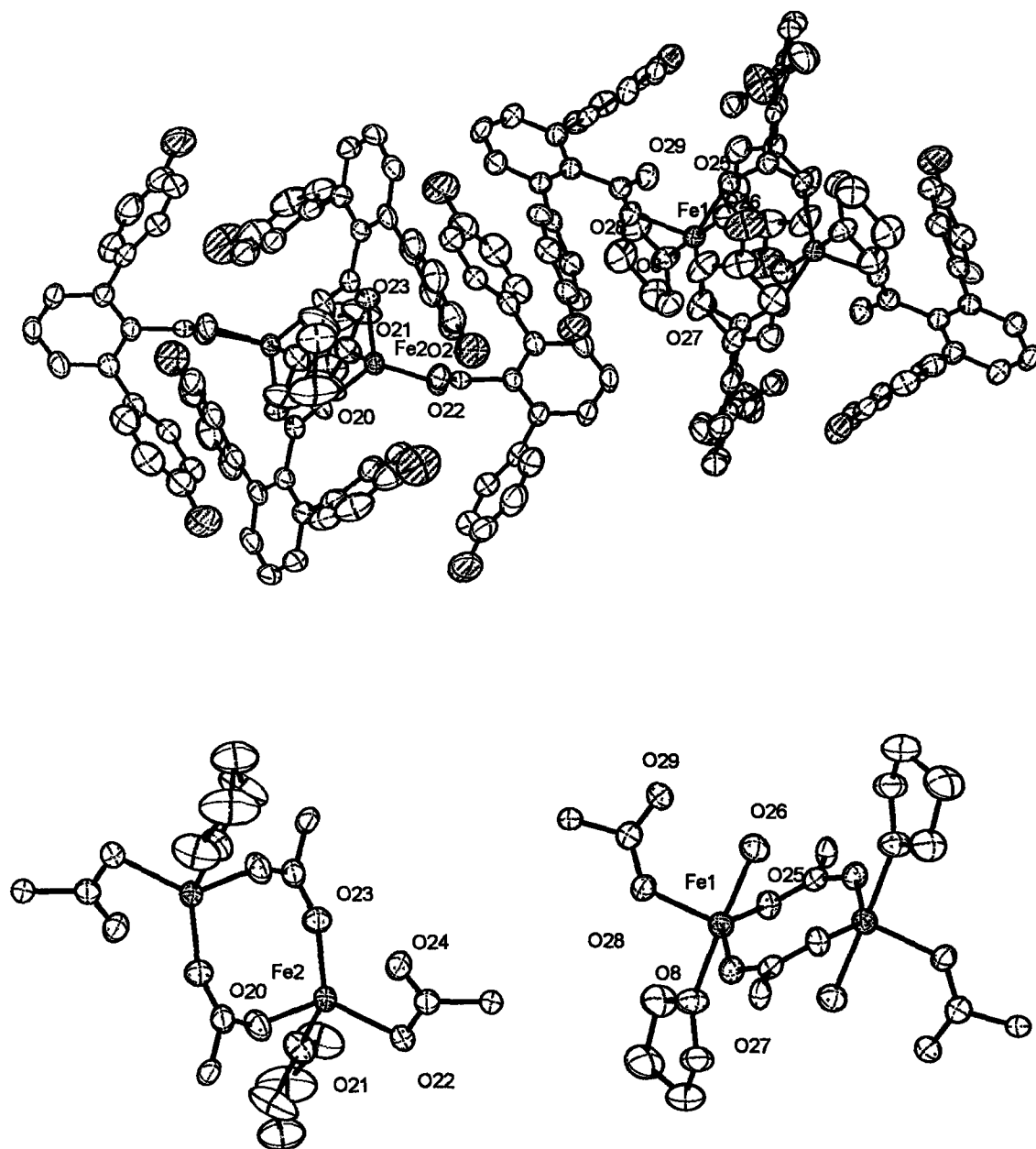
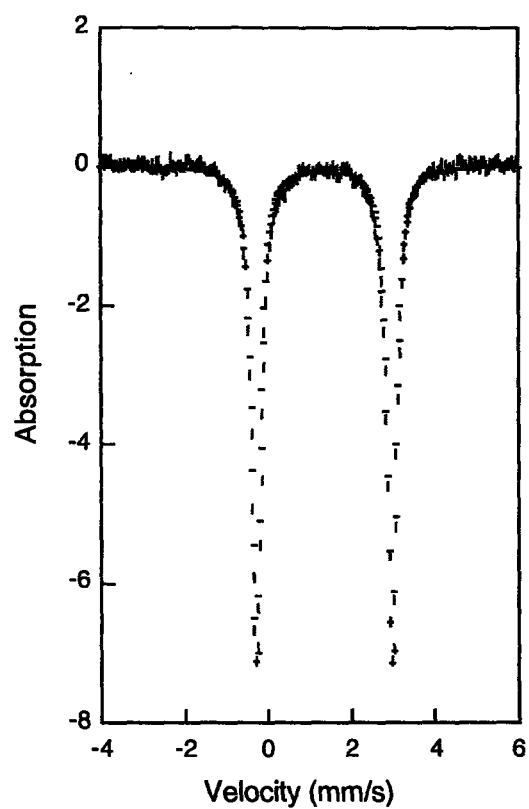


Figure 7.4. Top: ORTEP diagram of  $[\text{Fe}_2(\text{OH}_2)_2(\mu\text{-O}_2\text{CAr}^{4\text{F-Ph}})_2(\text{O}_2\text{CAr}^{4\text{F-Ph}})_2(\text{THF})_2][\text{Fe}_2(\mu\text{-O}_2\text{CAr}^{4\text{F-Ph}})_2(\text{O}_2\text{CAr}^{4\text{F-Ph}})_2(\text{THF})_2]$  (**3**) showing 50 % probability thermal ellipsoids for all non-hydrogen atoms. Bottom left: The aromatic rings of  $\text{Ar}^{\text{Tot}}\text{CO}_2^-$  ligands are omitted for clarity and hydrogen-bonding interactions are depicted with dot lines.



**Figure 7.5.** Zero-field Mössbauer spectrum (experimental data (|), calculated fit (—)) recorded at 4.2 K of the solid sample of  $[\text{Fe}_2(\mu\text{-OH}_2)_2(\mu\text{-O}_2\text{CAr}^{4\text{F-Ph}})(\text{O}_2\text{CAr}^{4\text{F-Ph}})_3(\text{THF})_2(\text{OH}_2)]$  (2).

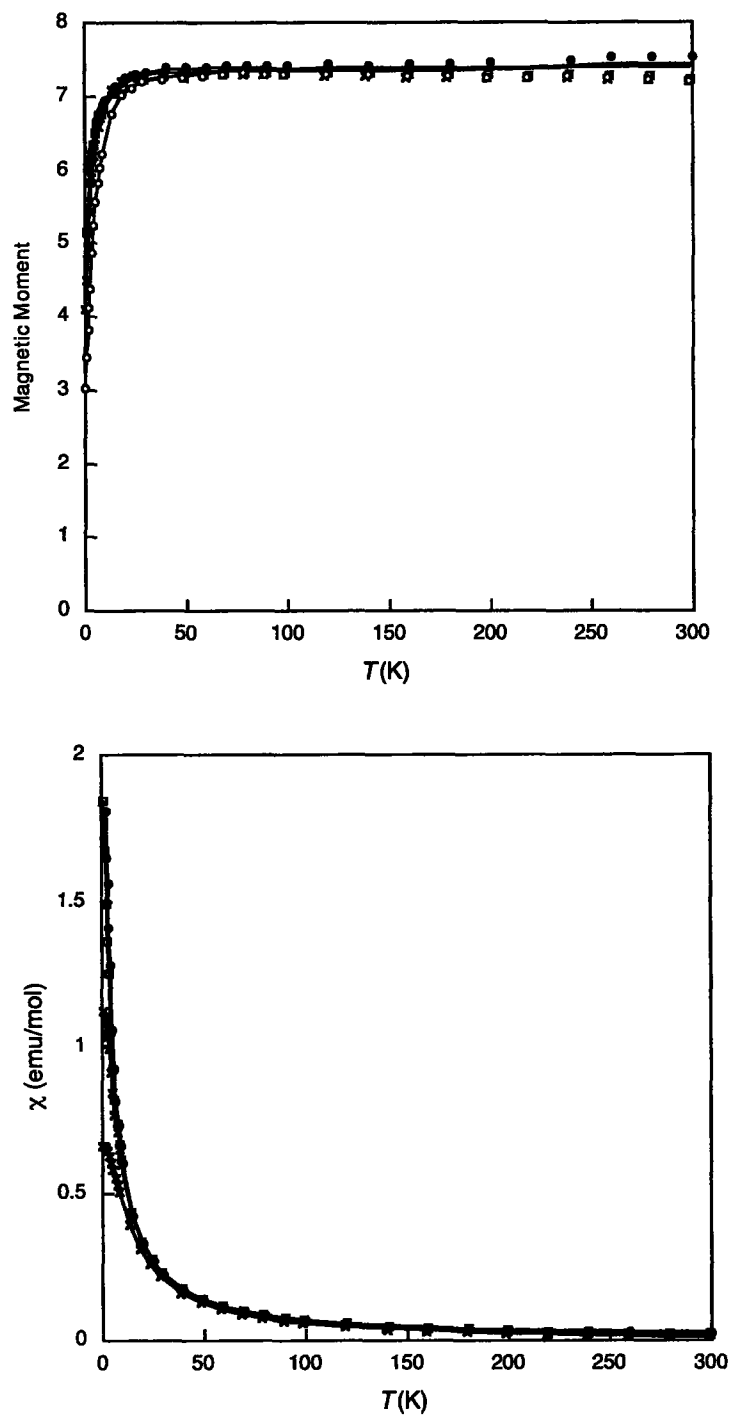


Figure 7.6. Plots of the effective magnetic moment ( $\mu_{eff}$ ) per molecule versus temperature (Top) and molar susceptibility ( $\chi_M$ ) versus temperature (Bottom) for  $[\text{Fe}_2(\mu\text{-OH}_2)_2(\mu\text{-O}_2\text{CAr}^{4F\text{-Ph}})(\text{O}_2\text{CAr}^{4F\text{-Ph}})_3(\text{THF})_2(\text{OH}_2)]$  (2). The lines represent the fit.

## **Chapter 8**

### **Water Affects the Dioxygen Reactivity of Carboxylate-Rich Diiron(II) Complexes as Models for Diiron Centers in Dioxygen-Dependent Non-Heme Enzymes**

## Introduction

Carboxylate-bridged diiron units constitute a commonly occurring element in a growing member of dioxygen-dependent metalloenzymes. Important members of this class include class I ribonucleotide reductase (RNR),<sup>1,2</sup> soluble methane monooxygenase (sMMO),<sup>3</sup> fatty acid desaturase ( $\Delta^9$ D),<sup>4</sup> and toluene monooxygenase (ToMO).<sup>5</sup> Although these metalloproteins share a common structural motif, their diiron centers are tuned to achieve diverse functions. There are subtle differences among the crystallographically characterized enzyme active sites, including the binding modes of the carboxylates and the existence of variable numbers of water molecules. These distinctions and the surrounding polypeptide matrix alter the chemical properties of the core. Understanding how these carboxylate-bridged diiron(II) units work and how their mechanisms relate to one another represents a challenging and active area of research in bioinorganic chemistry.

Numerous diiron complexes have been prepared to understand the chemistry of these systems at the molecular level.<sup>6-8</sup> Much effort has focused on reproducing the architecture of the active sites using carboxylate-based ligand frameworks and on studying oxygenation of the resulting carboxylate-rich diiron(II) complexes to address the roles of this basic unit shared by these enzymes. On the other hand, understanding other factors, such as the presence of water molecules in iron coordination sphere or the influence of the surrounding polypeptide matrix, has until now been forthcoming mainly through direct studies of the biomolecule itself and by theoretical methods. The importance of certain amino acid residues in the surrounding polypeptide has been probed by selective mutagenesis. The effect of water on the oxygenation cycle has been a focus of computational studies. In recently published DFT calculations, the coordinated H<sub>2</sub>O molecule, used as a hydrogen-bond donor, was considered to be a key com-

ponent in the formation of reactive intermediate(s) formed upon oxygenation of the diiron(II) site.<sup>9,10</sup>

Recently, we have begun to address the role that coordinated water might play in the oxygenation cycle of carboxylate-rich diiron sites in metalloenzymes by using small molecule synthetic mimics. The reaction between water and carboxylate-rich diiron(II) complexes has been investigated and iron(II) complexes with varying numbers of water ligands isolated, revealing that tetracarboxylate-bridged diiron complexes are quite responsive to water influx.<sup>11,12</sup> In the present chapter, we report our efforts to treat the water-dependent equilibria quantitatively and to address the effects of water on oxygenation of the diiron(II) carboxylate complexes. In addition, the physical properties of water containing diiron(II) complexes are described. These studies have been facilitated by the introduction of 4-cyanopyridine (4-NCC<sub>5</sub>H<sub>4</sub>N) as a ligand, which shifts the metal-to-ligand charge transfer bands of the starting diiron(II) compounds into visible region of the spectrum.

## Experimental Section

**General Considerations.** All reagents, including 4-cyanopyridine, were obtained from commercial suppliers and used as received unless otherwise noted. Dichloromethane, pentane, toluene, and THF were saturated with argon and purified by passage through activated Al<sub>2</sub>O<sub>3</sub> columns under argon.<sup>13</sup> Dioxygen (99.994%, BOC Gases) was dried by passing the gas stream through Drierite. The compounds [Fe<sub>2</sub>(μ-O<sub>2</sub>CAr<sup>Tol</sup>)<sub>2</sub>(O<sub>2</sub>CAr<sup>Tol</sup>)<sub>4</sub>(THF)<sub>2</sub>],<sup>7</sup> where <sup>-</sup>O<sub>2</sub>CAr<sup>Tol</sup> is 2,6-di-(*p*-tolyl)benzoate,<sup>14</sup> [Fe<sub>2</sub>(μ-O<sub>2</sub>CAr<sup>4F-Ph</sup>)<sub>2</sub>(CAr<sup>4F-Ph</sup>)<sub>4</sub>(THF)<sub>2</sub>],<sup>7</sup> where <sup>-</sup>O<sub>2</sub>CAr<sup>4F-Ph</sup> is 2,6-di-(*p*-flurorphenyl)benzoate,<sup>14</sup> and {H(OEt)<sub>2</sub>}{BAR'<sub>4</sub>},<sup>15</sup> where BAR'<sub>4</sub> is tetra(3,5-di(trifluoromethyl)phenyl)borate, were

prepared as described in the literature. Air-sensitive manipulations were carried out under nitrogen in an MBraun glovebox. FT-IR spectra were recorded with a Thermo Nicolet Avatar 360 spectrometer. UV-vis spectra were obtained on a Hewlett-Packard 8453 diode array spectrophotometer. In variable temperature UV-vis studies, the temperature was controlled with an Oxford ITC 601 cryostat.

**[Fe<sub>2</sub>(μ-O<sub>2</sub>CAr<sup>Tol</sup>)<sub>4</sub>(4-NCC<sub>5</sub>H<sub>4</sub>N)<sub>2</sub>] (1).** To a light yellow solution of [Fe<sub>2</sub>(μ-O<sub>2</sub>CAr<sup>Tol</sup>)<sub>2</sub>(O<sub>2</sub>CAr<sup>Tol</sup>)<sub>2</sub>(THF)<sub>2</sub>]<sup>7</sup> (1.85 g, 1.26 mmol) in CH<sub>2</sub>Cl<sub>2</sub> (100 mL) was added solid 4-NCC<sub>5</sub>H<sub>4</sub>N (263 mg, 2.53 mmol) and the dark red pink solution was stirred for 20 min. The solution was filtered through Celite and pentane was layered on top. Dichroic red pink blocks of **1** (1.44 g, 75 %) formed overnight. The best crystals for X-ray crystallography were obtained by recrystallization from THF/pentane. FT-IR (KBr, cm<sup>-1</sup>) 3050 (w), 3021 (w), 2918 (w), 2862 (w), 2236 (w, ν<sub>C-N</sub>), 1609 (s), 1551 (w), 1513 (w), 1493 (w), 1440 (m), 1404 (m), 1384 (s), 1303 (w), 1215 (w), 1188 (w), 1109 (w), 1065 (w), 843 (w), 814 (s), 789 (m), 762 (w), 727 (w), 706 (m), 580 (w), 558 (w), 526 (m). Anal. Calcd. For 1·0.5(CH<sub>2</sub>Cl<sub>2</sub>), C<sub>103</sub>H<sub>93</sub>Fe<sub>2</sub>N<sub>4</sub>O<sub>8</sub>Cl: C, 73.93; H, 4.95; N, 3.57. Found: C, 74.44; H, 5.10; N, 3.40.

**[Fe<sub>2</sub>(μ-O<sub>2</sub>CAr<sup>4F-Ph</sup>)<sub>4</sub>(4-NCC<sub>5</sub>H<sub>4</sub>N)<sub>2</sub>] (2).** To a rapidly stirred solution of [Fe<sub>2</sub>(μ-O<sub>2</sub>CAr<sup>4F-Ph</sup>)<sub>2</sub>(O<sub>2</sub>CAr<sup>4F-Ph</sup>)<sub>2</sub>(THF)<sub>2</sub>]<sup>7</sup> (762 mg, 51.0 mmol) in CH<sub>2</sub>Cl<sub>2</sub> (50 mL) was added solid 4-NCC<sub>5</sub>H<sub>4</sub>N (106 mg, 102 mmol), yielding a red solution. A red precipitate of **2** (512 mg, 65 %) formed immediately and was isolated by filtration and washed with pentane. The solid (20.3 mg) was dissolved in CH<sub>2</sub>Cl<sub>2</sub> (10 mL), and exposure of the solution to pentane vapor diffusion yielded dichroic yellow red blocks, suitable for X-ray crystallography. FT-IR (KBr, cm<sup>-1</sup>) 3056 (w), 2239 (w, ν<sub>C-N</sub>), 1610 (s), 1569 (w), 1551 (w), 1509 (s), 1452 (w), 1404 (m), 1382 (s), 1299 (w), 1220 (s), 1159 (m), 1095 (w), 844 (m), 832 (m), 818 (m),



793 (w), 773 (w), 727 (w), 706 (w), 582 (w), 556 (m), 532 (w). Anal. Calcd. For  $C_{88}H_{52}F_8Fe_2N_4O_8$ : C, 67.88; H, 3.37; N, 3.60. Found: C, 67.55; H, 3.45; N, 3.72.

$[Fe_2(\mu-O_2CAr^{Tol})_2(O_2CAr^{Tol})_2(4-NCC_5H_4N)_2(OH_2)_2]$  (3). To a stirred yellow solution of  $[Fe_2(\mu-O_2CAr^{Tol})_4(4-NCC_5H_4N)_2]$  (49.5 mg, 29.8  $\mu$ mol) in THF (1 mL) was added dropwise  $H_2O$  (7  $\mu$ L) under nitrogen. Dichroic yellow red needle crystals of 3 (20.3 mg, 44% yield), suitable for X-ray crystallography, were obtained by vapor diffusion of pentanes into the solution. FT-IR (KBr,  $cm^{-1}$ ) 3653 (w), 3423 (w, br), 2918 (w), 2235 (w,  $\nu_{C-N}$ ), 1609 (s), 1515 (s), 1452 (s), 1411 (m), 1381 (s), 1217 (w), 1190 (w), 1109 (w), 860 (w), 846 (w), 818 (s), 797 (m), 790 (m), 781 (m), 766 (w), 734 (w), 713 (w), 586 (w), 559 (m), 540 (w), 521 (w), 454 (w). Anal. Calcd for  $C_{96}H_{80}Fe_2N_4O_{10}$ : C, 73.85; H, 5.16; N, 3.59. Found: C, 73.85; H, 5.48; N, 3.81.

$[Fe_2(\mu-O_2CAr^{4F-Ph})_2(O_2CAr^{4F-Ph})_2(4-NCC_5H_4N)_2(OH_2)_2]$  (4). Compound 4 was synthesized as described for 3 and identified by X-ray crystallography (yield 58%). FT-IR (KBr,  $cm^{-1}$ ) 3655 (w), 3420 (w, br), 3054 (w), 2244 (w,  $\nu_{C-N}$ ), 1604 (s), 1510 (s), 1451 (s), 1409 (m), 1380 (s), 1301 (w), 1224 (s), 1160 (m), 1093 (w), 1011 (w), 852 (m), 833 (s), 814 (s), 807 (s), 789 (m), 773 (m), 733 (w), 712 (m), 701 (w), 556 (m), 527 (m), 464 (w). Anal. Calcd for  $C_{88}H_{56}F_8Fe_2N_4O_{10}$ : C, 65.04; H, 3.47; N, 3.45. Found: C, 65.55; H, 3.57; N, 3.70.

$[Fe_2(\mu-O_2CAr^{Tol})_3(4-NCC_5H_4N)_2][BAR'_4]$  (5). To a stirred solution of  $[Fe_2(\mu-O_2CAr^{Tol})_4(4-NCC_5H_4N)_2]$  (14.5 mg, 8.7  $\mu$ mol) in  $CH_2Cl_2$  (3 mL) was added 1 equiv of  $[H(OEt)_2]\{BAR'_4\}$ , yielding a yellow solution under anaerobic conditions. The solution was filtered through Celite and pentane was diffused into it. Yellow red blocks of 5 (12.3 mg, 68% yield), suitable for X-ray crystallography, formed overnight. FT-IR (KBr,  $cm^{-1}$ ) 3051 (w), 2920 (w), 2237 ( $\nu_{C-N}$ ), 1614 (m), 1585 (s), 1514 (s), 1493 (s), 1436 (w), 1405 (m), 1385 (m), 1271 (m), 1219 (w), 1030 (w), 832 (s), 807 (s), 791 (m), 636 (w), 586 (m), 560

(w), 528 (w). Anal. Calcd. For  $5 \cdot 0.5(\text{CH}_2\text{Cl}_2)$  or  $\text{C}_{107.5}\text{H}_{72}\text{BClF}_{24}\text{Fe}_2\text{N}_4\text{O}_6$ : C, 60.63; H, 3.41; N, 2.63. Found: C, 60.74; H, 3.56; N, 3.02.

$[\text{Fe}_2(\mu\text{-OH})_2(\mu\text{-O}_2\text{CAr}^{\text{Tol}})_2(\text{O}_2\text{CAr}^{\text{Tol}})_2(4\text{-NCC}_5\text{H}_4\text{N})_2] \cdot 2(\text{HO}_2\text{CAr}^{\text{Tol}})$  (6) and  $[\text{Fe}_6(\mu\text{-O})_2(\mu\text{-OH})_4(\mu\text{-O}_2\text{CAr}^{\text{Tol}})_6(4\text{-NCC}_5\text{H}_4\text{N})_4(\text{Cl})_2]$  (7). A red pink solution of 1 (15 mg, 0.017 mmol) in  $\text{CH}_2\text{Cl}_2$  (10 mL) was saturated with dry dioxygen by bubbling over a period of 10 min, resulting in a green yellow solution. The solution was filtered through Celite and pentane was diffused into it. Light green blocks of 6 and brown yellow blocks of 7 were obtained after several days. Although the structures of 6 and 7 could be determined by X-ray crystallography, the bulk samples could not be obtained.

**X-ray Crystallographic Studies.** Single crystals were mounted at room temperature on the tips of quartz fibers, coated with Paratone-N oil, and cooled under a stream of cold nitrogen. Intensity data were collected on a Bruker (formerly Siemens) APEX CCD diffractometer running the SMART software package, with Mo  $K\alpha$  radiation ( $\lambda = 0.71073 \text{ \AA}$ ). Data collection and reduction protocols are described in detail elsewhere.<sup>16</sup> The structures were solved by both direct and Patterson methods and refined on  $F^2$  by using the SHELXTL software package.<sup>17</sup> Empirical absorption corrections were applied with SADABS,<sup>18</sup> part of the SHELXTL program package, and the structures were checked for higher symmetry by the program PLATON.<sup>19</sup> All non-hydrogen atoms were refined anisotropically. In general, hydrogen atoms were assigned idealized positions and given thermal parameters equivalent to either 1.5 (methyl hydrogen atoms) or 1.2 (all other hydrogen atoms) times the thermal parameter of the carbon atom to which they were attached. Hydrogen atoms of the bridging hydroxides and water molecules were located on difference electron density maps. In the structure of 1, four THF molecules were assigned in the lattice and refined isotropically. The structure of 2

contains four  $\text{CH}_2\text{Cl}_2$  molecules in the lattice. In the structure of 5, three 3,5-difluorophenyl rings in  $\text{BAr}'_4$  were severely disordered. Four  $\text{CH}_2\text{Cl}_2$  molecules were found in the lattice of compound 6. There were six  $\text{CH}_2\text{Cl}_2$  molecules in the lattice of compound 7. Data collection and experimental details for the complexes are summarized in Table 8.1 and relevant interatomic bond lengths and angles for 1 - 7 are listed in Tables 8.2 - 8.5.

**$^{57}\text{Fe}$  Mössbauer Spectroscopy.** Zero-field Mössbauer spectra were obtained on an MS1 spectrometer (WEB Research Co.) with a  $^{57}\text{Co}$  source in a Rh matrix maintained at room temperature in the Massachusetts Institute of Technology Department of Chemistry Instrument Facility (MIT DCIF). Solid samples were prepared by suspending ca 30 mg of the powdered solids in Apeizon N grease and packing the mixture into a nylon sample holder. Data were collected at 4.2 K and the isomer shift ( $\delta$ ) values are reported with respect to natural iron foil that was used for velocity calibration at room temperature. The spectra were fit to Lorentzian lines by using the WMOSS plot and fit program.<sup>20</sup>

**Electrochemistry.** Cyclic voltammetric measurements were performed in an MBraun glovebox under nitrogen with an EG&G model 263 potentiostat. A three-electrode configuration consisting of a platinum working electrode, a  $\text{AgNO}_3/\text{Ag}$  (0.1 M in acetonitrile with 0.5 M  $(\text{Bu}_4\text{N})\text{PF}_6$ ) reference electrode, and a platinum mesh auxiliary electrode were used. The supporting electrolyte was 0.5 M  $(\text{Bu}_4\text{N})\text{PF}_6$  and the solvent was  $\text{CH}_2\text{Cl}_2$ . All cyclic voltammograms were externally referenced to the  $\text{Cp}_2\text{Fe}/\text{Cp}_2\text{Fe}^+$  couple.

**Resonance Raman Spectroscopy.** Resonance Raman spectra were obtained by using an  $\text{Ar}^+$  ion laser with excitation provided at 514 nm. A monochromator (1200 grooves/nm grating) with an entrance slit of 10 microns and a TE-CCD-1100-PB-VISAR

detector cooled to  $-30\text{ }^{\circ}\text{C}$  with a circulating water bath was employed in a standard backscattering configuration. Data were collected at  $23\text{ }^{\circ}\text{C}$  in dichloromethane using an NMR tube. Each sample concentration was 6 mM. Measurements were made on more than one freshly prepared sample and made in triplicate to ensure the authenticity of the results. The dichloromethane bands at  $1156\text{ cm}^{-1}$ ,  $897\text{ cm}^{-1}$ ,  $704\text{ cm}^{-1}$ , and  $286\text{ cm}^{-1}$  were used as an internal calibration standard. Data were processed using WinSpec 3.2.1 (Princeton Instruments, Inc.) and were further manipulated by Kaleidagraph.

**Stopped-flow Kinetics Experiments.** All ambient-pressure kinetics experiments were carried out by using a Canterbury Stopped-Flow SF-40 and MG-6000 Rapid Diode array System (Hi-Tech Scientific). The solutions of **1** in  $\text{CH}_2\text{Cl}_2$  (ca. 0.385 mM) were prepared in a glove box under a nitrogen atmosphere and stored in a gas-tight syringe prior to loading into the stopped-flow apparatus. A saturated solution of dioxygen was prepared by bubbling the gas through  $\text{CH}_2\text{Cl}_2$  for 20 min in a round-bottomed flask closed with a septum and maintained at  $20\text{ }^{\circ}\text{C}$ . The saturated  $\text{CH}_2\text{Cl}_2$  solution of dioxygen containing 2 mM water was prepared by bubbling the dioxygen gas into a solution of that composition.

## Results and Discussion

In contrast to the relatively rich spectra afforded by the low-spin iron(II) complex, high-spin iron(II) analogues are typically colorless, making it difficult to apply standard optical-based spectroscopic methods to follow their chemistry. For example, the charge-transfer band in the visible region of the spectrum are well documented for low spin iron(II) complexes having pyridine ligands.<sup>21,22</sup> On the other hand, most high-spin iron(II) complexes are colorless or almost light yellow.<sup>23,24</sup> In our previous studies, the detection of water-dependent equilibria in carboxylate-rich diiron(II) complexes was

achieved by using solid-state methods, chiefly X-ray crystallography.<sup>11,12</sup> To treat water-dependent equilibrium in a quantitative manner and to address the effects of water on the oxygenation reactions of high-spin diiron(II) complexes, an optical probe was highly desired. Just such a probe was discovered with the introduction of 4-cyanopyridine as a ligand.

**Synthesis and Structural Characterization of Diiron(II) Complexes**  $[\text{Fe}_2(\mu\text{-O}_2\text{CAr}^{\text{Tol}})_4(4\text{-NCC}_5\text{H}_4\text{N})_2]$  (1) and  $[\text{Fe}_2(\mu\text{-O}_2\text{CAr}^{4\text{F-Ph}})_4(4\text{-NCC}_5\text{H}_4\text{N})_2]$  (2). A clue for how to access high-spin diiron(II) complexes with visible absorption bands came from the electronic spectrum of the  $[\text{Fe}_2(\mu\text{-O}_2\text{CAr}^{\text{Tol}})_4(4\text{-}^t\text{BuC}_5\text{H}_4\text{N})_2]$ ,<sup>25</sup> which has a shoulder at 370 nm with  $\epsilon = 1400 \text{ cm}^{-1}\text{M}^{-1}$ , assigned as a charge transfer transition from Fe(II) to the  $\pi^*$  orbitals of the pyridine ligand (MLCT). If so, by lowering the energy of acceptor it should be possible to narrow the energy gap between the orbitals involved in this transition. This hypothesis was tested by synthesizing analogues of  $[\text{Fe}_2(\mu\text{-O}_2\text{CAr}^{\text{Tol}})_4(4\text{-}^t\text{BuC}_5\text{H}_4\text{N})_2]$  with 4-NCC<sub>5</sub>H<sub>4</sub>N, anticipating a red shift of the electronic transition. Upon addition of 2 equiv of 4-NCC<sub>5</sub>H<sub>4</sub>N, the light yellow solution of  $[\text{Fe}_2(\mu\text{-O}_2\text{CAr}^{\text{Tol}})_2(\text{O}_2\text{CAr}^{\text{Tol}})_2(\text{THF})_2]$  in CH<sub>2</sub>Cl<sub>2</sub> instantaneously turned red pink, affording the expected diiron(II) complex  $[\text{Fe}_2(\mu\text{-O}_2\text{CAr}^{\text{Tol}})_4(4\text{-NCC}_5\text{H}_4\text{N})_2]$  (1) (Scheme 8.1). When isolated from solution, however, the crystals developed fissures, probably due to loss of the solvent molecule(s) in the lattice. The best crystals for X-ray analysis were obtained by dissolution of 1 in THF, followed by vapor diffusion of pentane. Figure 8.1 shows the structure and Table 8.2 lists selected interatomic lengths and angles. Two crystallographically inequivalent square-pyramidal iron(II) centers, separated by 2.7754(9) Å, are linked by four bridging carboxylate ligands. The 4-NCC<sub>5</sub>H<sub>4</sub>N ligands coordinate to the iron(II) sites in axial positions through pockets that are generated by the four bulky

carboxylate ligands. Most of geometric features of **1** are the same as in the previously characterized paddle-wheel complexes  $[\text{Fe}_2(\mu\text{-O}_2\text{CAr}^{\text{Tol}})_4(4\text{-}^t\text{BuC}_5\text{H}_4\text{N})_2]$ <sup>25</sup> and  $[\text{Fe}_2(\mu\text{-O}_2\text{CAr}^{\text{Tol}})_4(\text{BA}^{p\text{-OMe}})_2]$ ,<sup>26</sup> where  $\text{BA}^{p\text{-OMe}}$  is 4-methoxybenzylamine. A powdered sample of **1** is stable in the solid state for over 2 months in air, judging by the maintenance of its distinctive color of compound.

Treatment of a light yellow  $\text{CH}_2\text{Cl}_2$  solution of  $[\text{Fe}_2(\mu\text{-O}_2\text{CAr}^{\text{AF-Ph}})_2(\text{O}_2\text{CAr}^{\text{AF-Ph}})_2(\text{THF})_2]$ <sup>7</sup> with 2 equiv of 4-NCC<sub>5</sub>H<sub>4</sub>N afforded the red diiron(II) complex  $[\text{Fe}_2(\mu\text{-O}_2\text{CAr}^{\text{AF-Ph}})_4(4\text{-NCC}_5\text{H}_4\text{N})_2]$  (**2**) (Scheme 8.1), which has the same structure (Figure 8.2). Selected interatomic distances and angles are in Table 8.2. Since compound **2** is not very soluble in most solvents, further studies were performed exclusively with compound **1**.

**Syntheses and Structural Characterization of Water-Containing Diiron(II) Complexes**  $[\text{Fe}_2(\mu\text{-O}_2\text{CAr}^{\text{Tol}})_2(\text{O}_2\text{CAr}^{\text{Tol}})_2(4\text{-NCC}_5\text{H}_4\text{N})_2(\text{OH}_2)_2]$  (**3**) and  $[\text{Fe}_2(\mu\text{-O}_2\text{CAr}^{\text{AF-Ph}})_2(\text{O}_2\text{CAr}^{\text{AF-Ph}})_2(4\text{-NCC}_5\text{H}_4\text{N})_2(\text{OH}_2)_2]$  (**4**). Addition of **1** to a wet  $\text{CH}_2\text{Cl}_2$  or THF solution resulted in an instantaneous color change from red pink to light yellow-red. Out of these solutions compound **3** was crystallized following vapor diffusion of pentane into it.

The structure of **3** is displayed in Figure 8.3 and the selected interatomic distances and angles are listed in Table 8.3. Two distorted octahedral iron(II) centers are bridged by two carboxylate ligands with an Fe...Fe separation of 4.465 Å. This value is 1.69 Å longer than the Fe...Fe separation (2.7754(9) Å) in **1** and arises from water-induced shifting of two carboxylate ligands from a bridging to a terminal chelating mode. The reaction typifies how the binding of water in carboxylate-bridged diiron(II) complexes can induce a dramatic structural change. The non-bridging coordination sites are occupied by 4-NCC<sub>5</sub>H<sub>4</sub>N, water, and the bidentate terminal carboxylate ligands. The assignment of water as the ligand rather than hydroxide is based on the

Fe–O(aqua) distance, 2.1686(15) Å, the location and refinement of the associated hydrogen atoms in the X-ray structure determination (O–H, 0.71 and 0.86 Å), and charge considerations. Inter- and intramolecular hydrogen bonding interactions between the metal-bound water molecules and the carboxylate ligand are characterized by short O–H···O distances, ranging from 2.731 Å to 2.755 Å (Figure 8.3 Bottom). Intermolecular hydrogen bonds may contribute to the observed hardness of the crystals. When **3** is dissolved in anhydrous CH<sub>2</sub>Cl<sub>2</sub>, a red pink color is obtained, indicating that the coordinated water ligands observed in the solid state are readily displaced from the first coordination sphere. The compound **4** is essentially isostructural with **3** (Figure 8.4 and Table 8.3).

**Synthesis and Characterization of [Fe<sub>2</sub>(μ-O<sub>2</sub>CAr<sup>Tol</sup>)<sub>3</sub>(4-NCC<sub>5</sub>H<sub>4</sub>N)<sub>2</sub>](BAR'<sub>4</sub>) (**5**)**

**Upon Reaction of **1** with H<sup>+</sup>.** When compound **1** was titrated with a CH<sub>2</sub>Cl<sub>2</sub> solution of [H(OEt<sub>2</sub>)<sub>2</sub>](BAR'<sub>4</sub>),<sup>15</sup> the intense red-pink color disappeared following addition of ca 1.2 equiv of the acid, generating a yellow solution. Yellow blocks of **5** were obtained by vapor diffusion of pentanes into the solution. Although the structure of **5** could be determined by X-ray crystallography, the large unit cell volume and severe disorder in the BAR'<sub>4</sub><sup>-</sup> counteranion prohibited satisfactory refinement of the structure. The drawing of **5** is depicted in Figure 8.5. The two pseudo tetrahedral iron(II) sites with NO<sub>3</sub> coordination geometries are bridged by three carboxylates at an Fe···Fe distance of 3.111 Å. Two 4-NCC<sub>5</sub>H<sub>4</sub>N ligands coordinate to the iron(II) sites through the pockets generated by the three bulky carboxylates.

**Mössbauer Properties.** Zero-field Mössbauer spectra of solid samples of **1**, **2**, **3**, and **5** were recorded at 4.2 K in the absence of an external field. These spectra are displayed in Figures 8.6 and 8.7 and Mössbauer parameters are listed in Table 8.6, which

also includes those of related carboxylate-rich iron(II) complexes and enzymes of interest. The Mössbauer spectra of both 1 and 2 exhibit slightly asymmetric quadropole doublet, probably reflecting the crystallographic inequivalent sites of the two iron atoms. By contrast, the iron centers of compounds 3 and 5 are crystallographically equivalent, resulting in spectra that are symmetric. The isomer shifts of these compounds compare well with those of other high-spin iron(II) complexes having oxygen rich coordination environments.<sup>27</sup>

There is one obvious trend in the data of Table 8.6, namely, that the iron(II) sites with coordination number 4 tend to have lower isomer shifts (1.0 - 1.1 mm s<sup>-1</sup>) compared to the coordinatively saturated iron(II) sites (~ 1.3 mm s<sup>-1</sup>). A possible explanation for this trend is the following. The isomer shift is defined by the expression in eq 1,

$$\delta = \text{constant} \times (|\psi_s(0)_S|^2 - |\psi_s(0)_A|^2) \quad (1)$$

where S and A are two different chemical environments of which S is the sample and A is a reference absorber.  $|\psi_s(0)_S|^2$  is the *s*-electron density at the iron nucleus. The isomer shift of an iron complex is dictated by two major factors, a direct contribution from 4*s*-electron density, and indirect contributions from the 3*d*-electrons that shield interpenetration by the *s*-electrons. Since the direct contribution in the ferrous complexes is fixed, only the indirect contributions are variable. In particular, the shielding can be considered as arising from the non-bonding effect of the 3*d*<sup>6</sup> configuration of iron(II), covalency of ligands in which filled ligand orbitals donate an effective total of *x* electrons to the 3*d*-orbitals, and covalency with ligands into which metal 3*d*-orbitals donate an effective total of *y* 3*d*-electrons into the  $\pi^*$  ligand orbitals. Thus, the effective number of shielding 3*d*-electrons can be described by  $N_{\text{eff}} = 6 + x - y$ . Because the complexes listed in Table 8.6 have ligand frameworks that are only weakly  $\pi$  acidic, the *y* contribution



can be considered to be negligible. The covalency contribution,  $x$ , is expected to follow the order six- > five- > four-coordinate complexes. Larger isomer shifts will therefore occur for complexes having higher  $N_{\text{eff}}$  value, as observed for the compounds in Table 8.6.

The isomer shift of the diiron(II) sites in reduced sMMOH is reported to be  $\sim 1.30$  mm s<sup>-1</sup>, which is in the range of six coordinate iron(II) sites, indicating that the metal centers in the enzyme may be six coordinate.<sup>28</sup> The isomer shift of the diiron(II) sites in RNR-R2 is 1.26 mm s<sup>-1</sup>, slightly smaller than most six-coordinate iron(II) model sites.<sup>1</sup>

**Magnetic Properties.** The effective magnetic moment ( $\mu_{\text{eff}}$ ) of **1** steadily increases from 1.0  $\mu_B$  at 5 K to 8.0  $\mu_B$  at 300 K, with a plateau at 120 K (Figure 8.8). This behavior signals a weak antiferromagnetic exchange coupling interaction between the two high-spin iron(II) centers of the tetracarboxylate-bridged dimer. Although similar behavior was reported for an analogous complex,  $[\text{Fe}_2(\mu\text{-O}_2\text{CAr}^{\text{Tol}})_4(4\text{-}^t\text{BuC}_5\text{H}_4\text{N})_2]$ ,<sup>29</sup> a reasonable model to explain the existence of a plateau in magnetic moment is currently unavailable.

**Electronic and Resonance Raman Spectroscopy.** The intense respective red pink and red colors of **1** and **2** observed in solid state are also evident in CH<sub>2</sub>Cl<sub>2</sub> solutions of the compounds, with  $\lambda_{\text{max}}$  occurring at 510 nm ( $\epsilon = 2200$  cm<sup>-1</sup> M<sup>-1</sup>) and 480 nm ( $\epsilon = 2300$  cm<sup>-1</sup> M<sup>-1</sup>) (Figure 8.9). Considering that the iron(II) sites of **2** are coordinated by carboxylates with more electron-withdrawing groups, the observed difference (blue shift) in the electronic transition supports the hypothesis that it is a MLCT. To gain more insight into the origin of this unusual electronic transition, a resonance Raman spectrum of **1** was measured in CH<sub>2</sub>Cl<sub>2</sub> solution at ambient temperature with excitation at 514 nm. The result is presented in Figure 8.10, which displays the spectra of **1** and, for composi-

tion, 4-NCC<sub>5</sub>H<sub>4</sub>N (literature data). Several strong resonance enhanced peaks appeared in the 700 cm<sup>-1</sup> - 1800 cm<sup>-1</sup> region for **1**. These features are also present in the rR spectrum of the 4-NCC<sub>5</sub>H<sub>4</sub>N ligand, indicating that the chromophore involves the N-donor ligand. Based on the high intensities of the electronic transitions, the blue shift of the more electron-poor iron(II) complex, and the resonance enhanced peaks corresponding to the 4-NCC<sub>5</sub>H<sub>4</sub>N ligand, the visible bands of **1** and **2** are preliminarily assigned to an Fe(II) → 4-NCC<sub>5</sub>H<sub>4</sub>N charge transfer (MLCT) transition. A detailed calculation is currently in progress.

**Equilibria Related to Coordinating Solvents.** No marked thermochromism of **1** occurs in CH<sub>2</sub>Cl<sub>2</sub> or toluene solutions of **1**. When coordinating solvents such as THF, acetonitrile, or benzonitrile are employed, however, the visible band of **1** disappears at ambient temperature and then grows in as the temperature is lowered (Figure 8.11 Top). The effect is fully reversible. This thermochromism involving solvent was further investigated in THF solution, where the complex is more soluble. Addition of 2 equiv of 4-NCC<sub>5</sub>H<sub>4</sub>N ligand to a THF solution of **1** restored the color, indicating the existence of the equilibrium shown in Scheme 8.2 and eq 2, where **W** is [Fe<sub>2</sub>(μ-O<sub>2</sub>CAr<sup>Tol</sup>)<sub>2</sub>(O<sub>2</sub>CAr<sup>Tol</sup>)<sub>2</sub>(THF)<sub>2</sub>].



Quantitative treatment of the equilibrium was performed by fitting the measured absorbance change over a temperature range. A mathematical equation describing this model (eq 2) and the derivation is provided in the Appendix, which assumes no change in extinction coefficient ( $\epsilon$ ) of **1** over the entire temperature range and the presence of only two metal containing species, **W** and **1**. The resulting thermodynamic parameters

are  $\Delta H = 50.6$  (7)  $\text{kJ mol}^{-1}$ ,  $\Delta S = 130$  (2)  $\text{J mol}^{-1}\text{K}^{-1}$ , and  $\epsilon_{490} = 2413$  (51)  $\text{M}^{-1}\text{cm}^{-1}$  with  $R = 1.00$  (Figure 8.11, Bottom). The observed thermochromism originates from the small positive enthalpy for the reaction. Excess coordinating THF solvent displaces the 4-NCC<sub>5</sub>H<sub>4</sub>N ligands from compound **1**. Because of the tendency for coordinating solvents to react with **1**, further studies were carried out in non-coordinating CH<sub>2</sub>Cl<sub>2</sub>.

**Water-Dependent Reactions.** Recently we reported the observation of a water-dependent equilibrium involving the compound  $[\text{Fe}_2(\mu\text{-OH}_2)_2(\mu\text{-O}_2\text{CAr}^{\text{Tol}})_2(\text{O}_2\text{CAr}^{\text{Tol}})_2(4\text{-}^t\text{BuC}_5\text{H}_4\text{N})_2]$ .<sup>29</sup> A quantitative treatment of the equilibrium was not possible, however, due to the absence of optical spectroscopic bands. When the light yellow-red compound **3** is dissolved in anhydrous CH<sub>2</sub>Cl<sub>2</sub>, the solution becomes red-pink in color, matching exactly the UV-vis spectrum of **1**. This result indicates that the coordinated water molecules dissociate from the first coordination sphere of the iron(II) centers as indicated in eq 3, where A is a {**1**·H<sub>2</sub>O} adduct



Upon lowering the temperature from 273 K to 203 K, there is a gradual shift of the peak maximum from 510 nm to 460 nm, with two isosbestic points at 480 nm and 420 nm (Figure 8.12). The electronic transition at 460 nm (the color of solid compound **3**) can be reproduced by dissolving **1** in CH<sub>2</sub>Cl<sub>2</sub> saturated with water. These results indicate that the existence of a water-dependent equilibrium in CH<sub>2</sub>Cl<sub>2</sub> solutions of **1**. The peak at 510 nm originates from **1** and the peak at 460 nm is assigned to a water-containing species A. The two observed isosbestic points suggest that compound **1** and A are the only spectroscopically active species involved in the thermochromic behavior. Below  $-70$  °C, however, the absorbance at 460 nm continues to increase and the isosbestic points dis-

appear. A possible explanation for the observed thermochromism is the sequential incorporation of water molecules to **1**, as displayed in Scheme 8.3. Dissolution of **3** effects the dissociation of water molecules from the diiron site, generating **1** and two water molecules. Binding of a water molecule to **1** decreases the absorbance at 510 nm while increasing that at 460 nm, indicating the generation of a single water-containing species **A**. Below  $-70\text{ }^{\circ}\text{C}$ , at which point conversion of **1** to **A** is complete, additional water molecules are taken up by **A**, possibly generating the diiron(II) complex **2**, which carries two water molecules. A mathematical equation describing this model (eq 3) and the derivation is provided in the Appendix. Fitting of the observed absorbance change at 510 nm resulted in the thermodynamic parameters  $\Delta H = -95\text{ (11) kJ mol}^{-1}$ ,  $\Delta S = -250\text{ (50) J mol}^{-1}\text{K}^{-1}$ ,  $\epsilon_{510} = 2000\text{ (30) M}^{-1}\text{cm}^{-1}$  for **1**, and  $\epsilon_{510} = 1089\text{ (10) M}^{-1}\text{cm}^{-1}$  for **A** with  $R = 0.99$ . The negative enthalpy results from the energy of bond formation between water and iron(II), and the negative entropy corresponds to a bimolecular combination. Although water binding is not tight at room temperature, it becomes very favorable at low temperature. Recently reported oxygenation studies of diiron(II) complexes in a carboxylate-rich coordination environment described, without explanation, the inhibition of the generation of intermediates at low temperature by a trace amount of water.<sup>30</sup> We believe the binding of water molecules to their carboxylate-rich diiron(II) complexes at low temperature to be the cause of this behavior.

**Electrochemistry.** The electrochemical properties of **1** were investigated by cyclic voltammetry. Compound **1** in  $\text{CH}_2\text{Cl}_2$  undergoes a quasi-reversible one-electron oxidation ( $E_{1/2} = 27\text{ mV}$  vs  $\text{Cp}_2\text{Fe}^+/\text{Cp}_2\text{Fe}$ ;  $\Delta E_p = 120\text{ mV}$ , scan rate =  $50\text{ mV/s}$ , Figure 8.13). As expected, there is a positive shift ( $\Delta E = +243\text{ mV}$ ) in reduction potential compared to the

analogue  $[\text{Fe}_2(\mu\text{-O}_2\text{CAr}^{\text{Tol}})_4(4\text{-}^t\text{BuC}_5\text{H}_4\text{N})_2]$ ,<sup>31</sup> consistent with the more electron-withdrawing nature of the 4-cyanopyridine ligand.

Cyclovoltammograms of compound **3** in  $\text{CH}_2\text{Cl}_2$  are shown in Figure 8.14. One irreversible oxidation at  $E_{1/2} = 27$  mV (scan rate = 50 mV/s) accompanied by a broad reduction wave at ca.  $-697$  mV vs  $\text{Cp}_2\text{Fe}^+/\text{Cp}_2\text{Fe}$  was observed (Figure 8.14 A). When the voltammogram was only scanned between  $-149$  mV and  $-949$  mV and recorded, the reduction wave at  $-697$  mV was no longer present (Figure 8.14 B). Combined with the variable temperature UV-vis spectroscopic data, these results can be rationalized in the following manner (Scheme 8.4). Dehydration of **3** in  $\text{CH}_2\text{Cl}_2$  can occur to afford two molecules of water and **1**, which has a quasi-reversible  $\text{Fe}_2(\text{II,II})/\text{Fe}_2(\text{II,III})$  couple at  $E_{1/2} = 27$  mV. Oxidation of **1** provides the mixed-valent cation,  $[\text{Fe}_2(\mu\text{-O}_2\text{CAr}^{\text{Tol}})_4(4\text{-NCC}_5\text{H}_4\text{N})_2]^+$ , which is stable in the absence of water. Such oxidations occur for the  $[\text{Fe}_2(\mu\text{-O}_2\text{CAr}^{\text{Tol}})_4(4\text{-}^t\text{BuC}_5\text{H}_4\text{N})_2]$  analogues. In presence of water molecules, however, an aquated  $[\text{Fe}_2(\text{O}_2\text{CAr}^{\text{Tol}})_4(4\text{-NCC}_5\text{H}_4\text{N})_2(\text{OH}_2)_x]^+$  species may form, in which  $x$  can be one or two. This complex should exhibit different electrochemical behavior, and its reduction may give rise to the wave at ca  $-697$  mV. The complex  $[\text{Fe}_2(\text{O}_2\text{CAr}^{\text{Tol}})_4(4\text{-CNC}_5\text{H}_4\text{N})_2(\text{OH}_2)_x]$ , generated in this manner, would readily lose water molecules to form **1** (see above), giving no oxidation wave on the reverse sweep until a potential greater than  $-149$  mV is attained. Uptake of water thus appears to lower the reduction potential of the diiron(II) core by  $\sim 700$  mV, as might be expected from the addition of good  $\sigma$  donors to the dimetallic center. This result is in line with the previously observed electrochemistry of  $[\text{Fe}_2(\mu\text{-OH}_2)_2(\mu\text{-O}_2\text{CAr}^{\text{Tol}})_4(4\text{-}^t\text{BuC}_5\text{H}_4\text{N})_2]$ .<sup>12</sup>

**Effect of Water on the Oxygenation Rate of Compound 1.** The influence of water on the oxygenation chemistry of carboxylate-rich diiron(II) complexes is of interest

because the active sites in sMMOH contain two water molecules in the first and second coordination spheres. Such water may modulate the oxygenation reactions of the diiron(II) sites in the enzymes. The reaction of compound **1** with dioxygen instantaneously leads to the formation of a light green yellow solution. This process was followed by stopped-flow kinetics, monitoring the charge transfer band, a broad feature centered at 510 nm for **1** (Figure 8.15). When studied under conditions of excess dioxygen, the decay of compound **1** follows a pseudo first-order rate law. Rate constants (Table 8.7) were derived from time-dependent absorbance changes by using a nonlinear least squares fitting procedure based on eq 4. The fast oxygenation of **1** contrasts with its observed inertness to dioxygen in the solid state, indicating that the reactive species in solution may not have a quadruply bridged structure. An equilibrium between doubly and quadruply bridged isomers of **1** in the solution state is likely to exist through carboxylate shifts. Such an equilibrium has been proposed and is generally accepted for the analogous complex,  $[\text{Fe}_2(\mu\text{-O}_2\text{CAr}^{\text{Tot}})_4(4\text{-}^t\text{BuC}_5\text{H}_4\text{N})_2]$ . One of these isomers, probably a doubly bridged complex, would react with dioxygen.

$$A_t = A_\infty - (A_\infty - A_0)\exp(-k_{\text{obs}}t) \quad (4)$$

where  $A_\infty$  and  $A_0$  respectively are the optical absorbance at infinite time and time zero

Competition between dioxygen and water for **2** was investigated between 193 K and 293 K using stopped-flow kinetics (Figure 8.16). To obtain pseudo-first order conditions, the concentrations of **1**, water, and dioxygen were maintained at 0.19, 1.00, and 2.9 mM, respectively. The reaction proceeds through the extremely fast generation of a species that absorbs at 460 nm, followed by decay of this species (Figure 8.16 Top). The

first steps were only detectable at temperature below  $-50\text{ }^{\circ}\text{C}$  and went to completion within 1 sec. The time dependent absorbance changes follow a pseudo first-order rate law and the fit results are listed in Table 8.8. The second step proceeds relatively more slowly than the first. The decay at 460 nm also follows a pseudo first-order rate law and rate constants were determined by a linear squares fit to eq 4. The kinetic behavior can be rationalized by the following scenario (Scheme 8.5). The species with an absorption at 460 nm, the formation of which is correlated with the decrease at 510 nm, is assigned as the single water-containing species **A**, generated by hydration of **1** (see above), and the decay of this peak occurs through oxygenation. The two-fold understanding is achieved from this analysis. First, hydration of **1** is at least 1000 times faster than oxygenation of **1**. The rate constant for hydration ( $k_{2_{obs}}$ ) of **1** at  $-50\text{ }^{\circ}\text{C}$  is  $63.5(8)\text{ s}^{-1}$ , whereas the oxygenation rate constant ( $k_{1_{obs}}$ ) of **1** at  $-30\text{ }^{\circ}\text{C}$  is  $0.045(5)\text{ s}^{-1}$ . This dramatic difference in rates may originate from the small but obvious size difference between water and dioxygen and the hydrogen bond donating ability of the former. Secondly, the water-containing species (**A**) reacts with dioxygen ca 10-fold faster than does **1**. We suggest that the binding of water generates an open coordination site for dioxygen binding in **A**. This event may facilitate Fe–O bond formation, which is presumably the rate-determining step of the oxidation process.

**Isolation and Structural Characterization of Iron(III) Complexes**  $[\text{Fe}_2(\mu\text{-OH})_2(\mu\text{-O}_2\text{CAr}^{\text{Tol}})_2(\text{O}_2\text{CAr}^{\text{Tol}})_2(^4\text{-CN}\text{C}_5\text{H}_4\text{N})_2]\cdot 2(\text{HO}_2\text{CAr}^{\text{Tol}})$  (**6**) and  $[\text{Fe}_6(\mu\text{-O})_2(\mu\text{-OH})_4(\mu\text{-O}_2\text{CAr}^{\text{Tol}})_6(4\text{-CNC}_5\text{H}_4\text{N})_4(\text{Cl})_2]$  (**7**). The light greenish-yellow  $\text{CH}_2\text{Cl}_2$  solution generated upon oxygenation of **1** affords crystals upon vapor diffusion of pentane, an inseparable mixture of the quadruply bridged diiron(III) complex **6** and the hexairon(III) species **7**. The structure of **6** is depicted in Figure 8.17 and selected interatomic distances and an-

gles are listed in Table 8.4. Two distorted octahedral iron(III) atoms are bridged by two hydroxide and two carboxylate ligands. The Fe...Fe distance of 2.8323(10) Å is in the ~ 2.85 Å range typical for quadruply bridged  $\{\text{Fe}_2(\mu\text{-OH})_2(\mu\text{-O}_2\text{CR})_2\}^{2+}$  cores. Two intramolecular hydrogen bonding interactions occur between the terminal, metal-bound carboxylates and the bridging hydroxo groups, with O-H...O distances of 2.818(6) and 2.888(5) Å. In addition, two carboxylic acids ( $\text{HO}_2\text{CAr}^{\text{Tot}}$ ) are located in proximity to the terminal carboxylates in the crystal lattice, generating hydrogen-bonding interactions.

The hexairon(III) species **7** was isolated with compound **6**. The structure of **7** is best described by the diagrams in Figure 8.18, and a list of selected interatomic distances and angles is included in Table 8.5. The structure of **7**, which has an inversion center, combines two ( $\mu_3\text{-oxo}$ )triiron(III) units through a four OH<sup>-</sup> and two  $\text{O}_2\text{CAr}^{\text{Tot}}$  bridging groups. Four octahedral and two distorted trigonal bipyramidal iron(III) sites result. It is noteworthy that the structure of **7** also contains two Cl<sup>-</sup> ligands coordinated to each of the octahedral iron(III) sites. The same experiment, performed in the absence of light, afforded the same mixture of **6** and **7**. This result indicates that a photochemical reaction is not involved in generating the Cl<sup>-</sup> anion.

**Mechanistic Considerations.** Based on the spectroscopic, structural and kinetic data obtained, a mechanism is proposed to account for the observed chemical conversions (Scheme 8.5). An equilibrium between the doubly and quadruply bridged isomers of **1** in the solution state can occur through carboxylate shifts. One of these isomers, most likely the doubly bridged complex, reacts with dioxygen faster than the other, quadruply bridged one. This explanation accounts for the marked difference in the oxygenation of solid versus solution samples of **1**. In the competition between water and dioxygen, aquation occurs first and the resulting aqua complex then reacts with di-



oxygen. The faster reaction rate of the aquated species compared to **1** is due to the expected formation of an open coordination site generated by a carboxylate shift upon binding of water. Oxidation of the solvent,  $\text{CH}_2\text{Cl}_2$ , generates  $\text{Cl}^-$  anions which coordinate to the iron(III) site, leading to reorganization of the diiron species to hexanuclear **7**. The dissociated carboxylic acid interacts with a diiron(III) unit through hydrogen-bondings in compound **6**.

### Summary.

In summary, high-spin 4-cyanopyridine diiron(II) complexes with distinctive electronic transitions in the visible region have been prepared and used to investigate quantitatively a water-dependent reaction chemistry. Utilizing this charge transfer band, we have addressed the effects of water molecules on the oxygenation of the diiron(II) complex **1**. The binding of water to the diiron(II) site generates an open coordination site via a carboxylate shift, leading to the acceleration of the oxygenation step over oxygenation under anhydrous conditions. The final products of the oxidation are the dinuclear complex **6** and a Cl-containing iron(III) complex. Finally, by comparison of the new diiron(II) complexes with related ones in the literature, we established a correlation between Mössbauer effect isomer shifts and coordination number for high-spin iron(II) complexes in an oxygen-rich coordination environment. The trend was rationalized on the basis of the s-electron density at the iron nucleus over the series.

**References**

- (1) Stubbe, J.; van der Donk, W. A. *Chem. Rev.* **1998**, *98*, 705-762.
  - (2) Logan, D. T.; Su, X.-D.; Åberg, A.; Regnström, K.; Hajdu, J.; Eklund, H.; Nordlund, P. *Structure* **1996**, *4*, 1053-1064.
  - (3) Merckx, M.; Kopp, D. A.; Sazinsky, M. H.; Blazyk, J. L.; Müller, J.; Lippard, S. J. *Angew. Chem. Int. Ed.* **2001**, *40*, 2782-2807.
  - (4) Lindqvist, Y.; Huang, W.; Schneider, G.; Shanklin, J. *EMBO Journal* **1996**, *15*, 4081-4092.
  - (5) Sazinsky, M. H.; Bard, J.; Di Donato, A.; Lippard, S. J. *J. Biol. Chem.* **2004**, *279*, 30600-30610.
  - (6) Kuzelka, J.; Farrell, J. R.; Lippard, S. J. *Inorg. Chem.* **2003**, *42*, 8652-8662.
  - (7) Lee, D.; DuBois, J. L.; Pierce, B.; Hedman, B.; Hodgson, K. O.; Hendrich, M. P.; Lippard, S. J. *Inorg. Chem.* **2002**, *41*, 3172-3182.
  - (8) Mizoguchi, T. J.; Lippard, S. J. *J. Am. Chem. Soc.* **1998**, *120*, 11022-11023.
  - (9) Gherman, B. F.; Dunietz, B. D.; Whittington, D. A.; Lippard, S. J.; Friesner, R. A. *J. Am. Chem. Soc.* **2001**, *123*, 3836-3837.
  - (10) Gherman, B. F.; Baik, M.-H.; Lippard, S. J.; Friesner, R. A. *J. Am. Chem. Soc.* **2004**, *126*, 2978-2990.
  - (11) Yoon, S., In *Department of Chemistry*; M.I.T.: Cambridge, 2004, 221-245.
  - (12) Yoon, S.; Kelly, A. E.; Lippard, S. J. *Polyhedron* **2004**, in press.
  - (13) Pangborn, A. B.; Giardello, M. A.; Grubbs, R. H.; Rosen, R. K.; Timmers, F. J. *Organometallics* **1996**, *15*, 1518-1520.
  - (14) Du, C.-J. F.; Hart, H.; Ng, K.-K. D. *J. Org. Chem.* **1986**, *51*, 3162-3165.
-

- (15) Brookhart, M.; Grant, B. *Organometallics* **1992**, *11*, 3920-3922.
- (16) Kuzelka, J.; Mukhopadhyay, S.; Springler, B.; Lippard, S. J. *Inorg. Chem.* **2004**, *43*, 1751-1761.
- (17) Sheldrick, G. M.; University of Göttingen: Göttingen, Germany, 1997.
- (18) Sheldrick, G. M.; University of Göttingen: Göttingen, Germany, 1996.
- (19) Spek, A. L.; Utrecht University: Utrecht, The Netherlands, 1998.
- (20) Kent, T. A.; v2.5 ed.: Minneapolis, 1998.
- (21) Roelfes, G.; Vrajmasu, V.; Chen, K.; Ho, R. Y. N.; Rohde, J.-U.; Zondervan, C.; la Crois, R. M.; Schudde, E. P.; Lutz, M.; Spek, A. L.; Hage, R.; Feringa, B. L.; Münck, E.; Que, L., Jr. *Inorg. Chem.* **2003**, *42*, 2639-2653.
- (22) Monat, J. E.; McCusker, J. K. *J. Am. Chem. Soc.* **2000**, *122*, 4092-4097.
- (23) Lee, D.; Lippard, S. J. *Inorg. Chem.* **2002**, *41*, 827-837.
- (24) Hagadorn, J. R.; Que, L., Jr.; Tolman, W. B. *J. Am. Chem. Soc.* **1998**, *120*, 13531-13532.
- (25) Lee, D.; Du Bois, J.; Petasis, D.; Hendrich, M. P.; Krebs, C.; Huynh, B. H.; Lippard, S. J. *J. Am. Chem. Soc.* **1999**, *121*, 9893-9894.
- (26) Yoon, S.; Lippard, S. J. *Inorg. Chem.* **2003**, *42*, 8606-8608.
- (27) Yshuva, E. Y.; Lippard, S. J. *Chem. Rev.* **2004**, *104*, 987-1012.
- (28) Whittington, D. A.; Lippard, S. J. *J. Am. Chem. Soc.* **2001**, *123*, 827-838.
- (29) Lee, D.; Pierce, B.; Krebs, C.; Hendrich, M. P.; Huynh, B. H.; Lippard, S. J. *J. Am. Chem. Soc.* **2002**, *124*, 3993-4007.
- (30) Kryatov, S. V.; Chavez, F. A.; Reynolds, A. M.; Rybak-Akimova, E. V.; Que, L., Jr.; Tolman, W. B. *Inorg. Chem.* **2004**, *43*, 2141-2150.
- (31) Lee, D.; Krebs, C.; Huynh, B. H.; Hendrich, M. P.; Lippard, S. J. *J. Am. Chem. Soc.* **2000**, *122*, 5000-5001.

Table 8.1. Summary of X-ray Crystallographic Data

Compound	1·4THF	2·4CH <sub>2</sub> Cl <sub>2</sub>	3	4
empirical formula	Fe <sub>2</sub> C <sub>112</sub> H <sub>108</sub> N <sub>4</sub> O <sub>12</sub>	Fe <sub>2</sub> C <sub>96</sub> H <sub>60</sub> N <sub>4</sub> O <sub>8</sub> Cl <sub>8</sub>	Fe <sub>2</sub> C <sub>96</sub> H <sub>80</sub> N <sub>4</sub> O <sub>10</sub>	Fe <sub>2</sub> C <sub>88</sub> H <sub>56</sub> N <sub>4</sub> O <sub>10</sub> F <sub>8</sub>
weight	1813.72	2000.82	1561.34	1593.07
space group	P $\bar{1}$	P $\bar{1}$	P $\bar{1}$	P $\bar{1}$
<i>a</i> , Å	16.1429(17)	14.624(3)	10.501(3)	10.4297(19)
<i>b</i> , Å	16.8733(18)	16.815(3)	13.256(4)	13.260(2)
<i>c</i> , Å	17.3090(19)	19.000(4)	15.364(4)	14.204(3)
$\alpha$ , deg	89.578(2)	101.087(4)	112.975(4)	110.408(3)
$\beta$ , deg	89.332(2)	108.835(4)	100.074(4)	99.903(3)
$\gamma$ , deg	88.507(2)	96.944(4)	94.916(4)	96.652(3)
<i>V</i> , Å <sup>3</sup>	4712.7(9)	4254.2(14)	1910.4(9)	1780.5(5)
<i>Z</i>	2	2	1	1
$\rho_{\text{calc}}$ , g/cm <sup>3</sup>	1.278	1.562	1.357	1.486
crystal size, mm	0.10×0.10×0.05	0.15×0.10×0.05	0.30×0.08×0.05	0.20×0.07×0.05
<i>T</i> , °C	-100	-100	-100	-100
$\mu$ (Mo Ka), mm <sup>-1</sup>	0.374	0.676	0.447	0.497
total no. of data	35789	31482	14453	13413
no. of unique data points	16917	14839	6858	6379
no. of parameters	1080	1126	517	513
R1 (%) <sup>a</sup>	8.29	10.99	3.80	4.06
wR2 (%) <sup>b</sup>	20.70	26.78	9.86	9.62

<sup>a</sup> R1 =  $\Sigma||F_o| - |F_c||/\Sigma|F_o|$ . <sup>b</sup> wR2 =  $\{\Sigma[w(F_o^2 - F_c^2)^2]/\Sigma[w(F_o^2)^2]\}^{1/2}$

Table 8.1. Continued

Compound	5	6·4CH <sub>2</sub> Cl <sub>2</sub>	7·6CH <sub>2</sub> Cl <sub>2</sub>
empirical formula	Fe <sub>2</sub> C <sub>107</sub> H <sub>71</sub> N <sub>4</sub> O <sub>6</sub> F <sub>24</sub> B	Fe <sub>2</sub> C <sub>132</sub> H <sub>122</sub> N <sub>4</sub> O <sub>14</sub> Cl <sub>8</sub>	Fe <sub>6</sub> C <sub>156</sub> H <sub>136</sub> N <sub>8</sub> O <sub>20</sub> Cl <sub>14</sub>
weight	2087.19	2383.64	3274.13
space group	I <sub>2</sub> /a	P $\bar{1}$	P $\bar{1}$
a, Å	25.97(3)	16.155(3)	15.623(17)
b, Å	24.50(3)	17.578(3)	16.588(18)
c, Å	33.37(5)	23.105(4)	16.961(18)
$\alpha$ , deg	93.60(10)	92.951(3)	63.993(18)
$\beta$ , deg		91.752(3)	88.56(2)
$\gamma$ , deg		94.955(3)	72.31(2)
V, Å <sup>3</sup>	21190(45)	6524.2(18)	3733(7)
Z	8	2	1
$\rho_{\text{calc}}$ , g/cm <sup>3</sup>	1.308	1.213	1.456
crystal size, mm	0.08×0.06×0.05	0.30×0.25×0.07	0.15×0.10×0.10
T, °C	-100	-100	-100
$\mu$ (Mo K $\alpha$ ), mm <sup>-1</sup>	0.654	0.445	0.887
total no. of data	20695	48044	28264
no. of unique data points	13241	22735	13405
no. of parameters	1271	1587	948
R1 (%) <sup>a</sup>	24.36	8.27	9.57
wR2 (%) <sup>b</sup>	51.56	23.29	23.34

$$^a \text{R1} = \Sigma |F_o| - |F_c| / \Sigma |F_o|, \quad ^b \text{wR2} = \{ \Sigma [w(F_o^2 - F_c^2)^2] / \Sigma [w(F_o^2)] \}^{1/2}$$

**Table 8.2.** Selected interatomic bond lengths (Å) and angles (deg) for  $[\text{Fe}_2(\mu\text{-O}_2\text{CAr}^{\text{Tot}})_4(4\text{-NCC}_5\text{H}_4\text{N})_2]$  (**1**) and  $[\text{Fe}_2(\mu\text{-O}_2\text{CAr}^{4\text{F-Ph}})_4(4\text{-NCC}_5\text{H}_4\text{N})_2]$  (**2**).

Compound	1·4THF	2·4CH <sub>2</sub> Cl <sub>2</sub>
Fe1···Fe2	2.7754(9)	2.7415(16)
Fe1–O1	2.131(3)	2.036(5)
Fe1–O3	2.004(3)	2.112(5)
Fe1–O5	2.145(3)	2.040(5)
Fe1–O7	2.010(3)	2.120(5)
Fe2–O2	2.032(3)	2.057(5)
Fe2–O4	2.132(3)	2.070(5)
Fe2–O6	2.016(3)	2.064(5)
Fe2–O8	2.133(3)	2.082(5)
Fe1–N1	2.100(4)	2.086(7)
Fe2–N3	2.091(4)	2.097(7)
O1–Fe1–N1	98.39(14)	104.8(3)
O3–Fe1–N1	100.72(14)	96.8(2)
O5–Fe1–N1	94.50(14)	96.5(3)
O7–Fe1–N1	101.22(14)	96.3(2)
O2–Fe2–N3	99.65(14)	93.3(2)
O4–Fe2–N3	96.79(14)	99.2(3)
O6–Fe2–N3	102.16(14)	101.0(2)
O8–Fe2–N3	96.22(14)	98.6(2)
O1–Fe1–O3	89.94(12)	86.5(2)
O1–Fe1–O5	167.11(12)	158.7(2)
O1–Fe1–O7	87.90(12)	92.2(2)
O3–Fe1–O5	87.35(11)	91.1(2)
O3–Fe1–O7	158.03(13)	166.7(2)
O5–Fe1–O7	89.91(11)	85.4(2)
O2–Fe2–O4	89.68(12)	88.2(2)
O2–Fe2–O6	158.19(13)	165.6(2)
O2–Fe2–O8	87.68(12)	87.1(2)
O4–Fe2–O6	88.17(12)	87.5(2)
O4–Fe2–O8	166.99(12)	161.8(2)
O6–Fe2–O8	89.56(11)	92.7(2)

Numbers in parentheses are estimated standard deviations of the last significant figure.

**Table 8.3.** Selected interatomic bond lengths (Å) and angles (deg) for  $[\text{Fe}_2(\mu\text{-O}_2\text{CAr}^{\text{Tol}})_2(\text{O}_2\text{CAr}^{\text{Tol}})_2(4\text{-NCC}_5\text{H}_4\text{N})_2(\text{OH}_2)_2]$  (**3**) and  $[\text{Fe}_2(\mu\text{-O}_2\text{CAr}^{4\text{F-Ph}})_2(\text{O}_2\text{CAr}^{4\text{F-Ph}})_2(4\text{-NCC}_5\text{H}_4\text{N})_2(\text{OH}_2)_2]$  (**4**).

Compound	3	4
Fe1...Fe2	4.466	4.402
Fe1-O1	2.1686(15)	2.1552(18)
Fe1-O2	2.0285(13)	2.0485(15)
Fe1-O3	2.0871(13)	2.0714(14)
Fe1-O4	2.1475(13)	2.1565(15)
Fe1-O5	2.3278(14)	2.3352(15)
Fe1-N1	2.1505(16)	2.1412(18)
O1-Fe1-O2	81.01(6)	80.60(7)
O1-Fe1-O3	172.53(6)	171.11(7)
O1-Fe1-O4	94.68(6)	91.10(7)
O1-Fe1-O5	79.07(6)	78.12(7)
O1-Fe1-N1	93.63(6)	95.73(7)
O2-Fe1-O3	106.34(6)	108.03(6)
O2-Fe1-O4	112.02(5)	115.24(6)
O2-Fe1-O5	156.99(5)	157.59(6)
O2-Fe1-N1	95.30(6)	89.93(6)
O3-Fe1-O4	83.85(5)	83.32(6)
O3-Fe1-O5	93.97(5)	93.05(6)
O3-Fe1-N1	84.51(6)	86.57(6)
O4-Fe1-O5	58.69(5)	58.58(5)
O4-Fe1-N1	152.36(6)	154.71(6)
O5-Fe1-N1	97.32(5)	99.06(6)
O1...O2	2.727	2.720
O1...O5 <sup>a</sup>	2.755	2.748

Numbers in parentheses are estimated standard deviations of the last significant figure.

**Table 8.4.** Selected interatomic bond lengths (Å) and angles (deg) for 6.

Fe1··Fe2	2.8323(10)	Fe2–O6	2.033(3)
Fe1–O1	1.950(3)	Fe2–N3	2.127(4)
Fe1–O2	1.978(3)	O8··O1	2.888(5)
Fe1–O3	2.045(3)	O8··O11	2.639(5)
Fe1–O5	2.076(3)	O10··O13	2.636(5)
Fe1–O7	1.955(3)	O10··O2	2.814(6)
Fe1–N1	2.132(4)	Fe1–O1–Fe2	43.50(10)
Fe2–O1	1.999(3)	Fe1–O2–Fe2	43.33(10)
Fe2–O2	1.945(3)	O1–Fe1–O2	88.19(14)
Fe2–O4	2.053(3)	O1–Fe2–O1	87.75(14)

Numbers in parentheses are estimated standard deviations of the last significant figure



**Table 8.5.** Selected interatomic bond lengths (Å) and angles (deg) for 7.

Fe1...Fe2	3.064(4)	Fe2-O10	2.059(7)
Fe2...Fe3	2.960(3)	Fe2-O6	2.085(7)
Fe1...O1	1.881(7)	Fe2-O12	2.019(8)
Fe1-O2	2.029(7)	Fe3-O7	2.063(7)
Fe1-O3	2.004(7)	Fe3-N2	2.181(9)
Fe1-O4	2.042(8)	Fe3-Cl(1)	2.311(3)
Fe1-O11	2.103(7)	Fe1-O3-Fe2	99.9(3)
Fe2-O3	1.999(7)	Fe1-O4-Fe2	97.5(4)
Fe2-O4	2.034(9)	Fe2-O12-Fe3	95.7(3)

Numbers in parentheses are estimated standard deviations of the last significant figure

**Table 8.6.** 4.2 K zero-field Mössbauer parameters for  $[\text{Fe}_2(\mu\text{-O}_2\text{CAr}^{\text{Tot}})_4(4\text{-NCC}_5\text{H}_4\text{N})_2]$  (1),  $[\text{Fe}_2(\mu\text{-O}_2\text{CAr}^{\text{Tot}})_2(\text{O}_2\text{CAr}^{\text{Tot}})_2(4\text{-NCC}_5\text{H}_4\text{N})_2(\text{H}_2\text{O})_2]$  (3),  $[\text{Fe}_2(\mu\text{-O}_2\text{CAr}^{\text{Tot}})_3(4\text{-NCC}_5\text{H}_4\text{N})_2(\text{BAR}'_4)]$  (5), reported carboxylate-rich iron(II) complexes, and enzymes of interest.

Compound	Coordination Geometry	Coordination Geometry	$\delta$ (mm s <sup>-1</sup> )	$\Delta E_Q$ (mm s <sup>-1</sup> )
$[\text{Fe}(\text{O}_2\text{CAr}^{4\text{-Ph}})_2(\text{Hdmpz})_2]$ 5	<i>Td</i> <sup>a</sup>	N <sub>2</sub> O <sub>2</sub>	1.04(2)	3.19(2)
$[\text{Fe}(\text{O}_2\text{CAr}^{\text{Tot}})_2(1\text{-Bnlm})_2]$	<i>Td</i>	NO <sub>3</sub>	1.04(2)	2.85(2)
$[\text{Fe}_2(\mu\text{-O}_2\text{CAr}^{\text{Tot}})_3(\text{O}_2\text{CAr}^{\text{Tot}})_2(2,6\text{-lutidine})_2]$	<i>Td</i>	N <sub>2</sub> O <sub>2</sub>	1.08(2)	2.46(2)
		NO <sub>3</sub>	1.05(2)	2.18(2)
		O <sub>5</sub>	1.23(2)	2.80(2)
$[\text{Fe}(\text{O}_2\text{CAr}^{\text{Tot}})_2(\text{BPTA})_2]$	<i>Tbp</i>	N <sub>3</sub> O <sub>2</sub>	1.10(2)	3.52(2)
$[\text{Fe}_2(\mu\text{-O}_2\text{CAr}^{\text{Tot}})_2(\text{O}_2\text{CAr}^{\text{Tot}})_2(\text{Hdmpz})_2]$ 1	<i>Tbp</i>	NO <sub>3</sub>	1.11(2)	2.78(2)
		NO <sub>4</sub>	1.11(2)	3.02(2)
		NO <sub>4</sub>	1.12(2)	3.05(2)
$[\text{Fe}_2(\mu\text{-O}_2\text{CAr}^{\text{Tot}})_4(^+\text{BuC}_3\text{H}_4\text{N})_2]$	<i>Tbp</i>	N <sub>2</sub> O <sub>3</sub>	1.13(2)	2.91(2)
$[\text{Fe}(\text{O}_2\text{CAr}^{4\text{-tBuPh}})_2(2,2'\text{-bipy})_2]$	<i>Tbp</i>	NO <sub>4</sub>	1.19(2)	2.90(2)
$[\text{Fe}_2(\mu\text{-O}_2\text{CAr}^{\text{Tot}})_2(\text{O}_2\text{CAr}^{\text{Tot}})_2(\text{C}_6\text{H}_5\text{N})_2]$	<i>Tbp</i>	NO <sub>4</sub>	1.19(2)	2.99(2)
$[\text{Fe}_2(\mu\text{-O}_2\text{CAr}^{\text{Tot}})_2(\text{O}_2\text{CAr}^{\text{Tot}})_2(\text{Bn}_2\text{en})_2]$	<i>Tbp</i>	O <sub>5</sub>	1.26(2)	2.90(2)
$[\text{Fe}_2(\mu\text{-O}_2\text{CAr}^{\text{Tot}})_2(\text{O}_2\text{CAr}^{\text{Tot}})_2(\text{THF})_2]$ 3	<i>Oh</i>	NO <sub>5</sub>	1.29(2)	3.09(2)
		O <sub>6</sub>	1.31(2)	2.86(2)
$[\text{Fe}_2(\mu\text{-OH})_2(\mu\text{-O}_2\text{CAr}^{\text{Tot}})_3(\text{THF})_2]$	<i>Oh</i>	O <sub>6</sub>	1.35(2)	3.26(2)
$[\text{Fe}_2(\mu\text{-OH})_2(\mu\text{-O}_2\text{CAr}^{4\text{-FPh}})_3(\text{THF})_2(\text{OH}_2)]$	<i>Oh</i>	O <sub>6</sub>	1.30(2)	3.53(2)
$[\text{Fe}_4(\mu_3\text{-OCH}_3)_4(\text{O}_2\text{CAr}^{\text{Tot}})_4(\text{HOCH}_2)_6]$	<i>Tbp</i>	O <sub>5</sub>	1.17(2)	2.35(2)
MMOH			1.30	2.87
RNR-R2			1.3	2.4–3.1
Δ9D			1.26	3.13
			1.30	3.04–3.36

Table 8.7. Rate constants  $k1_{obs}$  for oxygenation of 1 in  $\text{CH}_2\text{Cl}_2$ 

Temperature (K)	$k1_{obs}$ ( $\text{s}^{-1}$ ) <sup>a</sup>
293	1.4(3)
283	0.71(6)
273	0.40(2)
263	0.20(1)
253	0.10(1)
243	0.045(5)

<sup>a</sup>  $k1_{obs}$  in oxygenation of 1 is defined by following the reaction pathway

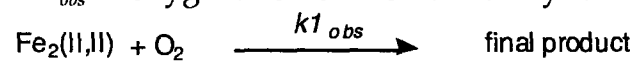
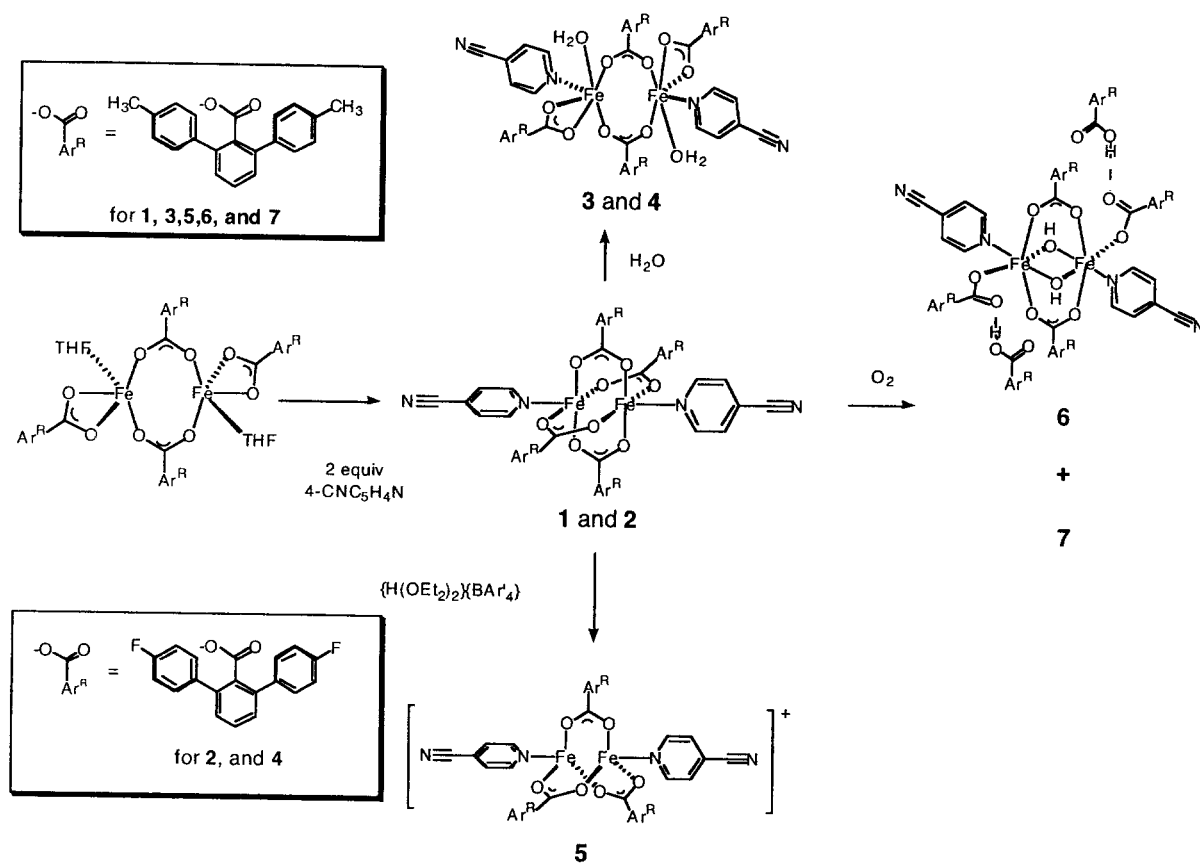


Table 8.8. Rate Constants  $k_{2_{obs}}$  and  $k_{3_{obs}}$  for oxygenation of 1 in  $\text{CH}_2\text{Cl}_2$  with water

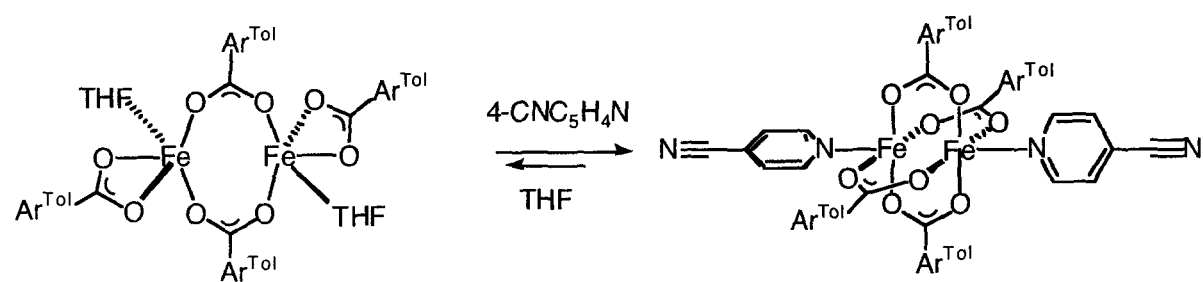
Temperature (K)	$k_{2_{obs}} (\text{s}^{-1})^a$	Temperature (K)	$k_{3_{obs}} (\text{s}^{-1})^a$
223	62.8(5)	293	14.6(7)
218	43.0(24)	283	9.1(10)
213	23.7(17)	273	5.5(5)
208	11.1(8)	263	2.7(2)
203	5.1(2)	253	1.21(17)
198	2.5(1)	243	0.39(12)
		233	0.12(1)

<sup>a</sup>  $k_{2_{obs}}$  and  $k_{3_{obs}}$  in oxygenation of 1 are defined by following the reaction pathway.

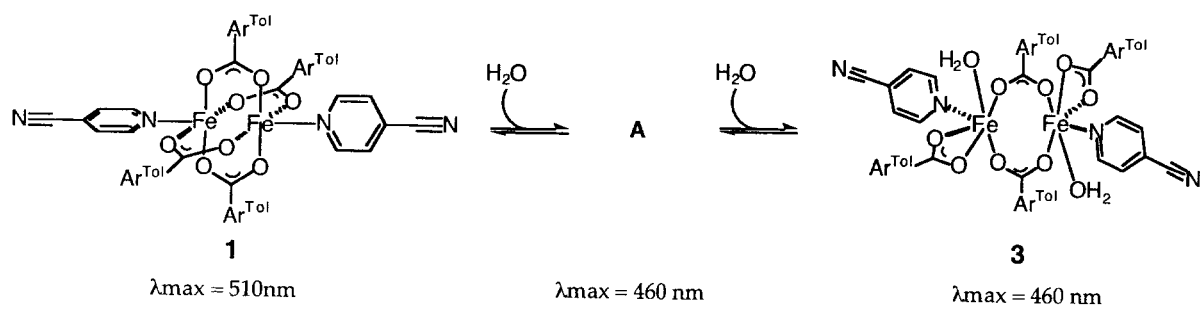




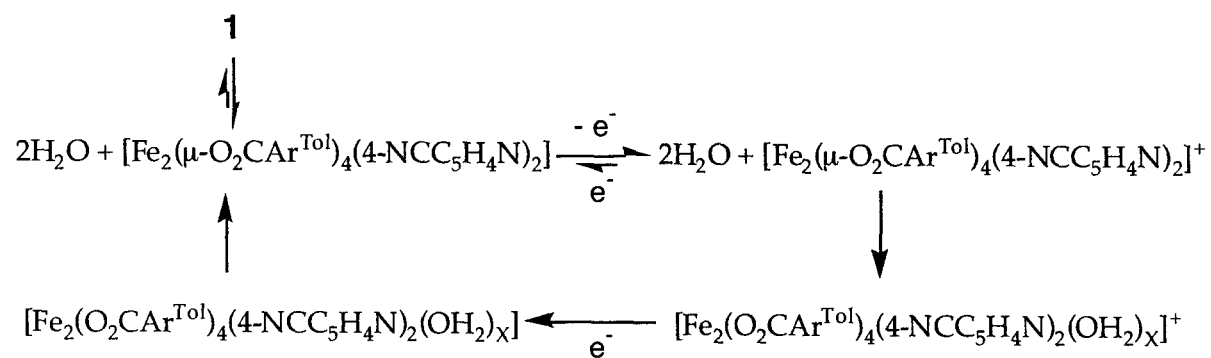
Scheme 8.1



Scheme 8.2

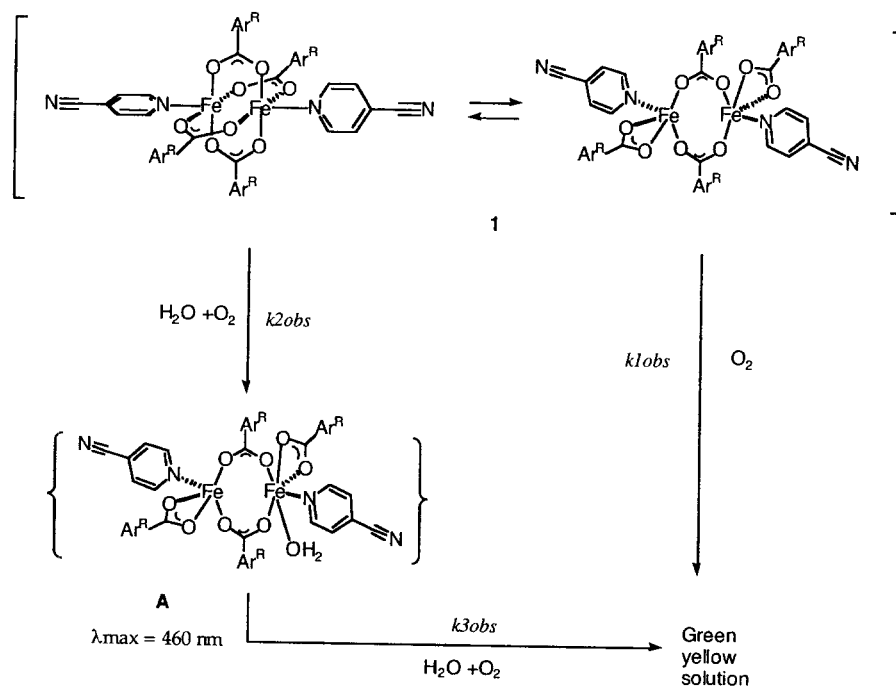


Scheme 8.3



Scheme 8.4





Scheme 8.5

## Appendix 1. Derivation of a mathematical model for eq 2.

The reaction is



where W is  $[\text{Fe}_2(\mu\text{-O}_2\text{CAr}^{\text{Tot}})_2(\text{O}_2\text{CAr}^{\text{Tot}})_2(\text{THF})_2]$

Keq can be defined by

$$\text{Keq} = \frac{[\text{W}][4\text{-NCC}_5\text{H}_4\text{N}]^2}{[\text{1}][\text{THF}]^2} \quad (\text{II})$$

where [THF] is a constant as 12.2 M.

$$[\text{T}] = [\text{1}] + [\text{W}] \quad (\text{III})$$

where [T] is a constant as total diiron(II) concentration.

$$[4\text{-NCC}_5\text{H}_4\text{N}] = 2 \cdot [\text{W}] \quad (\text{IV})$$

Applying eq II with eq III and eq IV gives

$$\text{Keq} = \frac{4([\text{T}] - [\text{1}])^3}{148.84[\text{1}]} \quad (\text{V})$$

$$\text{Absorbance (A)} = \epsilon_1[\text{1}] + \epsilon_w[\text{W}] \quad (\text{VI})$$

where  $\epsilon_1$  = extinction coefficient of 1 and  $\epsilon_w$  = extinction coefficient of W = 0.

Applying eq VI with eq III

$$[\text{1}] = A/\epsilon_1 \quad (\text{VII})$$

Since

$$-RT \ln(\text{Keq}) = \Delta H - T\Delta S$$

We can write

$$-R \ln\left(\frac{4([\text{T}] - (A/\epsilon_1))^3}{148.84((A/\epsilon_1))}\right) = \Delta H/T - \Delta S$$

Solving for 1/T vs A gives us

$$1/T = \Delta S/\Delta H - (R \ln\left(\frac{4([\text{T}] - (A/\epsilon_1))^3}{148.84((A/\epsilon_1))}\right))/\Delta H \quad (\text{VIII})$$

## Appendix 2. Derivation of a mathematical model for eq 3.

The reaction is



where A is a  $\{1 \cdot \text{H}_2\text{O}\}$  adduct

Keq can be defined by

$$\text{Keq} = ([\text{A}] \cdot [\text{H}_2\text{O}]) / ([1] \cdot [\text{H}_2\text{O}]^2) = [\text{A}] / ([1] \cdot [\text{H}_2\text{O}]) \quad (\text{II})$$

$$[\text{T}] = [1] + [\text{A}] \quad (\text{III})$$

where [T] is a constant as total diiron(II) concentration.

$$[\text{H}_2\text{O}] = 2 \cdot [\text{T}] - [\text{A}] = [\text{T}] + [1] \quad (\text{IV})$$

Applying eq II with eq III and eq IV gives

$$\text{Keq} = ([\text{T}] - [1]) / \{([\text{T}] + [1]) \cdot [1]\} \quad (\text{V})$$

$$\text{Absorbance (a)} = \epsilon_1[1] + \epsilon_w[\text{A}] \quad (\text{VI})$$

where  $\epsilon_1$  = extinction coefficient of 1 and  $\epsilon_A$  = extinction coefficient of A.

Applying eq VI with eq III

$$[1] = (a + \epsilon_A[\text{T}]) / (\epsilon_1 - \epsilon_A) \quad (\text{VII})$$

Since

$$-RT \ln(\text{Keq}) = \Delta H - T \Delta S$$

We can write

$$\begin{aligned} -R \ln \{ ([\text{T}] - \{(a + \epsilon_A[\text{T}]) / (\epsilon_1 - \epsilon_A)\}) / \{ ([\text{T}] + \{(a + \epsilon_A[\text{T}]) / (\epsilon_1 - \epsilon_A)\}) \cdot \{(a + \epsilon_A[\text{T}]) / (\epsilon_1 - \epsilon_A)\} \} \} \\ = \Delta H / T - \Delta S \end{aligned}$$

Solving for  $1/T$  vs. a gives us

$$1/T = \Delta S / \Delta H$$

$$- (R \ln \{ ([\text{T}] - \{(a + \epsilon_A[\text{T}]) / (\epsilon_1 - \epsilon_A)\}) / \{ ([\text{T}] + \{(a + \epsilon_A[\text{T}]) / (\epsilon_1 - \epsilon_A)\}) \cdot \{(a + \epsilon_A[\text{T}]) / (\epsilon_1 - \epsilon_A)\} \} \} ) / \Delta H \quad (\text{VIII})$$

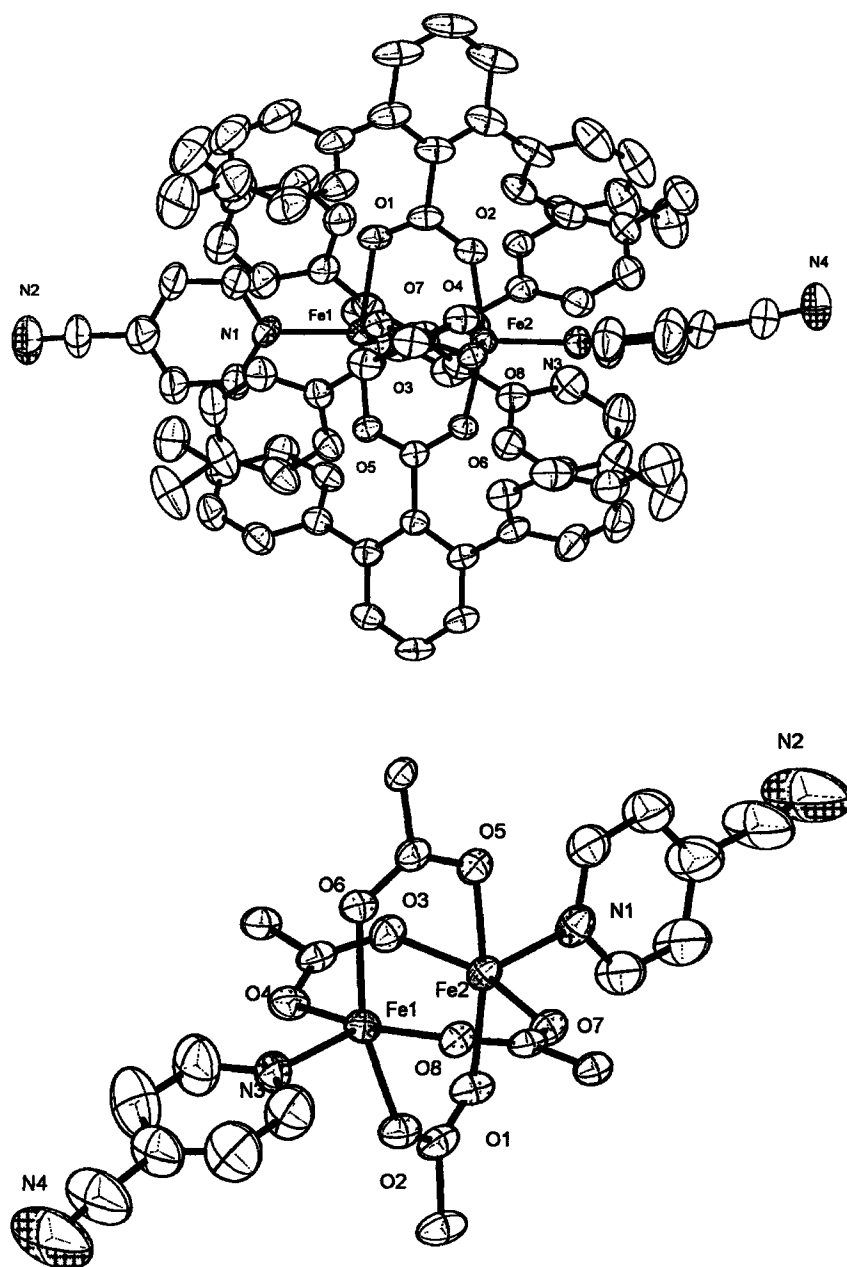


**Figure 8.1.** Top: ORTEP diagram of  $[\text{Fe}_2(\mu\text{-O}_2\text{CAr}^{\text{Tol}})_4(4\text{-CNC}_5\text{H}_4\text{N})_2]$  (1) showing 50 % probability thermal ellipsoids for all non-hydrogen atoms. Bottom: The aromatic rings of  $\text{Ar}^{\text{Tol}}\text{CO}_2^-$  ligands are omitted for clarity.

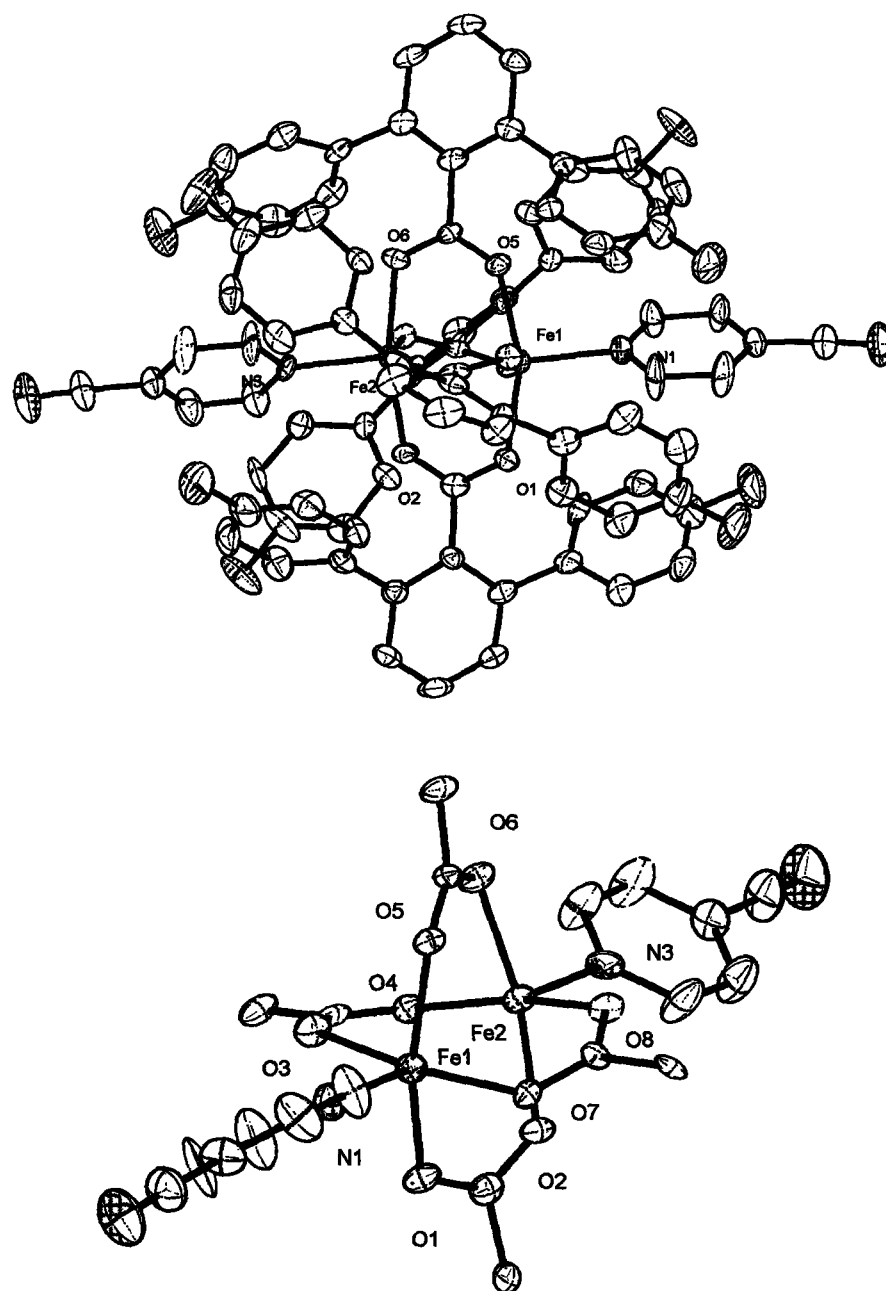


**Figure 8.2.** ORTEP diagram of  $[\text{Fe}_2(\mu\text{-O}_2\text{CAr}^{\text{AF-Ph}})_4(4\text{-CNC}_5\text{H}_4\text{N})_2]$  (2) showing 50 % probability thermal ellipsoids for all non-hydrogen atoms. Bottom: The aromatic rings of  $\text{Ar}^{\text{AF-Ph}}\text{CO}_2^-$  ligands are omitted for clarity.

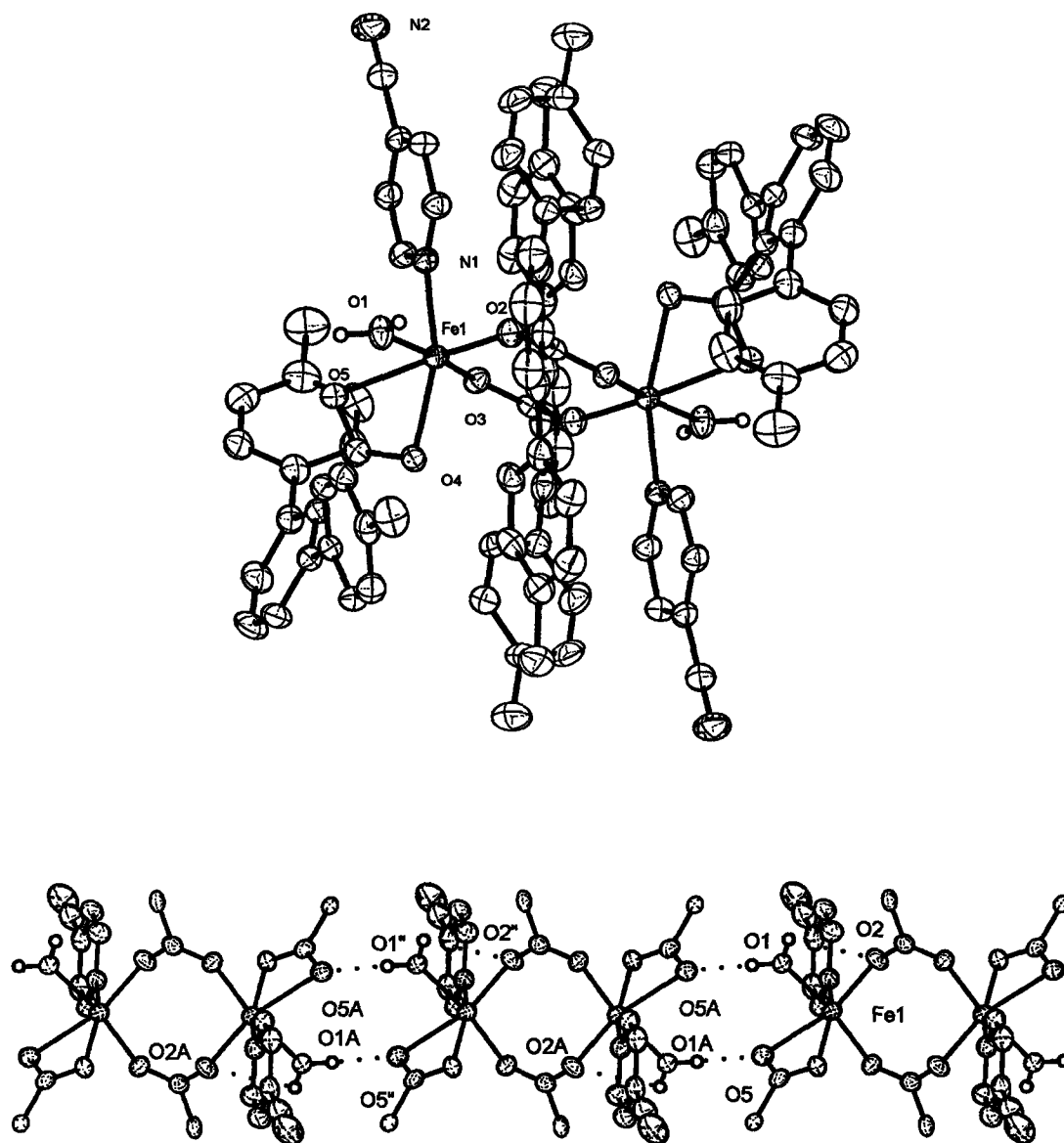


**Figure 8.3.** Top: ORTEP diagram of  $[\text{Fe}_2(\mu\text{-O}_2\text{CAr}^{\text{Tot}})_2(\text{O}_2\text{CAr}^{\text{Tot}})_2(4\text{-CNC}_5\text{H}_4\text{N})_2(\text{OH}_2)_2]$  (3) showing 50 % probability thermal ellipsoids for all non-hydrogen atoms. Bottom: The aromatic rings of  $\text{Ar}^{\text{Tot}}\text{CO}_2^-$  ligands are omitted for clarity.

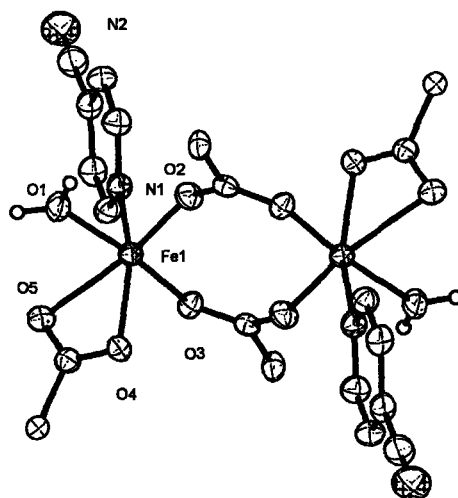
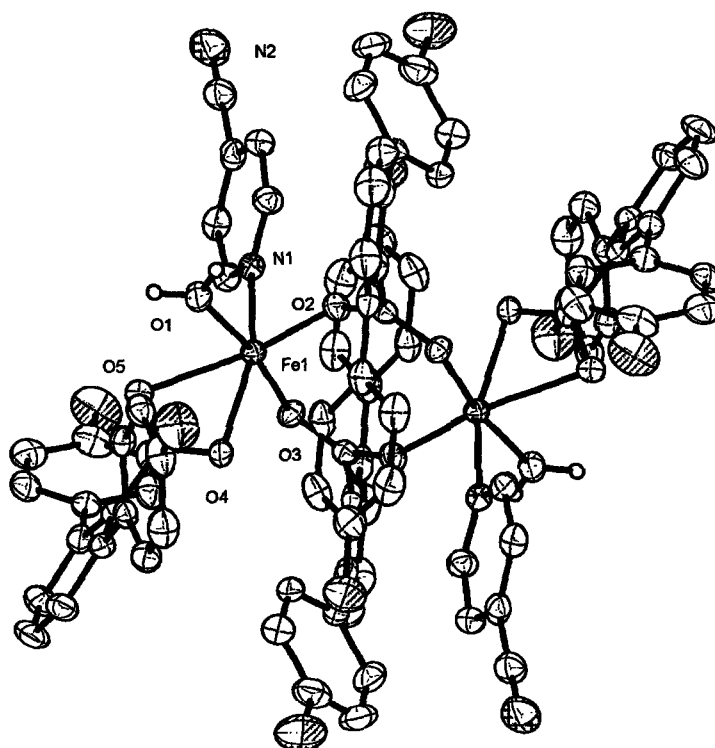


**Figure 8.4.** Top: ORTEP diagram of  $[\text{Fe}_2(\mu\text{-O}_2\text{CAR}^{4\text{F-Ph}})_2(\text{O}_2\text{CAR}^{4\text{F-Ph}})_2(4\text{-CNC}_5\text{H}_4\text{N})_2(\text{OH}_2)_2]$  (4) showing 50 % probability thermal ellipsoids for all non-hydrogen atoms. Bottom: The aromatic rings of  $\text{Ar}^{4\text{F-Ph}}\text{CO}_2^-$  ligands are omitted for clarity.

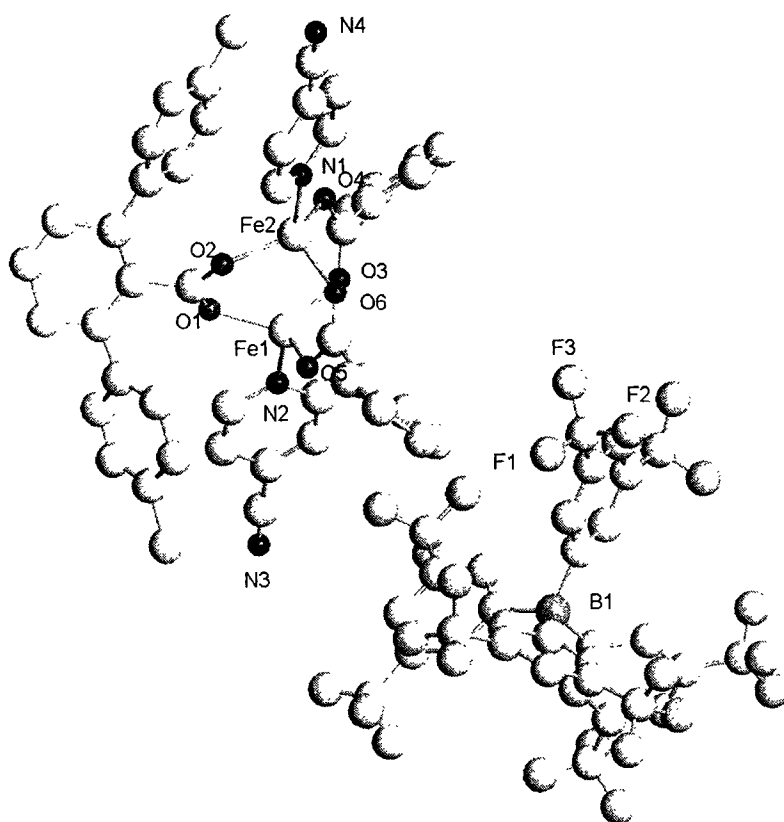


**Figure 8.5.** Ball and stick diagram of  $[\text{Fe}_2(\mu\text{-O}_2\text{CAr}^{\text{Tol}})_3(4\text{-CNC}_5\text{H}_4\text{N})_2][\text{BAr}'_4]$  (5) for all non-hydrogen atoms.



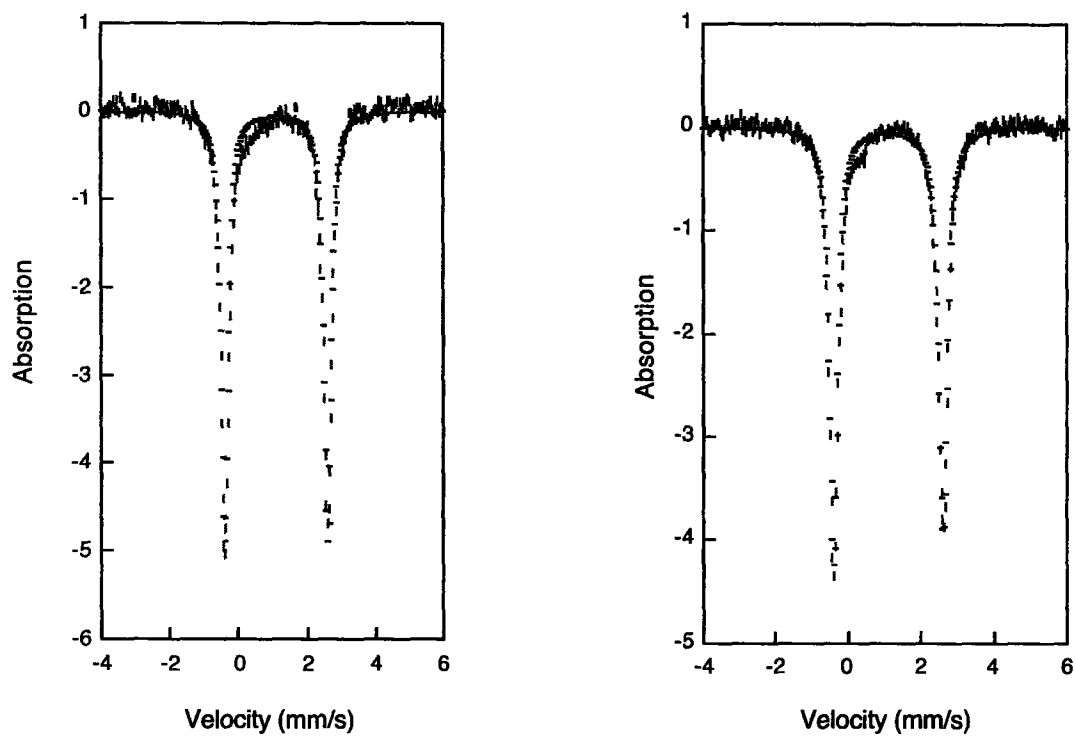


**Figure 8.6.** Mössbauer spectra (experimental data (|), calculated fit (—)) recorded at 4.2 K for a solid sample of  $[\text{Fe}_2(\mu\text{-O}_2\text{CAr}^{\text{Tol}})_4(4\text{-CNC}_5\text{H}_4\text{N})_2]$  (1) and  $[\text{Fe}_2(\mu\text{-O}_2\text{CAr}^{4\text{F-Ph}})_4(4\text{-CNC}_5\text{H}_4\text{N})_2]$  (2). Left to Right

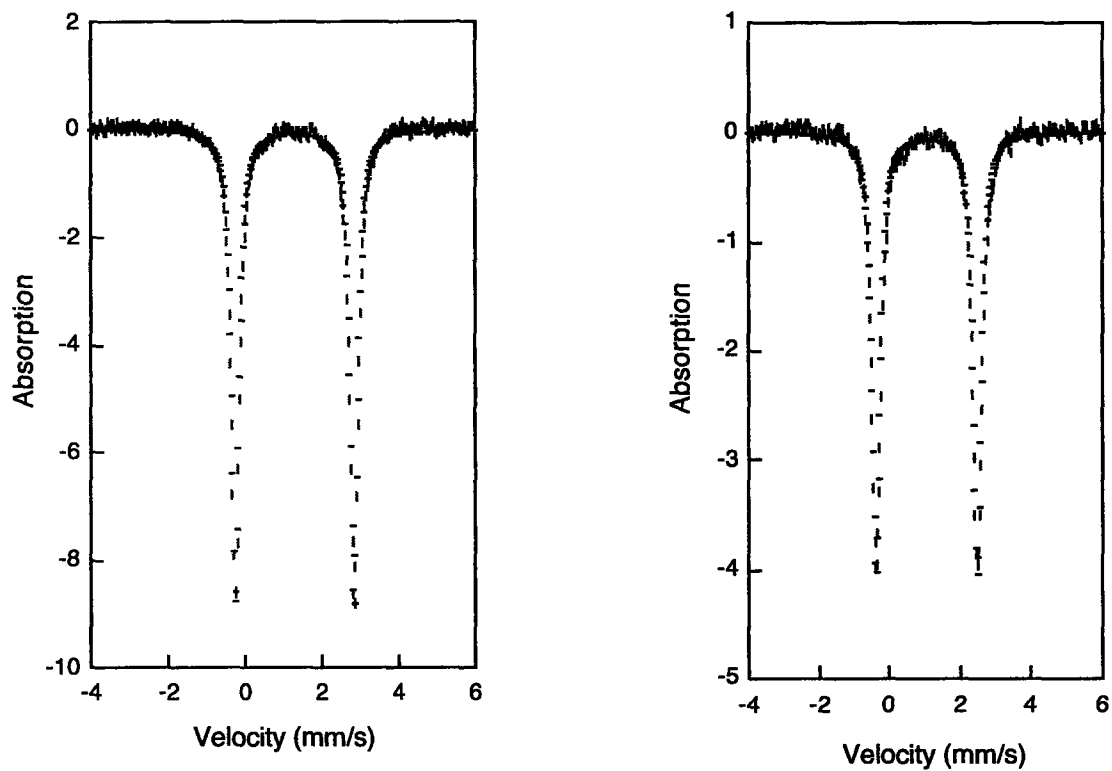


Figure 8.7. Mössbauer spectra (experimental data (|), calculated fit (-)) recorded at 4.2 K for a solid sample of 3 and 5. Left to Right

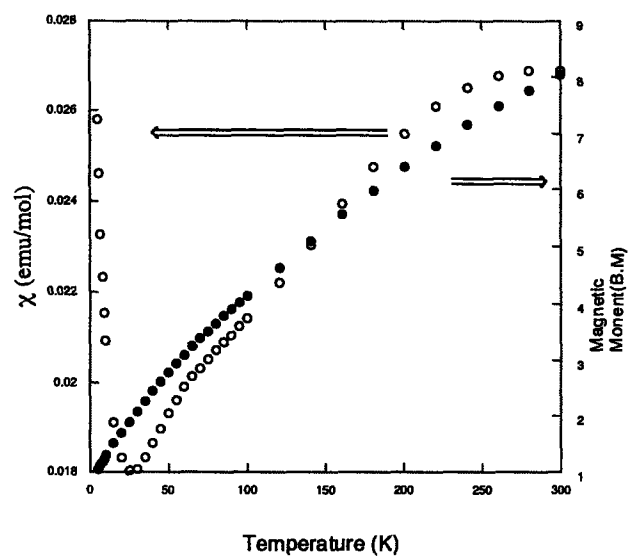
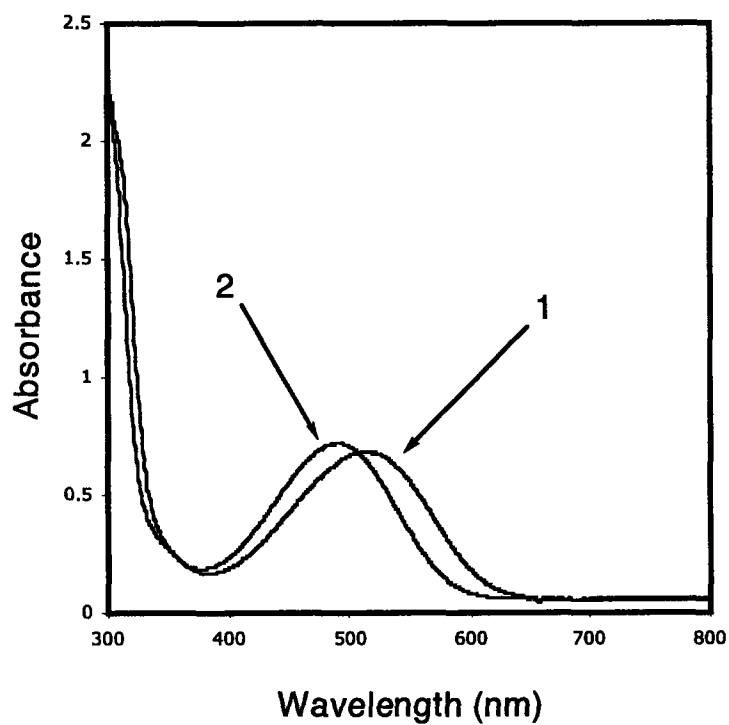
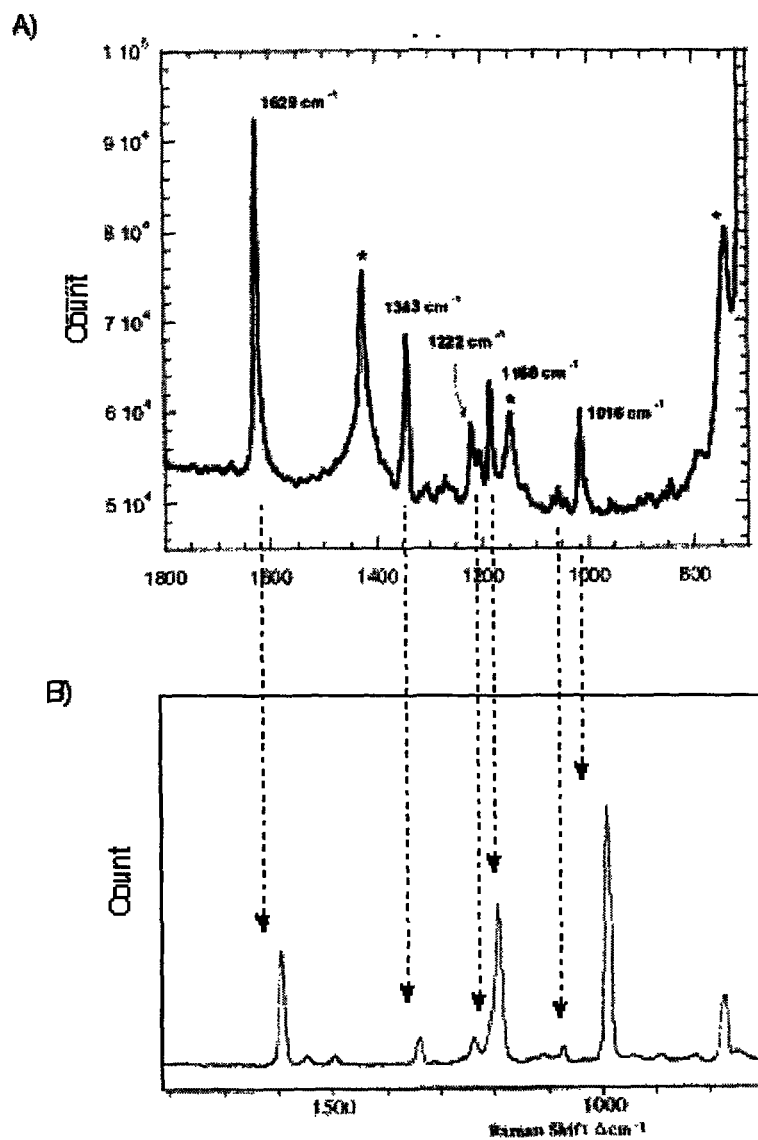


Figure 8.8. Plots of  $\chi_M$  (o) and  $\mu_{\text{eff}}$  (•) vs T for solid  $[\text{Fe}_2(\mu\text{-O}_2\text{CAr}^{\text{Tol}})_4(4\text{-CNC}_5\text{H}_4\text{N})_2]$  (1).



**Figure 8.9.** UV-vis spectra of  $[\text{Fe}_2(\mu\text{-O}_2\text{CAr}^{\text{Tol}})_4(4\text{-CNC}_5\text{H}_4\text{N})_2]$  (1) and  $[\text{Fe}_2(\mu\text{-O}_2\text{CAr}^{\text{4F-Ph}})_4(4\text{-CNC}_5\text{H}_4\text{N})_2]$  (2) in  $\text{CH}_2\text{Cl}_2$ .



**Figure 8.10.** A) Resonance Raman spectrum of a  $\text{CH}_2\text{Cl}_2$  solution of  $[\text{Fe}_2(\mu\text{-O}_2\text{CAr}^{\text{Tol}})_4(4\text{-CNC}_5\text{H}_4\text{N})_2]$  (1) at 23 °C. The asterisk indicates a solvent band. B) Resonance Raman spectrum of 4-CNC<sub>5</sub>H<sub>4</sub>N at 23 °C (Literature data).

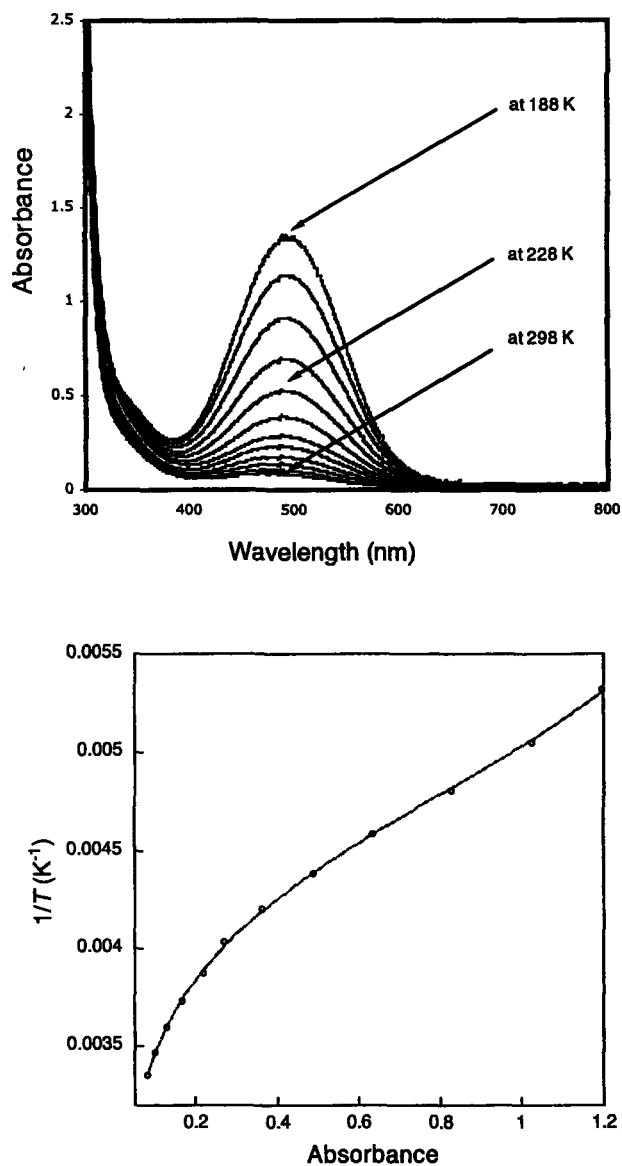


**Figure 8.11.** (Top) UV-vis spectra of  $[\text{Fe}_2(\mu\text{-O}_2\text{CAr}^{\text{Tot}})_4(4\text{-CNC}_5\text{H}_4\text{N})_2]$  (1) in THF, measured at variable temperatures. (Bottom) The absorbance change at 490 nm was fit to eq (2)

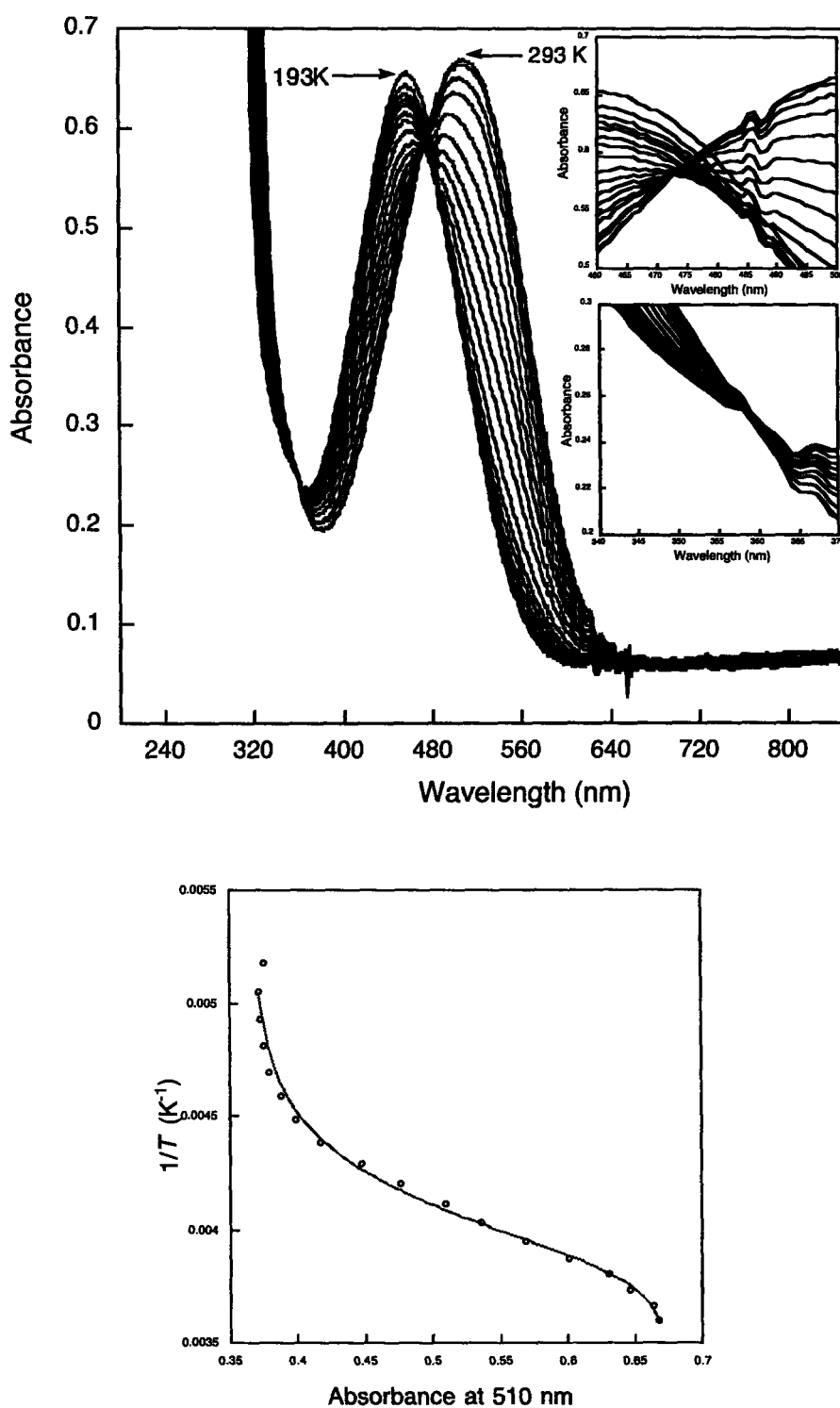


**Figure 8.12.** (Top) UV-vis spectra of  $[\text{Fe}_2(\mu\text{-O}_2\text{CAr}^{\text{Tol}})_4(4\text{-CNC}_5\text{H}_4\text{N})_2]$  (3) in  $\text{CH}_2\text{Cl}_2$ , measured at variable temperatures. (Bottom) The absorbance change at 510 nm was fit to eq (3)

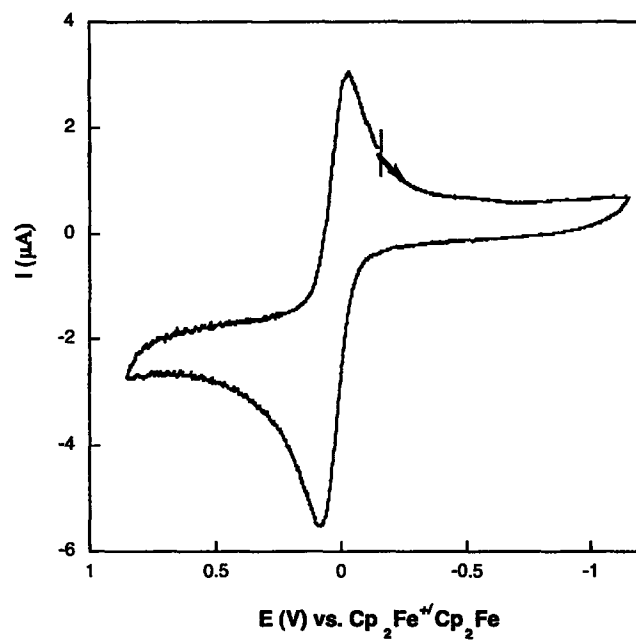


**Figure 8.13.** Cyclic voltammograms of  $[\text{Fe}_2(\mu\text{-O}_2\text{CAr}^{\text{Tol}})_4(4\text{-CNC}_5\text{H}_4\text{N})_2]$  (**1**) in  $\text{CH}_2\text{Cl}_2$  with 0.5 M  $(\text{Bu}_4\text{N})\text{PF}_6$  as supporting electrolyte and a scan rate of 50 mV/s.



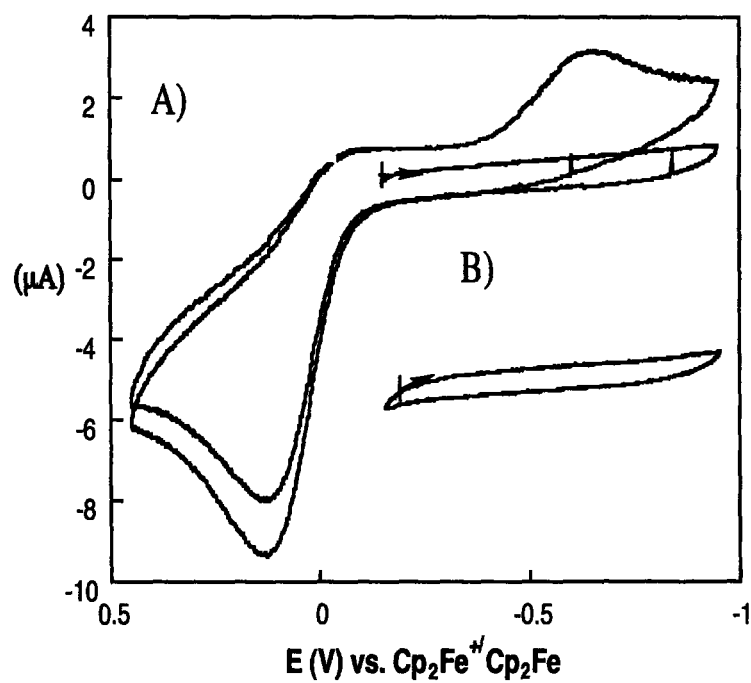


**Figure 8.14.** Cyclic voltammograms of  $[\text{Fe}_2(\mu\text{-O}_2\text{CAr}^{\text{Tol}})_2(\text{O}_2\text{CAr}^{\text{Tol}})_2(4\text{-CNC}_5\text{H}_4\text{N})_2(\text{OH}_2)_2]$  (3) in  $\text{CH}_2\text{Cl}_2$  with 0.5 M  $(\text{Bu}_4\text{N})\text{PF}_6$  as supporting electrolyte and a scan rate of 50 mV/s.

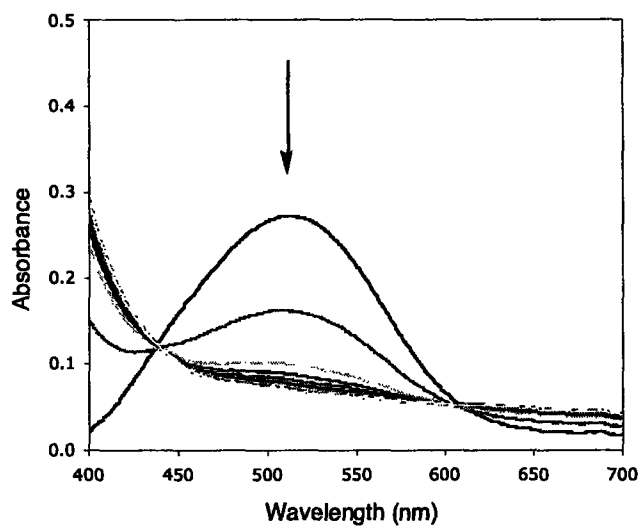


**Figure 8.15.** Spectral changes occur during oxygenation of **1** ( $1.74 \times 10^{-4}$  M) without water in  $\text{CH}_2\text{Cl}_2$  at  $0^\circ\text{C}$  over 20 sec.

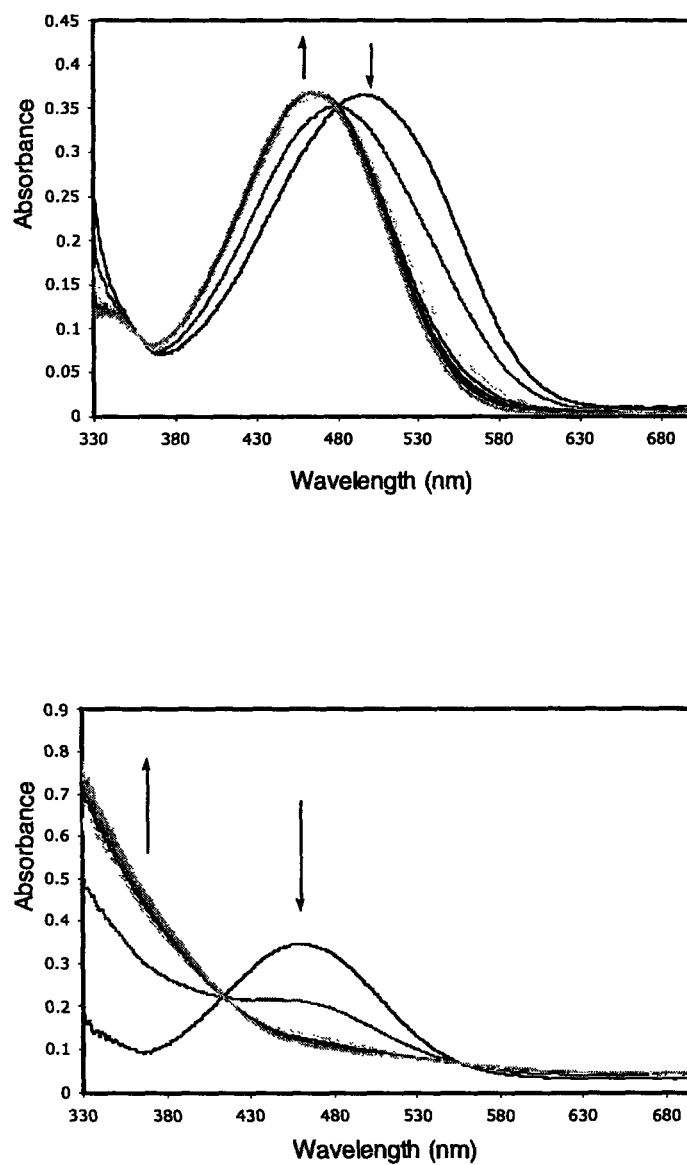


**Figure 8.16.** (Top) Spectral changes that occur during the hydration of **1** ( $1.60 \times 10^{-4}$  M) with dioxygen and water in  $\text{CH}_2\text{Cl}_2$  at  $-60$  °C over 1 sec. (Bottom) Spectral changes that occur during oxygenation of **1** ( $1.60 \times 10^{-4}$  M) with dioxygen and water in  $\text{CH}_2\text{Cl}_2$  at  $-20$  °C over 10 sec.

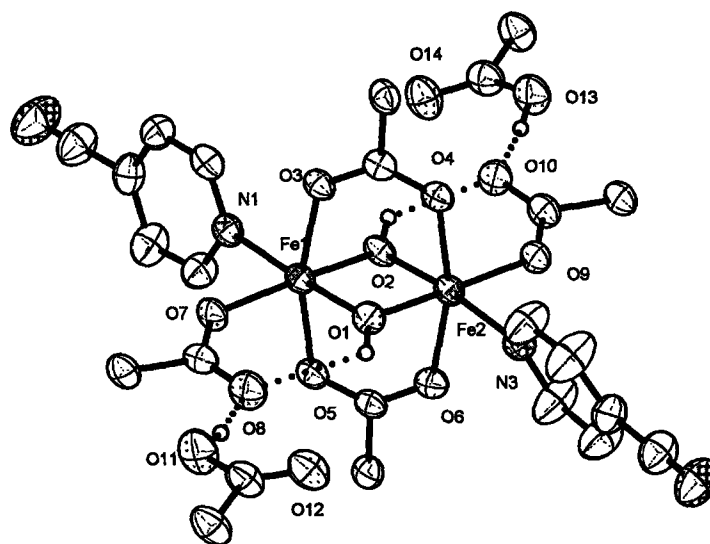
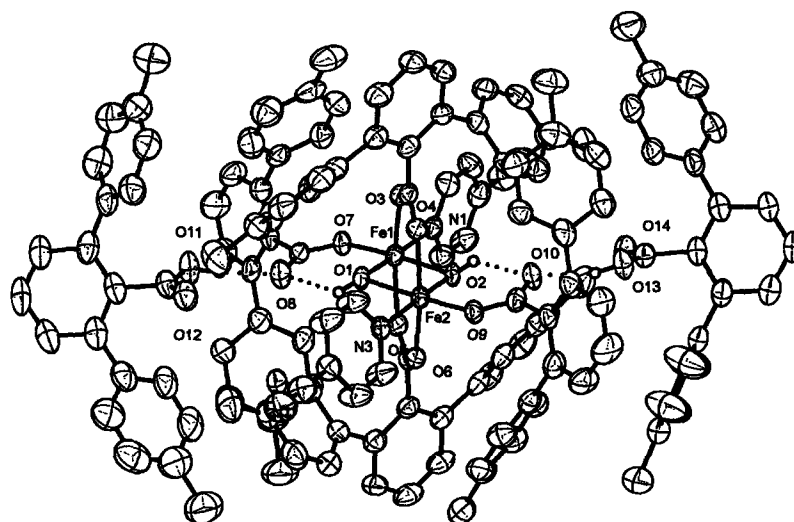


**Figure 8.17.** Top: ORTEP diagram of  $[\text{Fe}_2(\mu\text{-OH})_2(\mu\text{-O}_2\text{CAr}^{\text{Tol}})_2(\text{O}_2\text{CAr}^{\text{Tol}})_2(4\text{-CNC}_5\text{H}_4\text{N})_2(\text{OH}_2)_2] \cdot 2(\text{HO}_2\text{CAr}^{\text{Tol}})_2$  (**6**) showing 50 % probability thermal ellipsoids for all non-hydrogen atoms. Bottom: The aromatic rings of  $\text{Ar}^{\text{Tol}}\text{CO}_2^-$  ligands are omitted for clarity.

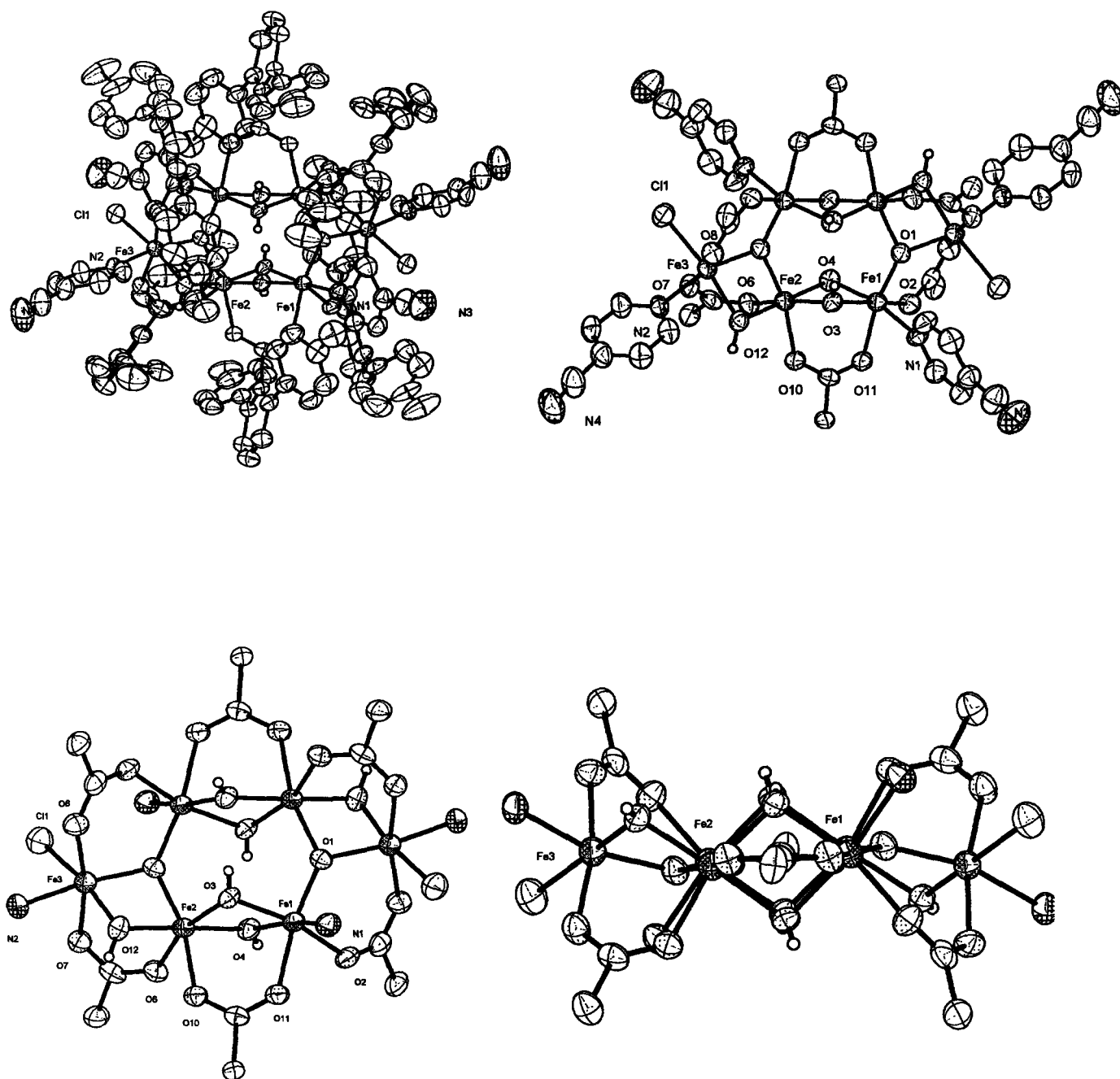


**Figure 8.18.** Top left: ORTEP diagram of 7 showing 50 % probability thermal ellipsoids for all non-hydrogen atoms. Top Right: The aromatic rings of Ar<sup>Tol</sup>CO<sub>2</sub><sup>-</sup> ligands are omitted for clarity. Bottom: The aromatic rings of Ar<sup>Tol</sup>CO<sub>2</sub><sup>-</sup> and 4-CNC<sub>5</sub>H<sub>4</sub>N ligands are omitted for clarity